UNIVERSIDAD Ð LA LAGUNA
Departamento de Astrofísica

Characterising exoplanet atmospheres by means of high-resolution spectroscopy

Memoria que presenta
Núria Casasayas Barris
para optar al grado de
Doctora en Ciencias Físicas.

INSTITUTO Ð ASTROFISICA Ð CANARIAS
San Cristóbal de la Laguna
diciembre de 2020

Examination date: November, 2020
Thesis supervisor: Prof. Enric Pallé & Dr. Guo Chen

ISBN: xx-xxx-xxxx-x
Depósito legal: TF-xxxx/2020
published Some of the material included in this document has been already published in *Astronomy & Astrophysics*.

A la meva mare.
Per encendre els llums quan s'ha fet fosc,
i encendre'ls sempre de colors.

Acknowledgements

First of all, I would like to thank my supervisors for all their support and help during these four years. A l'Enric, per agafar-se rient el meu mal humor i, sobretot, per creure en mi des del primer dia. To Guo, who knew exactly the moments I needed a dose of self-confidence. And to Fei, my non-official supervisor but the person who helped me more; this thesis is also yours.

Per altra banda, vull donar les gràcies a la meva família. A la meva germana i la meva mare, per estar sempre orgulloses de mi i no poder-ho amagar. Al meu pare, a qui he trobat a faltar infinites vegades per explicar-li què feia. Sé que t'hauria agradat. Als meus avis, per no descuidar-se mai de demanar què fan els planetes de les canàries i fer-se els sorpresos quan havia de tornar a marxar. Al Jaume, el meu suport durant aquest camí; amb qui vaig començar aquesta aventura fa més de 5 anys i amb qui vull seguir compartint-les totes. I per suposat, a l'Urà, per obligar-me a desconnectar sí o sí.

A la Maria, la Mònica, el Bernat i a la Bach, per totes les seves visites i tenir sempre els braços oberts per veure'm a les tornades. A mi familia de doctorado: la Paula, la Núria, la Vir, Federica, Nacho, Rafa, Punam, Héctor, Raúl y Virginia. Por cada aventura, tarde de juegos, excursión, cumpleaños... por hacerse imprescindibles y convertir Tenerife en un hogar. A Jonathan, el explorador más intrépido y mi gran amigo. Quien demostró que un océano no es suficiente para separarnos. Y a Elena, por creer más en mi que yo misma.

Not less important, to the whole exoplanets group at IAC. I could not have been in a better group, and this would not have been the same without them. Especially, to my little sister-in-science, Monika, for fighting together until the end. To Felipe, the person that helped me to plot my first high-resolution spectrum. To Mahmoud, who just started working with us but has become a necessary person and a friend. And to Víctor, who I think now believes more in exoplanet atmospheres.

Núria

Resumen

Después de tres décadas desde el primer descubrimiento de un planeta extrasolar, el número de descubrimientos ha aumentado de forma exponencial hasta llegar a los más de 4000 exoplanetas conocidos en la actualidad. Esta rápida evolución ha sido debida, principalmente, al lanzamiento de dos misiones espaciales especializadas en la búsqueda masiva de exoplanetas: Kepler y TESS.

El descubrimiento de los primeros planetas motivó rápidamente el estudio de la composición de sus atmósferas. La mayor dificultad para su análisis con observaciones directas, sin embargo, era debida al gran contraste planeta-estrella. Afortunadamente, pocos años después se descubrió un valioso grupo de planetas que haría posible la primera detección de una atmósfera exoplanetaria: los planetas transitantes del tipo Júpiter caliente. Este grupo está formado principalmente por planetas del tamaño de Júpiter con órbitas de pocos días muy cercanas a su estrella, los cuales tienen alta probabilidad de transitar en algún punto de su órbita. Un tránsito ocurre cuando el planeta pasa entre la estrella y la línea de visión del observador. Durante un tránsito, una pequeña fracción de la luz de la estrella pasa a través de la atmósfera del planeta que, dependiendo de su composición, actúa como filtro e imprime pequeñas señales en el espectro estelar. Este método se llama espectroscopía de transmisión.

Esta tesis se centra en la búsqueda y caracterización de señales debidas a la atmósfera de los exoplanetas, el llamado espectro de transmisión, usando observaciones con espectrógrafos de muy alta resolución. En particular, se analizan las observaciones de cuatro planetas diferentes. Durante los últimos años, la espectroscopía de alta resolución se ha convertido en una de las técnicas más potentes para el estudio de atmósferas planetarias, dada su capacidad para resolver líneas individuales en el espectro de transmisión.

El primer planeta analizado en esta tesis es el Júpiter caliente HD 189733b, el primero con una detección de sodio neutro (NaI) usando espectroscopía en alta resolución. Aquí, con el uso de datos de archivo del instrumento HARPS

y siguiendo la metodología de estudios previos, se reproduce la detección de NaI junto con una pequeña mejora de la corrección de la contaminación de la atmósfera terrestre, enfatizando la importancia del movimiento de la Tierra durante las observaciones. En paralelo, la misma metodología se aplica a nuevas observaciones con HARPS-N del planeta tipo Saturno WASP-69b. Los resultados muestran NaI en su atmósfera, aunque sólo se resuelve una línea del doblete, probablemente debido a la baja señal-a-ruido de los datos. Este análisis considera, por primera vez, el impacto en el espectro de transmisión de dos efectos que ocurren durante el tránsito: la variación centro-limbo (CLV) y el efecto Rossiter-McLaughlin (RM). Estos efectos se deben al bloqueo por parte del planeta de luz proveniente de diferentes regiones del disco estelar con diferentes características. Su impacto depende de la geometría del sistema, la velocidad de rotación de la estrella y su tipo espectral. Aunque en este estudio el impacto de estos efectos es irrelevante, se subraya su importancia en estudios atmosféricos. Estos resultados se detallan en Casasayas-Barris et al. (2017).

El tercer planeta analizado en esta tesis es el Júpiter ultra caliente llamado MASCARA-2b, caracterizado por una temperatura de equilibrio de unos 2300 K. Las observaciones obtenidas con HARPS-N durante un solo tránsito del planeta sugieren la presencia de NaI y hidrógeno en su atmósfera, y una alta temperatura en su atmósfera superior. Los resultados se presentan en Casasayas-Barris et al. (2018). Con la combinación de dos observaciones más con HARPS-N y una con CARMENES, las señales tentativas son confirmadas, junto con la primera detección del triplete de calcio ionizado y líneas de hierro ionizado. Los resultados confirman las predicciones teóricas de que las atmósferas de los Júpiter ultra calientes están parcialmente formadas por iones provenientes de su hemisferio extremadamente caliente donde el día es permanente. Además, este estudio muestra la importancia de realizar un análisis en dos dimensiones de los resultados como confirmación de su origen planetario y la visualización de otros efectos estelares, como es el caso del RM y CLV. Estos resultados se detallan en Casasayas-Barris et al. (2019).

Finalmente, se estudia la atmósfera de HD 209458b, uno de los exoplanetas más famosos. En este análisis se usan datos de archivo de HARPS-N y CARMENES, así como observaciones de tiempo garantizado obtenidas con ESPRESSO. Los resultados se muestran en Casasayas-Barris et al. (2020a,b). En contraste con estudios previos donde se detecta NaI en su atmósfera, las nuevas observaciones muestran resultados consistentes con el impacto de los efectos del RM y CLV en el espectro de transmisión del planeta, sin la necesidad de considerar ninguna contribución debida a su atmósfera. En este estudio se acentúa la importancia de considerar estos efectos en la extracción de los espectros de transmisión con el uso de observaciones en alta resolución espectral.

Abstract

After three decades of the discovery of the first extrasolar planet, the number of known exoplanets has grown exponentially to more than 4000. This rapid evolution in the number of discoveries has been mainly produced by the launch of the two most effective planet-hunter missions, Kepler and TESS, which have been performing a massive search of exoplanets from space.

The discovery of the first exoplanets motivated the study of their atmospheres. However, the main difficulty when attempting to detect exoplanet atmospheres using direct observations is the large planet-to-star contrast ratio. Fortunately, a very valuable sample of exoplanets was discovered soon thereafter, the transiting planets, which made possible the first detection of an exoplanet atmosphere. This sample is mainly formed by close-in planets with short orbital periods, which have a higher probability to present transit events at a given time along their orbit. Transits occur when an exoplanet crosses the stellar disc with respect of the observer's line-of-sight. During the transit of an exoplanet, part of the stellar light goes through the exoplanet atmosphere and, depending on the composition of the atmosphere, faint spectral features will be imprinted in the stellar spectrum that we observe. This methodology is called transmission spectroscopy.

This thesis is focused on the search and characterisation of atmospheric signals from the exoplanet atmosphere, the transmission spectrum, using high resolution transmission spectroscopy observations of four different exoplanets. During the last few years, high resolution spectroscopy has become one of the most used and powerful techniques to study the exoplanets atmosphere, due to its capability to resolve single spectral lines in the transmission spectrum.

The first exoplanet analysed in this thesis is the hot Jupiter HD 189733b, a benchmark exoplanet on which the first detection of neutral sodium (NaI) using high resolution spectroscopy observations was reported. Using HARPS archival data and following the methodology from previous studies, we repro-

duce the NaI detection in the transmission spectrum and slightly improve the correction of the Earth atmospheric contamination, while pointing out the importance of considering the Earth's movement during the night. In parallel, this same methodology is applied to new HARPS-N observations of the Saturn-mass planet WASP-69b, resulting in the detection of NaI, but only resolving one line of the doublet, probably due to the signal-to-noise ratio of the observations. This analysis considers, for the first time, the impact of two transit effects that modify the transmission spectrum of an exoplanet: the centre-to-limb variation (CLV) and the Rossiter-McLaughlin (RM) effect. During the transit, the exoplanet blocks the light from different regions of the stellar surface which have different characteristics. This lack of flux results in a deformation of the stellar spectral lines that is propagated to the transmission spectrum. Its impact depends on the geometry of the system, the rotational velocity of the star, and the spectral type. Although in this study the effects remain at the noise level precision of the observations, their importance in atmospheric studies is stressed out. These results are compiled in Casasayas-Barris et al. (2017).

The third exoplanet is the ultra hot Jupiter MASCARA-2b, which has an equilibrium temperature around 2300 K. The observations performed with HARPS-N during only one transit of the exoplanet suggest the presence of NaI and hydrogen in its atmosphere, and a high temperature in the upper atmosphere. The results of this study are presented in Casasayas-Barris et al. (2018). After two more transit observations with HARPS-N and one with CARMENES, the suggested features are confirmed, together with the first detection of the ionised calcium triplet and ionised iron lines. The results confirm the theoretical predictions that the upper atmosphere of ultra hot Jupiters is made up of ions probably coming from their extremely hot permanent day-side. On the other hand, this study shows the importance of a two-dimensional tomographic analysis of the different species as a confirmation of their planetary origin, and the visualisation of other stellar effects such as the RM and CLV. These last results are detailed in Casasayas-Barris et al. (2019).

Finally, HD 209458b, one of the most famous exoplanets, is studied using HARPS-N and CARMENES archival data, and ESPRESSO Guaranteed Time Observations. The results are compiled in Casasayas-Barris et al. (2020a,b). In contrast with previous studies claiming a NaI detection, our results are consistent with the modelled RM and CLV effects on the stellar lines, without considering the contribution from the exoplanet atmosphere. In this study we stress the importance of accounting for these effects when attempting to extract the atmosphere of an exoplanet from high resolution observations.

Contents

1

Introduction

- Dad, do you think there's people on other planets?
- I don't know, Sparks. But I guess I'd say if it is just us... seems like an awful waste of space.

Contact, 1997

This thesis is focused on the atmospheric characterisation of extrasolar planets using high resolution spectroscopy observations. This chapter presents an overview of the field of exoplanets, which starts with the description of the most relevant aspects of the search for new worlds. Then, it moves to a general review of the current knowledge on exoplanet atmospheres in terms of theoretical and observational studies, and finishes with a dedicated section on the study of atmospheres using high resolution spectroscopy.

1.1 Looking for other worlds

One of humanity's most ancient questions is whether there is life elsewhere in the universe. It was only around thirty years ago, in 1992, when the two first extrasolar planets (exoplanets) were discovered around PSR 1257+12, a pulsar in the constellation of Virgo (Wolszczan & Frail, 1992). Three years later, in 1995, the first exoplanet orbiting a sun-like star, 51 Pegasi b, was discovered (Mayor & Queloz, 1995), and the discovery of the first transiting exoplanet, HD 209458b, came in the 2000s (Henry et al., 2000; Charbonneau et al., 2000). These discoveries became the starting point for the massive search for other worlds and alien life.

In the last three decades, the number of exoplanets discovered has grown

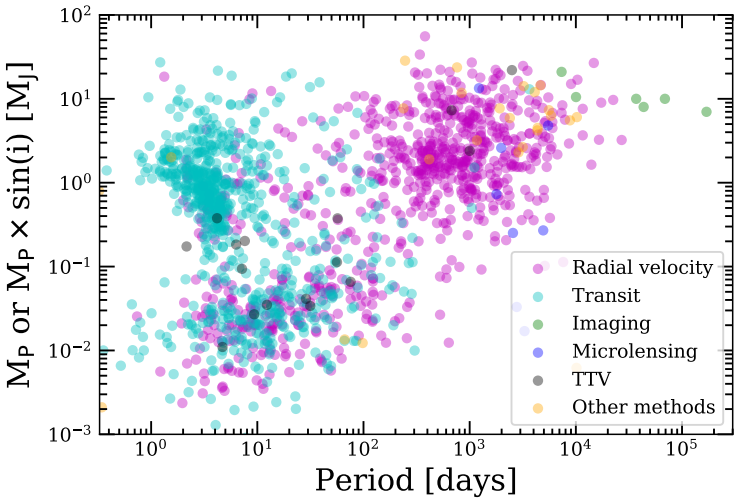

FIGURE 1.1— Confirmed exoplanets in terms of their mass and period. The different colours indicate the method used for their discovery. In "other methods" we include those with small number of discoveries such as astrometry, eclipse and pulsar timing variations, disc kinematics and orbital brightness modulation. Data extracted from the NASA Exoplanet Archive.

to more than 4000. Based on the NASA exoplanet exploration catalogue[1], at the moment of writing this thesis, there are 4164 confirmed planets and 5220 additional candidates. This rapid increment in the number of discoveries is mainly produced by two of the most effective planet-hunter missions: Kepler (Borucki et al., 2010) and TESS (Transiting Exoplanet Survey Satellite; Ricker et al. 2015). Before Kepler's launch in 2009, only around 600 exoplanets were known. After 10 years, the Kepler mission had discovered more than 2600 exoplanets of the 4000 known today. TESS, on the other hand, has discovered 51 new exoplanets since it was launched in 2018. In Figure 1.1 the confirmed exoplanets are shown, with different colours depending on the discovery method used. The efficiency of the transit and radial-velocity methods with respect the other methodologies can be clearly observed.

Among these thousands of planets discovered, the diversity is surprisingly high. Taking the Solar System as reference, we can distinguish between three

[1] https://exoplanetarchive.ipac.caltech.edu

big groups: terrestrial planets, gas and ice giants. Terrestrial planets are formed by metals and rocks, and have very thin or no atmospheres that have strongly evolved from their primitive stages. This is the case of Mercury, Venus, Earth and Mars in the Solar System. Gas giants (Jupiter and Saturn) are in between the terrestrial planets and brown dwarfs in terms of mass ($10\ M_{Earth} \lesssim M_p \lesssim 1000\ M_{Earth}$). The main components of their atmospheres are hydrogen and helium, with possible rocky cores. Finally, Uranus and Neptune are ice giants, which are basically composed by methane, water and ammonia ices, with a thinner atmosphere than gas giants. At least in the Solar System, the atmosphere of giant planets presents little evolution since their formation.

However, most known exoplanets do not present counterparts in the Solar System. This is the case, for example, of those terrestrial (or rocky) planets with masses between 1 and $10M_{\ Earth}$, also known as super-Earths. Between 10 and $15M_{\ Earth}$ we can define the mini Neptune region. Of particular interest have become those exoplanets located very close to their host stars, at distances smaller than Mercury from the Sun, and consequently completing an orbit around their host stars in only a few days. These planets have higher probability to present observable eclipses that allow the study of their atmosphere (see Section 1.3). This is the case for hot Jupiters and hot super-Earths.

Currently, the number of gas giants, Neptune-like planets and super-Earths is very similar ($\sim$ 30 % of all known planets), while the number of the terrestrial planets is around 5 %, but the discovery of these smaller planets remains biased by the fact that they are more difficult to be detected. One of the most surprising observations in exoplanet demographic studies was the large number of planets with radii larger than Earth but smaller than Neptune ($1.0\ R_{Earth} < R_p < 3.9\ R_{Earth}$; Batalha et al. 2013), namely mini-Neptunes, which are the most common exoplanet type in the *Kepler* sample, but are not present in the Solar System. One of the major questions related to these sub-Neptune sized planets is whether they are mostly rocky or present low-density envelopes that contribute to their size. Their discovery triggered different theoretical studies with the aim of solving this particular question (e.g. Wu & Lithwick 2013). After measuring the mass of a sample of planets, the derived low density values revealed that those planets with radius larger than $1.6\ R_{Earth}$ require gaseous envelopes, while those with smaller radius are consistent with a purely rocky composition (Rogers, 2015; Weiss & Marcy, 2014). At that moment, planet formation theories were not expecting this large number of intermediate planets, and could not predict their observed population. Only small planets that could not accrete enough material to become super-Earths, and those accreting all surrounding gas to become gas giant planets could be reproduced (Mordasini et al. 2009, among others). Nowadays, modern formation theories are able to

reproduce the super-Earth population (e.g. Mordasini et al. 2012; Hansen & Murray 2012).

In the Solar System, gas giants such as Jupiter and Saturn are cold planets, which are at very long distances from the Sun. Cold gas giants are common among the exoplanets discovered, but "hot Jupiters" whose sizes and masses are very similar to Jupiter and Saturn but having orbital periods of less than 10 days are also common. After the discovery of the first hot Jupiter, 51 Pegasi b (Mayor & Queloz, 1995), a challenge appeared when trying to form these close-in planets with the conventional giant planet formation theories (Pollack et al., 1996), based on the core-accretion mechanism. Despite the numerous efforts to resolve the problem of hot Jupiter formation, their origin is still an open question. With the evolution of the formation theories, three very broad formation pathways of close-in gas giants have emerged (Bailey & Batygin, 2018): smooth migration, violent migration and in-situ conglomeration. For the migration theories, the formation of giant planets occurs at large distances from their host star, similar to the Solar System planets. At the end of their primary accretion stage, the distance of the planet and the star suffers a large-scale decay, decreasing by a factor around 10^2 (Lin et al., 1996), due to interactions between the planet and its original disk (Kley & Nelson 2012; smooth migration), or planet-planet scattering (Naoz et al. 2011; violent migration), among others. When this distance is particularly small, the planet is tidally captured in a close-in orbit. In the in-situ approximation (Batygin et al., 2016) the migration is assumed to be limited, and the majority of planetary mass is accreted locally onto the planet (at separations of order of ~ 0.1 AU).

There are several observational ways to have insights into the formation histories of gas giants. On the one hand, one particularity of these planets is that they are composed of a combination of hydrogen and helium accreted during their formation from the protoplanetary disc. Consequently, their atmospheres are primordial and contain information about their formation conditions. Thus, the study of their composition can reveal information about their history, formation and evolution. On the other hand, with measurements of the spin-orbit angle of extrasolar systems (angle between the planet's orbit and the rotation axis of the host star) one can have an idea of the architecture of the systems, which is also related to their formation and evolution (Albrecht et al., 2012; Albrecht, 2012). The different migration mechanisms, for example, can move giant planets from their formation place, at several AU, to the position where we find the hot Jupiters, at less than 0.1 AU. Depending on the migration process, the spin-orbit angle of the system can be modified (e.g. Fabrycky & Tremaine 2007) or preserved (Lin et al., 1996). Therefore, the obliquity of the systems is a valuable measurement for planetary formation theories.

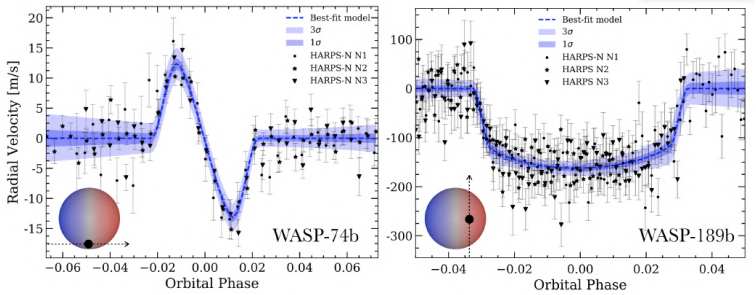

FIGURE 1.2— Radial-velocity time series of two systems, WASP-74b (*left*; Luque et al. 2020) and WASP-189b (*right*; Stangret et al. 2021 in prep.), where the RM anomaly is clearly observed. WASP-74 is an aligned system ($\lambda \sim 0^o$) with impact parameter $b = 0.9$ and $v \sin i_\star = 4\,\mathrm{km\,s^{-1}}$. WASP-189b is a polar planet with $\lambda \sim 90^o$, $b = 0.5$, which orbits a very fast rotating star ($v \sin_\star = 97\,\mathrm{km\,s^{-1}}$). Both results use the RM model from Ohta et al. (2005).

One of the most common techniques to obtain the obliquity of a system is by measuring the Rossiter-McLaughlin (RM) radial-velocity anomaly, firstly measured by Rossiter (1924) and McLaughlin (1924), and normally referred to as the classical RM. With time, other alternative methods have emerged, such as the Doppler tomography (Collier Cameron et al., 2010) and the reloaded-RM (Cegla et al., 2016a). These three methodologies are based on high resolution observations when the exoplanet transits the stellar disc. The main concept is that the stellar disc rotates with respect the observer, showing two different hemispheres: one red-shifted and the other blue-shifted. When the planet crosses the host star disc (transits), it blocks regions of the disc with different projected velocities. These hidden regions will be missing in the observed stellar spectrum, producing a deformation of the spectral lines. The RM has an strong dependence on the geometry of the system and the projected rotation velocity of the host star ($v \sin i_\star$). The impact of this effect on atmospheric studies is discussed in Section 1.4.3.

In the classical RM the radial-velocity change of the stellar lines caused by the deficit of flux on the blue or red-shifted hemispheres during the transit is measured: if the planet during the transit hides blue-shifted regions of the stellar disc, the observed spectral lines will be red-shifted and vice versa (see Figure 1.2). To a first order, when assuming a spin-orbit angle $\lambda \sim 0^o$, the

semi-amplitude of the RM effect can be estimated as follows (Triaud, 2017):

$$A_{RM} \simeq \frac{2}{3}\left(\frac{R_p}{R_\star}\right)^2 v \sin i_\star \sqrt{1-b^2}, \tag{1.1}$$

where b is the impact parameter, R_p is the planet radius, and $R_\star$ the radius of the star. For fast rotating stars and for big planets around small stars A_{RM} becomes larger, as in the latter case the planet blocks a larger part of the disc. These radial-velocity time series can be analytically described (see Ohta et al. 2005; Hirano et al. 2011 models for example), and used to fit the observations and estimate the main parameters such as λ.

The Doppler tomography technique is based on studying the line shape variations during the transit of an exoplanet. After removing the mean line shape obtained with observations performed when the planet is not transiting, the dark inhomogeneities of the stellar surface (the exoplanet) appear as positive bumps that change their position in radial-velocity depending on the position of the exoplanet on the stellar disc. The evolution of this bump trace produces a signal called *Doppler shadow*, which can then be modelled using similar parameters to those used for the classical RM effect. Finally, the reloaded-RM relies on reconstructing the velocity field that the planet obscures during the transit, studying the lines profile. This methodology is sensitive to differential rotation, can recover the real inclination of the star $i_\star$, and accounts for other stellar effects such as the convective blueshift and limb-darkening variations. Recently, Bourrier et al. (2017) reported that classical RM measurements of λ could be strongly biased due to changes in the lines' profile.

Comparing spin-orbit measurements for different systems, Winn et al. (2010) suggested that hot stars with transiting hot Jupiters present a broad range of obliquities, while cooler stars present aligned planets. The transition between aligned and misaligned systems occurs around the stellar effective temperature $T_{\rm eff} \approx 6250$ K, probably indicating that the hot Jupiter formation mechanisms depend strongly on stellar mass. With a different methodology, this difference between cool and hot stars was also noticed by Schlaufman (2010). In Figure 1.3 the so-called λ-$T_{\rm eff}$ diagram is shown, including all hot Jupiters with obliquity measurements from the TEPCat[2] orbital obliquity catalogue (Southworth, 2011). The dispersion of spin-orbit values is observed to be larger for effective temperatures larger than 6250 K, while cooler stars have mostly planets in aligned orbits.

Going back to the current statistics of exoplanets discovered, it is been observed that some expected samples are missing in the radius-period diagram

[2] http://www.astro.keele.ac.uk/jkt/tepcat/rossiter.html

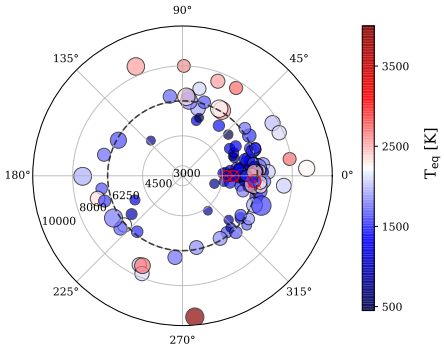

FIGURE 1.3— Polar plot of the exoplanets with spin-orbit measurements versus the effective temperature of their host star (radial lines). The colour shows the equilibrium temperature of the planet, and the marker size is indicative of the radius of the planet. The data is extracted from the TEPCat orbital obliquity catalogue (Southworth, 2011) filtered for hot Jupiters ($R_p \geq 0.5\ R_J$). In red-crossed dots the results obtained in this thesis are shown. The dashed black line at 6250K corresponds to the effective temperature transition suggested by Winn et al. (2010).

(see Figure 1.4). Fulton et al. (2017) observed a deficit of close-in planets, those with orbital periods shorter than 100 days, in the radius region between 1.5 and 2 R_{Earth}. This region is called the radius valley and it is situated around 1.8 R_{Earth}. With smaller masses than hot Jupiters and Saturns, one would expect the presence of hot sub-Saturns. However, only a very small number of planets have been discovered in this region called the evaporation desert (see the yellow region in Figure 1.4). Although the origin of the radius valley and evaporation desert is still not clear, there are several potential explanations. One of the most likely mechanisms is photoevaporation (Owen & Wu, 2013). The evaporation process affects significantly low-mass planets with hydrogen envelopes at distances shorter than ∼0.1 AU. In their study, Owen & Wu (2017) conclude that evaporation can naturally explain the lack of exoplanets observed around the radius valley (∼1.8 R_{Earth}) and the evaporation desert, depending on the atmospheric masses that they had before starting the atmospheric mass-loss. In particular, those planets unstable to atmospheric mass-loss will lose mass until completely stripped, or reach stable atmospheric mass. The evaporation or radius valley is observed between planets with stripped cores and those that are able to maintain their atmospheres. The lack of planets in this region is

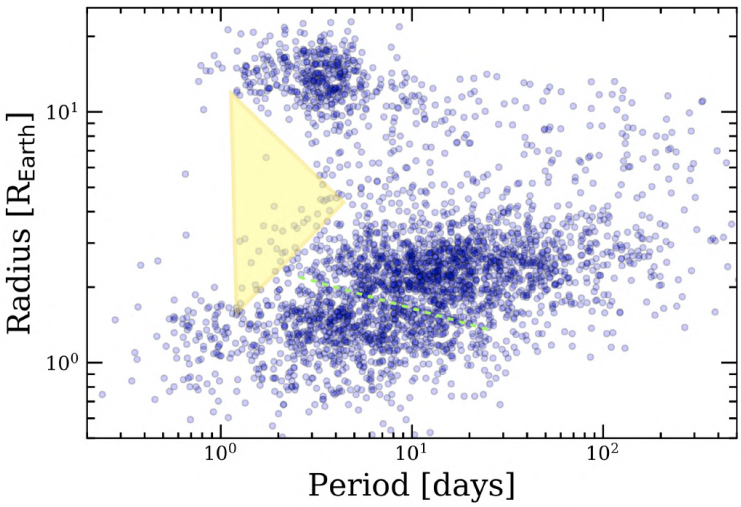

FIGURE 1.4— Radius and orbital period of confirmed planets, extracted from the NASA Exoplanet Archive. The green-dashed line indicates the radius valley around 1.8 R_{Earth} (Fulton et al., 2017). The triangular yellow region indicates the evaporation desert of hot sub-Saturns.

created by the complete removal of their envelopes, if their atmospheric mass fraction (M_{atm}/M_{core}) was initially below 0.01. The evaporation desert, on the other hand, results from planets with atmospheric mass fractions around 1 that evolved to lower mass (Owen, 2019).

1.2 Exoplanet atmospheres

With the increasing diversity of discovered exoplanets and the detection of the first transiting planets, substantial effort has been put into the detection and understanding of their atmospheres. HD 209458b was the first transiting planet discovered and became the first with an atmospheric detection by Charbonneau et al. (2002), using STIS (Space Telescope Imaging Spectrograph) observations on board the *Hubble* Space Telescope (HST). In particular, excess of absorption was detected in the sodium (NaI) lines. This detection, which is revisited in detail later in this thesis, opened the door to a field that has expanded considerably in only a few years, not only due to the improvement of astronomical instrumentation, but also thanks to the large efforts on atmospheric

modelling. Theoretical studies are particularly important to understand the species expected in a particular exoplanet atmosphere.

1.2.1 Hot Jupiters

Hot Jupiters are the most studied objects in the exoplanet atmospheric science field, as the expected spectral features are relatively large due to their extended scale heights, from their high temperatures and their relatively large circumference, due to their size. The scale height of the hot Jupiter HD 209458b is $H \approx 550\,km$ (Lecavelier Des Etangs et al., 2008), while $H \approx 11\,km$ for the Earth. Moreover, its orbital period is only ~ 3.5 days. Due to their proximity to the host star, hot Jupiters are strongly irradiated, reaching equilibrium temperatures higher than 1 000 K. These high temperatures were firstly predicted by Seager & Sasselov (1998) and observationally confirmed with secondary eclipse observations performed with *Spitzer*, showing strong infrared emission from several exoplanets.

At these temperatures, a planetary atmosphere is expected to be mainly composed by H_2O (water vapour) and H_2, being the H_2O the most significant spectral feature expected in their atmosphere (Seager & Sasselov, 2000), particularly in the infrared. Water vapour absorption has been identified in the atmosphere of several hot Jupiters (e.g. Deming et al. 2013). Depending on the metallicity and temperature of these planets, other atoms and molecules can also be found in their atmosphere, such as CO, CO_2, and methane (CH_4). CH_4 becomes more abundant than CO at temperatures below $\sim 1300\,K$, as should also happen for NH_3 below $\sim 700\,K$ (Burrows et al., 1998), although the latter one has not been detected in any exoplanet atmosphere. Several detections of CH_4, CO and CO_2 have been performed in hot Jupiters (e.g. Snellen et al. 2010; Brogi et al. 2012; Todorov et al. 2014). At the higher temperatures of very hot Jupiters, titanium oxide (TiO) and vanadium oxide (VO) could also cause strong features in the transmission spectra.

The presence of hazes, small particles suspended in the atmosphere of exoplanets, can be probed by the detection of a Rayleigh scattering slope in the transmission spectrum (Lecavelier Des Etangs et al., 2008), which results from the dispersion of starlight at bluer wavelengths by small particles. This feature has already been observed in several hot Jupiters and Neptune-sized planets (e.g. Murgas et al. 2020; Pont et al. 2013). However, star spots in the stellar surface could mimic the Rayleigh scattering feature (Oshagh et al., 2014). On the other hand, the presence of clouds in an atmosphere, masses of solid and/or liquid particles produced by the condensation of atmospheric gases, can naturally explain featureless transmission spectra.

Since the first detection in HD 209458b, the NaI doublet at 590nm has become one of the most detected species in hot planets atmospheres. The main reason is that NaI and KI (neutral potassium) absorption are due to strong resonance lines that probe low pressure levels and high altitudes of the atmosphere. These alkali lines were predicted to be present in the atmosphere of hot planets by Seager & Sasselov (2000) and, due to their extension in the atmosphere, are potential candidates to learn about the temperature profiles of the exoplanets thermosphere (Huitson et al., 2012). A large number of detections of alkali lines in hot Jupiters can be found in the literature using different techniques (e.g. Chen et al. 2018; Redfield et al. 2008).

1.2.2 Ultra hot Jupiters

In the last couple of years, a new sample of extreme hot Jupiters has emerged: the so-called ultra hot Jupiters. These planets are tidally locked gas giants that orbit around early (A-F) type stars in only a few hours or days, at very small distances from their hosts. The high amount of irradiation received from their host star leads to extreme temperature differences between their day and night-sides (Komacek & Showman, 2016). This irradiation heats the gas and can expand their atmospheres to larger distances than the Roche lobe (e.g. Yan & Henning 2018; Jensen et al. 2018), leading to atmospheric evaporation processes (Fossati et al., 2015). Their equilibrium temperatures are larger than 2000 K (Parmentier et al., 2018; Arcangeli et al., 2018) and can achieve temperatures higher than $\sim 10\,000$ K in their day-side exospheres (Wyttenbach et al., 2020). Their night-side is expected to be cloudy and depleted of elements, while their day-side is cloud-free and formed by a thermal ionosphere, as the neutral elements have been ionised by the stellar irradiation received (Helling et al., 2019). Contrarily to what is observed in their cooler counterparts, ultra hot Jupiters do not present water vapour in their day-side atmospheres, as molecules have been dissociated at these higher temperatures. This has been probed observationally in several occasions, with the detection of a wide collection of metals in their atmosphere such as NaI, CaI, CaII, FeI, FeII, MgI, among others (e.g. Seidel et al. 2019; Hoeijmakers et al. 2019).

One of the particularities of these planets is their atmospheric structure. Several observations of ultra hot Jupiters have shown the presence of thermal inversions in their atmosphere, this is a layer where the temperature increases with altitude. The detection of emission of different species in their atmosphere such as FeI, TiO, and H_2O (e.g. Yan et al. 2020; Pino et al. 2020; Nugroho et al. 2017; Evans et al. 2017) is a direct evidence of temperature inversion in their atmospheres. Recently, Lothringer & Barman (2019) theoretically predicted

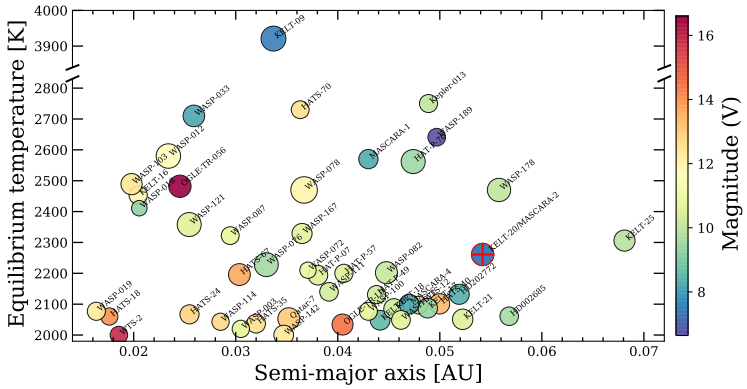

FIGURE 1.5— Transiting planets with temperatures larger than 2000 K and radius larger than $0.8R_J$, identified as ultra hot Jupiters. The distance between the planet and the star (semi major axis) is shown in the horizontal axis, the equilibrium temperature of the planets is presented in the vertical axis, and the magnitude of the host stars in the colour bar. The size of the markers is indicative of planetary radius. The red cross indicates MASCARA-2b, an ultra hot Jupiter studied in this thesis (see chapters 3 and 4). The parameters are extracted from the TEPCat catalogue (Southworth, 2011).

that ultra hot Jupiters orbiting early type stars present stronger temperature inversions. In addition, the day-night differences probably lead to significant atmospheric circulation with horizontal winds that can achieve velocities of the order of the speed of sound (Showman et al., 2010). Although only a relative small sample of planets in the ultra hot Jupiter category are known (see Figure 1.5), they have become one of the most studied planets, as the magnitude of their stars, their temperature and their planet-to-star radius ratio make them the most accessible targets for atmospheric studies (see Chapters 3 and 4).

1.2.3 Mini-Neptunes and super Earth atmospheres

Mini-Neptunes and super Earths, together with hot Jupiters, are one of the most surprising discoveries in the exoplanet field, as they do not present counterparts in the Solar System. These planets, in contrast with the primitive atmospheres of giant planets, present evolved atmospheres, which could contain a large diversity of species, giving valuable information about their formation and evolution.

Seager & Sasselov (2000) predicted that those exoplanets receiving a large amount of extreme ultraviolet (EUV, 10-92 nm) and X-ray (0.5-10 nm) radiation in their atmosphere could present strong absorption of HeI (at 1083 nm) in their transmission spectrum. The EUV flux excites the HeI atoms to the triplet 2^3S metastable state, which are then scattered in the 2^3S-2^3P transition. HeI was proposed by Oklopčić & Hirata (2018) as an alternative line to study atmospheric evaporation, which happens when the stellar irradiation heats the gas of the atmosphere and expands it, producing mass loss. Previous studies were usually performed studying the hydrogen Lyman α (Ly-α) line, but this line is strongly affected by interstellar medium absorption. Hot super Earths and sub-Neptune sized planets are expected to be the most affected by evaporation, as they could totally loose their atmospheres due to mass loss (Lundkvist et al., 2016).

Although efforts have been made to detect the hydrogen and/or helium envelopes and to study their evaporation, it has only been possible to find these species in larger planets such as hot Jupiters (e.g. Alonso-Floriano et al. 2019b), some Saturn-mass planets (e.g. Nortmann et al. 2018; Allart et al. 2018), and warm neptunes (e.g. Palle et al. 2020a; Ehrenreich et al. 2015).

1.3 Observing exoplanetary atmospheres

The ultimate objective when studying exoplanet atmospheres is the characterisation of other Earths in order to infer whether or not they are habitable. Although Earth-like planets are relatively common in the universe (Bryson et al., 2020), with the current telescopes and instrumentation, attempting to study the atmosphere of an Earth twin is still out of reach.

The main difficulty to study exoplanet atmospheres using direct imaging observations is their enormous planet-to-star contrast ratio. Currently, this is only possible using space telescopes or very large ground-based telescopes equipped with extremely precise adaptive optics to correct for the effects introduced by our atmosphere. The objects that can be studied with this technique are very massive, young exoplanets orbiting at long distances from their host star. Fortunately, the discovery of a relatively large sample of exoplanets that orbit very close to their host stars, at less than ~ 0.05 AU, and with orbital periods of days has permitted to start studying the atmosphere of some of them. Due to their proximity to their host, these planets present large temperatures that result in larger planet-to-star contrasts. For hot Jupiters, their equilibrium temperatures expand from $\sim$ 1000K to 2000K, giving a brightness of 10^{-3} in comparison to their host stars (in the near infrared), which is around 10^7 times larger than what we expect from an Earth-like twin orbiting a sun-like star in

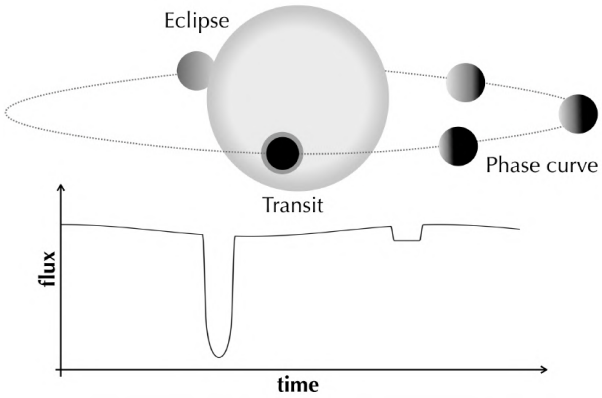

FIGURE 1.6— Schematic illustration of the observational phenomena that occur along the orbit of a transiting planet. The primary transit produces the deepest change of the stellar flux. The fainter transit-like phenomena corresponds to the eclipse (occultation) of the planet, and the overall continuum modulation corresponds to the phase curve.

the visible (Seager, 2010).

In addition to direct imaging, three main observational techniques have been used to study the atmosphere of the exoplanets: transits, eclipse (or occultation) and phase curves observations (Crossfield, 2015). This thesis is focused on transit observations (transmission spectroscopy), but some insights on eclipse and phase curve observations are given in this section. In Figure 1.6 a scheme of these three different techniques is presented.

1.3.1 Transmission spectroscopy

Planets with short orbital periods, located very close to their host stars, have higher probability to present transit events (around 10 % for hot Jupiters, Brown 2001). During a transit, the exoplanet passes in front of its parent star with respect our line-of-sight, blocking part of the stellar light that we receive (see Figure 1.6). The deficit of stellar flux received, $\Delta f/f$, can be measured very precisely, and it is proportional to the projected area between the planet and the star, given approximately by

$$\frac{\Delta f}{f} \approx \left(\frac{R_p}{R_\star}\right)^2, \tag{1.2}$$

where R_p is the radius of the planet and $R_\star$ is the radius of the star, which is usually well determined, whereas second order effects from the stellar limb-darkening are ignored in Equation 1.2.

When a transit is observed from Earth, part of the starlight crosses the optically thin exoplanet atmosphere annulus or the commonly called "terminator" (see Figure 1.7), and its signatures appear imprinted in the stellar flux. When the stellar light penetrates through the exoplanet atmosphere, this light is absorbed and scattered at characteristic frequencies depending on the atoms and molecules that compose this atmosphere. This means that the exoplanet atmosphere will become opaque at this particular wavelengths and, consequently, the planet will have a slightly larger apparent radius at these wavelengths, which can be directly measured from the transit depth (see equation 1.2 and Figure 1.7). Therefore, the measurement of the transit depth at different wavelengths provides the transmission spectrum of the exoplanet.

Although transiting planets are a relatively small fraction of the planet population, the atmospheric information that can be measured make these planets extremely valuable. For this reason, transiting systems have become the most favourable targets for atmospheric studies. When attempting to observe exoplanet transits for atmospheric studies it is common to use the so-called Kempton metric (Kempton et al., 2018) in order to distinguish the known planets that could be potential candidates. This metric is based on the calculation of the exoplanet atmosphere annulus surface (TS) with respect the stellar disc area, which can be defined as follows:

$$\mathrm{TS} = \frac{\pi(R_p + nH)^2 - \pi R_p^2}{\pi R_\star^2}, \tag{1.3}$$

where R_p is the planet radius, H is the atmospheric scale height, n is the number of H needed to define the total thickness of the atmosphere ($n \times H$), and $R_\star$ is the stellar radius. If we expand this equation, and neglect the second order term $\sim H^2$, we obtain the approximate strength of the spectral features

$$\mathrm{TS} \approx \frac{2R_p nH}{R_\star^2}. \tag{1.4}$$

The scale height is defined as $H = kT_{eq}/\mu_m m_H g$, with k the Boltzmann's constant, T_{eq} the equilibrium temperature of the planet, m_H the mass of the hydrogen atom, μ_m the mean molecular weight, and g the gravity. Note that $g = GM_p/R_p^2$ with G the gravitational constant and M_p the mass of the exoplanet.

Considering the definitions above and including the brightness of the star (mag) as an estimation of the signal-to-noise ratio (S/N), from equation 1.4

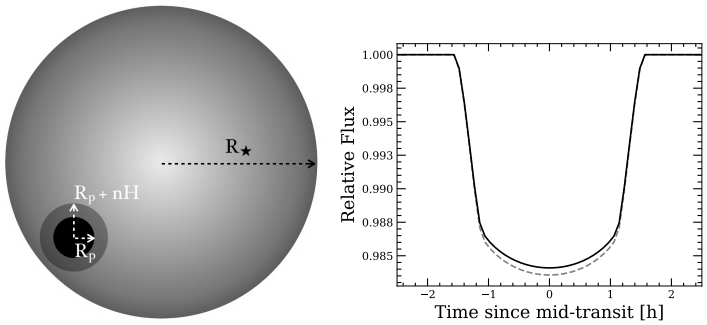

FIGURE 1.7— *Left:* Schematic illustration of the exoplanet atmosphere annulus area (terminator) defined by a radius $n \times H$, with respect the planet and stellar discs surface, defined by the planet radius (R_p) and stellar radius ($R_\star$), respectively. *Right:* illustration of the transit of a particular exoplanet considering a planetary radius R_p (black) and $R_p + nH$ (gray-dashed line). Transits reproduced using `PyTransit` (Parviainen, 2015).

we obtain the transmission spectroscopy metric (TSM) as defined in Kempton et al. (2018):

$$\text{TSM} = (\text{Scale factor}) \times \frac{R_p^3 T_{eq}}{M_p R_\star^2} \times 10^{-mag/5}. \tag{1.5}$$

The scale factor includes the different constants together with μ and n. These two last parameters are difficult to determine. For a H_2 and HeI dominated atmosphere, $\mu = 2.3$ is a good approximation, for example. $\mu = 1.3$ would be the case of an atomic hydrogen atmosphere, while $\mu = 1$ is considered for totally dissociated hydrogen atmospheres. On the other hand, n depends on the particular atmosphere but also on the spectral resolution of the observations. Estimating the TSM parameter, it is possible to compare the expected transmission spectroscopic signal for different known planets. In Figure 1.8, this calculation is performed for all transiting planets tabulated in TEPCat catalogue (Southworth, 2011), and for which the properties from Equation 1.5 have been measured. In this same figure, we indicate those exoplanets that are analysed in this thesis.

In Figure 1.8, we observe that the most suitable exoplanet for atmospheric studies is HD 209458b. Follow-up observations of Ly-α in the far ultraviolet found that HD 209458b has an escaping HI atmosphere (Vidal-Madjar et al., 2003) which showed a transit depth of 15%, and also carbon and oxygen de-

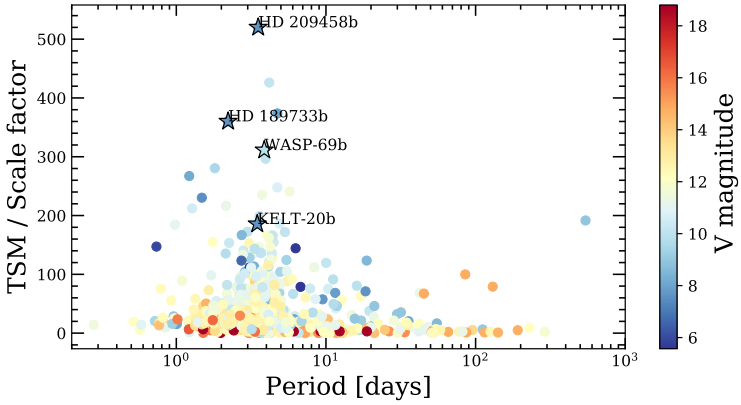

FIGURE 1.8— Transmission spectroscopy metric (TSM; Kempton et al. 2018) calculated for the transiting exoplanets listed in TEPCat catalogue (Southworth, 2011), displayed in terms of their orbital period and magnitude (V) of their host stars (colour bar). The star markers indicate the exoplanets studied in this thesis.

tections in the exosphere (Vidal-Madjar et al., 2004). After thousands of exoplanet discoveries, HD 209458b has maintained the first position in the list of best planets for atmospheric characterisation. Although the first atmospheric studies were performed using space-based observations in order to avoid the Earth atmosphere contamination, ground-based facilities slowly started to gain importance due to the large apertures available from ground. For example, the NaI detection in HD 209458b's atmosphere was reproduced by Snellen et al. (2008) using the Subaru telescope, and by Albrecht et al. (2012) using UVES (Ultraviolet and Visual Echelle Spectrograph) observations at the Very Large Telecope (VLT).

With the rising number of transiting planets discovered, the number of transmission spectroscopy studies rapidly increased. In Figure 1.9 a computation of low-resolution transmission spectra obtained with the space-based telescope HST and the ground-based Gran Telescopio Canarias (GTC) are presented, together with their one-dimensional atmospheric models. The spectra are ordered from cooler (top) to hotter (bottom) planets, with equilibrium temperatures ranging from 615 K to 2500 K. In the transmission spectra of these planets some of the species described in Section 1.2 can be distinguished. In particular, for some of the planets, we clearly see the detection of water bands

at $1 - 1.5$ μm, absorption at the NaI and KI alkali lines, and Rayleigh slopes in the bluer wavelength regions.

Although transit observations are currently one of the best tools to study exoplanets atmospheres, the presence of clouds can become a limitation, especially at visible wavelengths. According to models, clouds are an additional source of opacity, and reduce the scale height of the clear atmosphere above the clouds, which is observable by transmission spectroscopy. This limitation is translated into a weakening or totally masking of the atmospheric spectral features, depending on the altitude of the cloud deck (Fortney, 2005). In hot Jupiters, the atmospheric temperature is close to the condensation temperatures of several abundant components (Seager & Sasselov, 2000). When a grey cloud is assumed (whose opacity has little dependence with wavelength), all features below the cloud deck are masked in the transmission spectrum. This is the case of the muted water vapour absorption in HD 209458b (Deming et al., 2013), for example. To date, most of the exoplanets characterised have shown some degrees of cloudiness (Sing et al., 2016).

1.3.2 Eclipse and phase curve observations

The atmosphere of an exoplanet can also be characterised by observing its emission spectrum. If observations are performed during secondary eclipse, when the planet is occulted behind the star (see Figure 1.6), the flux contribution from the exoplanet is not visible, and only the stellar contribution is observed. Consequently, both planet and stellar flux contribution can be isolated by comparison to the off-eclipse flux. In the infrared, the flux emitted by the planet depends on its temperature. Thus, it is possible to probe the black-body emission of hot exoplanets, whose peak is expected at $\sim 1000\,\mathrm{K}$, and to measure their brightness temperatures. In the optical, secondary eclipse observations permit the measurement of the geometric albedo; this is the reflectively of the exoplanet at a particular wavelength (or passband) observed when it is fully illuminated. The reflected and thermal emission are usually difficult to disentangle. To this aim, colour observations are needed: the thermal emission is expected to be strong at infrared wavelengths at which the parent star is fainter, and the albedo has a significant effect at optical wavelengths.

On the other hand, when the observations are performed along the orbit of the exoplanet, one can measure the phase curve (see Figure 1.6), this is, the temporal changes in the planet-star flux combination. These differences occur because our geometric view of the exoplanet surface changes during the observations. Using phase curve observations, the temperature difference between the day and night side can be inferred, but it is also possible to map the

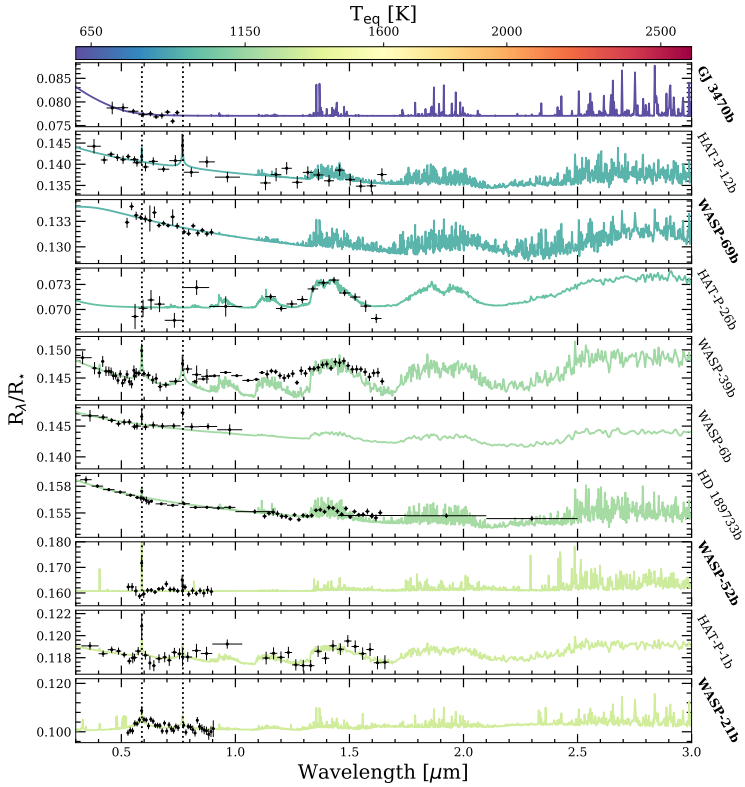

FIGURE 1.9— Low-resolution transmission spectra of several exoplanets with different temperatures, retrieved using the space-based *Hubble* Space Telescope and the ground-based Gran Telescopio Canarias (GTC; bold planet names). The observations are shown in black dots, and the modelled transmission spectra are shown in different colours. The colours correspond to the equilibrium temperature of the exoplanets, shown in the colour bar. The dotted vertical lines show the NaI doublet and KI position (at 590 nm and 770 nm). The HST results are extracted from the Exoplanet Atmospheric Spectral Library[4], published in Sing et al. (2016). WASP-121b and HAT-P-26b transmission spectra were published in Evans et al. (2018) and Wakeford et al. (2017), respectively. For GTC observations, the transmission spectra are extracted from Chen et al. (2017a), Murgas et al. (2020), Chen et al. (2017b), Chen et al. (2020a), Chen et al. (2018), and Murgas et al. (2017). This figure continues in the following page.

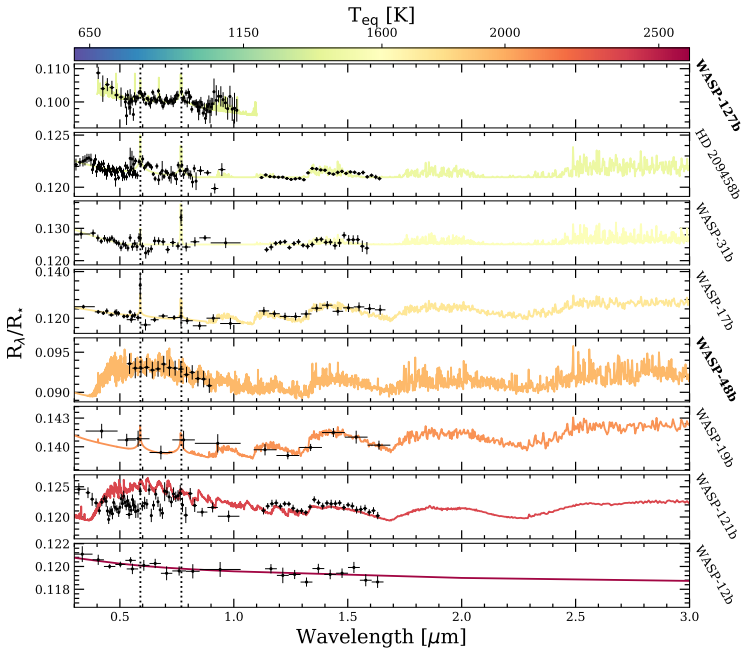

FIGURE 1.9 (CONT.)— Continued from previous page.

atmospheric temperature around the planet. Although phase curve studies do not require a transiting planet, these have been the most studied planets due to their ephemeris precision (Bozza et al., 2018). Phase curves are one of the most demanding and challenging observations, as they require a photometric precision of the order of 100 ppm, and long, continuous observations (∼ days). Therefore, they arise mostly from satellite mission data.

When attempting to characterise an exoplanet by means of secondary eclipse observations, it is important to quantify their expected day-side flux, as not all exoplanets are suitable for this kind of observations. The exoplanet day-side flux is the combination of two components: thermal and reflected. The thermal component can be estimated assuming that the planet and star are black-bodies in thermal equilibrium, with their respective radiation temperatures. On the

other hand, the light reflected by a planet depends on the radiation received from its parent star and the albedo (p_λ) at a particular wavelength. The radiation that a planet receives can be defined as $F_{rec} = F_\star \pi R_p^2$ where $F_\star = L_\star / 4\pi a^2$, being $L_\star$ the luminosity of the star and a the planet-star distance (semi major axis). Consequently, the eclipse depth at wavelength λ can be defined as

$$\left(\frac{\Delta f}{f}\right)_\lambda = p_\lambda \left(\frac{R_p}{a}\right)^2 + \frac{B_\lambda(T_{day})}{B_\lambda(T_{eff})} \times \left(\frac{R_p}{R_\star}\right)^2, \tag{1.6}$$

where T_{eff} is the effective temperature of the star and T_{day} the day-side temperature of the planet, and B_λ are the respective black-body emissivities, given by Plank's equation.

As done for the TSM (equation 1.5), it is possible to estimate the secondary eclipse observability by considering the magnitude of the host star. If we assume that the thermal emission is the main component, the emission spectroscopy metric (ESM) can be defined as follows (Kempton et al., 2018):

$$\mathrm{ESM} = \frac{B_\lambda(T_{day})}{B_\lambda(T_{eff})} \times \left(\frac{R_p}{R_\star}\right)^2 \times 10^{-mag/5}. \tag{1.7}$$

The first secondary eclipse measurements were achieved by Deming et al. (2005) and Charbonneau et al. (2005) who observed HD 209458b and TrES-1b, respectively, using the *Spitzer* Space Telescope. With these measurements, the brightness temperature of the exoplanets could be derived. Shortly after, Knutson et al. (2008) combined HD 209458b *Spitzer* observations taken between 3 and 30 μm to construct the first broad band emission spectrum, finding evidence of a thermal inversion in the atmosphere of the hot Jupiter. At the same time, de Mooij & Snellen (2009) detected the first ground-based secondary eclipse with the William Hershel Telescope (WHT). One of the first phase curves measurements was made with *Spitzer* observations of the exoplanet HD 189733b (Knutson et al., 2007), and the first secondary eclipse map of an exoplanet was performed by Majeau et al. (2012) using observations of this same planet. Lately, using HST and *Spitzer* phase curve observations of WASP-43b, the H_2O features around the planet were mapped (Stevenson et al., 2014). For more details on planet mapping see Cowan & Fujii (2018).

1.4 High-resolution transmission spectroscopy

During the last decade, studying exoplanetary atmospheres by means of high resolution spectroscopy observations ($\Re \gtrsim 40\,000$) has become one of the most used techniques. In contrast with low-resolution, high-resolution techniques do

not analyse the changes of the planet-to-star radius ratio at different wavelengths, but search for the direct contribution of the exoplanet atmosphere to the observed host star spectrum, which appears as additional spectral features, taking advantage of the differential velocities of the star, the Earth, and the exoplanet.

The first atmospheric study at high resolution was performed using the Hobby-Eberly Telescope ($\Re \sim 60\ 000$) by Redfield et al. (2008), where NaI doublet lines were resolved in the atmosphere of HD 189733b. After a couple of years, using the cross-correlation technique, Snellen et al. (2010) detected a molecule (CO) for the first time in an exoplanet atmosphere using the CRyogenic high-resolution InfraRed Echelle Spectrograph (CRIRES; $\Re \sim 50\ 000 - 100\ 000$) at VLT. The first study presenting the current methodology to extract the transmission spectrum from high resolution observations was presented by Wyttenbach et al. (2015), using observations with the High Accuracy Radial velocity Planet Searcher (HARPS; $\Re \sim 115\ 000$) at the European Southern Observatory (ESO) La Silla 3.6m telescope. In this case, the NaI detection was confirmed in HD 189733b's atmosphere. Since then, the number of atmospheric studies using high resolution spectroscopy observations has increased exponentially.

1.4.1 Methodology

Two main techniques have arisen when attempting to study the atmosphere of an exoplanet by means of high resolution spectroscopy observations. The first one is based on extracting the transmission spectrum of an exoplanet around single spectral lines, such as the NaI doublet, the HeI triplet or other species that may form a small number of lines in the transmission spectrum and are strong enough to be detected. The second technique is mainly used to search for those species that form thousands of faint individual spectral lines in the transmission spectrum: the cross-correlation technique. Both techniques are complementary and can be applied using the same observing strategy, namely, continuous observations of the host star before, during, and after the transit of the exoplanet. These techniques can be applied to transiting (transit and secondary eclipse observations) and non-transiting planets, with small changes in the methodology and observing strategy. Here, we focus on transit observations, the main goal of this thesis.

Transmission spectrum of single lines

Wyttenbach et al. (2015) has become one of the benchmark references when attempting to extract the transmission spectrum around single lines of an exo-

planet by means of high resolution spectroscopy observations. This methodology is based on the differential spectroscopy, namely the comparison between those stellar spectra taken when the planet is crossing the stellar disc (transiting) and when it is not. Although the methodology is apparently simple, there are a few critical points related to the high resolution nature of the spectra that need to be considered along the process: the correction of the Earth's atmospheric contamination, and dealing with the radial-velocities of the (at least) three bodies involved in the observations.

One of the main steps in transmission spectroscopy is the correction of the Earth's atmospheric contamination. For a time, the most common technique was the one presented in Vidal-Madjar et al. (2010) and Astudillo-Defru & Rojo (2013), which has been applied to several atmospheric studies (e.g. Wyttenbach et al. 2015, 2017). This method assumes that the variation of the telluric lines during the night follows linearly the airmass variation. Under this assumption, all telluric lines can be scaled to the same airmass in all spectra. However, as pointed out in Casasayas-Barris et al. (2017), taking into account that the Earth is moving along its orbit during the night, when two spectra that are not in the Earth rest frame are divided, residuals appear in the telluric lines position due to their small misalignment. Fast rotating standard stars have also been used to correct the telluric lines (e.g. Casasayas-Barris et al. 2018; Redfield et al. 2008; Frasca et al. 2000). Currently, one of the most used tools is `Molecfit` (Smette et al., 2015; Kausch et al., 2015), as the telluric lines are totally corrected, achieving a noise level precision.

When using high resolution observations, the radial velocities of the observer and the target are noticeable as shifts in the stellar spectra (see Figure 1.10). First, as we are observing from Earth, we need to consider its radial-velocity variation during the observations. Although this change is small during the night ($\lesssim 1\,\mathrm{km\,s^{-1}}$) its absolute radial velocity can be of the order of tens of $\mathrm{km\,s^{-1}}$ depending on the position in the orbit around the Sun, the target we are observing, and the position of the observatory on the Earth surface.

Second, the star we are observing (and the planets that are part of the extrasolar system) is approaching or moving away from the Solar system. This is the so-called systemic velocity, and it is due to the movement of the stars inside the Galaxy. Third, the target of our observations is a star hosting at least one planet. If we imagine a two-body system (one planet and one star) for simplicity, due to the gravitational field, the planet pulls the star around the centre of the system while moving along its orbit, and vice-versa. This movement is translated to a radial-velocity change of the star that can be well defined by a Keplerian orbit around the system barycentre. As presented in Cumming et al. (1999), the radial-velocity semi-amplitude $K_\star$ of a star with

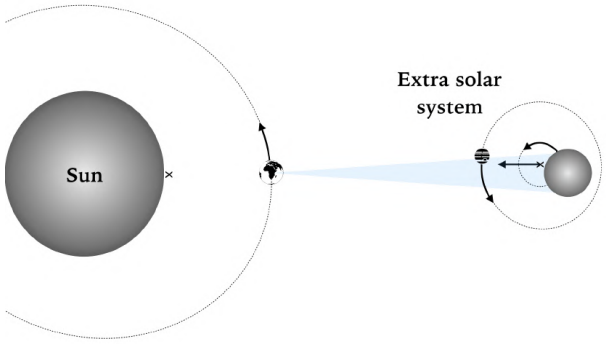

FIGURE 1.10— Sketch of the bodies involved in the observations and their corresponding movements. We observe that the Earth is moving around the Solar System barycentre and the extrasolar system is, in this case, approaching to the Solar System. The star orbits around the star-planet system barycentre, and the exoplanet rotates around the host star.

mass $M_\star$ produced by a companion with mass M_p, orbital period P, inclination i, and eccentricity e is described as follows:

$$K_\star = \left(\frac{2\pi G}{P}\right)^{1/3} \frac{M_p \sin i_\star}{(M_p + M_\star)^{2/3}} \frac{1}{\sqrt{1-e^2}}. \tag{1.8}$$

Finally, during the transit, the exoplanet changes its position along the orbit with respect the observer's line-of-sight. Similarly to equation 1.8, assuming a circular orbit ($e = 0$) and $M_p \ll M_\star$, the planet radial-velocity semi-amplitude is given by:

$$K_p = \frac{2\pi a}{P} \sin i_\star, \tag{1.9}$$

where a is the semi-major axis of the planetary orbit. K_p can also be derived from $K_\star$ and mass ratios (Birkby, 2018):

$$\frac{K_\star}{K_p} = \frac{M_p}{M_\star}. \tag{1.10}$$

Once the spectra have been corrected of telluric contamination and are shifted to the stellar rest frame where all stellar lines are exactly at the same position, we can proceed with the extraction of the transmission spectrum. A scheme of the methodology can be observed in Figure 1.11 using synthetic

spectra at very high S/N for better visualisation. First of all, we need to remove the stellar contribution from our spectra. In order to do this, we compute a high S/N stellar spectrum that results from the combination of all spectra taken when the planet is not transiting. Then, all spectra are divided by this stellar spectrum. After this division, in an ideal case, we would expect to see tilted absorption features during the transit with the expected radial-velocity change of the planet, as those presented in *panel d*. The planet radial velocity at each exposure can be calculated as $v_p = K_p \sin(2\pi\phi)$, where ϕ is the orbital phase of the planet at that particular exposure. With these values, the absorption features can be shifted to the planet rest frame using the Doppler effect equation ($\frac{\Delta\lambda}{\lambda} = \frac{v_p}{c}$; see *panel e*), where all of them are aligned. Finally, all in-transit residuals are combined to built the transmission spectrum (see *panel f*).

The cross-correlation technique

When looking for atoms and molecules that may originate hundreds to thousands of individual absorption lines in the transmission spectrum, the most powerful tool is the cross-correlation technique. Using this methodology, the contribution of all these lines is combined, reducing the photon noise and permitting the detection of atoms and molecules hidden in the noise when analysed individually (Snellen et al., 2010).

The cross-correlation technique is based on the comparison of a synthetic atmospheric spectrum with the reduced data at the stage of *panel d* from Figure 1.11, this is, after removing the stellar contribution from the observed spectra. There are different ways to reach this step. The first one is following the same steps as described in the previous section (*panels a* to *d* from Figure 1.11), using a wider wavelength region. The second one is using algorithms such as SYSREM (Tamuz et al., 2005), which uses a principal component analysis (PCA; Murtagh & Heck 1987; Press et al. 1992) which has successfully been applied to detect molecules in the atmosphere of several exoplanets (e.g. Birkby et al. 2017; Nugroho et al. 2017; Sánchez-López et al. 2019). PCA finds common modes over time for each pixel (wavelength) in the spectral time series. As the exoplanet moves fast during the transit, it produces features that change their position (in pixels) with time. Consequently, the exoplanet features will not be identified as common modes and will persist in the residuals. On the contrary, the telluric and stellar lines will be identified as common modes over time and removed, as they remain (almost) at the same position during the observations. The main advantage of using these kind of algorithms is that they account for instrumental systematic effects that may occur during the observations. However, due to their iterative nature, after a certain number of iterations, the

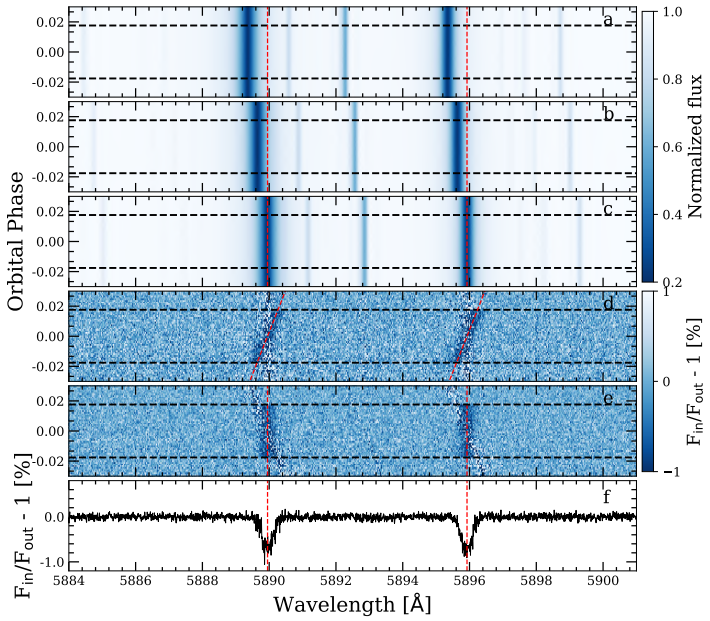

FIGURE 1.11— Scheme showing the steps followed to extract the transmission spectrum of an exoplanet using high resolution spectroscopy (based on Wyttenbach et al. 2015). The stellar synthetic spectra around the NaI are computed using MARCS stellar models (Gustafsson et al., 2008). A Gaussian-like absorption from the exoplanet atmosphere with excess of 0.7 % and full width at half maximum (FWHM) of 0.4 Å is injected in the stellar spectra. These calculations are performed assuming the transit parameters of HD 209458b (Chapter 5). The assumed barycentric Earth radial-velocity values have been calculated using Wright & Eastman (2014). In the five first panels (a to e), the vertical axis corresponds to the time evolution increasing towards the top. The colour is indicative of the flux (see colour bar), where the continuum corresponds to white and and the absorption features are shown in blue. The horizontal black-dashed lines indicate the first and last contacts of the transit. *Panel a:* stellar spectra in the terrestrial rest frame. *Panel b:* stellar spectra shifted to the Solar System barycentric rest frame. *Panel c:* stellar spectra in the stellar rest frame. The dashed-vertical lines show the laboratory position of the NaI doublet lines at 5889.951 Å (D2) and 5895.924 Å (D1). *Panel d:* division of all spectra by the combination of all stellar spectra taken when the planet is not transiting. The red dashed-tilted lines show the position of the NaI doublet lines from the exoplanet atmosphere, shifted due to the planet radial-velocity during the transit. *Panel e:* same as *Panel d* but after correcting by the planet radial-velocity change during the transit. *Panel f:* transmission spectrum of the exoplanet around the NaI.

planetary atmospheric features become perceptible to the algorithm and start being removed. How to select the best iteration is still under debate (Birkby et al., 2017; Nugroho et al., 2017; Alonso-Floriano et al., 2019a).

Once the telluric and stellar lines have been removed from the time series and the data is in the stellar rest frame (see *panel a* of Figure 1.12 as example), we want to measure if the data and a template model of the exoplanet atmosphere are correlated and where the maximum correlation happens. In general, the strength of the correlation can be measured with the correlation coefficient:

$$r = \frac{\sum_{i=1}^{N}(x_i - \bar{x})(y_i - \bar{y})}{\left(\sqrt{\sum_{i=1}^{N}(x_i - \bar{x})^2}\right)\left(\sqrt{\sum_{i=1}^{N}(y_i - \bar{y})^2}\right)} \tag{1.11}$$

where there are N pairs of values (x_i, y_i) which correspond to the data and the template in this case, and $\bar{x}$ and $\bar{y}$ are their respective means. When both data and template are perfectly correlated $r = 1$. For a perfect anti-correlation $r = -1$, and if they are not correlated $r = 0$. In the case of a detectable exoplanet atmosphere, we expect a positive correlation to pop up where both data and template overlap during the transit, and no correlation is expected in the out-of-transit exposures.

As shown for individual lines, the radial velocity of the exoplanet changes during the observations, so the position of the best match between the model and the data (maximum correlation) is expected to be shifted depending on the planet position at a given exposure. For this reason, for each exposure of the time series, the correlation coefficient is computed shifting the template in a significant range of radial velocities, allowing to scan different positions in the data and find the position where the best match occur. This is the cross-correlation methodology.

A scheme of the cross-correlation methodology is shown in *panel b* and *c* of Figure 1.12 using synthetic data with very high S/N for a better visualisation. For a given exposure of the time series, in this particular example, we scan the radial velocity region from -100 to $+100\,\mathrm{km\,s^{-1}}$. When the template and data start to correlate (blue dashed line in *panel b*) the correlation coefficient starts to increase (blue dot in *panel c*). When the template is shifted $0\,\mathrm{km\,s^{-1}}$ the correlation is maximum (red colour in panels *panel b* and *c*), and when the template is shifted to large enough velocities, the correlation values become zero (with fluctuations due to the noise and possible overlap with nearby lines; green colour in panels *panel b* and *c*). After applying the cross-correlation

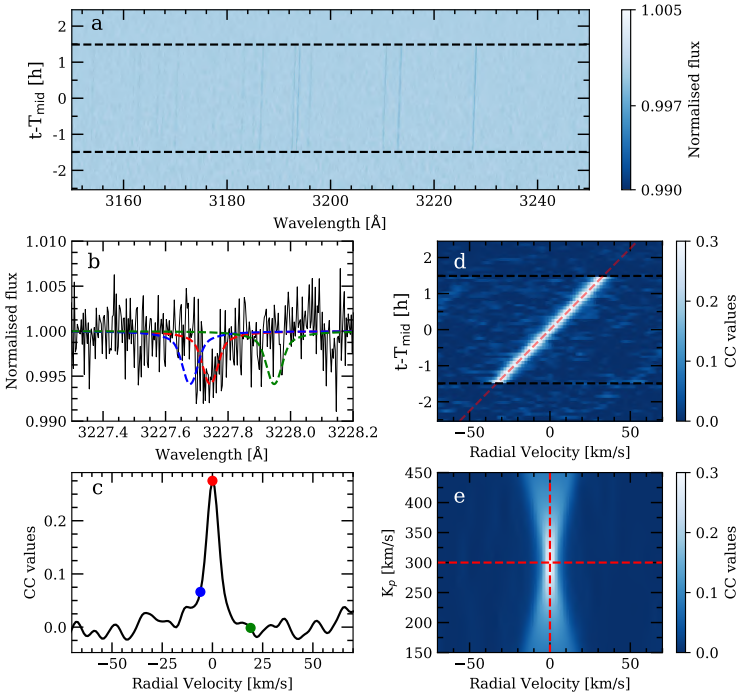

FIGURE 1.12— Scheme of the cross-correlation methodology using synthetic FeII atmospheric models computed with `petitRADTRANS` (Mollière et al., 2019), and assuming very high S/N for a better visualisation. *Panel a:* spectral time series after removing the telluric and stellar contributions, and only the planet atmosphere remains. The strong spectral lines can be observed during the transit, while the fainter are blurried in the noise. The normalised flux information is shown in the colour bar: values smaller than one mean absorption. The horizontal-dashed lines show the first and last contacts of the transit. *Panel b:* small wavelength range of the mid-transit time spectrum from *panel a*. The coloured dashed-lines show the template model shifted with three different radial-velocity values. *Panel c:* correlation coefficients obtained in the cross-correlation shown in *panel b*. The coloured dots correspond to the values obtained when the template is located at the positions shown in *panel b* with the same colour. *Panel d:* time series of the cross-correlation values. The position of the maximum correlation peak changes during the transit, and no correlation is observable when the planet is not transiting. The red-dashed line indicates the expected planet radial-velocity ($K_p = 300\,\mathrm{km\,s^{-1}}$). *Panel e:* K_p-map computed using the results from *panel d*. The maximum signal is found at $0\,\mathrm{km\,s^{-1}}$ and $K_p = 300\,\mathrm{km\,s^{-1}}$ (indicated in red-dashed lines), as expected.

technique to each individual exposure of the time series, in case of detecting the atmosphere of an exoplanet, the position of the maximum correlation peak appears shifted in time. This radial-velocity change corresponds to the planet movement during the transit, and becomes clearer when the time series cross-correlation values are shown together (see panel *d* of Figure 1.12). When using the cross-correlation technique it is very common to use the so-called K_p-map when presenting the results (see example in *panel e*). Each row of this map is computed moving the cross-correlation values from *panel d* to the planet rest frame using a particular K_p value, and then averaging all the in-transit exposures. When using a wide range of K_p values, we would expect to find the maximum correlation signal at the K_p value of the exoplanet, as for very different values this signal is diluted. Moreover, these maps give us information about possible winds when the maximum signal appears shifted from $0\,\mathrm{km\,s^{-1}}$ (see horizontal axis of *panel e*).

One of the main challenges of the cross-correlation technique is the generation of the atmospheric models. There are different codes to generate atmospheric models at high resolution, such as `petitRADTRANS` (Mollière et al., 2019), the `HELIOS` (Malik et al., 2017, 2019) code to generate the atmospheric structure of the planet and `turbospectrum` (Plez, 2012) to solve the radiative transfer problem, among many others. All these codes require line lists to calculate the atmospheric models, and it is known that some species do not have accurate line lists at high spectral resolution, as observed for TiO and VO molecules (Merritt et al., 2020; McKemmish et al., 2019), for example. The lack of an accurate line list is a critical aspect when searching for atmospheric features using the cross-correlation technique (Hoeijmakers et al., 2015), as their contributions will not be considered constructively. For example, Désert et al. (2008) found spectral features probably associated to TiO and VO in low resolution HST-STIS observations of HD 209458b, while Hoeijmakers et al. (2015) found no evidence of TiO in this same planet using the cross-correlation technique in Subaru observations, arguing the impact of using inaccurate line lists in this kind of studies.

1.4.2 State-of-the-art of high-resolution observations

One of the major advantages of using high resolution spectroscopy is that we are not only able to detect chemical species, but also to resolve single spectral lines from an exoplanet atmosphere, opening a window to study the dynamics and properties of the layers where the spectral lines are formed (Lecavelier Des Etangs et al., 2008). Redfield et al. (2008) resolved, for the first time, the NaI D lines in the atmosphere of an exoplanet (HD 189733b) using high

resolution observations with the Hobby-Eberly telescope. After some years, Wyttenbach et al. (2015) re-discovered the NaI in the atmosphere of this same planet using HARPS observations (see Figure 1.13), and subsequent studies using HARPS and HARPS-N (north) transit observations of other hot Jupiters would result in similar detections (e.g. Wyttenbach et al. 2017; Casasayas-Barris et al. 2017; Chen et al. 2020a). This specie has also been detected using the Echelle SPectrograph for Rocky Exoplanets and Stable Spectroscopic Observations (ESPRESSO; $\Re \sim 140\,000$; Pepe et al. 2010, 2014) in the WASP-52b atmosphere (Chen et al., 2020b). Taking advantage of resolving single lines, Wyttenbach et al. (2015) and Casasayas-Barris et al. (2018) (see Chapter 3) attempted to reconstruct the temperature profile of the atmosphere of two different exoplanets by adjusting isothermal models in the core and wings of the NaI spectral lines, as their origin resides in different layers of the atmosphere.

On the other hand, using the near-infrared arm of the CARMENES spectrograph (Calar Alto high-Resolution search for M dwarfs with Exoearths with Near-infrared and optical Echelle Spectrographs; Quirrenbach et al. 2014, 2018), the first detection of metastable HeI at 1038 nm was possible in the atmosphere of the sub-Saturn mass planet WASP-69b (Nortmann et al. 2018; see Figure 1.13) and the Neptune-mass planet HAT-P-11b (Allart et al., 2018). After these discoveries, other studies found HeI in the atmospheres of the benchmark hot jupiters HD 209458b (Alonso-Floriano et al., 2019b) and HD 189733b (Salz et al., 2018), and in smaller planets such as the warm Neptune GJ 3470b (Palle et al., 2020a). Recently, the first detection of HeI in HD 189733b, using the GIANO-B spectrograph, located at the Telecopio Nazionale Galileo (TNG), has been claimed (Guilluy et al., 2020). Using the cross-correlation technique, it has been possible to detect water vapour in the atmosphere of hot Jupiters (e.g. Birkby et al. 2013, 2017; Alonso-Floriano et al. 2019a; Brogi et al. 2018; Sánchez-López et al. 2019), CO in the day and night-side (de Kok et al., 2013; Snellen et al., 2010), and methane and CO in non-transiting exoplanets (Brogi et al., 2012; Guilluy et al., 2019), for example.

Due to their extremely high temperatures, several ions have been detected in the atmospheres of ultra hot Jupiters, with most of the studies performed using high resolution spectroscopy observations and the cross-correlation technique. Absorption of single lines such as the NaI doublet, magnesium (MgI), ionised calcium (CaII), and the hydrogen Balmer lines have been detected in several of them with different facilities (e.g. Yan & Henning 2018; Casasayas-Barris et al. 2018, 2019; Seidel et al. 2019; Yan et al. 2019; Cauley et al. 2019; Wyttenbach et al. 2020; Cauley et al. 2020; see chapters 3 and 4). Using the cross-correlation technique, neutral and ionised iron (FeI, FeII) have been one of the most detected species in their atmosphere (e.g. Hoeijmakers et al. 2018,

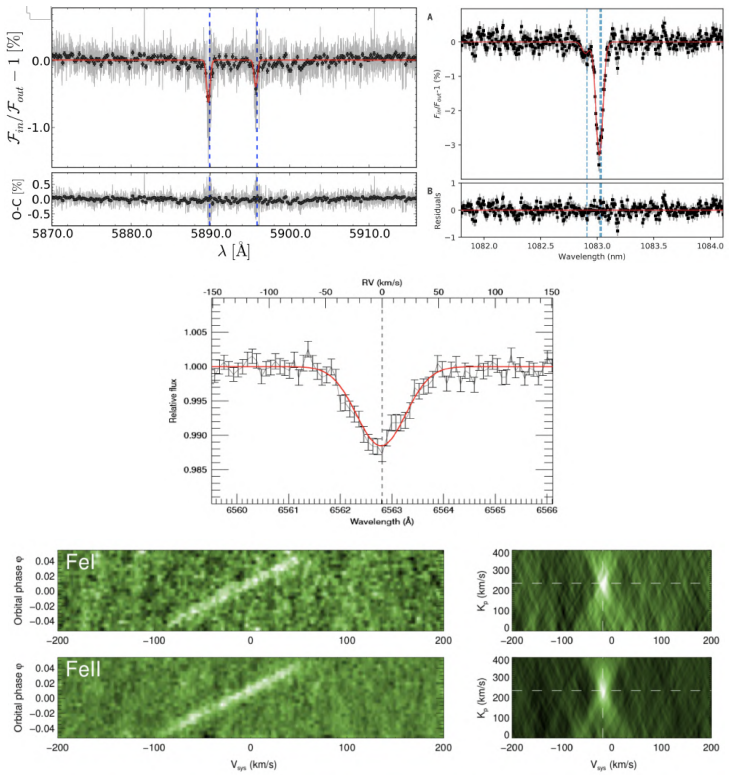

FIGURE 1.13— Transmission spectra of different exoplanets obtained in five benchmark studies. The panels are described from top to bottom. *First row, left panel:* NaI D detection in the atmosphere of the hot Jupiter HD 189733b using HARPS observations, where the two lines of the doublet are clearly resolved. Figure extracted from Wyttenbach et al. (2015). *First row, right panel:* HeI triplet detection in the atmosphere of the sub-Saturn mass planet WASP-69b using CARMENES observations in the NIR arm. Extracted from Nortmann et al. (2018). *Second row:* Hα detection in the atmosphere of the ultra hot Jupiter KELT-9b using CARMENES observations in the visible arm. Extracted from Yan & Henning (2018). In all panels the data is shown in grey and black dots and the best-fit Gaussian profiles are shown in red. The vertical dashed lines show the expected spectral lines position. *Third row:* detection of FeI and FeII in the atmosphere of the ultra-hot Jupiter KELT-9b using the cross-correlation technique. Figure adapted from Hoeijmakers et al. (2019). In the left panel we observe the cross-correlation time series, and the right panel shows the K_p-maps.

2020a,b; Nugroho et al. 2020; Stangret et al. 2020; Bourrier et al. 2020; see Figure 1.13), even allowing to see variation between the morning and evening terminators using the observations performed with the ESPRESSO spectrograph (Ehrenreich et al., 2020). For the hottest planet known to date, KELT-9b, with an equilibrium temperature around 4000 K, in addition to the previous species (see Figure 1.13), the observations show an extremely rich atmosphere. Hoeijmakers et al. (2019) ended up with detections of rare neutral and ionised metals such as ScII, TiII, CrII, and YII. Very recently, with secondary eclipse observations, it has been possible to survey the day-side atmosphere of ultra hot Jupiters, observing emission of iron (Nugroho et al., 2020; Pino et al., 2020; Yan et al., 2020) and TiO (Nugroho et al., 2017).

Although using very high resolution we are able to resolve the spectral lines taking advantage of the Doppler velocities, one of the disadvantages is that this technique suffers from the contamination of the Earth's atmosphere when the observations are performed from ground. The Earth's atmosphere modifies the stellar continuum spectrum and it is not calibrated. Thus, the absolute flux information is lost, and we are only able to measure relative differences of the local continuum (excess of absorption or emission). This situation is different when using observations with space-based spectrographs or ground-based spectrographs at low-resolution, but most of the space-based spectrographs operate at low-resolution. At low-resolution, although the absolute flux information can be measured, we are only able to probe the wings of the spectral features, as the lines cores are smoothed over a wide range of wavelengths. At high-resolution, contrarily, only the core of the lines is measured. The power of combining low- and high-resolution observations was highlighted by de Kok et al. (2014), showing that it would help to constrain the continuum level of the planet and remove degeneracies with composition. Therefore, for a complete picture of an exoplanet atmosphere, multi-resolution spectroscopy observations are needed (Brogi et al. 2017; Pino et al. 2018).

1.4.3 Challenges

Together with the rapid improvement of high-resolution transmission spectroscopy techniques, several challenges have arisen. The first group of difficulties is related to stellar variability. This group includes all stellar processes that may change the stellar spectrum in the time scales of the observations, such as stellar activity or pulsations. In the visible, stellar activity can become very important for particular stars (Cauley et al., 2018a), making the atmospheric study of the exoplanets in these systems extremely challenging (Cauley et al., 2018b). This is the case, for example, of the recently discovered exoplanet

Au Mic b, a Neptune-sized planet orbiting a very young ($\sim$ 20Myr) pre-main sequence M dwarf (Addison et al., 2020). Palle et al. (2020b) attempted to study the atmosphere of Au Mic b, concluding that the strong emission observed in the stellar lines produced by stellar activity and its variation during the observations does not permit the study of the exoplanet atmosphere. One the other hand, pulsating stars introduce time-variations in the stellar continuum and lines. When searching for absorption excess from the exoplanet atmosphere in the stellar spectrum, the identification of the exoplanet signals can be hampered by pulsation features. One example is WASP-33b, an ultra hot Jupiter orbiting a δ Scruti star that pulsates every $\sim$ 1 hour (von Essen et al., 2014). Although the detection of WASP-33b's atmosphere has been possible (Yan et al., 2019), several pulsation features are observable in the transmission spectrum.

Recently, two effects have started to gain importance as additional challenges when attempting to detect exoplanetary atmospheres: the RM effect (see also Chapter 1.1) and the centre-to-limb variation (CLV). During a transit, the exoplanet blocks different parts of the stellar disc, which are characterised by different physical properties. Keeping in mind that, during the observations, we always receive the integrated disc stellar spectrum, if we now observe the star when the planet is crossing the disc, the regions of the disc obscured by the planet will be missing in the final integrated spectrum that we receive (see scheme in Figure 1.14). This lack of information in the stellar spectrum during the transit of the planet produces variations in the stellar lines profile that could partially or totally mimic the atmospheric spectral features, when compared to the full integrated disc spectrum, depending on the host star spectral-type and the system architecture (see Chapters 4 and 5 of this thesis).

The importance of the RM effect in atmospheric studies was first pointed out by Louden & Wheatley (2015). This effect is produced due to the different projected velocities of the stellar surface that are blocked by the planet (see Figure 1.14). Due to the symmetry of the RM, this effect is expected to be small in the stellar rest frame. However, in the planet rest frame (where the absorption of the exoplanet is expected) the symmetries are broken and spurious signals appear in the transmission spectrum. It is very important to note that, in additional to the intrinsic strength of the RM, which depends on the geometry of the planet-star system (see equation 1.1), the planet radial-velocity change during the observation is crucial in order to disentangle the atmospheric absorption from the RM effect. For example, in a given system showing very strong RM and a planet that moves faster/slower than this effect in radial-velocity, the atmospheric absorption could be distinguished (e.g. MASCARA-2b; see Chapters 3 and 4). For a polar planet, which only blocks a red/blue part of the stellar disc without producing an RM induced line variation during its transit,

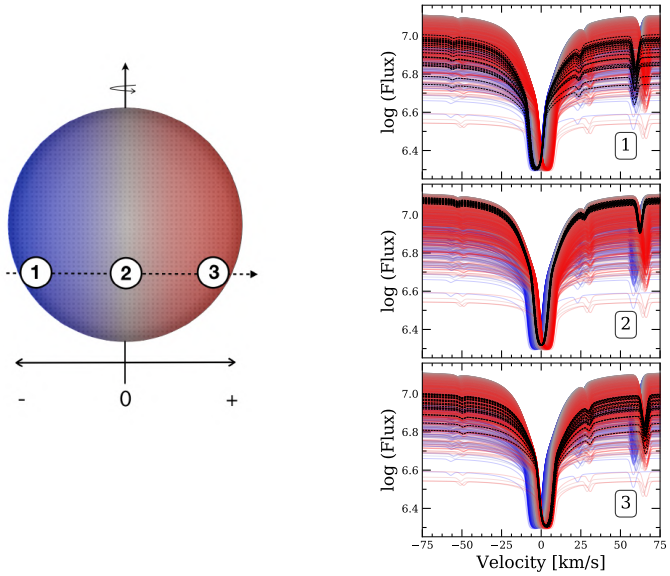

FIGURE 1.14— The effect that a transiting exoplanet produces in the integrated stellar disc spectrum during the observations, considering the RM and CLV effects. *Left panel:* illustration of a star-planet system. The colour of the stellar disc indicates the projected rotational velocities (blue means negative and red positive). The white circles represent the transiting exoplanet at three different positions during the transit. *Right panel:* modelled stellar spectra at different points of the stellar disc considering the limb-darkening effect. The colours represent the spectra at the stellar disc positions shown in the illustration (*left panel*). The sum of all coloured spectra would give the integrated disc spectrum observed when the planet is not transiting. The black-dashed lines indicate the spectra of the stellar disc regions obscured by the planet in the three positions shown in the *left panel* (top, middle, and bottom panels, respectively). When the observations are performed during the transit, the observed stellar spectrum does not contain the spectra of the stellar disc regions that are blocked by the planet. The models are computed for a HD 209459b-like system assuming an impact parameter $b = 0.5$ and obliquity $\lambda = 0\,\mathrm{deg}$, using the MARCS (Gustafsson et al., 2008) stellar models, the Spectroscopy Made Easy (SME ; Valenti & Piskunov 1996; Piskunov & Valenti 2017), and the line lists from VALD3 (Ryabchikova et al., 2015).

the atmosphere of the planet could also be distinguished (e.g. KELT-9b; Yan & Henning 2018).

The CLV may also potentially affect the line profiles during transits. The stellar continuum in the photosphere has lower intensity near the stellar limb with respect to the centre of the disc. This effect is related to the optical depth of the photosphere. The balance between the lines formed at different heights depends on the limb angle and the stellar latitude (Abetti & Castelli, 1935; Appenzeller & Schröter, 1967). Although the impact of this effect in the final transmission spectrum is usually fainter than the RM effect, it has been observed that the strength of the CLV effect can be of the same order as some of the atmospheric signals detected on hot Jupiters (Yan et al., 2017; Czesla et al., 2015; Khalafinejad et al., 2017). For terrestrial planets, for which the atmospheric features in the transmission spectra will be fainter, the CLV and RM effects are expected to be critical.

In Figure 1.15 the combined impact of the CLV and RM effects on the transmission spectra of different planets are shown, around the NaI doublet. The planets have been selected for their different system architectures (impact parameter and obliquity), velocity of the planet, and projected rotation velocity of the host star ($v \sin i_\star$). For the HD 189733b system, for example, the radial-velocities of the exoplanet and the RM effect are very close, showing a relatively strong impact centred on the NaI lines. KELT-17b and MASCARA-1b systems show highly miss-aligned orbits and, consequently, the features are not centred on the NaI lines position. Finally, KELT-21b has an aligned orbit around a very fast rotating star ($v \sin i_\star = 146.0\,\mathrm{km\,s^{-1}}$). The planet radial velocity change during the transit is smaller than the RM, so the final effect (when combined in the planet rest frame) is spread over a wide wavelength range and becomes fainter.

1.4.4 Future prospects

The fast and considerable progress made in the characterisation of exoplanet atmospheres has accelerated the development of new instrumentation, observational techniques and modelling. To this aim, several space-based facilities are expected to see their first light in the near future. This is the case of the James Webb Space Telescope (JWST), with a 6.5 m diameter mirror, and four infrared instruments (1-30 μm) which are able to operate in different modes, from low to moderately high ($\Re \sim 3\,600$) spectral resolution. At these wavelengths, strong molecular bands are detectable, including methane, CO and CO_2. With JWST, it will be possible to study hot Jupiter atmospheres at high S/N and the atmospheric composition of warm Neptunes and super-Earths (Deming et al., 2009).

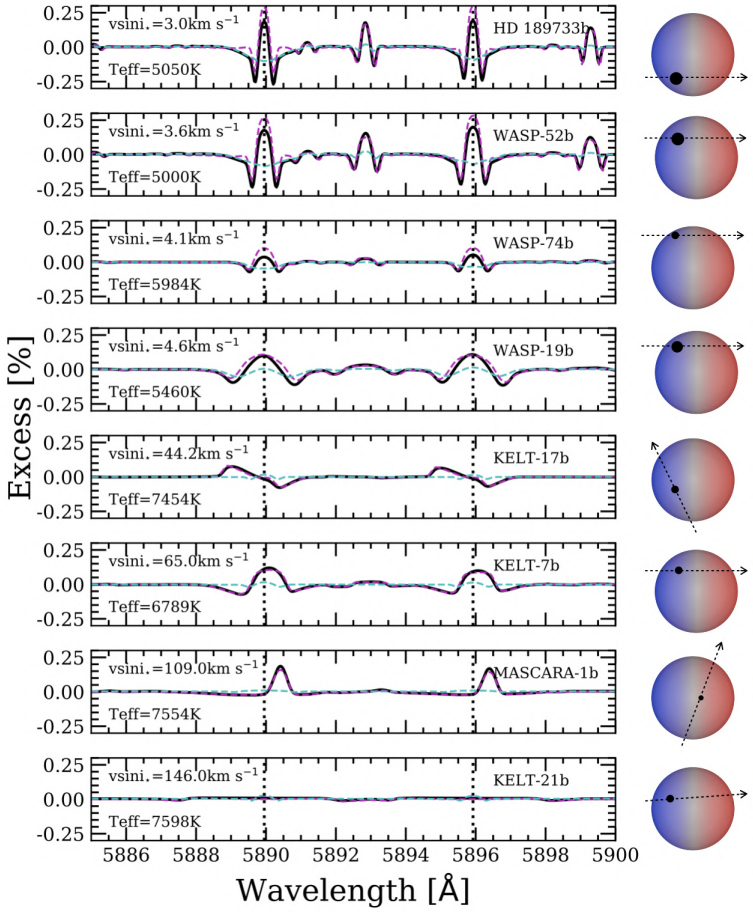

FIGURE 1.15— RM and CLV impact on the transmission spectrum around the NaI doublet lines, calculated for different exoplanets and integrated over the full transit in the planet-rest frame. In black-solid lines we show both CLV and RM effects combined. The magenta and cyan dashed lines show the RM and CLV effects, respectively. The planets are ordered from slow (top; 3.0 km s^{-1}) to fast (bottom; 146.0 km s^{-1}) projected rotation velocity of the stellar host ($v \sin i_\star$). The $v \sin i_\star$ and effective temperature of the host star (T_{eff}) are indicated in each panel. The dotted vertical lines show the laboratory position of the NaI doublet lines which, in this case, correspond to the the position where the exoplanet imprints would be expected. The architectures of the systems are illustrated in the right figures, where the radius of the planet is in scale with the radius of the host star.

In a longer term, three ambitious NASA's concepts called WFIRST, HabEx and LUVOIR are expected to observe, for the first time, Earth-like twins and other terrestrial planets orbiting solar-type stars via extreme high contrast direct imaging with coronographs and starshades. For the most favourable cases the detection of biosignatures in their spectra might be possible (Deming & Seager, 2017).

From ground, high-resolution transmission spectroscopy methods will be crucial in the near future in order to observe spectral features of those rocky planets and super-Earths, which will be out of reach of the JWST, but available with the upcoming large aperture ground-based facilities, the extremely large telescopes (ELTs). ESPRESSO on the VLT has already demonstrated to be an extremely powerful tool to study the atmospheric composition and dynamics of giant exoplanets (Ehrenreich et al., 2020; Borsa et al., 2020; Tabernero et al., 2020). The new generation of high dispersion spectrographs at 30-40 meter telescopes, like HIRES on E-ELT (Lovis et al., 2017), will open a window to the atmospheric exploration of smaller planets and fainter targets. Using tens of transits, transmission spectroscopy with ELTs will probably make possible the detection of molecular oxygen in the atmosphere of habitable exoplanets (Snellen et al., 2013).

1.5 Overview of the work presented in this thesis

In this section, a short overview over the publications that form part of this thesis is given. In Chapter 2, we present the reanalysis of HARPS observations of the hot Jupiter HD 189733b, which ended up in the detection of NaI by Wyttenbach et al. (2015). Here, we follow slightly different methodology to extract the transmission spectrum using high-resolution spectroscopy, but find consistent results. In parallel, we show the detection of NaI in the atmosphere of WASP-69b, a planet without previous atmospheric studies. Chapter 3 shows the analysis of one transit observation of the ultra hot Jupiter MASCARA-2b, performed with the HARPS-N spectrograph. The results show tentative signals of Hα and NaI with atmospheric origin. After adding more transit observations of this same planet with HARPS-N and CARMENES, we are able to confirm the previous findings and detect other species such as the ionised metals CaII and FeII in the atmosphere of the planet. This study is presented in Chapter 4. In Chapter 5, we present the atmospheric analysis at high resolution spectroscopy of one of the most studied exoplanets, the hot Jupiter HD 209458b. Using CARMENES and HARPS-N archival observations we focus on the study of the NaI doublet lines. In contrast with previous studies claiming the detection of this specie in the atmosphere of HD 209458b, our results show that the features

observed in the transmission spectrum, at low signal-to-noise ratio, come from the impact of the RM and CLV effects in the observations. The continuation of this study is shown in Chapter 6. In this case, we use high signal-to-noise observations with ESPRESSO, finding consistent results with CARMENES and HARPS-N observations and no evidence of the atmosphere of the exoplanet. In Chapter 7 we summarise the study performed in this thesis and point out the main conclusions. An overview of possible future work is also included at the end of this last chapter.

2

Sodium in the atmosphere of WASP-69b

Newton's third law.
You gotta leave something behind.

Interstellar, 2014

The first ground-based detection of NaI in the atmosphere of an exoplanet using high-resolution spectroscopy observations was performed using the High Resolution Spectrograph (HRS; $\Re \sim 60\ 000$) at the Hobby-Eberly Telescope by Redfield et al. (2008), in HD 189733b. However, the first study presenting the complete methodology to extract the transmission spectrum of single lines from high resolution observations was presented by Wyttenbach et al. (2015), using HARPS ($\Re \sim 115\ 000$) observations of HD 189733, and detecting NaI absorption from its atmosphere. Using the data from this previous study, in this chapter the transmission spectrum of HD 189733b is revisited. In parallel, the same methodology is applied to the new WASP-69b transit observations performed with the HARPS-N spectrograph. The analysis and results presented in this chapter are published in A&A under the bibcode 2017A&A...608A.135C (Casasayas-Barris et al., 2017).

Three HARPS archival transit observations of the hot Jupiter HD 189733b and two new transits of the sub-Saturn mass planet WASP-69b observed with the HARPS-N spectrograph are analysed to extract the transmission spectrum

of both planets around the NaI doublet lines at 590 nm. The methodology used to extract the transmission spectra of both planets is based on Wyttenbach et al. (2015). The unique difference appears when correcting the absorption and emission contamination from the Earth atmosphere, for which we use telluric models and sky observations, respectively. We detect NaI absorption from the atmosphere of both planets. The results obtained for HD 189733b are consistent with those presented in Wyttenbach et al. (2015). For WASP-69b we are able to observe a 5 σ absorption excess in the NaI D2 line. For the NaI D1 line, the excess measurement is consistent with a non-detection. Due to the low S/N of WASP-69 observations, more transits are needed to characterise the lines' profile.

Additionally, we estimate the impact of the RM and CLV of the stellar lines in the final transmission spectrum and light curves. Although they are clearly noticeable in the transmission light curves of HD 189733b, due to the S/N of the data, the impact of these effects remains inside the error bars of the transmission spectrum. We discuss how these effects could gain importance at higher S/N and influence the absorption measurements. On the other hand, we estimate the spin-orbit alignment of the two systems by fitting the stellar radial-velocity during the transit with the RM model from Ohta et al. (2005). The obliquity estimation of both systems points to an aligned orbit. For HD 189733b we measure $\lambda = -0.3 \pm 0.2$ deg, consistent with previous studies (e.g. Winn et al. 2006; Cegla et al. 2016a; Triaud et al. 2009). For WASP-69b, this measurement is performed for the first time, obtaining $\lambda = 0.4 \pm 2.0$ deg.

A&A 608, A135 (2017)
DOI: 10.1051/0004-6361/201731956

Astronomy & Astrophysics

Detection of sodium in the atmosphere of WASP-69b⋆

N. Casasayas-Barris[1,2], E. Palle[1,2], G. Nowak[1,2], F. Yan[3], L. Nortmann[1,2], and F. Murgas[1,2]

[1] Instituto de Astrofísica de Canarias, vía Láctea s/n, 38205 La Laguna, Tenerife, Spain
e-mail: nuriacb@iac.es
[2] Departamento de Astrofísica, Universidad de La Laguna, 38200 La Laguna, Spain
[3] Max Planck Institute for Astronomy, Königstuhl 17, 69117 Heidelberg, Germany

Received 14 September 2017 / Accepted 16 October 2017

ABSTRACT

Context. Transit spectroscopy is one of the most commonly used methods to characterize exoplanets' atmospheres. From the ground, these observations are very challenging due to the terrestrial atmosphere and its intrinsic variations, but high-spectral-resolution observations overcome this difficulty by resolving the spectral lines and taking advantage of the different Doppler velocities of the Earth, the host star, and the exoplanet.
Aims. We analyze the transmission spectrum around the Na I doublet at 589 nm of the extrasolar planet WASP-69b, a hot Jupiter orbiting a K-type star with a period of 3.868 days, and compare the analysis to that of the well-known hot Jupiter HD 189733b. We also present the analysis of the Rossiter-McLaughlin (RM) effect for WASP-69b.
Methods. We observed two transits of WASP-69b with the High Accuracy Radial velocity Planet Searcher (HARPS-North) spectrograph (R = 115 000) at the Telescopio Nazionale *Galileo* (TNG). We perform a telluric contamination subtraction based on the comparison between the observed spectra and a telluric water model. Then, the common steps of the differential spectroscopy are followed to extract the transmission spectrum. The method is tested with archival transit data of the extensively studied exoplanet HD 189733b, obtained with the HARPS-South spectrograph at ESO 3.6 m telescope, and then applied to WASP-69b data.
Results. For HD 189733b, we spectrally resolve the Na I doublet and measure line contrasts of 0.72 ± 0.05% (D2) and 0.51 ± 0.05% (D1), and full width half maximum (FWHM) values of 0.64 ± 0.04 Å (D2) and 0.60 ± 0.06 Å (D1), in agreement with previously published results. For WASP-69b only the contrast of the D2 line can be measured (5.8 ± 0.3%). This corresponds to a detection at the 5σ-level of excess absorption of 0.5 ± 0.1% in a passband of 1.5 Å. A net blueshift of ∼0.04 Å is measured for HD 189733b and no shift is obtained for WASP-69b. By measuring the RM effect, we get an angular rotation of $0.24^{+0.02}_{-0.01}$ rad/day and a sky-projected angle between the stellar rotation axis and the normal of orbit plane (λ) of $0.4^{+2.0\circ}_{-1.9}$ for WASP-69b. Similar results to those previously presented in the literature are obtained for the RM analysis of HD 189733b.
Conclusions. Even if sodium features are clearly detected in the WASP-69b transmission spectrum, more transits are needed to fully characterize the line profiles and retrieve accurate atmospheric properties.

Key words. planetary systems – planets and satellites: individual: WASP-69b – planets and satellites: individual: HD 189733b – planets and satellites: atmospheres – methods: observational – techniques: spectroscopic

1. Introduction

Over the last two decades there has been enormous progress in the search for planets outside our solar system, resulting in thousands of exoplanet detections. Moreover, the atmospheric characterization of some of these discovered planets has been rapidly expanding with the constant improvement of the astrophysical instrumentation, transiting systems being the most amenable targets for atmospheric studies. Transmission spectroscopy is one of the best-known methods for atmospheric characterization. During a transit, the stellar light penetrates the planetary atmosphere and its signatures appear imprinted in the stellar flux. Observing when the planet is crossing the stellar disk and when it is not, the transmission spectrum of the planet can be extracted through differential spectroscopy, comparing the in- and out-of-transit measurements.

The first detection of an exoplanet atmosphere by Charbonneau et al. (2002), which revealed the presence of atomic sodium (Na I), was only possible thanks to space-based instruments on-board the *Hubble* Space Telescope (HST). For a time, ground-based observations were thought to be too challenging, but the difficulties due to the terrestrial atmospheric variations and systematic effects during the observations of transiting systems have been slowly overcome, resulting in robust detections of Na, K, and Rayleigh-like slopes with low-spectral-resolution spectrographs (Sing et al. 2012; Murgas et al. 2014; Wilson et al. 2015; Chen et al. 2017; Palle et al. 2017, among others). The larger aperture of ground-based telescopes provides a significant advantage over space-based observations, but limitations still remain due to telluric absorption in the atmosphere. However, observations at high spectral resolution overcome this difficulty of dealing with the telluric atmosphere by resolving the spectral lines and taking advantage of the different Doppler velocities of the Earth, the host star, and the exoplanet.

The Na I doublet, with lines at 5895.924 Å (D1) and 5889.951 Å (D2), is one of the easiest species to detect in a hot planet upper atmosphere due to its high cross-section, and

⋆ The transmission spectra and the observed spectro-photometric light curves are only available at the CDS via anonymous ftp to cdsarc.u-strasbg.fr (130.79.128.5) or via http://cdsarc.u-strasbg.fr/viz-bin/qcat?J/A+A/608/A135

Table 1. Physical and orbital parameters of WASP-69 and HD 189733 systems.

	Parameters	Values	
		WASP-69	HD 189733
Star	V mag	9.9	7.7
	Spectral type	K5	K1-K2
	$T_{\rm eff}$ [K]	4700 ± 50	$5040 \pm 50^{*}$
	$V \sin i$ [km s^{-1}]	2.20 ± 0.4	$3.5 \pm 1^{*}$
	$M_\star$ [$M_\odot$]	0.826 ± 0.029	$0.806 \pm 0.048^{*}$
	$R_\star$ [$R_\odot$]	0.813 ± 0.028	$0.756 \pm 0.018^{*}$
Transit	T_0 [BJD]	$2\,455\,748.83344 \pm 0.00018$	$2\,454\,279.436714 \pm 0.000015^{\S}$
	P [days]	$3.8681382 \pm 1.7 \times 10^{-6}$	$2.21857567 \pm 1.5 \times 10^{-7\S}$
	$t_{\rm T}$ [days]	0.0929 ± 0.0012	$0.0760 \pm 0.0017^{\ddagger\ddagger}$
	a [AU]	0.04525 ± 0.00075	$0.03100 \pm 0.00062^{\dagger}$
	$a/R_\star$	12.00 ± 0.46	$8.84 \pm 0.27^{\S}$
	b [$R_\star$]	0.686 ± 0.023	$0.6631 \pm 0.0023^{\S}$
	$i_{\rm p}$ [degrees]	86.71 ± 0.2	$85.7100 \pm 0.0023^{\S}$
	e	0	$0^{\P}$
	ω [degrees]	90	$90^{\P}$
	γ [m/s]	-9.62826 ± 0.00023	$-2.57 \pm 0.143^{\ddagger}$
	K_1 [m/s]	38.1 ± 2.4	$205.0 \pm 6^{\P}$
Planet	M_P [$M_{\rm J}$]	0.260 ± 0.0185	$1.144 \pm 0.056^{\dagger}$
	R_P [$R_{\rm J}$]	1.057 ± 0.017	$1.138 \pm 0.027^{*}$
	$T_{\rm eq}$ [K]	963 ± 18	$1191 \pm 20^{\|}$
	H [km]	~650	~200

References. All WASP-69 parameters are taken from Anderson et al. (2014). (*) Torres et al. (2008). (§) Agol et al. (2010). (‡‡) Seager & Mallén-Ornelas (2003). (†) Butler et al. (2006). (¶) Bouchy et al. (2005). (‡) Boisse et al. (2009). (||) Southworth (2010).

the line cores can trace the temperature profiles up to the planet thermosphere. The first ground-based detection of Na I doublet in HD 189733b was performed with the High Resolution Spectrograph (HRS), with $R \sim 60\,000$, mounted on the 9.2 m Hobby-Eberly Telescope (Redfield et al. 2008). Soon after, the Na I was confirmed in HD 209458b using the High Dispersion Spectrograph (HDS), with $R \sim 45\,000$, on the 8 m Subaru Telescope (Snellen et al. 2008). Recent ground-based studies with the High Accuracy Radial velocity Planet Searcher (HARPS) spectrograph ($R \sim 115\,000$), at ESO 3.6 m telescope in La Silla (Chile), have been able to resolve the individual Na I line profiles of HD 189733b (Wyttenbach et al. 2015) and WASP-49b (Wyttenbach et al. 2017). Several studies have used these same data sets; for example, Heng et al. (2015) studied the existence of temperature gradients, Louden & Wheatley (2015) explored high-altitude winds in the atmosphere of HD 189733b, Barnes et al. (2016) studied stellar activity signals, and Yan et al. (2017) focused on center-to-limb variation (CLV) effect in the transmission light curve of this same exoplanet.

High-resolution transmission spectroscopy methods will be crucial in the near future in order to observe spectral features of rocky planets and super-Earths, which will be out of reach of the *James Webb* Space Telescope (JWST), but available with the upcoming facilities such as ESPRESSO on the Very Large Telescope (VLT) or HIRES on E-ELT (Snellen et al. 2013; Lovis et al. 2017).

Here, we present the results obtained with the HARPS-North spectrograph by analyzing two transit observations of WASP-69b. WASP-69b (Anderson et al. 2014) is a Saturn-mass planet (0.26 $M_{\rm Jup}$, 1.06 $R_{\rm Jup}$) in a 3.868-day orbit around a K5 star. Its large atmospheric scale height (~650 km) and the small size of the star make this planet a good target for transmission spectroscopy (see Table 1). We present an alternative reduction method, which we apply firstly to the well-studied exoplanet HD 189733b, using data from previous HARPS observations, and then to the new WASP-69b observations.

This paper is organized as follows. In Sect. 2, we present the observations. In Sect. 3, we describe the data-reduction process, including the telluric correction and the transmission spectrum extraction. In Sect. 4, we present and discuss the results obtained on the atomic sodium (Na I) absorption observed in the transmission spectrum and the transmission light curve of both HD 189733b and WASP-69b. In Sect. 5, we present the results of the Rossiter-McLaughlin (RM) effect measurement of WASP-69b.

2. Observations

We observed two transits of WASP-69b on 4 June 2016 and 4 August 2016 using the HARPS-North spectrograph mounted on the 3.58 m Telescopio Nazionale *Galileo* (TNG), located at Roque de los Muchachos Observatory (ORM). For the first transit, the observations started at 01:25 UT and finished at 05:19 UT. The airmass variation was from 2.2 to 1.2. On the second night, we observed from 22:29 to 02:51 UT, and the airmass changed from 1.5 to 1.2.

For both transits, we observed continuously during the night, exposing before, during, and after the transit in order to retrieve a good baseline and a high signal-to-noise (S/N) out-of-transit spectrum, which is important for the data-reduction process. Several transits are needed to reach enough S/N for the detection of the spectroscopic exoplanetary signatures. The observations were carried out using fiber A on the target and fiber B on the sky. Since WASP-69 has a magnitude of 9.87 (V), 900 s of

Table 2. Observations log for WASP-69 and HD 189733 for the employed data sets.

		Date	# Spectra[1]	Exp. time [s]	Airmass	S/N^2	S/N^3	Fiber B[4]
WASP-69	Night 1	2016-06-04	8/16	900	2.2–1.2	~45	~11	Yes
	Night 2	2016-08-04	8/18	900	1.5–1.2	~40	~8	Yes
HD 189733	Night 1	2006-09-07	9/20	900–600	1.6–2.1	~165	~40	No
	Night 2	2007-07-19	18/39	300	2.4–1.6	~115	~22	Yes
	Night 3	2007-08-28	19/40	300	2.2–1.6	~100	~20	Yes

Notes. [(1)] Number of in-transit spectra/total number of spectra. [(2)] S/N per pixel extracted in the continuum near 5900 Å. [(3)] S/N in the lines core of the Na I D lines. [(4)] Fiber B monitoring the sky simultaneously to the target observations.

exposure time were used, recording a total of 35 spectra, 16 of them forming our in-transit sample. The remaining spectra are out of transit.

There is one further transit dataset of WASP-69b in the HARPS archive (program: 089.C-0151(B), PI: Triaud) taken on 22 June 2012. However, telluric Na emission is observed during that night and the sky fiber B was not used, impeding telluric decontamination. Thus, we have not used these data in this paper.

HD 189733 was observed with HARPS on the ESO 3.6 m telescope in La Silla, Chile. Data were retrieved from the ESO archive, programs 072.C-0488(E), 079.C-0828(A) (PI: Mayor) and 079.C-0127(A) (PI: Lecavelier des Etangs). In total, HD 189733 was observed during four transits, the last night being affected by bad weather, and therefore not used here. As for the WASP-69 observations, all of the nights were dedicated to retrieving the largest baseline possible, recording 99 spectra in total, 46 of them obtained during transit. In these observations, sky spectra on fiber B were gathered only for the second and third nights. These data have been extensively studied by other authors, for example Triaud et al. (2009), Wyttenbach et al. (2015), Louden & Wheatley (2015), Di Gloria et al. (2015), Barnes et al. (2016), and Yan et al. (2017). The observing logs of the two data sets employed here are summarized in Table 2.

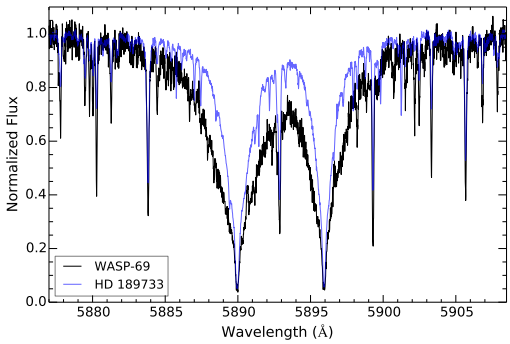

Fig. 1. Normalized spectra of WASP-69 (black) and HD 189733 (blue) after being reduced by the HARPS DRS around the Na I region. Both spectra are in their stellar reference frame.

3. Methods

3.1. Data reduction

The observations were reduced with the HARPS Data Reduction Software (DRS), version 1.1 of HARPS-North DRS for WASP-69 and version 3.5 of HARPS-South DRS for HD 189733. In both cases, the DRS extracts the spectra order-by-order, which are then flat-fielded using the daily calibration set. For each spectral order, a blaze correction is applied together with the wavelength calibration and, finally, all the spectral orders from each two-dimensional echelle spectrum are combined and resampled, ensuring flux conservation, into a one-dimensional spectrum. The resulting spectra are referred to the Solar System barycenter rest frame and the wavelengths are given in the air. The reduced one-dimensional spectra cover a wavelength range between 3800 and 6900 Å, with a wavelength step of 0.01 Å and a spectral resolution of $R \sim 115\,000$. Two representative spectra, one for each planet, around the Na doublet region are shown in Fig. 1.

3.2. Telluric correction

One of the major difficulties of ground-based observations is dealing with the telluric imprints from the Earth's atmosphere. Since the telluric transmission during a night depends on the airmass and on water column variations in the air, the atmospheric constituents contaminate the recorded spectra by producing a time-variable diversity of absorption and emission lines. The main contributors in the optical domain are water and molecular oxygen, nevertheless, we also expect telluric sodium signatures near the Na I doublet (Snellen et al. 2008). This telluric sodium suffers seasonal variations and, within a night, its behavior is different from the other telluric features, making it necessary to remove these two different contamination sources using different processes.

3.2.1. Telluric sodium

Each individual spectrum of both planets was examined for the presence of telluric sodium. For WASP-69b telluric sodium appears in the spectra as emission, as can also be observed in the sky spectra retrieved with fiber B simultaneously to the target data, which ensures exactly the same atmospheric conditions in both spectra (Fig. 2). Here, we remove the telluric sodium contamination in WASP-69 data by simply subtracting the sky spectra from the target spectra (see Fig. 3). The sky spectra taken together in HD 189733 observations were also checked but no sodium emission is observed.

These telluric signatures present a strong dependence on airmass, being more intense at higher airmass and rapidly disappearing at lower airmass. However, their behavior is not exactly the same as the other telluric lines, producing strong telluric residuals in the resulting transmission spectrum if we make the assumption that they can be corrected in the same way as the other telluric features (Wyttenbach et al. 2015). This shows the importance of using fiber B to monitor

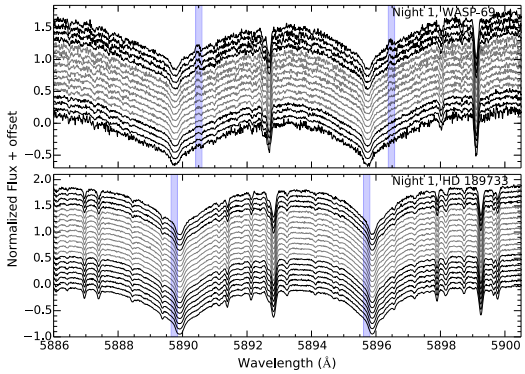

Fig. 2. Normalized spectra of WASP-69 (*top*) and HD 189733 (*bottom*) for night 1, in the region of the Na I doublet. Different flux offsets are added to each spectrum for a better visualization. In both cases, the spectra are organized by observing time: the first spectrum of the night is located in the upper position and the last one in the lowest position. For WASP-69 the airmass decreases with time and for HD 189733 it increases. In black are shown the out-of-transit spectra and in gray, the in-transit spectra. The blue regions show where the telluric sodium is observed for WASP-69 spectra and where the telluric sodium is expected for HD 189733 data. We note that the last spectrum of WASP-69 for the first night is not used in the reduction process because of the higher noise compared to other spectra of the same night.

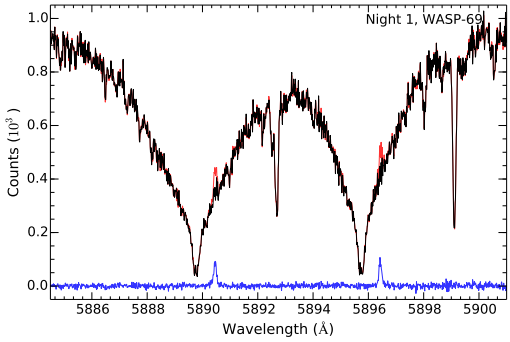

Fig. 3. Telluric sodium correction for WASP-69 spectra. The red spectrum is one of WASP-69 observed spectra for night 1, where the telluric sodium features can be observed in the wings of the stellar Na I lines. The blue line is the corresponding sky spectrum taken with the HARPS-N fiber B, and the black line is the resulting WASP-69 spectrum after the sky subtraction.

the sky background simultaneously to the observations. In Wyttenbach et al. (2017), telluric sodium is observed in some of the WASP-49 spectra. They find a random behavior of this telluric emission in their spectra, with no correlation between the sodium emission and the airmass. Not correcting for this effect could be a problem in case of a null barycentric Earth radial velocity (BERV) and a small stellar systemic velocity, where the telluric and exoplanetary sodium could overlap in the mid-transit position.

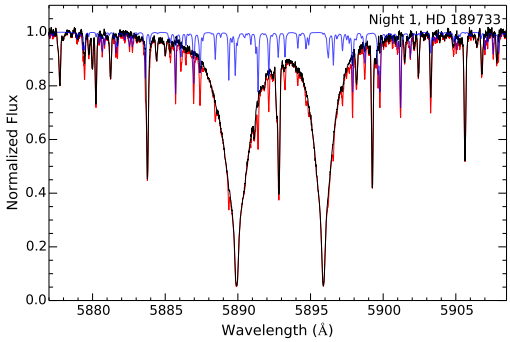

Fig. 4. Telluric correction of the observed spectra of HD 189733. The red spectrum is one of the observed HD 189733 spectra for night 1, the blue line is the shifted and scaled telluric water model from (Yan et al. 2015), and the black spectrum is the resulting spectrum after applying the telluric correction.

3.2.2. Other telluric features

In addition to removing telluric sodium, it is necessary to remove the telluric imprints produced by water vapor, the main contributor to the telluric contamination near the Na I doublet.

We present a different method to correct for the telluric contamination with respect to the methods described in Vidal-Madjar et al. (2010), Astudillo-Defru & Rojo (2013) and Wyttenbach et al. (2015), which consider that the variation of telluric lines follows the airmass variation linearly. Here, the telluric features are corrected by using the one-dimensional telluric water model presented in Yan et al. (2015), which uses the line list from HITRAN (Rothman et al. 2013). The spectra are referred to the solar system reference frame. In this frame the Earth's radial velocity (RV) variation during the night is reflected as a wavelength shift of the telluric lines with respect the air position. We note that the telluric lines absorption depth also changes with the airmass. For each observed spectrum, we shift the telluric water vapor model to the position of the telluric lines using the BERV information. This shifted model is then scaled to the same airmass of the observed spectrum and, finally, the observed spectrum is divided by the scaled telluric model, removing the telluric features from the data (see Fig. 4).

The variation in the transmission of the Earth's atmosphere is one of the main problems when a model is used to correct the telluric contamination. The line depth variation is not equal for all the telluric lines, leading to poor results in the removal of the telluric signatures when scaling the model, and possibly introducing small residuals into the final transmission spectrum. However, one of the benefits of using this method is that no additional noise is introduced in the corrected spectra, key in transit spectroscopy, taking into account the low S/N expected for the atmospheric planetary signals. On the other hand, we also consider the telluric line's movement during the night, since omitting this shift could produce signals of misalignment in the next reduction steps. This alternative method can also be useful when the baseline of the observations is insufficient to compute a high-quality telluric spectrum for an efficient correction of telluric lines.

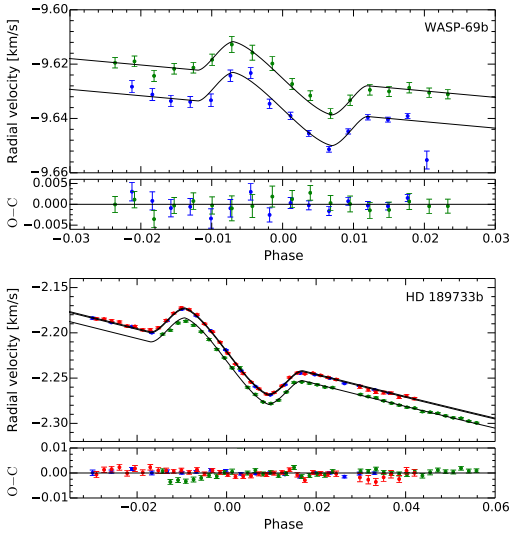

Fig. 5. Nightly evolution of the RV of WASP-69 (*top*) and HD 189733 (*bottom*) (in blue the night 1, in green the night 2, and in red the night 3). In the vertical axis we show the RV of the star in km s^{-1}. The RV and error values are taken from the HARPS files header. The black solid line is the best fit model for each individual night. The bottom panel of each plot shows the residuals between the data and the best fit model.

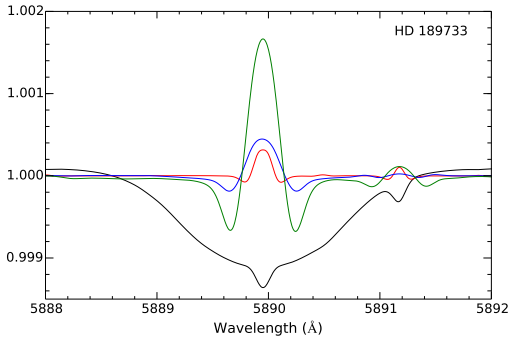

Fig. 6. Modeled CLV and RM effects of the HD 189733 D2 Na I line. The black line shows the modeled CLV effect and the red line shows the RM effect in the stellar rest frame. The RM effects in the planetary rest frame, with and without correcting the RM induced RV, are shown in blue and green, respectively. For the D1 line, the effects are slightly stronger.

3.3. Transmission spectrum

Transit spectroscopy requires observations when the planet is crossing the stellar disk and when it is not. The out-of-transit spectra contain the stellar flux partially absorbed by the Earth's atmosphere, while the in-transit spectra contain, additionally, the exoplanet atmosphere transmission. These data are used to compute their ratio spectrum and measure the extra absorption caused by the planet atmosphere.

Before computing this ratio spectrum, the stellar lines of all the spectra, which are shifted in wavelength due to the RV variation of the star during the transit of a planet, need to be aligned. The RV of WASP-69 is ±15 m s^{-1}, while for HD 189733 it is ±50 m s^{-1}. These shifts create artificial signals in the spectra if they are not corrected. In order to align the stellar lines to the null stellar RV, we use the HARPS files header information, where the star RV values are given, taking into account possible instrumental error, stellar activity, and the RM effects (see Fig. 5). Omitting the RM effect in the stellar RV when aligning the stellar lines introduces misalignments and spurious results in the final transmission spectrum.

Some methods obtain the transmission spectrum of the exoplanet atmosphere by dividing the combination of all the telluric-corrected in-transit spectra (master in) by the combination of all the out-of-transit spectra (master out; Redfield et al. 2008). However, the planet RV varies during the transit, which causes a shift of the planetary absorption lines across the stellar lines profile. The RV of WASP-69b changes from +7 km s^{-1} to −7 km s^{-1} and ±15 km s^{-1} for HD 189733b, meaning a wavelength shift of ±0.14 Å and ±0.30 Å, respectively. For 0.01 Å steps, like HARPS, this corresponds to a shift of more than 10 pixels. Here we correct for this effect by using the method presented in Wyttenbach et al. (2015), in which the planetary signal is shifted to the null RV at the planet rest frame (i.e., the RV in the middle of the transit). Each in-transit spectrum ($F_{\rm in}$) is divided by the master-out spectrum, $M_{\rm out} = \sum_{\rm out} F_{\rm out}(\lambda)$, and the result is shifted to the planet rest frame. Finally, all of these individual transmission spectra are combined,

$$\Re = \sum_{\rm in} \frac{F_{\rm in}(\lambda)}{M_{\rm out}}\Big|_{\rm Planet\ RV\ Shift} - 1. \quad (1)$$

This process is applied to all nights, obtaining a transmission spectrum for each night, which are then combined and normalized using a linear fit to the continuum outside the regions of interest.

The CLV effect and RM effect both have impacts on the obtained transmission spectrum. As shown in Yan et al. (2017), the CLV of the stellar lines profile along the stellar disk is an important effect for the transmission spectroscopy which needs to be corrected for a better characterization of the planetary Na I absorption. Omitting the RM effect in the stellar RV when aligning the stellar lines introduces misalignments and spurious results in the final transmission spectrum (Louden & Wheatley 2015; Barnes et al. 2016). We note that during the transit the planet occults different parts of the stellar disk, which have different velocities. Thus, in addition to the lines' shift, the RM also affects the stellar lines' shape, which can produce false-positive features in the transmission spectrum. The RM effect can be averaged out if the spectra are retrieved uniformly during a full transit and shifted to the stellar rest frame. However, if the spectra are shifted into the planetary rest frame, the RM effect still has a residual feature. This residual feature is large when the RM induced RV is not corrected but is much smaller when the RV has been corrected (see Fig. 6).

We model the CLV and RM effects together for the case in which the stellar RV (including the RM induced RV) is corrected and the spectra are shifted to the planetary rest frame. We use a similar model method as presented in Yan et al. (2017). The CLV and RM effects are then corrected, dividing the obtained transmission spectrum by the modeled result.

4. Results and discussion

We are interested in the detection of the transitions produced by the Na I doublet at λ5889.951 Å (D2) and λ5895.924 Å (D1). As the systemic velocity of the planetary system is −9.62826 km s^{-1} in the case of WASP-69 system and −2.2765 km s^{-1} for HD 189733, the expected wavelength positions of the Na I D lines in the solar system barycentric reference frame are λ5889.762 Å (D2) and λ5895.735 Å (D1), and λ5889.906 Å (D2) and λ5895.879 Å (D1), respectively.

In order to compute the relative absorption depths we calculate the weighted mean of the flux in a central pass-band (C), centered on each Na I D line, and compare it to bins of similar bandwidths taken in the transmission spectrum continuum, one in the blue (B) and one in the red region (R), as presented in Wyttenbach et al. (2017),

$$\delta(\Delta\lambda) = \frac{\sum_C w_i \Re(\lambda_i)}{\sum_C w_i} - \frac{1}{2}\left(\frac{\sum_B w_i \Re(\lambda_i)}{\sum_B w_i} + \frac{\sum_R w_i \Re(\lambda_i)}{\sum_R w_i}\right), \quad (2)$$

where the weights, w_i, are the inverse of the squared uncertanties on $\Re$, and $w_i = 1/\sigma_i^2$, which are calculated by propagating the photon noise and the readout noise from the observed spectra.

We choose the same bandwidths ($\Delta\lambda$) of the central pass-bands used in Wyttenbach et al. (2015) for easier comparison: 0.188 Å, 0.375 Å, 0.75 Å, 1.5 Å, 3 Å and a larger pass-band of 12 Å adjusted on the center of the doublet to perform the comparison between our results and those of Redfield et al. (2008), Jensen et al. (2011) and Huitson et al. (2012). In this last case, as reference we use slightly different wavelength intervals: 5874.89−5886.89 Å corresponding to the blue and 5898.89−5907.89 Å to the red regions. As noted by Wyttenbach et al. (2017), we also find that the choice of the reference bands has no impact on the results.

4.1. Transmission spectrum analysis

The S/N per extracted pixel in the continuum near 590 nm for HD 189733, retrieved with HARPS-South, ranges from 55 to 240 for all nights, while for WASP-69 spectra, with HARPS-North, the S/N is lower: 30–60. Combining the spectra to obtain the master in and master out spectra, the S/N increases to 310−640 for HD 189733 and 100−120 for WASP-69. When co-adding the nights, the total S/N for each master is about 800 for HD 189733 and 150 for WASP-69. Thus, a S/N of 1500 and 205 is reached in the final transmission spectrum for HD 189733b and WASP-69b, respectively.

As observed in Fig. 7, for HD 189733b, both Na I D lines can be distinguished from the continuum noise. However, for WASP-69b, even if the D2 line clearly peaks out of the continuum, the D1 line easily disappears when the resulting transmission spectrum data is binned with a large number of pixels. With a Gaussian fit to each Na I line, we measure line contrasts of 0.72 ± 0.05% (D2) and 0.51 ± 0.05% (D1) and full width at half maximum (FWHM) values of 0.64 ± 0.04 Å (D2) and 0.60 ± 0.06 Å (D1) for HD 189733b. Similar results of line contrasts are presented in Wyttenbach et al. (2015), but larger values of the FWHMs are obtained here. For WASP-69b, taking into account the low S/N reached, a Gaussian fit in the D1 Na I line is not possible. For the D2 line, even if the Gaussian fit is better and the line contrast can be measured (5.8 ± 0.3%), more transits are needed to estimate the FWHM.

For HD 189733b, a small net blueshift of ∼−0.04 Å is measured with respect to the expected wavelength position of the Na I lines. Taking into account that one pixel in the HARPS detector represents ∼0.8 km s^{-1}, the measured shift corresponds to ∼−2 km s^{-1}. This value is consistent with the wind speed detected by Brogi et al. (2016) ($-1.7^{+1.1}_{-1.2}$) using data from CRIRES (IR) and Louden & Wheatley (2015) ($-1.9^{+0.7}_{-0.6}$) using the same optical data analyzed here, suggesting almost no vertical wind shear. This shift is by far smaller than the ∼0.75 Å presented in Redfield et al. (2008) and smaller than the 0.16 Å measured in Wyttenbach et al. (2015). In this last paper the authors speculate that a global error on the planetary RV shift could introduce a 0.06 Å shift, considering the HARPS precision. For WASP-69b no blueshift is measured.

We measure relative absorption depth of the Na I lines in the transmission spectra for different passbands. For WASP-69b only the D2 Na I line is used while for HD 189733b the absorption depth of both lines is averaged. The values obtained for HD 189733b are 0.269 ± 0.032% (8.5σ) and 0.030 ± 0.014% (2.1σ) for 0.75 Å and 12 Å bandwidths, respectively (see first row of Table 3). Comparing these results with those in Wyttenbach et al. (2015) we obtain slightly smaller values possibly due to the differences between the data analysis methods. For the 12 Å pass-band our results are smaller than the ones presented in this latter paper (0.056 ± 0.007%), in Jensen et al. (2011; 0.053 ± 0.017%) and in Redfield et al. (2008; 0.067 ± 0.020%) from ground. Also in the detection from space by Huitson et al. (2012) (0.051 ± 0.006%) the results are larger than ours. However, taking into account the uncertainties of the values, the differences are not significant.

On the other hand, for WASP-69b we measure 3.819 ± 0.764 (5σ), 2.058 ± 0.491 (4.2σ), 0.703 ± 0.284 (2.5σ), 0.529 ± 0.142 (3.7σ) and 0.114 ± 0.080 (1.5σ) for 0.188 Å, 0.375 Å, 0.75 Å, 1.5 Å, 3 Å pass-bands, respectively (see second row of Table 3). We note that since the 12 Å pass-band includes both Na I lines and only the D2 line is used for WASP-69b, the absorption depth for this bandwidth is not calculated.

It is important to emphasize that WASP-69 is two magnitudes fainter than HD 189733. In order to extract the transmission spectrum of WASP-69b, two transits of this planet with approximately 15 spectra each were combined, while for HD 189733b three transits with 40 spectra, on average, were available. The fact that we can see Na absorption in WASP-69b's transmission spectrum means that the signal must be stronger than that from HD 189733b. Indeed, the scale height of WASP-69b is ∼650 km, three times larger than HD 189733b's (∼200 km); see Fig. 8. Nevertheless, more WASP-69b transit spectra will be needed to reach a S/N high enough to verify the D1 line detection and characterize the Na I line profiles. At present, there is no clear explanation for the difference in the intensity of both Na I lines. These lines are formed very high in the atmosphere and the theoretical line profiles of the two lines are different, presenting different oscillation strengths (f = 0.64 for the D2 and f = 0.32 for the D1; Huitson et al. 2012). As suggested in Slanger et al. (2000), the variability of the D2/D1 ratio could be due to different pathways, creating the two excited Na I levels with different temperature sensitivities. This would result in a different Na I line intensity depending on the local conditions in the exoplanet atmosphere. On Earth, for example, the telluric Na I absorption of D2 line is stronger than D1 line (Albrecht 2008).

In order to be sure that the results obtained are not caused by stellar residuals, some checks were performed to prove that the

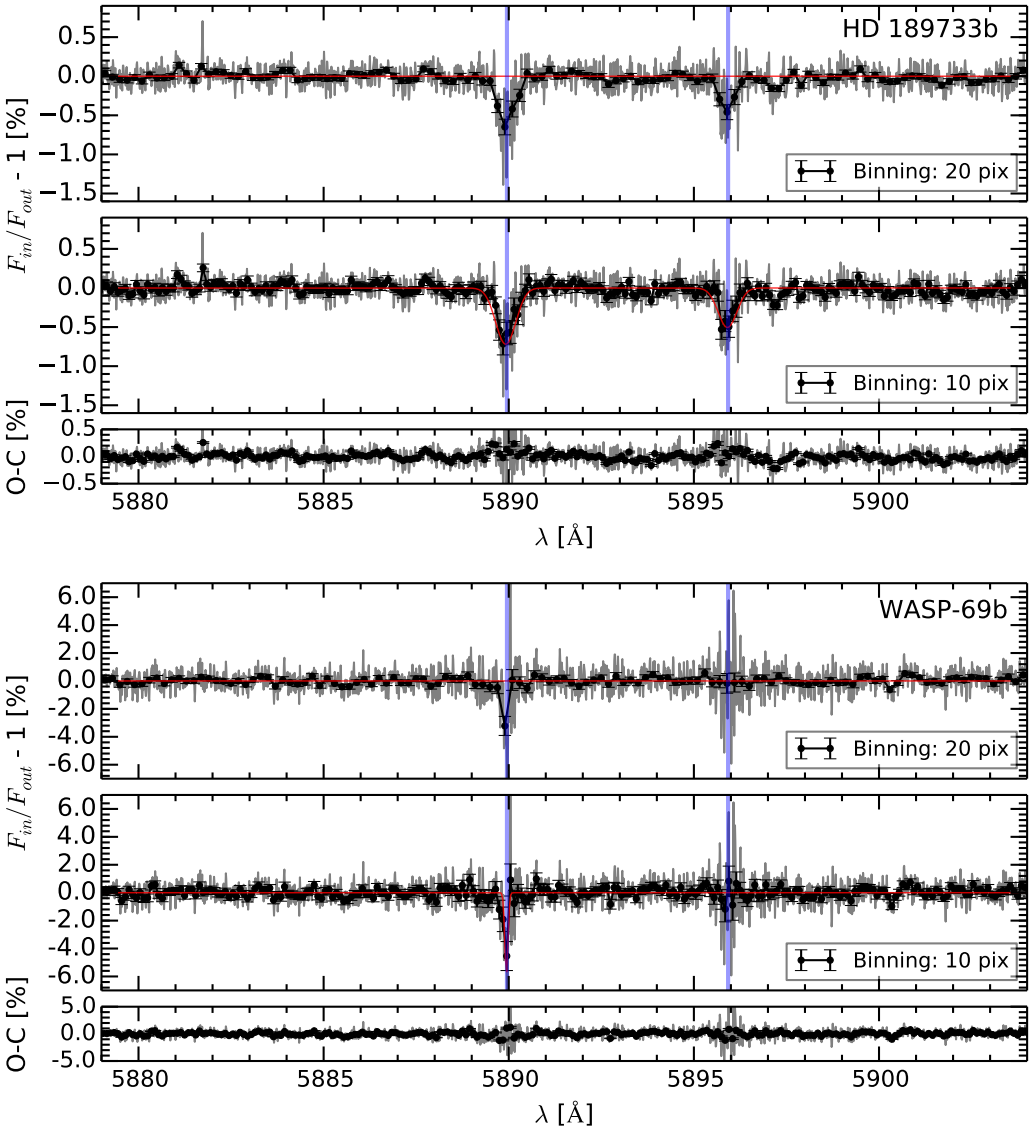

Fig. 7. Transmission spectrum of HD 189733b (*top panel*) and WASP-69b (*bottom panel*) atmospheres in the region of the Na I D doublet. The atmospheric transmission spectrum is presented in light gray. We show the binned transmission spectrum with black dots; 20 pixels (*top*) and 10 pixels (*middle*). The Gaussian fit to each Na I D line is shown in red with its residuals in the bottom. The expected wavelength position of the Na I doublet lines, in the planetary reference frame, are indicated with blue vertical lines and the red horizontal line is used as reference around zero. A net blueshift of ~3 km s^{-1} (~0.04 Å) is observed in the Na I lines of HD 189733b, possibly due to a global error on the planetary RV shift as a result of the HARPS precision. No shift is observed for WASP-69b Na I lines with respect to the reference wavelength frame. The uncertainties of the relative flux are assumed to come from photon and readout noise propagated from the original spectra.

resulting transmission spectrum can only be obtained with the correct selection of the in- and out-of-transit samples. In particular, we computed the transmission spectrum by considering a different combination of in- (F_1) and out-of-transit (F_2) files and following the same reduction steps. For the first check, we used the before-transit files and the second half of the in-transit files

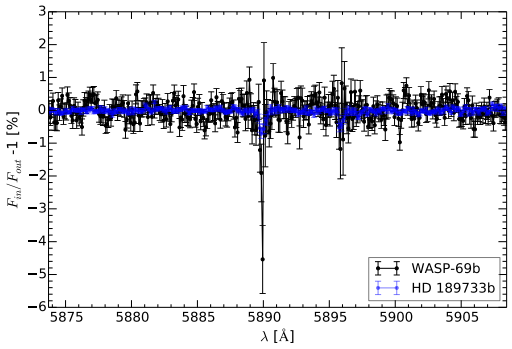

Fig. 8. Comparison between the transmission spectrum of WASP-69b (black) and HD 189733b (blue) in the region of the Na I doublet. Both transmission spectra are shown binned by 10 pixels and the wavelength shifted to the planet reference frame.

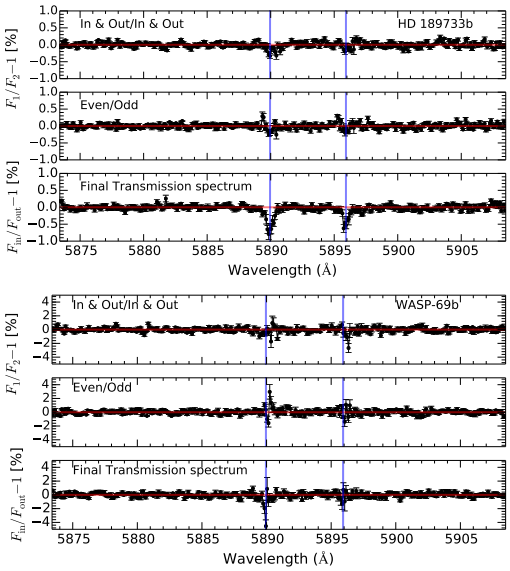

Fig. 9. Mock transmission spectra obtained with a different combination of in- (F_1) and out-of-transit (F_2) files of HD 189733 (*top panel*) and WASP-69 (*bottom panel*). The results are shown binned every ten pixels. The horizontal red line is used as reference around zero and the blue vertical lines are in the expected wavelength position of the Na I lines in the planet reference frame. *First row*: final transmission spectrum obtained using a synthetic in-transit sample formed by the data before transit and the second half of in-transit data (ordered according to time) and the rest as a synthetic out-of-transit sample. *Second row*: transmission spectrum obtained considering the even files as the in-transit sample and the odd ones as the out-of-transit sample. *Third row*: Final transmission spectrum from our data reduction.

(ordered according to time) as a synthetic in-transit sample, and the rest of the files (first half of in-transit and after-transit files) as a synthetic out-of-transit sample (see first row of Fig. 9). The second test was performed by considering the even files forming the in-transit sample and the odd ones (also organized by time) the out-of-transit sample (see second row of Fig. 9).

In both checks, the weight of real in-transit and out-of-transit files considered in F_1 and F_2 samples is the same, and we expect a flat transmission spectrum, despite possible stellar residuals caused by stellar activity, the RM effect (which is not completely averaged now), the CLV, among other possible sources of change in the stellar lines. For HD 189733b the resulting synthetic transmission spectra are mainly flat; only some strong residuals in the Na I lines' positions are observed, but with clear differences from the line depth of the real transmission spectrum. For WASP-69b, stronger residuals near the Na I position are observed. However, while the planetary RV correction has been applied to each single F_1/F_2, none of these residuals are in the position of the planetary Na I absorption, and are very likely of stellar origin. These stellar residuals illustrate the importance of correcting for the stellar line shifts, which can easily become false positives in the final transmission spectrum.

As discussed in the reduction process, missing some of the reduction steps could introduce residuals in the final transmission spectrum. Some of these steps are the telluric Na correction, the BERV consideration in the telluric line subtraction, the RM induced RV in the stellar line alignment, and the correction of the line's shape caused by CLV and RM effects. These residuals have been quantified by measuring the absorption depth values of the transmission spectrum of WASP-69b and HD 189733b by omitting these steps in the reduction process. The absorption depth values obtained for a representative 1.5 Å passband are shown in Table 4. The most important differences are observed omitting the telluric Na correction, for WASP-69b, and not considering the RM induced RV for HD 189733b.

4.2. (Spectro-)photometric light curve of Na I

The transit light curve of the Na I line is calculated using three different bandwidths: 0.75 Å, 1.5 Å, and 3.0 Å, which are centered at the line cores of both D1 and D2 lines, after dividing each spectrum (in- and out-of-transit, F_{in} and F_{out}) by the high-resolution master out (M_{out}). As reference passbands, for HD 189733b, we use similar ranges as in Wyttenbach et al. (2015) and Yan et al. (2017), 5874.89−5886.89 Å for the blue region and 5898.89−5907.89 Å for the red region. For WASP-69b, as the Na I lines are wider (see Fig. 1), the reference passbands are defined as 5874.89−5883.89 Å for the blue part and 5900.89−5907.89 Å for the red part (see Fig. 10).

In order to obtain the transit light curve of Na I, we use the method presented in Yan et al. (2017), where the relative flux of the Na I lines (F_{line}) is calculated using the ratio between the flux inside the band centered on the line core (F_{cen}) and the reference bands (F_{red} and F_{blue}) as follows,

$$F_{line} = \frac{2\,F_{cen}}{F_{red} + F_{blue}}. \quad (3)$$

This relative flux is obtained for both D2 and D1 lines in the case of HD 189733b, normalized to unity for all the out-of-transit values before the light curves of both lines are averaged. We note that only the first and third nights are used to calculate the relative flux, since for the second night there were no observations before transit. For WASP-69b the relative flux is calculated only for the D2 line. Finally, we binned the data points with a 0.002 phase step for HD 189733b, for an easier comparison with

Table 3. Summary of the measured relative absorption depth in [%] in the transmission spectra of HD 189733b and WASP-69b.

	Bandwidth					
	0.188 Å	0.375 Å	0.75 Å	1.5 Å	3.0 Å	12 Å
HD 189733b	0.506 ± 0.074	0.497 ± 0.050	0.269 ± 0.032	0.104 ± 0.017	0.059 ± 0.013	0.030 ± 0.014
WASP-69b	3.819 ± 0.764	2.058 ± 0.491	0.703 ± 0.284	0.529 ± 0.142	0.114 ± 0.080	–*

Notes. Both D2 and D1 Na I lines are averaged for HD 189733b, and only the D2 line is used for WASP-69b. (*) The bandwidth of 12 Å includes both Na I lines and only the D2 Na I line is used to compute the absorption depths of WASP-69b.

Table 4. Measured relative absorption depth in [%] in the transmission spectra of HD 189733b and WASP-69b omitting steps in the reduction process, for a 1.5 Å bandwidth.

		Omitted correction			
	Result‖	Telluric Na*	BERV in telluric lines†	RM induced RV‡	CLV+RM effects§
HD 189733b	0.104 ± 0.017	–¶	0.185 ± 0.018	0.196 ± 0.017	0.188 ± 0.017
WASP-69b	0.529 ± 0.142	0.628 ± 0.139	0.467 ± 0.142	0.492 ± 0.143	0.584 ± 0.142

Notes. Both D2 and D1 Na I lines are averaged for HD 189733b, and only the D2 line is used for WASP-69b. (‖) Measured absorption depth in the final transmission spectra following all the presented steps. (*) No telluric Na subtraction. (†) The BERV consideration in the telluric line subtraction. (‡) RM induced RV consideration in the stellar line alignment. (§) Correction of the line's shape caused by CLV and RM effects. (¶) No telluric Na is observed in HD 189733 spectra.

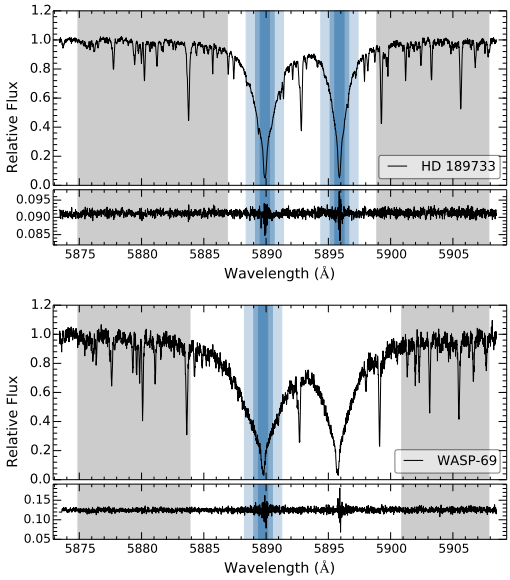

Fig. 10. Passbands used to perform the transmission light curves of HD 189733b (*upper panel*) and WASP-69b (*lower panel*). One observed spectrum is shown on the top of each panel and the ratio between this single in-transit spectrum and the master out is shown on *the bottom*. The blue regions mark the three different bandwidths (0.75 Å, 1.5 Å and 3.0 Å) centered at the line cores of D1 and D2, and the blue and red reference passbands used to measure the relative flux and calculate the transmission light curves are shown in gray. We note that, for WASP-69, only the D2 line is used.

similar results (Yan et al. 2017). For WASP-69b the observed spectra are more noisy ($S/N \sim 40$) than those retrieved from HD 189733b ($S/N \sim 130$; see Fig. 1). This noise is propagated along the calculation of the final transmission light curve values, which present a high dispersion. In order to reduce this dispersion we decided to increase the binned phase step to 0.005 for this planet. The final observed transmission light curves for the three different bandwidths are shown in the first row of Figs. 11 and 12.

The resulting light curves are the combination of the planetary absorption and the CLV effect. Here, we present the observed transmission light curves of the Na I lines which show the characteristic shape of the CLV effect. To correct for this effect we follow the same method as Yan et al. (2017), dividing the observed transmission light curve by the modeled CLV effect light curve from the same paper (see second row of Figs. 11 and 12). This makes it possible to obtain the observed Na I absorption light curve and calculate the true absorption depth (see third row of Figs. 11 and 12). For WASP-69b, the modeled Na I absorption is obtained using the PyTransit (Parviainen 2015) and PyLDTk (Parviainen & Aigrain 2015) Python packages, which use the library of PHOENIX stellar atmospheres (Husser et al. 2013). It is important to note that the modeled CLV light curve is directly derived from the model and the fit procedure is only applied to the Na I absorption model.

The transmitted flux or relative absorption depth of the transmission light curves can be easily calculated by the difference of the weighted mean of the flux in- and out-of-transit:

$$\delta(\Delta\lambda) = \frac{\overline{F_{\rm line}(\rm in)}}{\overline{F_{\rm line}(\rm out)}}. \quad (4)$$

For HD 189733b, the observed light curve can be well fitted with the combined model (CLV and Na I absorption), with an average chi-square value (χ^2) of 1.3 for the different bandwidths. In Yan et al. (2017), a $\chi^2 = 2.6$ with the combined model was reported. In both studies, the χ^2 values obtained by fitting only the Na I absorption model are larger than the ones obtained fitting the combined model ($\chi^2 = 2.0$ in our work). As in Yan et al. (2017), we clearly observe the CLV effect in our data, which is not obvious in the light curves presented in Wyttenbach et al. (2015). Similar CLV features are also shown in the light curves presented in Barnes et al. (2016). With the CLV effect correction applied, we measure absorption depths of 0.442 ± 0.074%,

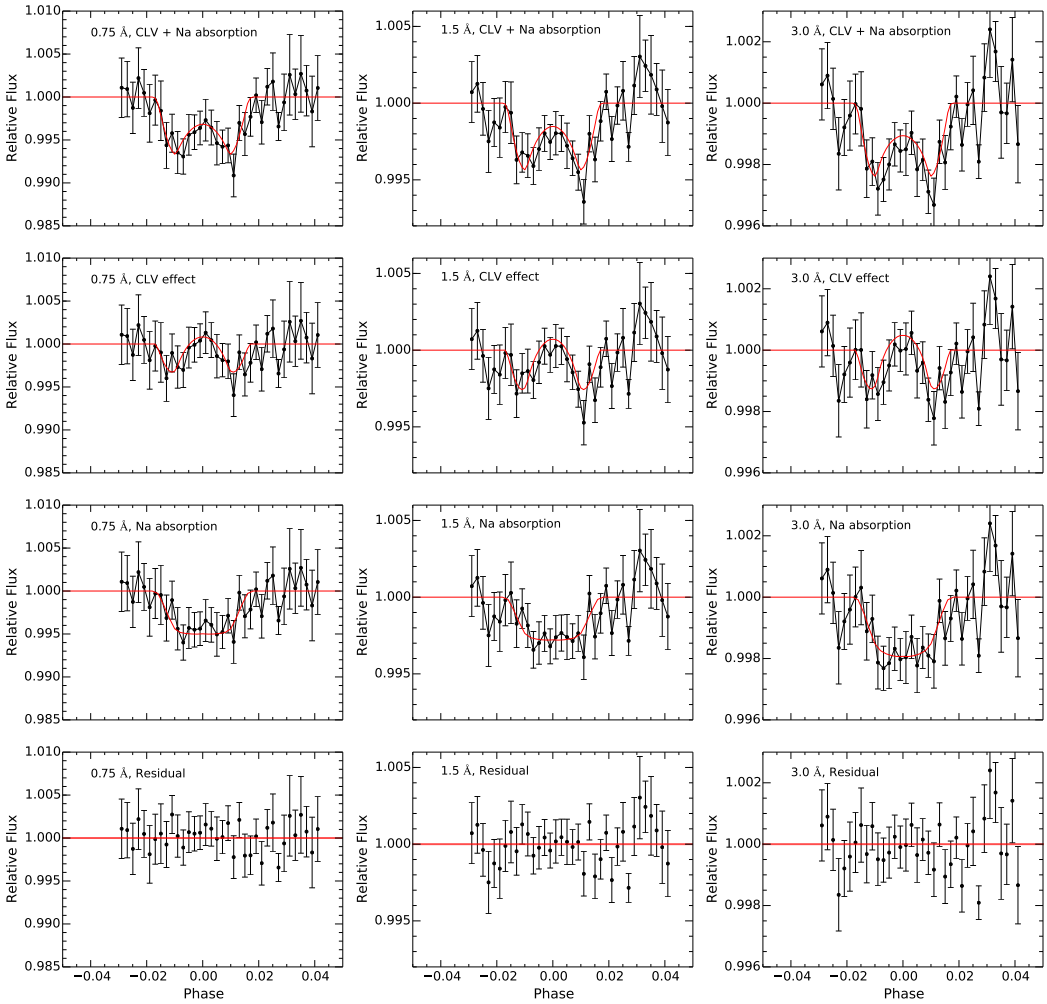

Fig. 11. Transmission light curves from HARPS observations of HD 189733b, for three different bandwidths: 0.75 Å (*left column*), 1.5 Å (*middle column*), and 3.0 Å (*right column*). Only nights 1 and 3 are used here. *First row*: final observed transmission light curve of the Na I D lines from our data reduction. The relative flux of D1 and D2 lines is averaged and binned with a 0.002 phase step (black line). The red line is the modeled transmission light curve, which is the combination of the best-fit Na I absorption and the CLV effect (Yan et al. 2017). This model is calculated theoretically and there is no fitting to the actual data. *Second row*: the CLV effect. The black line is the result of removing the Na I absorption model from the observed transmission light curve. The modeled CLV effect is shown in red. *Third row*: the Na I absorption light curve obtained dividing the observed transmission light curve by the modeled CLV effect (black line). The red line is the best-fit Na I absorption model. Forth row: residuals between the observed transmission light curve and the model. The errorbars represent the photon noise within the passband.

0.274 ± 0.052%, and 0.207 ± 0.031%, for the 0.75 Å, 1.5 Å, and 3.0 Å bandwidths, respectively (see Table 5). If the CLV effect is not considered, the absorption depths are overestimated (~0.508%, ~0.320%, and ~0.217%, respectively).

Comparing the results with those in Wyttenbach et al. (2015), we find that our absorption depths (without the CLV correction) are larger than theirs. In the case of the 0.75 Å passband, for example, the averaged absorption depth is 0.40%, while the results agree more closely with the ones presented in Barnes et al. (2016; 0.45%) and Yan et al. (2017; 0.512%). Comparing the absorption depths measured after the CLV correction, Yan et al. (2017) measure 0.414 ± 0.032% for the 0.75 Å bandwidth; slightly different from our result (0.442 ± 0.074%). The differences probably arise from the different reduction methods used, and fall within the uncertainties.

As previously discussed, the number of spectra retrieved during the observations of WASP-69b is small compared to the large number of spectra used to perform the HD 189733b transmission

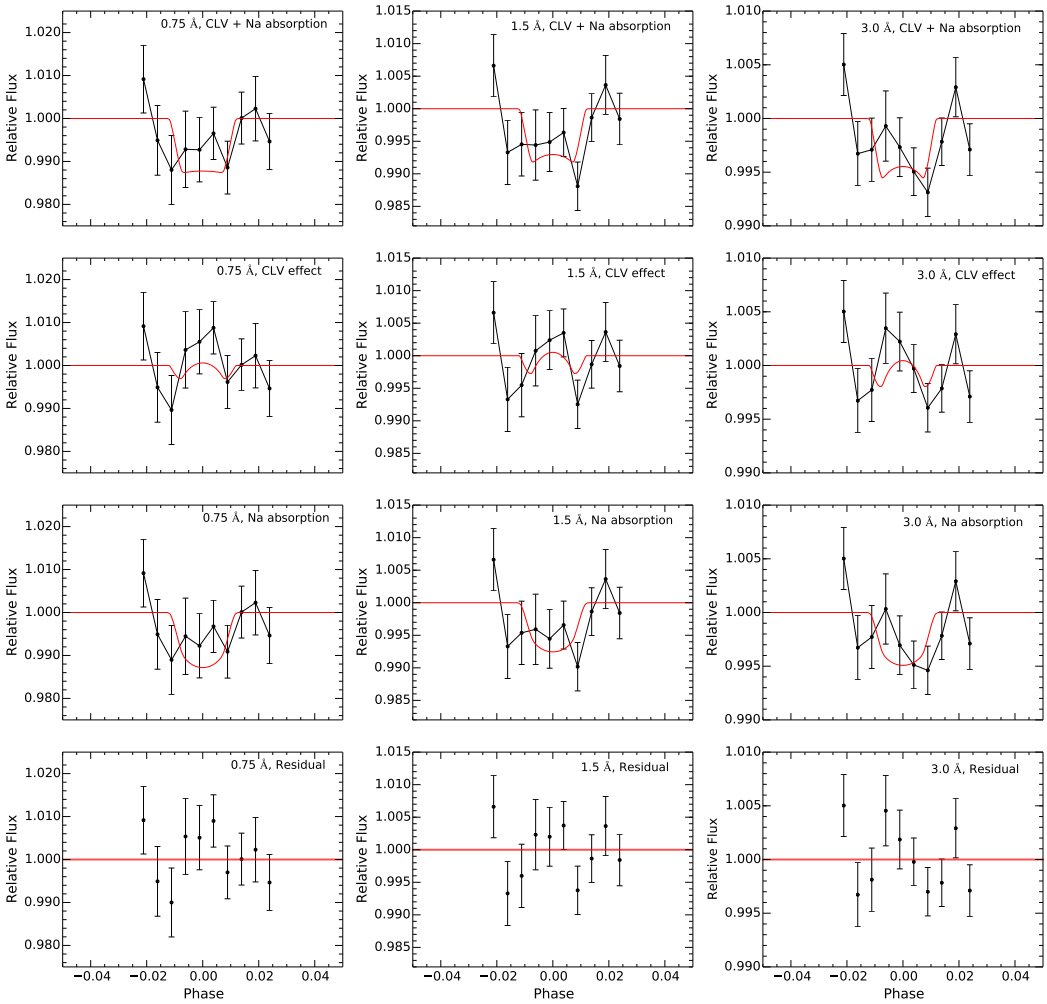

Fig. 12. Same as Fig. 11 but for the HARPS-N observations of WASP-69b. In this case, only the relative flux of D2 line is used and binned with a 0.005 phase step (black line).

light curves. Thus, the resulting transmission light curves of WASP-69b are noisy and the combined model does not fit the observed data as well as for HD 189733b ($\chi^2 = 4.2$). Even if the CLV is not obvious in the results because of the noise, this effect is predicted in our model and used to correct the observed transmission light curve. In this case, the fit is also better if both contributions (Na I absorption plus CLV) are considered. We measure absorption depths of 0.722 ± 0.411%, 0.470 ± 0.235%, and 0.286 ± 0.136%, for the 0.75 Å, 1.5 Å, and 3.0 Å bandwidths, respectively. We note that also larger values are obtained without considering the CLV effect.

In all cases, the measurement uncertainties are calculated with the error propagation of the photon noise level and the readout noise from the original data.

5. The Rossiter-McLaughlin effect of WASP-69b

The Rossiter-McLaughlin (RM) effect is an apparent RV shift of the stellar spectrum during the transit of a planet. As the planet moves across the stellar disk, it occults different regions with different RVs due to stellar rotation. Here, we measure this effect by fitting the analytical RV model presented by Ohta et al. (2005) to the stellar RV data given in the HARPS file headers, using a Markov chain Monte Carlo (MCMC) algorithm.

The RM model depends on the scaled semi-major axis ($a/R_\star$), the orbital period (P), the central transit time (T_0), the ratio of the planetary and stellar radius ($R_p/R_\star$), the inclination of the orbit (i_p), the inclination of the stellar rotation axis ($i_\star$), the sky-projected angle between the stellar rotation axis and the normal of orbit plane (λ), the angular rotation velocity of the

Table 5. Summary of the measured relative absorption depth in [%] in the light curves of HD 189733b and WASP-69b after the CLV correction.

	Bandwidth		
	0.75 Å	1.5 Å	3.0 Å
HD 189733b	0.442 ± 0.074%	0.274 ± 0.052%	0.207 ± 0.031%
WASP-69b	0.722 ± 0.411%	0.470 ± 0.235%	0.286 ± 0.136%

Notes. Both D2 and D1 Na I lines are averaged for HD 189733b, while for WASP-69b, only the D2 line is used. The results of nights 1 and 3 for HD 189733, and both nights for WASP-69b are averaged.

Table 6. MCMC observational results of the RM effect for WASP-69b and HD 189733b.

	WASP-69b		HD 189733b		
	Night 1	Night 2	Night 1	Night 2	Night 3
χ^2	1.1	0.5	2.1	4.3	1.5
Offset (km s^{-1})	-9.6364 ± 0.0004	-9.6251 ± 0.0005	$-2.2213^{+0.0001}_{-0.0002}$	$-2.2314^{+0.0001}_{-0.0002}$	-2.2204 ± 0.0002
Ω (rad/day)	$0.24^{+0.02}_{-0.01}$			0.559 ± 0.003	
λ (°)	$0.4^{+2.0}_{-1.9}$			-0.31 ± 0.17	
ϵ	0.779 ± 0.048			$0.877^{+0.011}_{-0.012}$	

star (Ω) and the linear limb dark coefficient (ϵ). We fix $a/R_\star$, P, T_0, $R_p/R_\star$, i_p and $i_\star$, and the remaining parameters remain free. The system was analyzed with 20 chains with a total of $\sim 1 \times 10^5$ steps. Each step is started at a random point near the expected values from the literature and λ is constrained to -180–$180°$. For WASP-69b, $i_\star$ is fixed at 90°. The best-fit values are obtained at 50% (median) and their error bars correspond to the 1σ statistical errors at the corresponding percentiles.

We note that the RV information measured by HARPS is given with possible instrumental and stellar activity effects, reflected as additional offsets to the data, which vary from night to night. For this reason, we add the stellar RV curve to the RM effect model, and the offsets between the data sets and the final model are fitted as free parameters when performing a joint analysis of all available nights. The MCMC results are presented in Table 6 and the correlation diagrams for the probability distribution are shown in Fig. A.1 of the Appendix.

For WASP-69b, we derive a stellar angular rotation of $0.24^{+0.02}_{-0.01}$ rad/day, consistent with the stellar rotational period of ≈23 days presented in Anderson et al. (2014). The small sky-projected angle between the stellar rotation axis and the normal of the orbital plane ($\lambda = 0.4^{+2.0}_{-1.9}$), means that the sky projections of the stellar spin-axis and the orbit normal are aligned to within a few degrees. Finally, we measure a limb darkening coefficient of 0.779 ± 0.048.

The same method is used to re-measure the RM effect of HD 189733b, obtaining the results presented in Table 6 and Fig. A.2. In this case, we fix $i_\star \approx 92^{+12°}_{-4}$ from Cegla et al. (2016). Previous studies retrieved λ values ranging from $-1.4 \pm 1.1°$ to $-0.35 \pm 0.25°$ (Winn et al. 2006; Triaud et al. 2009; Collier Cameron et al. 2010; Cegla et al. 2016). Our results are in line with these values. The measured angular rotation of the star ($\omega = 0.559 \pm 0.003$ rad/day) is also consistent with the equatorial period of 11.94 ± 0.16 days presented in Fares et al. (2010), and the resulting linear limb darkening coefficient ($\epsilon = 0.876 \pm 0.011$) is very similar to the one presented in Borsa et al. (2016) calculated over the HARPS wavelength range (0.7962 ± 0.0013).

6. Conclusions

We present an analysis of new transit observations of WASP-69b using the HARPS-North spectrograph at ORM (La Palma), and archive observations of the well-studied exoplanet HD 189733b using the HARPS-South spectrograph at La Silla (Chile). A new data analysis method is presented, which has been first applied to the HD 189733b data in order to compare with similar studies, and then to our WASP-69b observations. The method, based on correcting the telluric contamination with a one-dimensional telluric water model from Yan et al. (2015), can be very useful in observations where the baseline is not large enough to compute a high-quality telluric spectrum as in Astudillo-Defru & Rojo (2013), Wyttenbach et al. (2015), and Yan et al. (2017), and Wyttenbach et al. (2017), among others. Telluric sodium is present in WASP-69b observations, emphasizing the importance of using one of the HARPS fibers monitoring the sky simultaneously to the observations to correct for such effects. We observe atomic sodium (Na I) features in the transmission spectrum of both planets. For HD 189733b, the Na I doublet is clearly detected with line contrasts of 0.72 ± 0.05% for the D2 and 0.51 ± 0.05% for the D1, similar to those presented in Wyttenbach et al. (2015), and FWHMs of 0.64 ± 0.04 Å (D2) and 0.60 ± 0.06 Å (D1), larger than those measured in the same paper. For WASP-69b, even if the D2 Na I line is clearly detected, only its line contrast can be measured (5.8 ± 0.3%), and more transits will be needed to estimate the FHWM and reach a high enough S/N to characterize the D1 line.

Wyttenbach et al. (2015) reported a blueshift of 0.16 ± 0.04 Å in the Na I lines measured in the transmission spectrum of HD 189733b. Here, a blueshift of ∼0.04 Å (2 km s^{-1}) is measured, far smaller than in Redfield et al. (2008; ∼0.75 Å) but consistent with the wind speed detected by Louden & Wheatley (2015) and Brogi et al. (2016). Wyttenbach et al. (2015) speculate that this discrepancy can be attributed to global errors on the planetary RV considering the HARPS precision. On the other hand, no net blueshift is measured in the WASP-69b Na I lines.

The Na I transit light curves of both planets are also calculated. The observed transit light curve of HD 189733b shows the characteristic shape of the CLV effect presented in Yan et al. (2017), which is corrected in order to measure the true absorption depth at different bandwidths. For WASP-69b, the CLV effect is predicted to be much lower in comparison to the Na absorption, and not clearly distinguishable on the light curves, although the light curves are better fitted by a model containing this component.

By analyzing the RM effect of WASP-69b we obtain a stellar angular rotation velocity of $0.24^{+0.02}_{-0.01}$ rad/day, consistent with the stellar rotational period presented in Anderson et al. (2014) (≈23 days). We also measure a sky-projected angle between the stellar rotation axis and the normal of orbit plane (λ) of $0.4^{+2.0}_{-1.9}$. In the case of HD 189733b, the RM effect has been extensively studied in previous works (Winn et al. 2006; Triaud et al. 2009; Collier Cameron et al. 2010; Cegla et al. 2016), and consistent results are obtained here.

In the near future, high-resolution spectrographs like ESPRESSO on VLT and HIRES on E-ELT will perform transit observations of many exoplanets, making it possible to study their transmission spectra with a higher S/N. WASP-69b should be among the first targets of these instruments in order to further constrain sodium abundances and atmospheric temperature/pressure profiles for its atmosphere.

Acknowledgements. Based on observations made with the Italian Telescopio Nazionale *Galileo* (TNG) operated on the island of La Palma by the Fundación Galileo Galilei of the INAF (Istituto Nazionale di Astrofisica) at the Spanish Observatorio del Roque de los Muchachos of the Instituto de Astrofisica de Canarias. This work is partly financed by the Spanish Ministry of Economics and Competitiveness through projects ESP2014-57495-C2-1-R and ESP2016-80435-C2-2-R. We wish to thank D. Ehrenreich and A. Wyttenbach for pointing the authors to additional existing data in the HARPS archive and useful discussion.

References

Agol, E., Cowan, N. B., Knutson, H. A., et al. 2010, ApJ, 721, 1861
Albrecht, S. 2008, Ph.D. Thesis, Leiden University
Anderson, D. R., Collier Cameron, A., Delrez, L., et al. 2014, MNRAS, 445, 1114
Astudillo-Defru, N., & Rojo, P. 2013, A&A, 557, A56
Barnes, J. R., Haswell, C. A., Staab, D., & Anglada-Escudé, G. 2016, MNRAS, 462, 1012
Boisse, I., Moutou, C., Vidal-Madjar, A., et al. 2009, A&A, 495, 959
Borsa, F., Rainer, M., & Poretti, E. 2016, A&A, 590, A84
Bouchy, F., Udry, S., Mayor, M., et al. 2005, A&A, 444, L15
Brogi, M., de Kok, R. J., Albrecht, S., et al. 2016, ApJ, 817, 106
Butler, R. P., Wright, J. T., Marcy, G. W., et al. 2006, ApJ, 646, 505
Cegla, H. M., Lovis, C., Bourrier, V., et al. 2016, A&A, 588, A127
Charbonneau, D., Brown, T. M., Noyes, R. W., & Gilliland, R. L. 2002, ApJ, 568, 377
Chen, G., Guenther, E. W., Pallé, E., et al. 2017, A&A, 600, A138
Collier Cameron, A., Bruce, V. A., Miller, G. R. M., Triaud, A. H. M. J., & Queloz, D. 2010, MNRAS, 403, 151
Di Gloria, E., Snellen, I. A. G., & Albrecht, S. 2015, A&A, 580, A84
Fares, R., Donati, J.-F., Moutou, C., et al. 2010, MNRAS, 406, 409
Heng, K., Wyttenbach, A., Lavie, B., et al. 2015, ApJ, 803, L9
Huitson, C. M., Sing, D. K., Vidal-Madjar, A., et al. 2012, MNRAS, 422, 2477
Husser, T.-O., Wende-von Berg, S., Dreizler, S., et al. 2013, A&A, 553, A6
Jensen, A. G., Redfield, S., Endl, M., et al. 2011, ApJ, 743, 203
Louden, T., & Wheatley, P. J. 2015, ApJ, 814, L24
Lovis, C., Snellen, I., Mouillet, D., et al. 2017, A&A, 599, A16
Murgas, F., Pallé, E., Zapatero Osorio, M. R., et al. 2014, A&A, 563, A41
Ohta, Y., Taruya, A., & Suto, Y. 2005, ApJ, 622, 1118
Palle, E., Chen, G., Prieto-Arranz, J., et al. 2017, A&A, 602, L15
Parviainen, H. 2015, MNRAS, 450, 3233
Parviainen, H., & Aigrain, S. 2015, MNRAS, 453, 3821
Redfield, S., Endl, M., Cochran, W. D., & Koesterke, L. 2008, ApJ, 673, L87
Rothman, L. S., Gordon, I. E., Babikov, Y., et al. 2013, J. Quant. Spectr. Rad. Transf., 130, 4
Seager, S., & Mallén-Ornelas, G. 2003, ApJ, 585, 1038
Sing, D. K., Huitson, C. M., Lopez-Morales, M., et al. 2012, MNRAS, 426, 1663
Slanger, T. G., Huestis, D. L., & Cosby, P. C. 2000, in Amer. Astron. Soc. Meet. Abstr., BAAS, 32, 1599
Snellen, I. A. G., Albrecht, S., de Mooij, E. J. W., & Le Poole, R. S. 2008, A&A, 487, 357
Snellen, I. A. G., de Kok, R. J., le Poole, R., Brogi, M., & Birkby, J. 2013, ApJ, 764, 182
Southworth, J. 2010, MNRAS, 408, 1689
Torres, G., Winn, J. N., & Holman, M. J. 2008, ApJ, 677, 1324
Triaud, A. H. M. J., Queloz, D., Bouchy, F., et al. 2009, A&A, 506, 377
Vidal-Madjar, A., Arnold, L., Ehrenreich, D., et al. 2010, A&A, 523, A57
Wilson, P. A., Sing, D. K., Nikolov, N., et al. 2015, MNRAS, 450, 192
Winn, J. N., Johnson, J. A., Marcy, G. W., et al. 2006, ApJ, 653, L69
Wyttenbach, A., Ehrenreich, D., Lovis, C., Udry, S., & Pepe, F. 2015, A&A, 577, A62
Wyttenbach, A., Lovis, C., Ehrenreich, D., et al. 2017, A&A, 602, A36
Yan, F., Fosbury, R. A. E., Petr-Gotzens, M. G., et al. 2015, Int. J. Astrobiol., 14, 255
Yan, F., Pallé, E., Fosbury, R. A. E., Petr-Gotzens, M. G., & Henning, T. 2017, A&A, 603, A73

Appendix A: Probability distributions

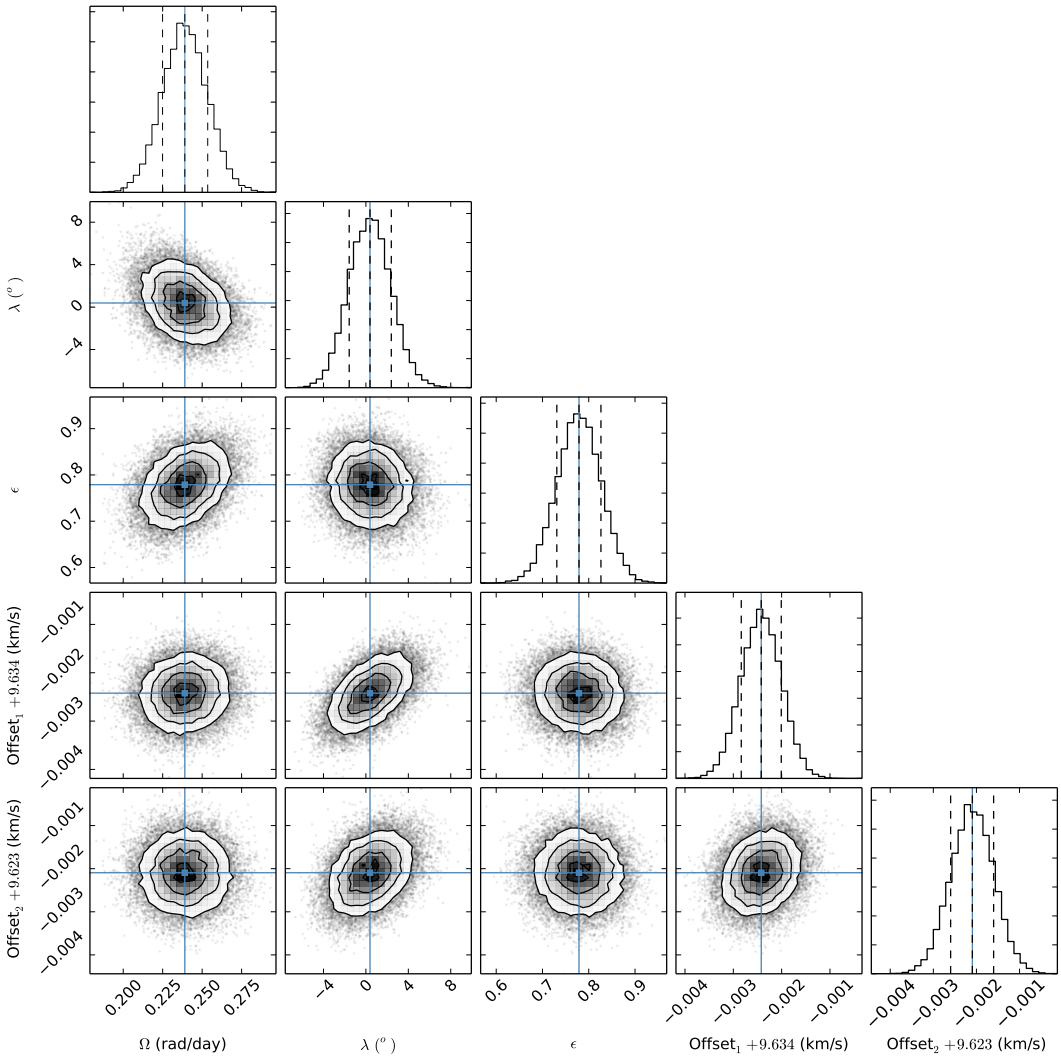

Fig. A.1. Correlation diagrams for the probability distribution of the RM model parameters for WASP-69b. The dashed lines on the histograms correspond to the 16 and 84 percentiles used to obtain the 1σ statistical errors. The blue lines show the resulting median values.

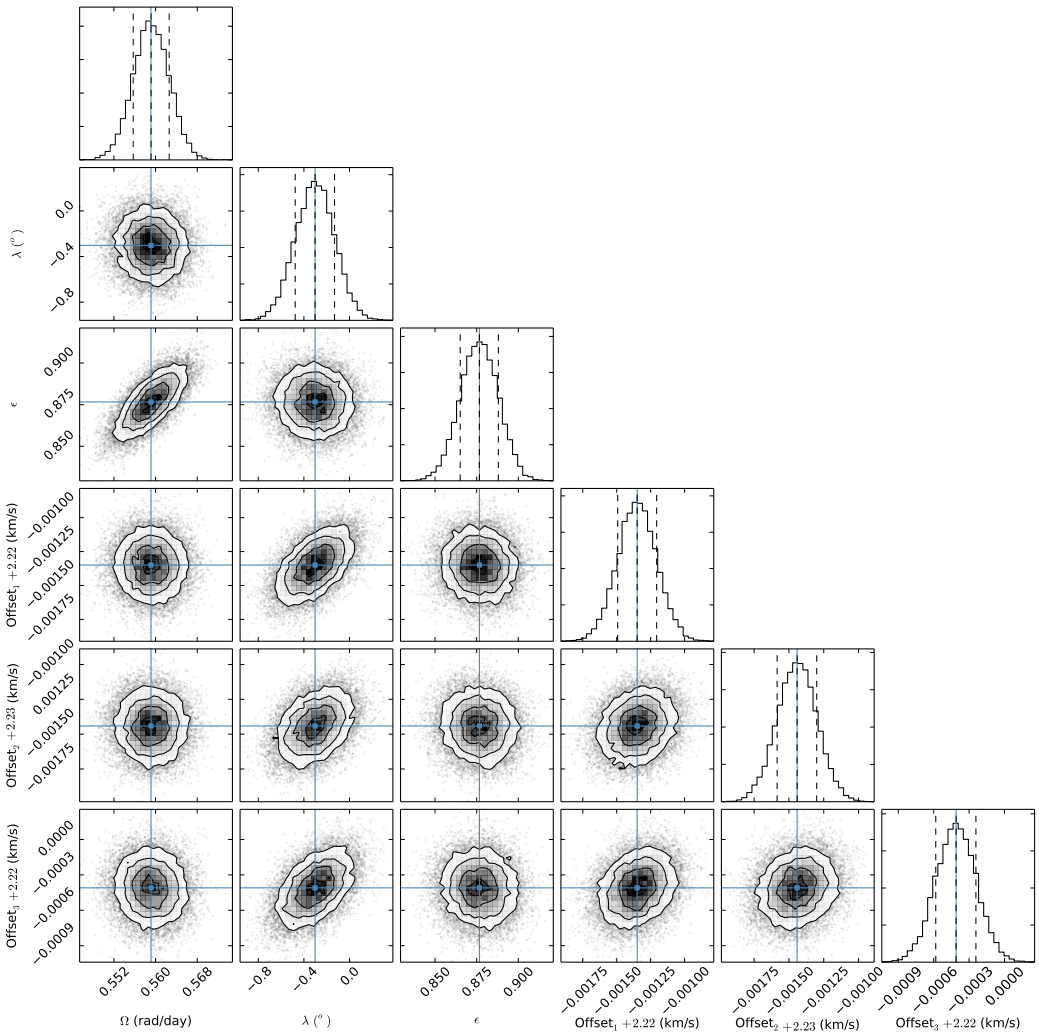

Fig. A.2. Correlation diagrams for the probability distribution of the RM model parameters for HD 189733bb.

3

NaI and Hα features in the atmosphere of MASCARA-2b

- Dr. Arroway will be spending her precious telescope time listening for... uh... listening for...
- Little green men.

Contact, 1997

MASCARA-2b (Talens et al., 2018), also known as KELT-20b (Lund et al., 2017), is one of the few tens of exoplanets included in the so-called ultra hot Jupiter sample (Parmentier et al., 2018; Arcangeli et al., 2018). These are extreme planets, located very close to their host stars and, consequently, receiving a large amount of energy on their upper atmosphere. Ultra hot Jupiter planets are characterised by equilibrium temperatures above 2000 K. In this chapter we study the atmosphere of this exoplanet using only one transit observation with HARPS-N. The analysis and results of this chapter are published in A&A under the bibcode 2018A&A...616A.151C (Casasayas-Barris et al., 2018).

The transmission spectrum of MASCARA-2b is extracted following the methodology described in the previous chapter, with the difference that the telluric contamination is corrected by taking advantage of the rapid-rotating standard star observations during the same night. We tentatively resolve the NaI and Hα spectral lines in the transmission spectrum of MASCARA-2b. The absorption is also visible during the transit in the transmission light curves,

which are clearly contaminated by the strong RM deformation of the stellar lines. After correcting the RM effect, we measure an averaged absorption excess of 0.4 ± 0.1 % in the NaI lines, and 0.6 ± 0.1 % in the Hα line, which corresponds to an altitude of 1.20 ± 0.04 R_p. Simple isothermal temperature profiles (Lecavelier Des Etangs et al., 2008) are fitted to the final transmission spectra, showing that temperatures larger than the equilibrium temperature of the planet (2260 K) are necessary to explain the absorption lines contrast. In particular, assuming a totally dissociated hydrogen atmosphere (molecular weight of $\mu = 1$), temperatures larger than 4000 K are needed.

Here, for the first time, we use a two-dimensional (2D) analysis to study the time-variations in the NaI and Hα spectral lines. The 2D maps clearly show the RM effect in the stellar lines, but the absorption of the exoplanet atmosphere remains hidden in the noise. The S/N of the features observed in the present analysis is not high enough to claim the detections. Note that, in atmospheric studies, as we are looking for faint changes in the stellar line profiles, at least two transit observations are normally required to confirm the findings (see Chapter 4).

A&A 616, A151 (2018)
https://doi.org/10.1051/0004-6361/201832963

Astronomy & Astrophysics

Na I and Hα absorption features in the atmosphere of MASCARA-2b/KELT-20b*

N. Casasayas-Barris[1,2], E. Pallé[1,2], F. Yan[3], G. Chen[1,2,4], S. Albrecht[5], L. Nortmann[1,2], V. Van Eylen[6], I. Snellen[6], G. J. J. Talens[6], J. I. González Hernández[1,2], R. Rebolo[1,2,7], and G. P. P. L. Otten[6]

[1] Instituto de Astrofísica de Canarias, Vía Láctea s/n, 38205 La Laguna, Tenerife, Spain
e-mail: nuriacb@iac.es
[2] Departamento de Astrofísica, Universidad de La Laguna, Spain
[3] Max Planck Institute for Astronomy, Königstuhl 17, 69117 Heidelberg, Germany
[4] Key Laboratory of Planetary Sciences, Purple Mountain Observatory, Chinese Academy of Sciences, Nanjing 210008, PR China
[5] Stellar Astrophysics Centre, Department of Physics and Astronomy, Aarhus University, Ny Munkegade 120, 8000 Aarhus C, Denmark
[6] Leiden Observatory, Leiden University, Postbus 9513, 2300 RA Leiden, The Netherlands
[7] Consejo Superior de Investigaciones Científicas, Spain

Received 6 March 2018 / Accepted 7 May 2018

ABSTRACT

We used the HARPS-North high resolution spectrograph ($\mathcal{R}$ = 115 000) at Telescopio Nazionale *Galileo* (TNG) to observe one transit of the highly irradiated planet MASCARA-2b/KELT-20b. Using only one transit observation, we are able to clearly resolve the spectral features of the atomic sodium (Na I) doublet and the Hα line in its atmosphere, which are corroborated with the transmission calculated from their respective transmission light curves (TLC). In particular, we resolve two spectral features centered on the Na I doublet position with an averaged absorption depth of 0.17 ± 0.03% for a 0.75 Å bandwidth with line contrasts of 0.44 ± 0.11% (D_2) and 0.37 ± 0.08% (D_1). The Na I TLC have also been computed, showing a large Rossiter-McLaughlin (RM) effect, which has a 0.20 ± 0.05% Na I transit absorption for a 0.75 Å passband that is consistent with the absorption depth value measured from the final transmission spectrum. We observe a second feature centered on the Hα line with 0.6 ± 0.1% contrast and an absorption depth of 0.59 ± 0.08% for a 0.75 Å passband that has consistent absorptions in its TLC, which corresponds to an effective radius of R_A/R_P = 1.20 ± 0.04. While the signal-to-noise ratio (S/N) of the final transmission spectrum is not sufficient to adjust different temperature profiles to the lines, we find that higher temperatures than the equilibrium (T_{eq} = 2260 ± 50 K) are needed to explain the lines contrast. Particularly, we find that the Na I lines core require a temperature of T = 4210 ± 180 K and that Hα requires a temperature of T = 4330 ± 520 K. MASCARA-2b, like other planets orbiting A-type stars, receives a large amount of UV energy from its host star. This energy excites the atomic hydrogen and produces Hα absorption, leading to the expansion and abrasion of the atmosphere. The study of other Balmer lines in the transmission spectrum would allow the determination of the atmospheric temperature profile and the calculation of the lifetime of the atmosphere with escape rate measurements. In the case of MASCARA-2b, residual features are observed in the Hβ and Hγ lines, but they are not statistically significant. More transit observations are needed to confirm our findings in Na I and Hα and to build up enough S/N to explore the presence of Hβ and Hγ planetary absorptions.

Key words. planetary systems – techniques: spectroscopic – planets and satellites: atmospheres – methods: observational – planets and satellites: individual: MASCARA-2b – planets and satellites: individual: KELT-20b

1. Introduction

After the first detection of an exoplanet atmosphere by Charbonneau et al. (2002), which revealed the presence of atomic sodium (Na I) thanks to space-based instruments, several studies have been carried out using ground-based facilities. These facilities have been slowly overcoming the limitations imposed by the telluric atmospheric variations, resulting in detections of spectral signatures arising from Rayleigh scattering, i.e., Na and K with low spectral resolution spectrographs (e.g., Sing et al. 2012; Murgas et al. 2014; Wilson et al. 2015; Nortmann et al. 2016; Chen et al. 2017; Palle et al. 2017). Observations with high resolution spectrographs are able to deal with the remaining limitations due to the telluric atmosphere by resolving the spectral lines and taking advantage of the various Doppler velocities of the Earth, host star, and exoplanet.

One of the most studied species in the upper atmosphere of hot exoplanets is the Na I doublet (D_2 at λ5889.951 Å and D_1 at λ5895.924 Å) as a consequence of its high cross section. The first ground-based detection of Na I was performed by Redfield et al. (2008) using the High Resolution Spectrograph (HRS), with $\mathcal{R} = \lambda/\Delta\lambda \sim 60\,000$, mounted on the 9.2 m *Hobby-Eberly* Telescope. Shortly after, Snellen et al. (2008) confirmed the Na I in HD 209458b atmosphere using the High Dispersion Spectrograph (HDS), with $\mathcal{R} \sim 45\,000$, on the 8 m Subaru Telescope. Recently, ground-based studies with the High Accuracy Radial velocity Planet Searcher (HARPS) spectrograph ($\mathcal{R} \sim 115\,000$), at ESO 3.6 m telescope in la Silla (Chile) and at 3.58 m Telescopio Nazionale

* The reduced HARPS spectra are only available at the CDS via anonymous ftp to cdsarc.u-strasbg.fr (130.79.128.5) or via http://cdsarc.u-strasbg.fr/viz-bin/qcat?J/A+A/616/A151

Galileo (TNG) in Roque de los Muchachos Observatory (ORM, la Palma), have been able to resolve the individual Na I line profiles of HD 189733b (Wyttenbach et al. 2015), WASP-49b (Wyttenbach et al. 2017), and WASP-69b (Casasayas-Barris et al. 2017). Using these same data sets Heng et al. (2015) were able to study the existence of temperature gradients, Louden & Wheatley (2015) explored the high-altitude winds of HD 189733b, Barnes et al. (2016) studied stellar activity signals, and Yan et al. (2017) analyzed the center-to-limb variation (CLV) effect in the transmission light curve (TLC) of this exoplanet. In the near future, high-dispersion methods will be very important in the observations of spectral features of temperate rocky planets and super-Earths; these features will be out of reach of the *James Webb* Space Telescope (JWST), but available with the upcoming facilities such as ESPRESSO on the Very Large Telescope (VLT) or HIRES on E-ELT (Snellen et al. 2013; Lovis et al. 2017).

We present the results from only one transit observation of MASCARA-2b, obtained with the HARPS-North spectrograph (la Palma). MASCARA-2b (Talens et al. 2018; Lund et al. 2017) is a hot Jupiter ($R_P = 1.83 \pm 0.07\ R_{Jup}$, $M_P < 3.510\ M_{Jup}$) transiting a rapidly rotating ($v \sin i_\star = 115.9 \pm 3.4$ km s^{-1}) A2-type star with an orbital period of $3.474119^{+0.000005}_{-0.000006}$ days (see Table 1 for details). This star, MASCARA-2 (also named KELT-20 or HD 185603), is the fourth brightest star ($m_v = 7.6$) with a transiting planet known to date. With the combination of the early spectral type, the brightness, and the rapid rotation of its host star, MASCARA-2b is an ideal target for transmission spectroscopy.

MASCARA-2b is one of the few exoplanets transiting an A-type star known to date with effective temperatures higher than ~7000 K. These planets typically receive a large amount of extreme ultraviolet radiation from its host star, exciting the atomic hydrogen to produce Hα absorption and leading to the expansion and possibly abrasion of their atmosphere (Bourrier et al. 2016). The study of the Balmer lines of these planets allows us to estimate the lifetime of the atmosphere from the escape rate measurement. Comparative studies of this planet population, which present different system properties, will help us to understand their origin and evolution.

2. Observations

We observed one transit of MASCARA-2b on 16 August 2017 using the HARPS-North spectrograph mounted on the 3.58 m TNG, located at the Observatorio del Roque de los Muchachos (ORM, La Palma). For this transit, the observations started at 21:21 UT and finished at 03:56 UT, with an airmass variation from 1.0 to 2.1.

The observations were carried out exposing continuously before, during, and after the transit to retrieve a good baseline, which is key for the data reduction process. We used fiber A on the target and fiber B on the sky to correct possible emission features from the Earth's atmosphere. Since MASCARA-2 is a bright star, with a magnitude of 7.6 (V), we exposed 200 s per exposure, recording a total of 90 consecutive spectra; 58 of these were recorded during the transit. The individual retrieved spectra have a signal-to-noise ratio (S/N) ranging from 40 to 80 per wavelength bin in the continuum near the Na I doublet. One spectrum of the rapid-rotator telluric standard HR 7390 (5.59 V) was also observed before MASCARA-2b observations, using 300 s of exposure time, with an airmass of 1.0, and obtaining a S/N of ~170 in the continuum. HR 7390 is a bright A0V-type star that has a projected rotation speed of 150 km s^{-1}.

Table 1. Physical and orbital parameters of MASCARA-2b.

Parameter	Symbol	Value
Stellar parameters		
Identifiers	–	KELT-20, HD 185603
V-band magnitude	m_V	7.6
Spectral type	–	A2
Effective temperature	T_{eff}	8980^{+90}_{-130} K
Projected rotation speed[a]	$v \sin i_\star$	115.9 ± 3.4 km s^{-1}
Surface gravity	$\log g$	4.31 ± 0.02 cgs
Metallicity	[Fe/H]	-0.02 ± 0.07
Stellar mass	$M_\star$	$1.89^{+0.06}_{-0.05}\ M_\odot$
Stellar radius	$R_\star$	$1.60 \pm 0.06\ R_\odot$
Planet parameters		
Planet mass[a]	M_p	$<3.510\ M_{Jup}$
Planet radius	R_p	$1.83 \pm 0.07\ R_{Jup}$
Equilibrium temperature	T_{eq}	2260 ± 50 K
Surface gravity[a]	$\log g_P$	<3.460 cgs
System parameters		
Right ascension	–	$19^h38^m38.73^s$
Declination	–	$+31°13'09.2''$
Epoch	T_c	$2457909.5906^{+0.0003}_{-0.0002}$ BJD
Period	P	$3.474119^{+0.000005}_{-0.000006}$ days
Transit duration	T_{14}	3.55 ± 0.03 h
Semimajor axis	a	0.057 ± 0.006 AU
Scaled semimajor axis	$a/R_\star$	7.5 ± 0.04
Inclination	i	$86.4^{+0.5}_{-0.4}$°
Eccentricity	e	0 (fixed)
Planet-to-star ratio	$R_p/R_\star$	0.1133 ± 0.0007
Systemic velocity	γ	-21.07 ± 0.03 km s^{-1}
Projected obliquity	λ	$0.6 \pm 4°$

Notes. [a] From Lund et al. (2017). All the remaining parameters are taken from Talens et al. (2018).

3. Methods

The observations were reduced with the HARPS-North Data reduction Software (DRS), version 1.1. The DRS extracts the spectra order-by-order, and these spectra are then flat-fielded using the daily calibration set. A blaze correction and the wavelength calibration are applied to each spectral order and, finally, all the spectral orders from each two-dimensional echelle spectrum are combined and resampled into a one-dimensional spectrum ensuring flux conservation. The resulting one-dimensional spectra covers a wavelength range between 3800 Å and 6900 Å and has a wavelength step of 0.01 Å, referred to the solar system barycenter rest frame and in air wavelengths. One representative spectrum of MASCARA-2 and the telluric standard HR 7390 are presented in Fig. 1.

The first step of our analysis is the telluric contamination subtraction. Near the Na I doublet, the main telluric contributors are water and telluric sodium (Snellen et al. 2008). Each individual target sky spectrum was examined to look for the presence of telluric sodium, but no sodium emission was observed. For an A-type star as MASCARA-2, the method used in Casasayas-Barris et al. (2017) to remove the telluric features produced by water and oxygen does not work as well as for other spectral types. Thus, we correct for this contamination using a combination of the methods of Wyttenbach et al. (2015) and Casasayas-Barris et al. (2017), taking advantage of the observations of the telluric standard HR 7390. With the method

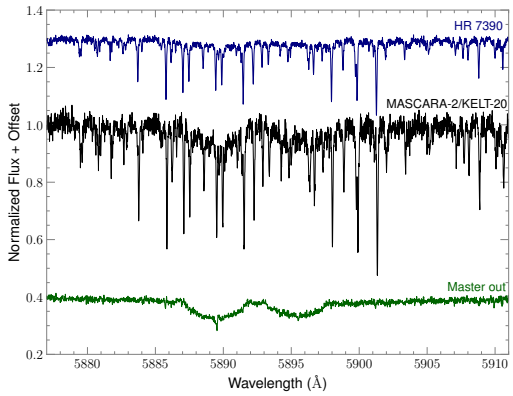

Fig. 1. Normalized spectra of the telluric standard HR 7390 (blue) and MASCARA-2 (black) around the Na I region after their reduction with the HARPS DRS. In green we show the MASCARA-2 master out spectrum after the telluric correction.

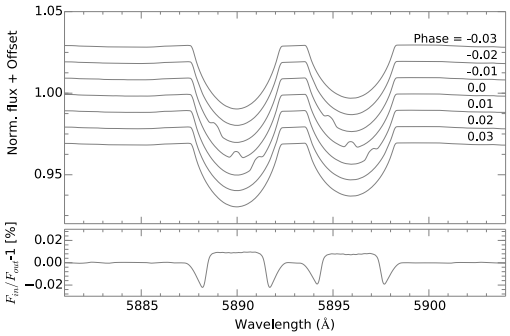

Fig. 2. Modeled spectra of MASCARA-2 for various orbital phases of the planet using LTE and a spin-orbit angle of 0° (Talens et al. 2018) for the RM effect (*top*) and modeled RM and CLV effects in the final transmission spectrum (*bottom*). We note the large RM effect in the stellar lines.

described in Astudillo-Defru & Rojo (2013), which makes the assumption that the variation of the telluric lines follows linearly the airmass variation, we computed a high-quality telluric spectrum. The difference is that, before computing the high-quality telluric spectrum, we aligned all the telluric lines via Barycentric Earth Radial Velocity (BERV) information from the HARPS-N file headers. Then, instead of scaling all the MASCARA-2 spectra to the averaged in-transit airmass as in Wyttenbach et al. (2015), we scaled them to the telluric standard airmass (i.e., 1.0 in this case). Finally, and after removing the small stellar features from the telluric standard spectrum as in Frasca et al. (2000), we divided each scaled MASCARA-2 spectrum by the final telluric standard spectrum, which has been also shifted to the Earth's reference frame.

Once the telluric contamination has been removed, we followed the steps described in Casasayas-Barris et al. (2017) to extract the transmission spectrum of the planet. We note that the stellar radial velocity (RV) information of MASCARA-2, as for other rapidly rotating A-type stars, is not well determined by the HARPS-N pipeline. For rapidly rotating early-type stars, which present very broad lines in their spectrum, the stellar RV correction is not very important and the possible uncorrected RV shift between the spectra does not result in a large difference. Therefore, we do not consider the stellar RV correction here. However, if the stellar lines are deep and narrow, the RV correction becomes important. In this way, the possible instrumental RV effects are not considered, but such effects produce offsets that similarly affect all spectra, resulting in a global wavelength shift with respect the expected rest-frame position.

The combination of all the out-of-transit spectra (master out) after subtracting the telluric contamination is shown in Fig. 1. Sharp residuals can be observed at ∼5890 Å and at ∼5896 Å (less deeper), which appear in each in-transit and out-of-transit spectra. The measured RV of both signals is -14.9 ± 0.5 km s^{-1} and there is no wavelength shift during the observation. In order to determine their origin, we used the LISM Kinematic Calculator (Redfield & Linsky 2008), which gives us information about the interstellar medium clouds that our line-of-sight traverses while observing a target. In the case of MASCARA-2b, according to the interstellar medium distribution in our Galaxy, the sight line went through the G, Mic and Oph clouds, which have -14.10 ± 0.97 km s^{-1}, -20.90 ± 1.34 km s^{-1}, -28.31 ± 0.93 km s^{-1} RVs, respectively. The very similar RV of the G cloud and the residuals observed in the data is the evidence of their possible interstellar origin. Since the interstellar sodium does not show any shift during the night and, in this particular case, we are not correcting for the stellar RV, the presence of interstellar species is not a problem, as it is compensated when dividing the in-transit spectra by the master out spectrum.

During the observation, the planet is moving along the orbit, changing its RV with respect to the observer. This RV change results in a wavelength shift of the measured planetary absorption lines that needs to be corrected. When the in-transit spectra are divided by the master out spectrum, each of these spectra contain residuals that need to be shifted to the planetary rest frame to become aligned before being co-added. In this work, this wavelength shift is obtained by calculating the theoretical RV of the planet along the orbit and projecting it to the line of sight of the observer. MASCARA-2b is a recently discovered planet and only an upper limit of its mass (∼3.5 $M_{\rm Jup}$; Lund et al. 2017) is known. For this reason, to calculate the RV we consider that $M_{\rm P} \ll M_\star$ (i.e., assuming the planetary mass does not significantly contribute to the reduced mass of the system). The calculated RV changes during the transit from -24 km s^{-1} to $+24$ km s^{-1}, approximately. The maximum difference of this RV between considering the mass upper limit and the $M_{\rm P} \ll M_\star$ approximation is $\sim\pm0.1$ km s^{-1}, which is not significant considering that a pixel in HARPS-N corresponds to ∼0.8 km s^{-1}.

Finally, we model the stellar spectrum for different orbital phases of the planet using ATLAS9 models (Heiter et al. 2002). The modeled spectra contain both the CLV and Rossiter-McLaughlin (RM) effects on the stellar lines shape (see top panel of Fig. 2). The CLV effect is obtained by computing the stellar spectra with various μ angles as in Yan et al. (2015) and the RM effect is obtained assuming rigid rotation with a spin-orbit angle of 0° (Talens et al. 2018 measured $\lambda = 0.6 \pm 4°$), stellar rotation of $v \sin i = 115$ km s^{-1}, and an impact parameter of 0.5 (Lund et al. 2017). By applying the same method to these synthetic spectra, we obtain how the RM and CLV affect the final transmission spectrum of the planet (see bottom panel of Fig. 2). As can be observed, although the expected RM effect is large,

the combination of both effects is on the order of $\sim 10^{-4}$ (i.e., one magnitude below the typical noise). This is because the CLV is very weak for these spectral-type stars and the RM is smeared when the in-transit spectra are combined. Nevertheless, we divide the final transmission spectrum by the model to correct for these effects.

A kind of two-dimensional representation of the original spectra and the results after the different processing steps described in this section are presented in the Appendix A. In these figures, the RM effect on the lines and the exoplanet absorption in the stellar and planetary rest frame can be seen.

4. Results

4.1. Transmission spectrum analysis of Na I

The S/N per extracted pixel in the continuum near the Na I doublet for the observed spectra of MASCARA-2, retrieved with HARPS-N, ranges from 40 to 80. When combining the spectra to obtain the master spectrum for in-transit observations and out-of-transit observations the S/N increases to ∼150, and when co-adding all the spectra to compute the final transmission spectrum the S/N increases to ∼450.

The final transmission spectrum of MASCARA-2b around the Na I is shown in Fig. 3. As can be observed in this Figure, both Na I D lines show a peak relative to the continuum. With a Gaussian fit to each Na I line, we measure line contrasts of 0.44 ± 0.11% (D_2) and 0.37 ± 0.08% (D_1) and a full width at half maximum (FWHM) of 0.26 ± 0.08 Å (D_2) and 0.33 ± 0.08 Å (D_1), centered on 5889.93 ± 0.03 Å (D_2) and 5895.88 ± 0.03 Å (D_1). The expected values for the D_2 and D_1 lines in the planetary rest frames are 5889.95 Å and 5895.92 Å, respectively, implying that no net blueshift or redshift is measured. In both cases the Gaussian fit has a reduced χ^2 value of ∼1.2. This fit procedure is performed using a simple Markov chain Monte Carlo (MCMC), and the best-fit values are obtained at 50% (median) and their error bars correspond to the 1σ statistical errors at the corresponding percentiles.

The absorption depth of the Na I lines is measured by calculating the weighted mean of the flux in a central passband of different bandwidths (0.188 Å, 0.375 Å, 0.75 Å, 1.5 Å, 3.0 Å, and 5.0 Å) centered on each Na I lines, and then compared with the average of two 12 Å bandwidths taken in the continuum of the transmission spectrum of the Na I lines: one in the blue (B = [5872.89 − 5884.89] Å) and one in the red (R = [5900.89 − 5912.89] Å) regions. The final values are presented in Table 2. We note that all the uncertainties are calculated with the error propagation of the photon noise level and the readout noise from the original data.

We performed various control distributions (not shown here) to ensure that the results are not caused by stellar or telluric residuals, but can only be obtained with the correct selection of the in- and out-of-transit samples. In particular, we computed the transmission spectrum by only considering the in-transit spectra, which were randomly selected to form the synthetic in- and out-of-transit samples. The same test was performed by considering only the out-of-transit files and also selecting the even files as the in-transit sample and the odd files as the out-of-transit sample. In all tests, the resulting synthetic transmission spectra are mainly flat and there is a clear difference between these spectra and the lines depth of the real transmission spectrum. The averaged absorption depth in the expected Na I D_2 and D_1 lines position for a 0.75 Å bandwidth are 0.021 ± 0.055%, 0.058 ± 0.040%, and 0.087 ± 0.032% for the out-out, in-in, and even-odd samples, respectively. The final transmission spectrum with a non-correction of the planet RV was also computed with no signals in the Na I position (0.045 ± 0.029% of absorption for a 0.75 Å bandwidth), supporting the theory that the possible interstellar sodium does not affect the final result and the Na I signals observed in the final transmission spectrum only appear in the planetary rest frame. In addition, this is evidence that we do not observe stellar activity signals, which would be visible in the stellar rest frame if they were present (Wyttenbach et al. 2017). As can be observed, the in-in and even-odd distributions absorption depths, the final transmission spectra are not totally flat as in the out-out sample. We note that in these distributions we do not correct for the CLV + RM effects and, as can be observed in the TLC, the in-transit absorption varies during the transit. These effects could introduce some variations in the absorption and not allow the total compensation of the planet absorption in the in-in and even-odd to control distributions. This does not happen in the out-out sample, as expected. On the other hand, the small absorption measured when the planet RV is not considered could be produced because the residuals partially overlap in the stellar rest frame.

As noted in Sect. 3, since no precise RV parameters have been measured for MASCARA-2b system, we tested the result with stellar RV corrected using the upper limit value of the RV semiamplitude (322.51 m s^{-1}, Lund et al. 2017) and a theoretical RM effect model calculated using Ohta et al. (2005). The resulting transmission spectrum is very similar to the result without stellar RV correction (see Fig. 4). As no significant differences are observed in the measurements when the stellar RV is corrected and when it is not, we show our analysis based on the case in which the stellar RV is not contemplated as this is the most correct procedure in this particular case.

4.2. Transmission light curve of Na I

The transit light curve of the Na I D lines is calculated as presented in Yan et al. (2017) and Casasayas-Barris et al. (2017) using four different bandwidths: 0.75 Å, 1.5 Å, 3.0 Å, 5.0 Å. Since the stellar lines are broad because of the rapid-rotation of the star ($v \sin i_\star$ = 115 km s^{-1}) and we expect a large RM effect, we included the calculation for a broad 5.0 Å passband, which encompasses the full Na I line. As reference passbands we use the same wavelength regions presented in Sect. 4.1. The results of both D_1 and D_2 lines are averaged and, finally, the data are binned with a 0.003 phase step (∼3.3 km s^{-1} of planetary RV), taking into account the S/N of the data. The final observed light curves for the various bandwidths are shown in the first row of Fig. 5.

The resulting light curves are the combination of the planetary absorption, CLV, and RM effects. For MASCARA-2 we expect a large RM (see Fig. 2 and Lund et al. 2017) and a small CLV effect. We note that both effects produce similar shapes in the TLC (see Yan et al. 2017) because in this case the RM has the most significant contribution. It is noticeable how the RM effect in the TLC diminishes as the width of the central passband is increased. This is because the deformation in the stellar sodium lines due to the RM effect occurs during different phases of the transit and, for small bandwidths, it can move in and out of the reference passbands. However, the 5 Å passband encompasses the complete stellar sodium lines, averaging out the effect in the TLC.

To correct for these effects we divide the observed TLC by the light curve with the modeled effects (see second and third

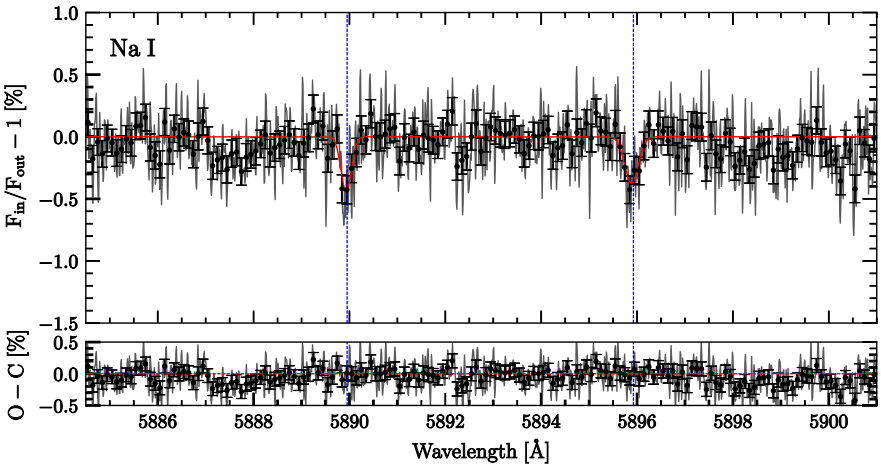

Fig. 3. Transmission spectrum of MASCARA-2b atmosphere in the region of Na I D doublet. In the *top panel* the atmospheric transmission spectrum is presented in light gray. Black dots indicate the binned transmission spectrum by 10 pixels and the Gaussian fit to each Na I D lines is shown in red; its residuals are shown in the *bottom panel*. The expected wavelength position of the Na I doublet lines, in the planetary reference frame, are indicated with blue vertical lines. The uncertainties of the relative flux come from the error propagation of the photon and readout noise from the original data.

Table 2. Summary of the measured relative absorption depth in [%] in the Na I D lines of the final transmission spectrum and the TLC of MASCARA-2b for various bandwidths.

	Na I			
Bandwidth (Å)	D_2	D_1	D doublet[a]	TLC[b]
0.188	0.435 ± 0.085	0.386 ± 0.083	0.411 ± 0.059	–
0.375	0.320 ± 0.058	0.337 ± 0.057	0.324 ± 0.041	–
0.75	0.168 ± 0.042	0.178 ± 0.041	0.172 ± 0.029	0.200 ± 0.046
1.5	0.066 ± 0.030	0.076 ± 0.030	0.071 ± 0.021	0.116 ± 0.033
3.0	0.057 ± 0.022	0.045 ± 0.021	0.051 ± 0.015	0.077 ± 0.024
5.0	0.072 ± 0.017	0.066 ± 0.017	0.069 ± 0.012	0.083 ± 0.019

Notes. [(a)] Average of both Na I D_1 and D_2 lines absorption depth. [(b)] Absorption measured in the final TLC (see third row of Fig. 5).

row of Fig. 5). We note that the modeled CLV + RM light curves are directly derived from the spectral models shown in Fig. 2, and the fitting procedure is only applied to the Na I absorption model. This fitting is performed using a simple MCMC algorithm and the model built with PyTransit (Parviainen 2015). This model depends on the orbital period (P), excentricity (e), planet-star ratio ($R_P/R_\star$), scaled semimajor axis ($a/R_\star$), orbital inclination (i), transit center (T_0), argument of periastron (ω) and quadratic limb darkening coefficients (u). The u coefficients are fixed to the estimated values calculated with the PyLDTk (Parviainen & Aigrain 2015) Python Package, which use the library of PHOENIX stellar atmospheres (Husser et al. 2013), $R_p/R_\star$ remains free and the other parameters are fixed to the values presented in Table 1.

As can be observed, the CLV + RM model is slightly underestimated compared to the measurements, which is possibly due to the assumption of local thermodynamical equilibrium (LTE) during the model computation (Yan et al. 2017). With the final Na I TLC it is possible to calculate the true absorption depth by comparing the weighted mean of the in-transit and out-of-transit values (see the results in Table 2). These values are consistent with the measured absorption depth values derived from the final transmission spectrum of MASCARA-2b; these findings are presented in the same table for a better comparison.

4.3. Analysis of Hα region

Following the same methods, we analyzed the region around the Hα line (λ6562.80 Å) in the MASCARA-2b spectrum; see the two-dimensional representation of the spectra in Appendix A. In the telluric correction, we subtract the sky spectrum to correct for possible telluric Hα emission. The Hα line observed in MASCARA-2 spectra is more than 50 Å (5000 pixels) broad, for this reason the transmission spectrum is binned by 30 pixels in this case (see Fig. 6) and larger bandwidths (3.0 Å, 5.0 Å, 10.0 Å, and 20.0 Å) are used to calculate the TLC (see Fig. 7),

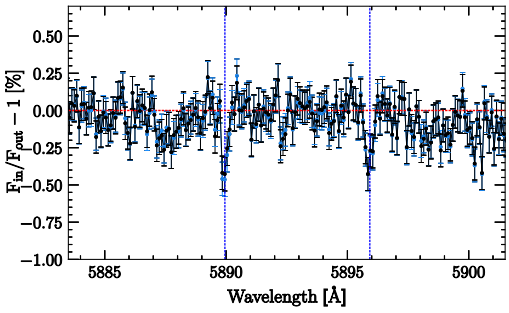

Fig. 4. Comparison between the transmission spectra obtained with (light blue line) and without (black line) stellar RV correction, before correcting for the final RM and CLV effects. In both cases the spectrum is binned by 10 pixels. The blue vertical lines show the expected wavelength position of the Na I D lines and the red horizontal line is the null-absorption reference.

Table 3. Summary of the measured relative absorption depth in [%] in the Hα line of the final transmission spectrum and the TLC of MASCARA-2b for various bandwidths.

Bandwidth (Å)	Hα	TLC[a]
0.188	0.521 ± 0.159	–
0.375	0.678 ± 0.110	–
0.75	0.594 ± 0.078	–
1.5	0.378 ± 0.056	–
3.0	0.235 ± 0.040	0.311 ± 0.044
5.0	0.206 ± 0.031	0.213 ± 0.034
10.0	–	0.054 ± 0.023
20.0	–	0.052 ± 0.023

Notes. [(a)] Absorption measured in the final TLC (see third row of Fig. 7).

with 12.0 Å reference passbands at $B = [6480.00 - 6492.00]$ Å and $R = [6628.00 - 6640.00]$ Å.

A Gaussian feature with a contrast of $0.63 \pm 0.09\%$ and a FWHM of 0.95 ± 0.16 Å is observed in the Hα position (6562.74 ± 0.08 Å), and the measured absorption depth is $0.378 \pm 0.056\%$ for a 1.5 Å passband (more values are presented in Table 3). As for the Na I, the Hα TLC present a strong RM shape for small passbands that slowly disappears for larger bandwidths (see Fig. 7). This RM effect is compensated at about ∼50.0 Å central passbands when the stellar line is totally encompassed. However, in this case the possible Hα absorption is attenuated in the large passband and the transit light curve becomes flat. The Hα absorption depths measured in the TLC measured with different passbands, after correcting for the RM+CLV effect, are presented in Table 3. Similar to the case of Na I absorption, these values are in agreement with the measured absorption depth values from the final transmission spectrum, giving strong confidence in our results.

The same control distributions to those presented for Na I are performed for Hα. For a 0.75 Å bandwidth we measure absorption depths of $0.016 \pm 0.141\%$, $0.075 \pm 0.110\%$, $0.136 \pm 0.085\%$, and $0.387 \pm 0.078\%$, for the out-out, in-in, even-odd, and no planet RV samples, respectively. In this case, when the planet RV correction is not applied we measure a significant absorption depth. This is probably because Hα is a very broad line and the planetary signals partially overlap even if the planet RV is not corrected.

4.4. (Non-)detections of Hβ, Hγ, and Mg I?

Following Hα we analyzed the Hβ (λ4861.28 Å), Hγ (λ4340.46 Å) and Mg I (λ4571.10 Å) regions, with no clear signals observed in any case (see Fig. B.1).

We measure the absorption depth in the expected line position using a central bandwidth of 0.75 Å. For Hβ we use reference passbands of $B = [4782.0, 4794.0]$ and $R = [4926.0, 4938.0]$, measuring an absorption depth of $0.079 \pm 0.059\%$. Using reference bandwidths of $B = [4282.00, 4294.00]$ and $R = [4366.0, 4378.0]$ for the Hγ line we get an absorption depth of $0.099 \pm 0.077\%$. Finally, for Mg I, with $B = [4492.00, 4504.00]$ and $R = [4636.00, 4648.00]$, the measured absorption depth is $0.002 \pm 0.034\%$.

For Hβ and Hγ the transmission spectrum is not totally flat but a lot of noise is concentrated in the expected line positions. Increasing the S/N by co-adding more transit observations is needed to determine the presence of these planetary absorption features.

5. Modeled Na I and Hα temperature profiles

Using high resolution spectroscopy we are not only able to detect chemical species in the atmosphere of exoplanets but also to resolve the spectral lines. When this happens, if the S/N of the final transmission spectrum is high enough, we can adjust isothermal models to different parts of these lines, whose origins reside in different layers of the atmosphere of the exoplanet and reconstruct the temperature profile.

To measure the temperature versus altitude profile from the Na I D transmission spectrum, we use the following atmospheric altitude, $z(\lambda)$, equation given in Lecavelier Des Etangs et al. (2008):

$$z(\lambda) = \frac{kT}{\mu g} \ln\left(\frac{\xi \sigma(\lambda) P_o}{\tau_{eq}}\right)\left(\frac{2\pi R_P}{kT\mu g}\right)^{1/2} + z_0, \quad (1)$$

where k is Boltzmann's constant, T is the temperature, μ is the mean molecular weight of the atmospheric composition, g is the surface gravity, $\xi = \xi_i/\xi_H$ is the elemental abundance of the chemical species i relative to the Hydrogen abundance, $\sigma(\lambda)$ is the absorption cross section, P_o is the pressure at the reference altitude, τ_{eq} is the optical depth at the transit radius, and R_P is the radius of the planet. The z_0 term is independent of the wavelength and can be determined by the altitude in the continuum wavelengths. This relation is derived from a plane-parallel atmosphere, assuming hydrostatic equilibrium and the ideal gas law.

The cross section, $\sigma(\lambda)$, of each line is determined by modeling the lines as a Voigt profile,

$$\sigma(\lambda) = \frac{\pi e^2}{m_e c} \frac{f}{\Delta\nu_D \sqrt{\pi}} H, \quad (2)$$

where e is the electronic charge, m_e is the electron mass, c is the speed of light, f is the absorption oscillator strength, H is the Voigt profile, which includes thermal and natural broadening, and $\Delta\nu_D$ is the Doppler width, given by

$$\Delta\nu_D = \frac{\nu_o}{c}\sqrt{2kT/\mu_i}, \quad (3)$$

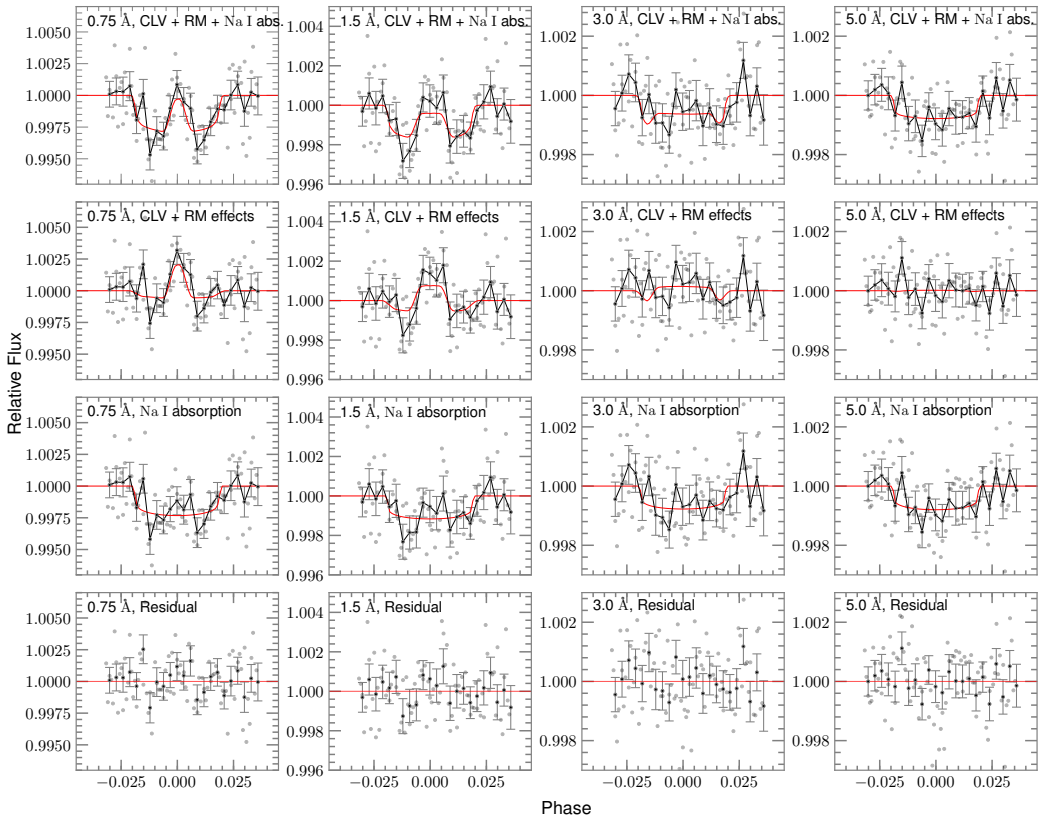

Fig. 5. Na I TLC from HARPS-N observations of MASCARA-2b for four bandwidths: 0.75 Å (*first column*), 1.5 Å (*second column*), 3.0 Å (*third column*), and 5.0 Å (*fourth column*). In all panels, the light gray dots indicate the values from all the spectra, and the black dots the same data binned with 0.003 phase step. *First row*: observed TLC of the Na I D lines from our data reduction. The relative flux of the D_1 and D_2 lines is averaged. The red line indicates the modeled TLC, which is the combination of the best-fit Na I absorption and the CLV and RM effects (Yan et al. 2017). This model is calculated theoretically and there is no fitting to the data. *Second row*: the CLV + RM effects. The black line indicates the result of removing the Na I absorption model from the observed TLC. The modeled CLV and RM effects are shown in red. *Third row*: the Na I absorption light curve obtained dividing the observed TLC by the modeled CLV + RM effects (black line). The red line is the best-fit Na I absorption model. *Fourth row*: residuals between the observed TLC and the model. We note the different y-scale of the panels.

where ν_o the central frequency and μ_i the mean molecular weight of the chemical species are computed. We note that for the Na I doublet lines, $\sigma(\lambda)$ is calculated for each line separately and the combined profile is calculated using $\sigma(\lambda) = \sigma(\lambda)_{D_2} + \sigma(\lambda)_{D_1}$.

For MASCARA-2b, given the presence of Hα, we assume a mean molecular weight of $\mu = 1$. We note that this assumption implies a totally dissociated hydrogen atmosphere, while in truth it could be only partially dissociated. In that latter case, the μ value would increase and the profile contrast would decrease for similar temperatures. On the other hand, we assume $\tau_{eq} = 0.56$, as it is shown to be mainly constant for planets with $R_P/H \sim 30-3000$ by Lecavelier Des Etangs et al. (2008). We fix P_o to 1 mbar. For the Na I, ξ is fixed to 1.995×10^{-6} as presented in Huitson et al. (2012) and, for Hα, we estimate ξ with the temperature-dependent relation presented in Huang et al. (2017),

$$\xi \equiv \frac{n_{2p}}{n_{1s}} \simeq 3\frac{n_{2s}}{n_{1s}} = \frac{J_{12}B_{12}}{A_{12}} \simeq 10^{-8}\frac{J_{12}}{10^{-9}\ \mathrm{erg\ cm^{-2}\ s^{-1}\ Hz^{-1}}}, \quad (4)$$

where the peak Lyα intensity is $J_{12} \simeq 0.1 F_{LyC}/\Delta\nu_D$, and $F_{LyC} \simeq 9.1 \times 10^4$ erg cm^{-2} s^{-1} (Lund et al. 2017) is the flux received by the planet. As defined in Eq. 3, $\Delta\nu_D$ depends on the local temperature. The values of the Na I and Hα parameters used are summarized in Table 4.

With this information and using the Levenberg–Marquardt algorithm through the *leastsq* tool (Jones et al. 2001), and similarly to Wyttenbach et al. (2015), we first determine the offset between the models and the data, z_0, by fixing the temperature to $T_{eq} = 2260$ K. Once the value is fixed, if the S/N were high enough, we could adjust models to different regions of the spectrum. However, the S/N of MASCARA-2b transmission spectrum is not sufficient to differentiate the wings regions (more

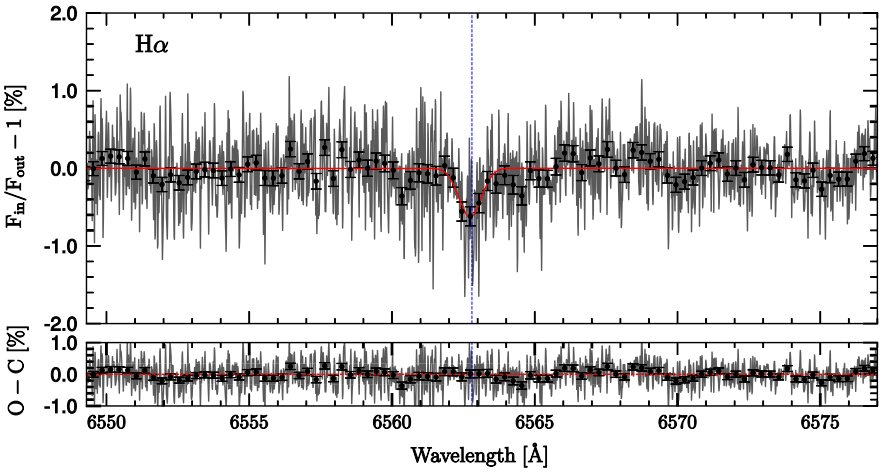

Fig. 6. Transmission spectrum of MASCARA-2b atmosphere in the region of Hα. *Top panel*: atmospheric transmission spectrum (light gray) and binned transmission spectrum by 30 pixels (black dots). The Gaussian fit is shown in red. *Bottom panel*: residuals of the Gaussian fit. The blue vertical line indicates the expected wavelength position in the planetary reference frame.

Table 4. Summary of the Na I and Hα values assumed when fitting $z(\lambda)$.

	Na I doublet		Hα
	D_2	D_1	
λ_o (Å)	5889.951	5895.924	6562.80
f	0.6405[a]	0.3199[a]	0.64108[d]
ξ	1.995×10^{-6}[b]		6.784×10^{-6}[c]
μ_i (AMU)	23		1

Notes. [(a)] Steck (2010). [(b)] A solar abundance (Lodders 2003). [(c)] Estimated during the temperature fitting with the temperature-dependent Eq. (4) (Huang et al. 2017). [(d)] Wiese & Fuhr (2009).

transit observations are needed). Still, it is possible to fit the lines core, observing that higher temperatures than T_{eq} are required to explain the contrast measured in the Na I doublet and Hα lines. In order to fit the temperature of the lines core, we use the data within a 0.3 Å bandwidth in case of both Na I lines and 0.9 Å for Hα centered to the lines peak, which correspond to the measured FWHM of the lines. We note that each Na I D_1 and D_2 lines are adjusted separately, with best-fit models at $T = 4240 \pm 200$ K and $T = 4180 \pm 310$ K, respectively, which results in consistent temperatures taking into account the uncertainties. For the Hα line the best-fit model presents a temperature of 4330 ± 520 K. The best-fit models can be observed in Figs. 8 and 9.

As noted, the best-fit models shown here consider a mean molecular weight of $\mu = 1$, which corresponds to a totally dissociated hydrogen atmosphere. For a molecular hydrogen atmosphere ($\mu = 2.3$), the best-fit profiles in the lines core correspond to temperatures larger than 9000 K for the Na I (9250 ± 480 K) and Hα (9790 ± 1770 K) lines, i.e., larger than the effective temperature of the host star. However, atmospheres are expected to be heated up to 10 000–20 000 K, still producing absorption features in transmission. On the other hand, assuming an atomic hydrogen atmosphere ($\mu = 1.3$) these temperatures decrease to 5400 ± 200 K and 5530 ± 770 K for the Na I and Hα lines core, respectively, and to ~4000 K when a totally dissociated hydrogen atmosphere ($\mu = 1$) is considered. The MASCARA-2b atmosphere could be only partially dissociated and, in that case, the μ value would be larger than 1. However, since the surface gravity of this planet has not been determined yet and only an upper limit has been estimated, we assume $\mu = 1$ given that if the real g value were lower, it would lead to a similar effect in the temperature as decreasing μ, i.e., increasing the profiles contrast for similar temperatures. Thus, the 9250 ± 480 K and 9790 ± 1770 K for the Na I and Hα lines, respectively, obtained assuming $\mu = 1$ and the g upper-limit value, can be considered as upper-limit estimations of the temperatures in these lines.

MASCARA-2b is part of the small sample of planets transiting an A-type star known to date, with effective temperatures higher than ~7000 K. These planets typically receive a large amount of extreme ultraviolet radiation from its host star (~9.1×10^4 ergs s^{-1} cm^{-2} in case of MASCARA-2b), which produce the expansion of their atmosphere and excite the atomic hydrogen to produce Hα absorption and possibly abrasion of the atmosphere (Bourrier et al. 2016). Hα is commonly used as a stellar activity indicator because it is difficult to detect in exoplanet atmospheres, but not for planets orbiting A-type stars, which are not usually active. The measurement of a 0.63 ± 0.09% of Hα absorption in the atmosphere of MASCARA-2b corresponds to an effective radius, R_λ/R_P, of 1.20 ± 0.04 and a temperature of 4330 ± 520 K. These values are obtained with only one transit observation, and considering the strong residuals observed in the Hβ and Hγ regions of MASCARA-2b transmission spectrum, by co-adding more transit observations we might be able to increase the S/N and study the temperature profile of the planet by observing these other Balmer lines and possibly calculate the lifetime of the atmosphere from escape rate measurements.

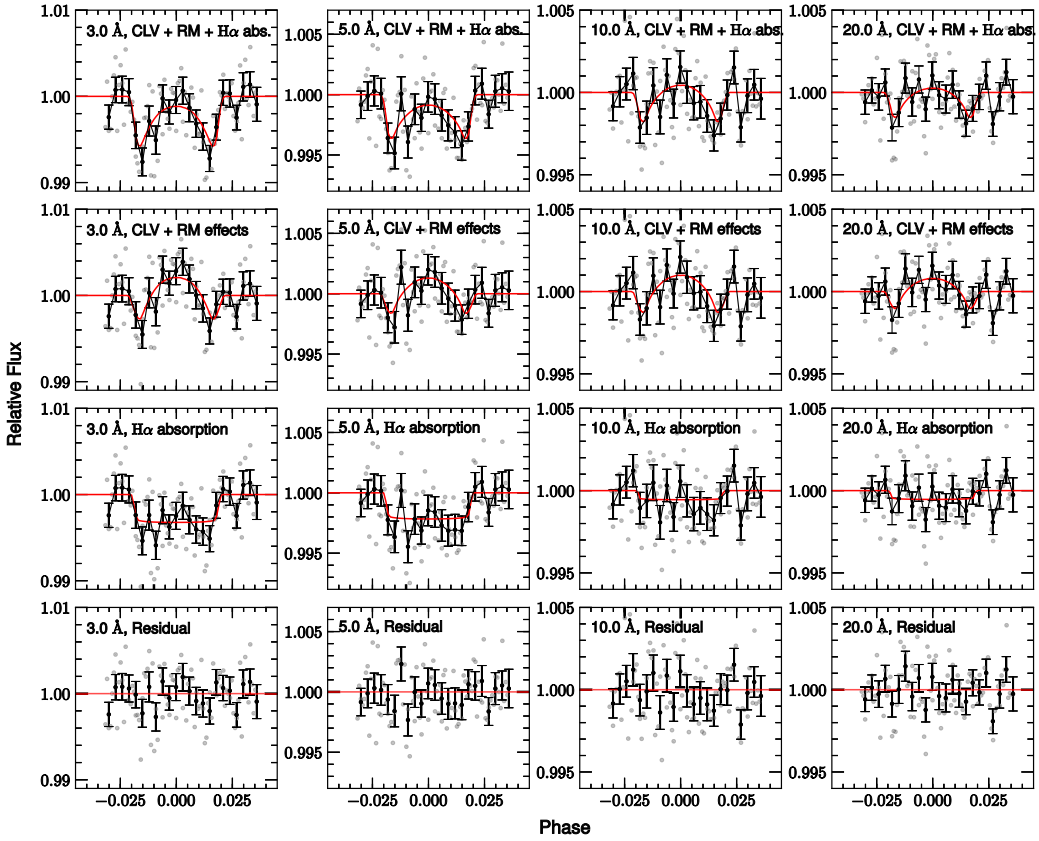

Fig. 7. Same as Fig. 5 but for the Hα line. In this case, the following larger bandwidths are used: 3.0 Å (*first column*), 5.0 Å (*second column*), 10.0 Å (*third column*), and 20.0 Å (*fourth column*).

6. Conclusions

We observed one transit of MASCARA-2b, the hot Jupiter orbiting the fourth brightest star with a transiting planet, using the HARPS-North spectrograph. In that dataset, we resolve two spectral features centered on the atomic sodium (Na I) doublet position with an averaged absorption depth of 0.172 ± 0.029% for a 0.75 Å bandwidth, measuring line contrasts of 0.44 ± 0.11% (D_2) and 0.37 ± 0.08% (D_1), and FWHM of 0.26 ± 0.08 Å (D_2) and 0.33 ± 0.08 Å (D_1) from the Gaussian fit. The Na I TLC are also calculated, observing a large RM effect for small passbands, which is clearly diluted when the bandwidths are increased. After correcting for the RM and CLV effects using synthetic spectra, we measure a 0.200 ± 0.046% Na I transit absorption for a 0.75 Å passband that is consistent with the absorption depth values measured from the final transmission spectrum. We measure the temperature of the Na I lines core, resulting in $T = 4240 \pm 200$ K and $T = 4180 \pm 310$ K for the D_2 and D_1 lines, respectively, consistent within uncertainties. The S/N of the final transmission spectrum is not sufficient to adjust temperatures in different regions of the lines wings, however, we clearly observe that the equilibrium temperature ($T_{eq} = 2260 \pm 50$ K) cannot define the contrast observed in the Na I lines.

The same method is applied to Hα, observing a Gaussian feature centered at 6562.74 ± 0.08 Å with 0.63 ± 0.09% contrast and FWHM of 0.92 ± 0.16 Å. This absorption is also observed in the final TLC, presenting consistent absorption depths as those measured in the transmission spectrum of Hα. We measure a temperature of $T = 4330 \pm 520$ K in the line core, corresponding to an effective radius R_λ/R_P of 1.20 ± 0.04. Since MASCARA-2b is one of the most irradiated planets to date, we expect the atomic hydrogen to be excited and produce Hα absorption. This extreme UV radiation, as for other similar planets transiting A-type stars, can lead to the expansion and abrasion of their atmosphere.

We stress that the results presented in this work are obtained with only one transit observation as a consequence of the brightness of MASCARA-2 and the favorable physical parameters of MASCARA-2b for transmission spectroscopy. Thus more transits are desired to confirm these results. In particular, we observe residual absorption features in the Hβ and Hγ regions of MASCARA-2b transmission spectrum, but are not statistically

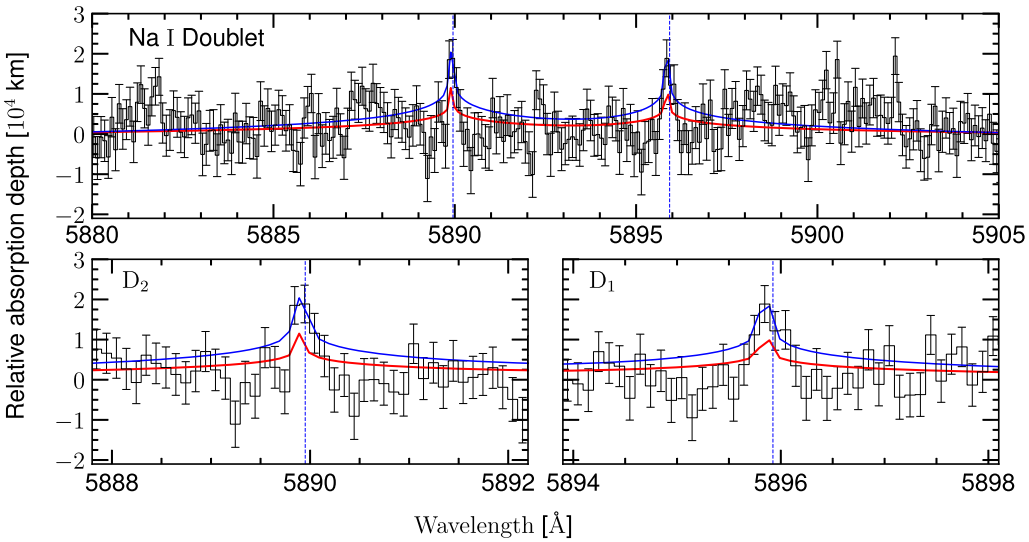

Fig. 8. Fit of isothermal models to the transmission spectrum of MASCARA-2b in the Na I region. The vertical scale is atmospheric altitude in [km] assuming a planet-to-star radius ratio of $R_p^2/R_\star^2 = 0.013$. In red we show a model at the equilibrium temperature ($T_{eq} = 2260$ K), which is adjusted to the continuum. One other model is adjusted to the lines core of each line using the data encompassed for a 0.3 Å bandwidth centered on the lines peak (shown in blue). For the D_2 line the best-fit model is at $T = 4240 \pm 200$ K and for the D_1 line is at $T = 4180 \pm 310$ K, i.e., the same temperature taking into account the uncertainties. In the *top panel* we show both Na I lines and the continuum surrounding. In the *bottom panels* we show each D_2 (*left*) and D_1 (*right*) lines zoomed. Data and models are presented binned by 10 pixels.

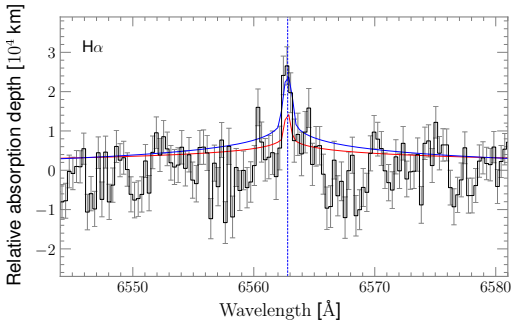

Fig. 9. Same as Fig. 8 but in the Hα region. The isothermal model at the equilibrium temperature ($T_{eq} = 2260$ K), which is adjusted to the continuum, is shown in red. The blue line represents the model at 4330 ± 520 K, which is adjusted to the data contained in a 1.2 Å bandwidth centered to the peak position. Data and models are presented binned by 30 pixels.

significant. More transits would help to build up enough S/N to determine the presence of these planetary absorptions.

Currently, a small sample of planets are known that transits A-type stars. The study and comparison of these planets, which present different system properties and are irradiated different amounts of energy from their host stars, will help us to learn about their origin and evolution.

Acknowledgements. This work is based on observations made with the Italian Telescopio Nazionale *Galileo* (TNG) operated on the island of La Palma by the Fundación Galileo Galilei of the INAF (Istituto Nazionale di Astrofisica) at the Spanish Observatorio del Roque de los Muchachos of the Instituto de Astrofisica de Canarias. This work is partly financed by the Spanish Ministry of Economics and Competitiveness through projects ESP2014-57495-C2-1-R and ESP2016-80435-C2-2-R. G.C. also acknowledges the support by the Natural Science Foundation of Jiangsu Province (Grant No. BK20151051) and the National Natural Science Foundation of China (Grant No. 11503088). I. Snellen acknowledges funding from the research programme VICI 639.043.107 funded by the Dutch Organisation for Scientific Research (NWO), and funding from the European Research Council (ERC) under the European Union's Horizon 2020 research and innovation programme under grant agreement No 694513. J. I. G. H. and R. R. L. acknowledge the Spanish ministry project MINECO AYA2014-56359-P. J. I. González Hernández also acknowledges financial support from the Spanish Ministry of Economy and Competitiveness (MINECO) under the 2013 Ramón y Cajal programme MINECO RYC-2013-14875.

References

Astudillo-Defru, N., & Rojo, P. 2013, A&A, 557, A56
Barnes, J. R., Haswell, C. A., Staab, D., & Anglada-Escudé, G. 2016, MNRAS, 462, 1012
Bourrier, V., Lecavelier des Etangs, A., Ehrenreich, D., Tanaka, Y. A., & Vidotto, A. A. 2016, A&A, 591, A121
Casasayas-Barris, N., Palle, E., Nowak, G., et al. 2017, A&A, 608, A135
Charbonneau, D., Brown, T. M., Noyes, R. W., & Gilliland, R. L. 2002, ApJ, 568, 377
Chen, G., Guenther, E. W., Pallé, E., et al. 2017, A&A, 600, A138
Frasca, A., Freire Ferrero, R., Marilli, E., & Catalano, S. 2000, A&A, 364, 179
Heiter, U., Kupka, F., van't Veer-Menneret, C., et al. 2002, A&A, 392, 619
Heng, K., Wyttenbach, A., Lavie, B., et al. 2015, ApJ, 803, L9
Huang, C., Arras, P., Christie, D., & Li, Z.-Y. 2017, ApJ, 851, 150
Huitson, C. M., Sing, D. K., Vidal-Madjar, A., et al. 2012, MNRAS, 422, 2477
Husser, T.-O., Wende-von Berg, S., Dreizler, S., et al. 2013, A&A, 553, A6
Jones, E., Oliphant, T., Peterson, P., et al. 2001, SciPy: Open source scientific tools for Python. http://www.scipy.org/
Lecavelier Des Etangs, A., Pont, F., Vidal-Madjar, A., & Sing, D. 2008, A&A, 481, L83
Lodders, K. 2003, ApJ, 591, 1220
Louden, T., & Wheatley, P. J. 2015, ApJ, 814, L24

Lovis, C., Snellen, I., Mouillet, D., et al. 2017, A&A, 599, A16
Lund, M. B., Rodriguez, J. E., Zhou, G., et al. 2017, AJ, 154, 194
Murgas, F., Pallé, E., Zapatero Osorio, M. R., et al. 2014, A&A, 563, A41
Nortmann, L., Pallé, E., Murgas, F., et al. 2016, A&A, 594, A65
Ohta, Y., Taruya, A., & Suto, Y. 2005, ApJ, 622, 1118
Palle, E., Chen, G., Prieto-Arranz, J., et al. 2017, A&A, 602, L15
Parviainen, H. 2015, MNRAS, 450, 3233
Parviainen, H., & Aigrain, S. 2015, MNRAS, 453, 3821
Redfield, S., & Linsky, J. L. 2008, ApJ, 673, 283
Redfield, S., Endl, M., Cochran, W. D., & Koesterke, L. 2008, ApJ, 673, L87
Sing, D. K., Huitson, C. M., Lopez-Morales, M., et al. 2012, MNRAS, 426, 1663
Snellen, I. A. G., Albrecht, S., de Mooij, E. J. W., & Le Poole, R. S. 2008, A&A, 487, 357
Snellen, I. A. G., de Kok, R. J., le Poole, R., Brogi, M., & Birkby, J. 2013, ApJ, 764, 182
Steck, D. A. 2010, Sodium D Line Data (Los Alamos National Observatory)
Talens, G. J. J., Justesen, A. B., Albrecht, S., et al. 2018, A&A, 612, A57
Wiese, W. L., & Fuhr, J. R. 2009, J. Phys. Chem. Ref. Data, 38, 565
Wilson, P. A., Sing, D. K., Nikolov, N., et al. 2015, MNRAS, 450, 192
Wyttenbach, A., Ehrenreich, D., Lovis, C., Udry, S., & Pepe, F. 2015, A&A, 577, A62
Wyttenbach, A., Lovis, C., Ehrenreich, D., et al. 2017, A&A, 602, A36
Yan, F., Fosbury, R. A. E., Petr-Gotzens, M. G., et al. 2015, Int. J. Astrobiol., 14, 255
Yan, F., Pallé, E., Fosbury, R. A. E., Petr-Gotzens, M. G., & Henning, T. 2017, A&A, 603, A73

Appendix A: Two-dimensional representations

Two- dimensional representations of the observed spectra and the residuals after some reduction steps presented in Sect. 3 for the Na I (Fig. A.1) and Hα (Fig. A.2) regions. The vertical axis of each matrix represents the sequence number of the spectrum and the horizontal axis represents the wavelength. A detailed description can be seen in Fig. A.1 caption.

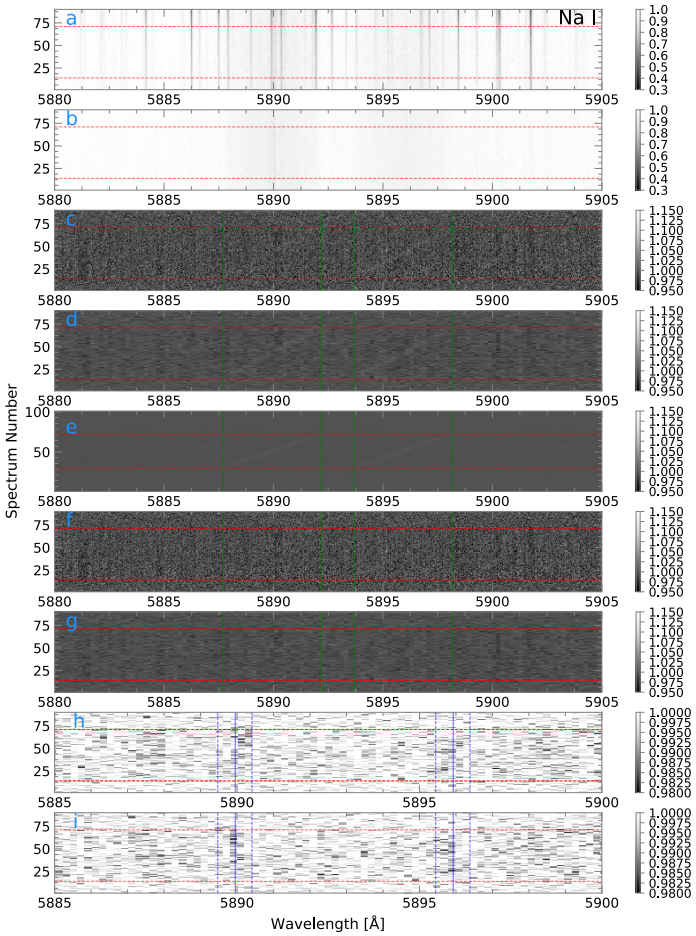

Fig. A.1. Two-dimensional representation of the MASCARA-2b spectra around Na I lines. The vertical axis of each panel represents the sequence number of the observed spectra (the time increases with the spectrum number); the red horizontal lines represent the limits between the in- and out-of-transit data. In the horizontal axis we present the wavelength in Å and the relative flux values are shown in the color bar. *Panel a*: original data after the normalization. *Panel b*: observed data after the telluric subtraction. *Panels c, d,* and *e*: residuals from the in-transit spectra and the master out spectrum ratio. The RM effect can be clearly observed in these panels. In *panel d* the data is binned by 20 pixels and in *e* we show the modeled RM residuals (without planetary absorption) obtained by applying to the modeled stellar spectra the same process as data from *panels c* and *d*. *Panels f* and *g*: residuals after correcting each single spectrum presented in *c* for the RM effect. We note in the process presented in Sect. 3 that the correction is applied to the final transmission spectrum after combining all $\mathrm{In}/M_{\mathrm{out}}$ with the planet RV correction applied so as not to affect the planetary absorption. In *panel g* the data is binned by 20 pixels. The green vertical lines show the limits in wavelength of the RM effect (from $-v \sin i$ to $+v \sin i$). *Panel h*: same as *g* decreasing the wavelength coverage and changing the contrast (see color-bar). *Panels i*: same as *h* after the planet RV correction. The blue vertical lines of *panels h* and *i* show the expected Na I position in wavelength due to the maximum and minimum RV of the planet during the transit (dashed line) and the mid-transit value, i.e., null RV (solid line).

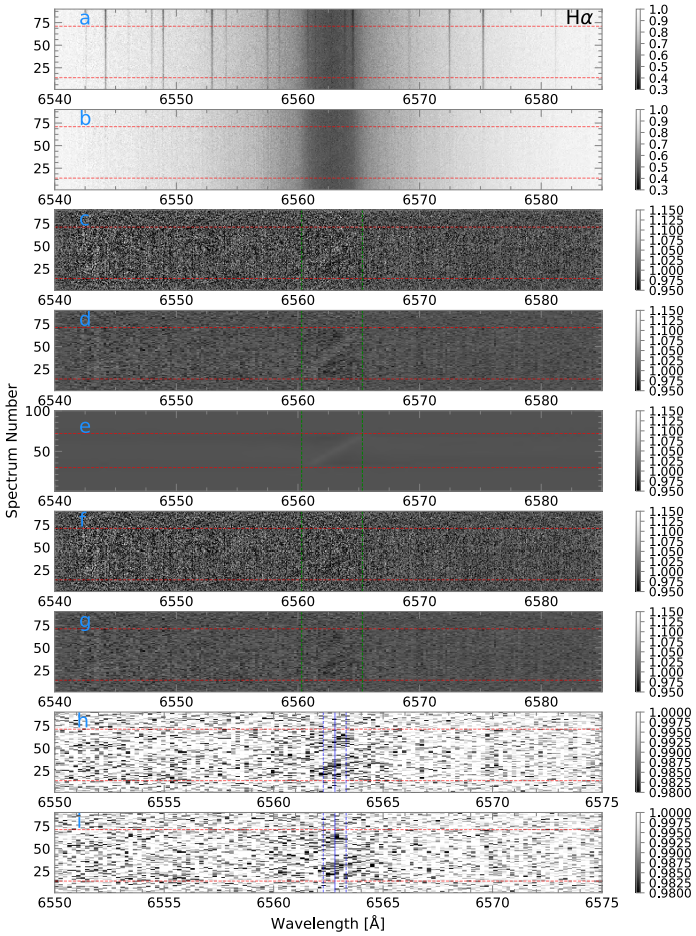

Fig. A.2. Same as Fig. A.1 but for the Hα line.

Appendix B: Hβ, Hγ and Mg I results

As referred in Sect. 4.4, other regions of the spectra are analyzed by applying the same method presented in Sect. 3. We present the resulting transmission spectra around Hβ, Hγ, and Mg I lines from which no clear conclusions can be extracted. The S/N needs to be increased by co-adding more transit observations to figure out the origin of their residuals.

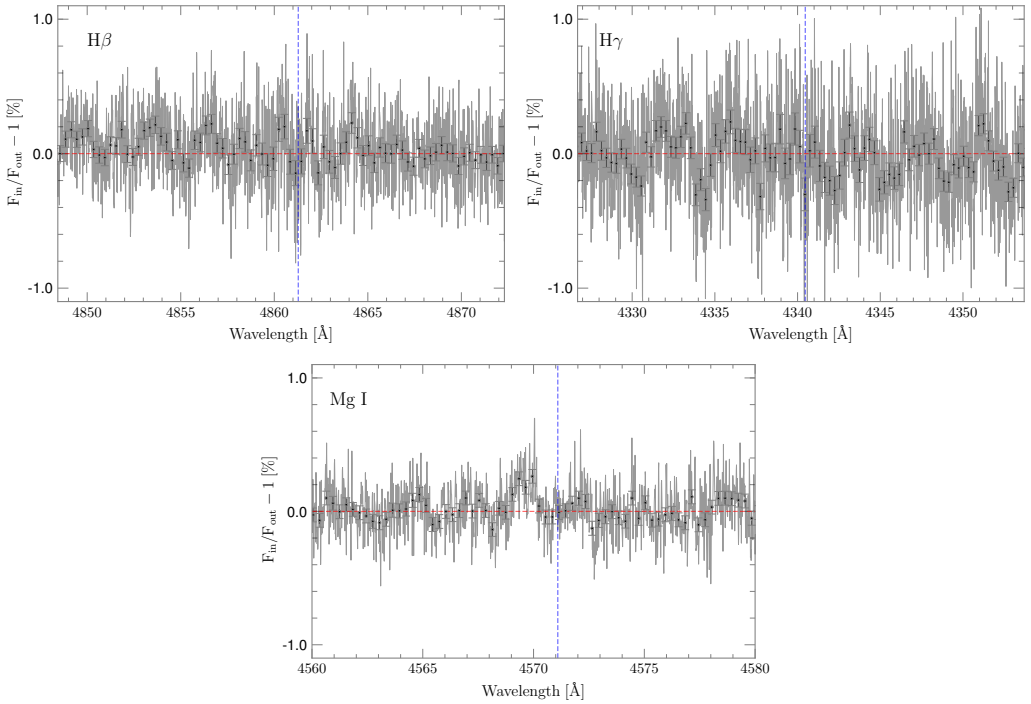

Fig. B.1. Transmission spectrum of MASCARA-2b atmosphere in the region of Hβ (*top left*), Hγ (*top right*), and Mg I (*bottom*). Transmission spectrum (light gray) and binned transmission spectrum by 30 pixels (black dots). The blue vertical line indicates the expected wavelength position in the planetary reference frame.

4

Atmospheric characterisation of MASCARA-2b

Just close your eyes and keep your mind wide open.

–Bridge to Terabithia, 2007

In this chapter we confirm the findings from Chapter 3 using two more transit spectroscopy observations of MASCARA-2b with HARPS-N and one with CARMENES. Using a total of four transit observations of MASCARA-2b we are able to confirm the presence of NaI and Hα in the exoplanet atmosphere, but also to detect Hβ, FeII, and the CaII infrared triplet lines for the first time, taking advantage of the redder wavelengths covered by CARMENES. The analysis and results presented in this chapter are published in A&A under the bibcode: 2019A&A...628A...9C (Casasayas-Barris et al., 2019).

MASCARA-2b orbits a bright (V=7.6) and very fast rotating star ($v \sin i_\star = 114\,\mathrm{km\,s^{-1}}$). As can be observed in equation 1.1, the semi amplitude of the RM effect is proportional to the projected rotation velocity of the host star. With the new transit observations, this effect is clearly distinguished in the 2D transmission maps together with the absorption from the planet, due to the high S/N of the observations. Here, we model the impact of the RM and CLV effects in the transmission spectrum of MASCARA-2b following Yan et al. (2015) and Yan & Henning (2018), and use a Markov chain Monte Carlo (MCMC) analysis to correct these features. After this correction the transmission spectrum and

light curves can be measured. Performing a 2D analysis of the observations we can visually distinguish, for the first time in individual spectral lines, the time-variations that the absorption produced by the exoplanet atmosphere suffers due to the planet movement during the transit.

MASCARA-2b shows a very rich atmosphere, composed by an slightly extended hydrogen envelope, and a large diversity of atoms and ions. Similar detections have been claimed in other ultra hot Jupiter atmospheres such as KELT-9b (Hoeijmakers et al., 2018; Cauley et al., 2019; Yan & Henning, 2018; Yan et al., 2019), and WASP-76b (Seidel et al., 2019), among others. In these tidally locked planets, the stellar radiation heats the upper atmosphere to temperatures higher than 3000 K causing the day-side atmosphere to be composed of atoms rather than molecules. At these temperatures some ionised atoms like FeII, are expected to be more abundant than its neutral form (Helling et al., 2019) due to thermal ionisation. Using transit observations, we are able to probe the terminator region of the exoplanet atmosphere between day- and night-sides. Recently, the findings presented in this chapter have been re-confirmed using observations with different instruments and methodologies (e.g. Stangret et al. 2020; Nugroho et al. 2020; Hoeijmakers et al. 2020a).

A&A 628, A9 (2019)
https://doi.org/10.1051/0004-6361/201935623

Astronomy & Astrophysics

Atmospheric characterization of the ultra-hot Jupiter MASCARA-2b/KELT-20b

Detection of CaII, FeII, NaI, and the Balmer series of H (Hα, Hβ, and Hγ) with high-dispersion transit spectroscopy*

N. Casasayas-Barris[1,2], E. Pallé[1,2], F. Yan[3], G. Chen[1,2,4], S. Kohl[5], M. Stangret[1,2], H. Parviainen[1,2], Ch. Helling[6,7,8], N. Watanabe[9,10], S. Czesla[5], A. Fukui[14,1], P. Montañés-Rodríguez[1,2], E. Nagel[5], N. Narita[9,11,12,1], L. Nortmann[1,2], G. Nowak[1,2], J. H. M. M. Schmitt[5], and M. R. Zapatero Osorio[13]

[1] Instituto de Astrofísica de Canarias, Vía Láctea s/n, 38205 La Laguna, Tenerife, Spain
e-mail: nuriacb@iac.es
[2] Departamento de Astrofísica, Universidad de La Laguna, La Laguna, Spain
[3] Institut für Astrophysik, Georg-August-Universität, Friedrich-Hund-Platz 1, 37077 Göttingen, Germany
[4] Key Laboratory of Planetary Sciences, Purple Mountain Observatory, Chinese Academy of Sciences, Nanjing 210008, PR China
[5] Hamburger Sternwarte, Universität Hamburg, Gojenbergsweg 112, 21029 Hamburg, Germany
[6] Centre for Exoplanet Science, University of St Andrews, St Andrews, UK
[7] SUPA, School of Physics & Astronomy, University of St Andrews, St Andrews, KY16 9SS, UK
[8] SRON Netherlands Institute for Space Research, Sorbonnelaan 2, 3584 CA Utrecht, The Netherlands
[9] National Astronomical Observatory of Japan, 2-21-1 Osawa, Mitaka, Tokyo 181-8588, Japan
[10] SOKENDAI (The Graduate University of Advanced Studies), 2-21-1 Osawa, Mitaka, Tokyo 181-8588, Japan
[11] Astrobiology Center, 2-21-1 Osawa, Mitaka, Tokyo 181-8588, Japan
[12] JST, PRESTO, 2-21-1 Osawa, Mitaka, Tokyo 181-8588, Japan
[13] Centro de Astrobiología (CSIC-INTA), Carretera de Ajalvir km 4, 28850 Torrejón de Ardoz, Madrid, Spain
[14] Department of Earth and Planetary Science, Graduate School of Science, The University of Tokyo, 7-3-1 Hongo, Bunkyo-ku, Tokyo 113-0033, Japan

Received 4 April 2019 / Accepted 29 May 2019

ABSTRACT

Ultra-hot Jupiters orbit very close to their host star and consequently receive strong irradiation, causing their atmospheric chemistry to be different from the common gas giants. Here, we have studied the atmosphere of one of these particular hot planets, MASCARA-2b/KELT-20b, using four transit observations with high resolution spectroscopy facilities. Three of these observations were performed with HARPS-N and one with CARMENES. Additionally, we simultaneously observed one of the transits with MuSCAT2 to monitor possible spots in the stellar surface. At high resolution, the transmission residuals show the effects of Rossiter-McLaughlin and centre-to-limb variations from the stellar lines profiles, which we have corrected to finally extract the transmission spectra of the planet. We clearly observe the absorption features of CaII, FeII, NaI, Hα, and Hβ in the atmosphere of MASCARA-2b, and indications of Hγ and MgI at low signal-to-noise ratio. In the case of NaI, the true absorption is difficult to disentangle from the strong telluric and interstellar contamination. The results obtained with CARMENES and HARPS-N are consistent, measuring an Hα absorption depth of 0.68 ± 0.05 and 0.59 ± 0.07%, and NaI absorption of 0.11 ± 0.04 and 0.09 ± 0.05% for a 0.75 Å passband, in the two instruments respectively. The Hα absorption corresponds to ~1.2 R_p, which implies an expanded atmosphere, as a result of the gas heating caused by the irradiation received from the host star. For Hβ and Hγ only HARPS-N covers this wavelength range, measuring an absorption depth of 0.28 ± 0.06 and 0.21 ± 0.07%, respectively. For CaII, only CARMENES covers this wavelength range measuring an absorption depth of 0.28 ± 0.05, 0.41 ± 0.05 and 0.27 ± 0.06% for CaII λ8498Å, λ8542Å and λ8662Å lines, respectively. Three additional absorption lines of FeII are observed in the transmission spectrum by HARPS-N (partially covered by CARMENES), measuring an average absorption depth of 0.08 ± 0.04% (0.75 Å passband). The results presented here are consistent with theoretical models of ultra-hot Jupiters atmospheres, suggesting the emergence of an ionised gas on the day-side of such planets. Calcium and iron, together with other elements, are expected to be singly ionised at these temperatures and be more numerous than its neutral state. The Calcium triplet lines are detected here for the first time in transmission in an exoplanet atmosphere.

Key words. planets and satellites: atmospheres – planetary systems – methods: observational – techniques: spectroscopic – planets and satellites: individual: MASCARA-2b – planets and satellites: individual: KELT-20b

* Reduced spectra are only available at the CDS via anonymous ftp to cdsarc.u-strasbg.fr (130.79.128.5) or via http://cdsarc.u-strasbg.fr/viz-bin/qcat?J/A+A/628/A9

1. Introduction

The study of hot Jupiters atmospheres has revealed a broad composition and structural diversity in gas-rich planets (Jensen et al. 2012; Sing et al. 2012; Crossfield 2015; Deming & Seager 2017; Madhusudhan et al. 2016). When these planets are under extreme conditions, in particular, located very close to their host stars and consequently being strongly irradiated, their temperatures increase and lead to different atmospheric chemistry between the day and night-sides of atmosphere (Arcangeli et al. 2018; Bell & Cowan 2018; Helling & Rimmer 2019) in comparison with cooler planets. This creates a new type of exoplanet called ultra-hot Jupiters (hereafter UHJ).

We define UHJs as planets with day-side temperatures higher than 2200 K (Parmentier et al. 2018). One of the most significant differences between hot and ultra-hot Jupiters is perhaps the presence of water vapour in their atmospheres. Water has become a common species in hot Jupiters but is missing in the day-side of ultra-hot Jupiters, even though the ingredients to form water vapor are present. The high irradiation received by the day-side of such UHJs causes the atmospheric gas temperature to increase to further more than 3000 K, as for example demonstrated for WASP-18b (Helling et al. 2019). The dominating gas species in the upper, day-side atmosphere is therefore atomic hydrogen (HI) instead of molecular hydrogen (H_2). Water (H_2O) is approximately five orders of magnitude less abundant on the day-side than on the night-side. Such high day-side gas temperatures further result in an increased number of H^- compared to cooler giant gas planets like HD 189733b. In the case of WASP-18b, in the upper low-pressure atmosphere, the day-side has more than ten orders of magnitude more H^- and H^+ than the night-side. Therefore, H^- opacity at the day-side plays an important role (Lothringer et al. 2018).

Several ultra-hot Jupiters have been studied: WASP-33b (Haynes et al. 2015), WASP-121b (Evans et al. 2017), WASP-103b (Kreidberg et al. 2018), WASP-18b (Sheppard et al. 2017; Arcangeli et al. 2018; Helling et al. 2019), HAT-P-7b (Armstrong et al. 2016), most of them presenting thermal inversions. Focusing on transmission spectroscopy at high resolution, a study of the atmosphere of KELT-9b, the hottest planet known to date (T_{eq} = 4050 K and day-side temperature of 4600 K), by Yan & Henning (2018) shows a detection of an extended atmosphere of Hα produced by irradiation. On the other hand, Hoeijmakers et al. (2018) study the atmosphere of this same planet, detecting Fe, Fe^+, and Ti^+ and concluding that at such these high temperatures metals are predominantly in their ionic forms. Cauley et al. (2019) further report the detection of Hβ and the optical MgI triplet, and find that planetary rotational broadening is needed to reproduce the Balmer line transmission profile shapes.

Here, we present the study of the atmosphere of MASCARA-2b (Talens et al. 2018), also known as KELT-20b (Lund et al. 2017), using four transit observations, three of them observed with the HARPS-North spectrograph and one observed with the CARMENES spectrograph. MASCARA-2b is an ultra-hot Jupiter with an equilibrium temperature of 2260 K, located in a 3.5 day orbit around an A-type star (m_V = 7.6) with an effective temperature (T_{eff}) of 8980 K and a rotation ($v \sin i$) of 114 km s^{-1}. MASCARA-2b orbits very close to its host star (a = 0.057 AU) and is strongly irradiated. Its mass, because radial-velocity measurements of rapid-rotators are very challenging, has not been measured, and only an upper limit is available: $M_p < 3.510\ M_J$. The details of the system are summarised in Table 1. In Fig. 1 our target can be contextualised among the other known ultra-hot Jupiters. MASCARA-2b orbits around the second hottest host star of the UHJ population, although its equilibrium temperature is typical for UHJs. Given that the effective temperature of MASCARA-2 is larger than WASP-18, the effect of thermal ionisation of the day-side can be expected to be stronger for MASCARA-2b/KELT-20b due to a stronger irradiation by the host star.

Table 1. Physical and orbital parameters of MASCARA-2b.

Description	Symbol	Value
Stellar parameters		
Identifiers	–	KELT-20, HD 185603
V-band magnitude	m_V	7.6
Effective temperature	T_{eff}	8980^{+90}_{-130} K
Projected rotation speed	$v \sin i_\star$	114 ± 3 km s^{-1}
Surface gravity	$\log g$	4.31 ± 0.02 cgs
Metallicity	[Fe/H]	-0.02 ± 0.07
Stellar mass	$M_\star$	$1.89^{+0.06}_{-0.05}\ M_\odot$
Stellar radius	$R_\star$	$1.60 \pm 0.06\ R_\odot$
Planet parameters		
Planet mass [(a)]	M_p	$<3.510\ M_{Jup}$
Planet radius	R_p	$1.83 \pm 0.07\ R_{Jup}$
Equilibrium temperature	T_{eq}	2260 ± 50 K
Surface gravity [(a)]	$\log g_P$	<3.460 cgs
System parameters		
Right ascension	–	$19^h38^m38.73^s$
Declination	–	+31°13'09.2"
Epoch	T_c	$2457909.5906^{+0.0003}_{-0.0002}$ BJD
Period [(a)]	P	3.4741070 ± 0.0000019 days
Transit duration [(a)]	T_{14}	$0.14882^{+0.00092}_{-0.00090}$ days
Ingress/Egress duration [(a)]	τ	$0.01985^{+0.00082}_{-0.00079}$ days
Semimajor axis [(a)]	a	$0.0542^{+0.0014}_{-0.0021}$ AU
Inclination [(a)]	i	$86.15^{+0.28}_{-0.27}$ deg
Eccentricity	e	0 (fixed)
Systemic velocity	γ	-21.07 ± 0.03 km s^{-1}
Projected obliquity	λ	0.6 ± 4 deg

References. [(a)]From Lund et al. (2017). All the remaining parameters are taken from Talens et al. (2018).

Due to its brightness and the fast rotation of the host star, MASCARA-2b is an ideal target for transmission spectroscopy. Its atmosphere is previously studied in Casasayas-Barris et al. (2018), where only the first HARPS-North transit on 16 August 2017 was analysed, finding evidence of Hα and NaI absorption features and noisy features at Hβ position. Here, combining four transits, we achieve higher signal-to-noise ratio (S/N) as we are able to clearly distinguish the centre-to-limb variation (CLV) and the Rossiter-McLaughlin effect (RME), whose treatment will become very important for atmospheric studies of this kind of planets when observing with ESPRESSO-like facilities.

This paper is organised in seven sections. In Sect. 1 we present a general introduction of transmission spectroscopy and ultra-hot Jupiters. In Sect. 2 we detail the observations. Methods to extract the colour-photometry light curves and high resolution transmission spectra are explained in Sect. 3. In Sect. 4 we explain how the CLV and RME are modelled. In Sect. 5 we present the results obtained in the analysis of high resolution transmission spectra. The analysis of the systematic effects are presented in Sect. 6 and the conclusions in Sect. 5.

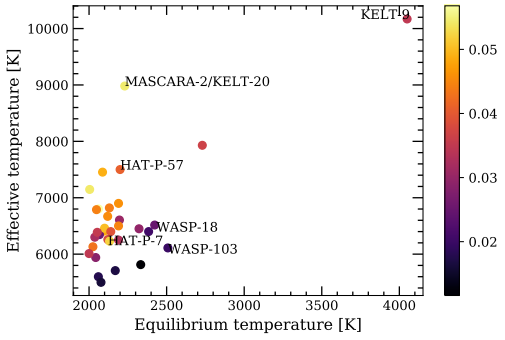

Fig. 1. Ultra-hot Jupiters sample from `exoplanets.eu`. This sample corresponds to all confirmed planets with equilibrium temperatures larger than 2000 K, which have been detected via radial-velocity or transits methods. In the horizontal axis we show the equilibrium temperature of the planet, and in the vertical axis the stellar effective temperature. The semi-major axes of the systems are colour-coded in the side bar (in AU). Some names of UHJs' host stars mentioned in this paper are shown as reference.

2. Observations

We observed a total of four transits of MASCARA-2b using the HARPS-N and CARMENES high resolution spectrographs. One of these transits was simultaneously observed with the Multicolour Simultaneous Camera for studying Atmospheres of Transiting exoplanets 2 (MuSCAT2), a four-colour simultaneous imager, in order to monitor possible stellar activity. One additional epoch was observed with MuSCAT2 to reproduce the results of the first observation. Details of the observations can be found in Table 2 and Fig. 3.

2.1. HARPS-N observations

We observed three transits of MASCARA-2b using the HARPS-North spectrograph mounted on the 3.58-m TNG telescope, located at the Observatorio del Roque de los Muchachos (ORM, La Palma). The observations were on 16 August 2017, 12 and 19 July 2018. For the two last observations we used the GIARPS mode, which permits simultaneous high resolution spectroscopy observations in the near-infrared and in the optical wavelength regions, using GIANO-B and HARPS-North, respectively.

We exposed continuously before, during and after the transit, using the fibre A on the target and fibre B on the sky in order to monitor possible sky emissions. For the first and second night we used an exposure time of 200 s while in the third night we increased it to 300 s, to obtain a higher S/N.

2.2. CARMENES observations

One more transit was observed with Calar Alto high-Resolution search for M dwarfs with Exoearths with Near-infrared and optical Echelle Spectrographs (CARMENES) spectrograph located at the Calar Alto Observatory, on 23 August 2017. The strategy of these observations was the same as with HARPS-North. For these observations an exposure time of 192 s was used, obtaining a S/N of around 100 near the Hα line.

2.3. Photometric observations with MuSCAT2

The transit of MASCARA-2b on 12 July 2018 was observed simultaneously using MuSCAT2 (Narita et al. 2019) located at the 1.52 m Carlos Sánchez Telescope (TCS) at the Teide Observatory. Another transit on 30 September 2018 was observed using MuSCAT2 only. Both observations were heavily defocussed to avoid saturation. While the first observation covered the whole transit event, the second observation had to stop at ~43 min after the mid-transit point due to low elevation of the target. Both nights were mostly clear. Although defocussed, the profile of point spread function (PSF) was not stable for either of the two observations. The observing log is presented in Table 2.

3. Methods

In this section we present the data processing applied to extract the four colour light curves observed with MuSCAT2 (photometry) and the transmission spectra using the high resolution observations (spectroscopy).

3.1. Photometry

Two independent approaches were used for the MuSCAT2 photometry, light curve detrending, and transit modelling to search for possible spot-crossing events. The first approach uses the dedicated MuSCAT2 photometry and transit modelling pipeline: the photometry follows the standard aperture photometry practices, the transit modelling is carried out with `PyTransit` (Parviainen 2015) and the priors for the quadratic limb darkening coefficients are calculated using `LDTk` (Parviainen & Aigrain 2015). The final transit light curve modelling was carried out jointly for the two nights and all passbands, using a Gaussian process (GP) based systematics model calculated with `george` (Ambikasaran et al. 2015) with the sky level, airmass, seeing, and CCD centroid shifts as co-variates.

Our second approach followed closely the approach described in Chen et al. (2014). The photometry was carried out with the DAOPHOT package in the NASA IDL Astronomy User's Library, the transit modelling was done with `batman` (Kreidberg 2015), `Celerite` (Foreman-Mackey et al. 2017) was used to implement a Gaussian process-based systematics model, and the method by Espinoza & Jordán (2015) was used to obtain priors on the quadratic limb darkening coefficients.

In both cases, `emcee` (Foreman-Mackey et al. 2013) was used to estimate the model parameter posteriors. The parameter posterior estimates are presented in Table 3, and the MuSCAT2 light curves are shown in Fig. 2. The transit light curves do not feature evident spot-crossing events, nor do they show significant colour-dependent depth variations.

3.2. Spectroscopy

The observations were reduced with the HARPS-North Data reduction Software (DRS), version 3.7. The DRS extracts the spectra order-by-order, which are then flat-fielded using the daily calibration set. A blaze correction and the wavelength calibration are applied to each spectral order and, finally, all the spectral orders from each two-dimensional echelle spectrum are combined and resampled into a one-dimensional spectrum. The resulting one-dimensional spectra cover the optical range between 3800 and 6900 Å and has a wavelength step of 0.01 Å. The spectra are referred to the Baricentric rest frame and the wavelengths are given in the air.

All nights present stable seeing at ~1 arcsec with the Moon at more than 90 deg from our target. HARPS-N Night 1 and CARMENES observations are observed to be very stable in terms of S/N during the night. For Night 2 and 3, however,

Table 2. Observing log of the MASCARA-2b transit observations.

Night	Tel.	Instrument	Date of observation	Start UT	End UT	Filter	T_{exp} (s)	N_{obs}	Airmass	Aperture (px)
1	TNG	HARPS-N	2017-08-16	21:21	03:56	–	200	90	1.089→1.001→2.089	Spec.
2	TNG	GIARPS	2018-07-12	21:27	05:15	–	200	116	1.604→1.001→1.527	Spec.
3	TNG	GIARPS	2018-07-19	21:25	04:23	–	300	78	1.442→1.000→1.389	Spec.
4	CA 3.5 m	CARMENES	2017-08-23	21:09	02:36	–	192	74	1.012→1.006→1.903	Spec.
2	TCS	MuSCAT2	2018-07-12	23:49	05:41	g	0.7	3365	1.066→1.001→1.767	14,23,29
2	TCS	MuSCAT2	2018-07-12	23:49	05:41	r	0.9	3262	1.066→1.001→1.767	14,14,23
2	TCS	MuSCAT2	2018-07-12	23:49	05:41	i	0.9	3205	1.066→1.001→1.767	15,23,29
2	TCS	MuSCAT2	2018-07-12	23:49	05:41	z_s	0.9	3117	1.066→1.001→1.767	14,14,23
5	TCS	MuSCAT2	2018-09-30	20:16	00:30	g	2	2321	1.002→1.001→1.801	29,32,37
5	TCS	MuSCAT2	2018-09-30	20:16	00:30	r	2	2322	1.002→1.001→1.801	27,32,37
5	TCS	MuSCAT2	2018-09-30	20:16	00:30	i	4	2322	1.002→1.001→1.801	28,30,35
5	TCS	MuSCAT2	2018-09-30	20:16	00:30	z_s	10	1320	1.002→1.001→1.801	29,36,40

Table 3. Best-fit parameters from MuSCAT2 transit light curve.

Parameter	Symbol	Units	Value
Transit epoch	T_0	BJD [(a)]	$2\,457\,503.120120 \pm 0.00018$
Period	P	days	$3.47410196 \pm 0.00000106$
Inclination	i	deg	85.61 ± 0.19
Radius ratio	$R_p/R_\star$	–	0.1176 ± 0.0014
	$(R_p/R_\star)^2$	–	0.01382 ± 0.00033
Semimajor axis	$a/R_\star$	–	7.254 ± 0.096
Mid-transit 1 [(b)]	T^1_{mid}	BJD	$2\,458\,312.58566 \pm 0.00022$
Mid-transit 2 [(c)]	T^2_{mid}	BJD	$2\,458\,392.48932 \pm 0.00042$

Notes. [(a)]All times are given in BJD TDB. [(b)]Mid-transit time of 12 July 2018. [(c)]Mid-transit time of 30 September 2018.

we noticed variable S/N and variations of the continuum similar to a bad blaze function correction. This was caused by a problem with the Atmospheric Dispersion Corrector (ADC) of the telescope, that causes PSF distortions and variations of the continuum. For both these nights, re-reducing the data with the DRS did not produce any improvement. Our method for correcting this variation is discussed in detail in Sect. 5.1. On the other hand, during the Night 2 we observe a drop in the S/N of some spectra before the transit, possibly caused by the presence of a cloud. We discarded the spectra from 22:58 UT until 23:24 UT (eight spectra), where the S/N is lower than 35 (around 6600 Å). Additionally, for consistency with the S/N established for the cloud region, for this night we also removed the spectra taken at 01:28UT which also present S/N smaller than 35 (i.e. a total of nine spectra are discarded).

CARMENES observations are processed with the CARMENES pipeline CARACAL (CARMENES Reduction And Calibration; Caballero et al. 2016), which considers bias, flat-relative optimal extraction (Zechmeister et al. 2014), cosmic ray correction, and a wavelength calibration described in Bauer et al. (2015). The reduced spectra are referred to the terrestrial rest frame and the wavelengths are given in the vacuum. At the beginning of the night some technical problems lead to some very short time exposures with very low S/N which are directly discarded. The spectra, S/N and airmass evolution of each night can be observed in Fig. 3.

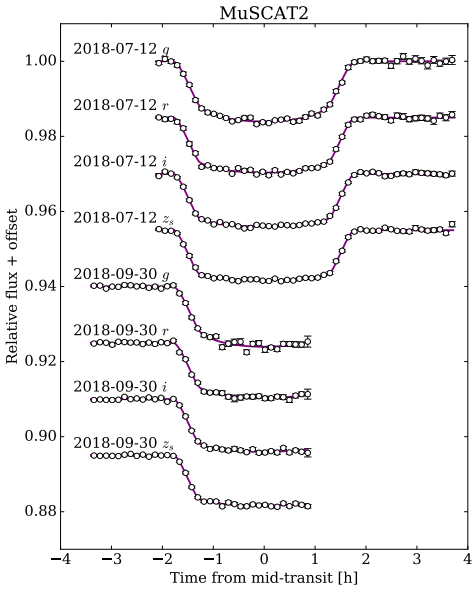

Fig. 2. MASCARA-2b transit light curves obtained with MuSCAT2. The data have been binned to 7.2 min intervals for display clarity.

3.2.1. Telluric correction

Taking advantage of the fact that the observations were carried out using fibre B monitoring the sky, we checked for possible atmospheric emissions features during the night. We observed no telluric emission feature needing to be corrected, and since subtracting the sky to the target spectra introduces additional noise, we did not apply this correction.

Following Allart et al. (2017), we corrected the telluric absorption contamination using version 1.2.0 of `Molecfit` (Smette et al. 2015 and Kausch et al. 2015). `Molecfit` is an ESO tool built to correct Earth atmospheric features in ground-based spectra, which uses a line-by-line radiative transfer

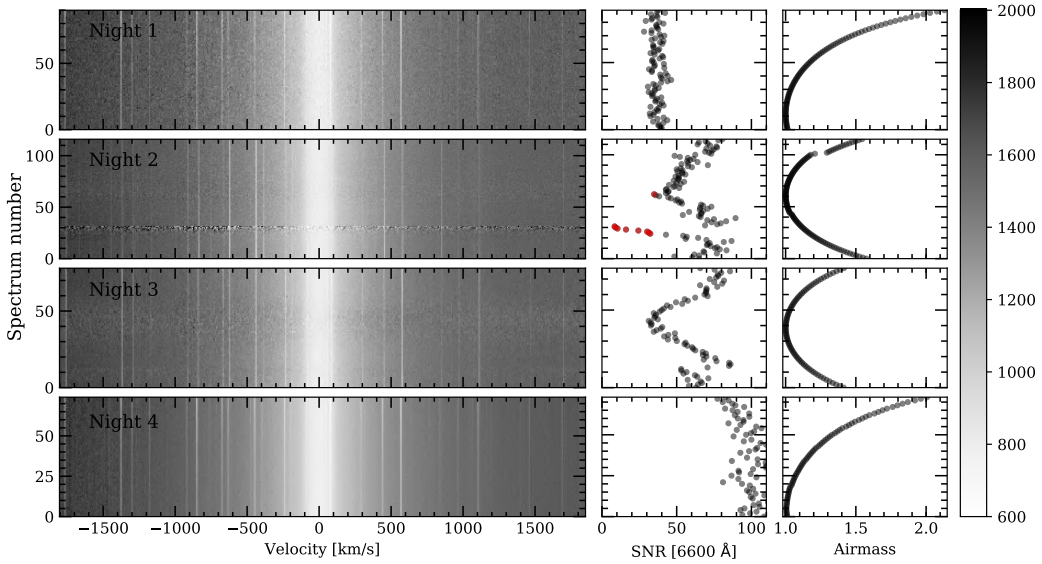

Fig. 3. Observed spectra around the Hα line (*left column*), for Night 1 (*first row*), Night 2 (*second row*), Night 3 (*third row*) and Night 4 (*fourth row*). The three first nights were observed with HARPS-N and the last night, with CARMENES. The spectra are normalised to the same continuum level (see colour bar) and moved to the stellar rest frame. In the *y*-axis we show the spectrum number starting from zero and in the *x*-axis the velocity in km s^{-1}. The narrow lines correspond to telluric contamination and the deepest central line (at 0 km s^{-1}) corresponds to the centre of the Hα line core. *Second and third columns*: S/N and the airmass variation during the night, respectively. The S/N per pixel is extracted in the continuum near the Hα line, specifically around 6600 Å as the Hα line for this target is very broad due to its rapid rotation. The red S/N values correspond to the spectra which are not considered in our analysis. In particular, we observe a stable S/N during Night 1. Night 2 shows a drop in the S/N for the presence of a cloud around spectrum number 25 and two stops of the instrument around spectrum number 50 and 100 because GIANO-B suddenly aborted itself and it was necessary to restart the exposure with both the HARPS-N and GIANO-B instruments.

model (LBLRTM). HARPS-North spectra are given in the solar system baricentric rest frame, while Molecfit models are computed in the terrestrial rest frame. For this reason, before fitting the telluric contamination we shifted the spectra to the terrestrial rest frame using the baricentric Earth radial velocity (BERV) information. We shifted the spectra using the IRAF (Tody 1986) routine `dopcor`. The parameters used to compute the high-resolution telluric spectrum are detailed in Allart et al. (2017), and the wavelength regions with strong lines used here are very similar to those used in that paper, but considering only those regions out of stellar features.

In the case of CARMENES data, the spectra after CARACAL reduction are already given in the terrestrial rest frame. The `Molecfit` correction applied is slightly different, and follows the method discussed in Nortmann et al. (2018) and Salz et al. (2018). The telluric uncorrected and corrected spectra in the atomic sodium (NaI) region for Night 4 obtained with CARMENES are shown in Fig. 4.

3.2.2. General transmission spectrum extraction

Once the telluric correction has been applied, we cut the spectra in the wavelength region we want to study and normalise them by the continuum. This is done recursively over the whole spectral range covered by both spectrographs to screen for all possible planetary signals. Then, as the spectra after the `Molecfit` correction is referred to the terrestrial rest frame, we shifted them to the stellar rest frame considering the system velocity (γ) and the BERV information. The stellar reflex motion is not considered because the mass of the planet (M_p) has not yet been determined, and the radial velocity measurements in rapid-rotating stars are difficult to determine. If we assume K_s = 322.51 m s^{-1} (i.e. the mass upper limit M_p = 3.510 M_J; Lund et al. 2017), the maximum stellar radial-velocity change is $\sim \pm 0.3$ km s^{-1}. Since one pixel in HARPS is around 0.8 km s^{-1} and the stellar lines present a large broadening caused by the fast stellar rotation, considering or not considering this reflex motion contribution to the radial velocity correction does not have any significant impact to the results, as presented in Casasayas-Barris et al. (2018). In addition, the spectra could be also affected by stellar activity and instrumental radial-velocity drifts. However, an A-type star like MASCARA-2 is not expected to be active, and the instrumental effects would similarly affect to all spectra, resulting in global wavelength offsets from the rest frame position (which after the daily calibration are expected to be of the order of 10 m s^{-1} for the instruments used here). For CARMENES observations, when shifting the spectra to the stellar rest frame, we rebinned the data to the same wavelength grid using the IDL routine `rebinw` from the `PINTofALE` package, which ensures flux conservation (Drake & Kashyap 2010).

For the next steps, we followed Wyttenbach et al. (2015): we computed the out-of-transit master spectrum (combination of all the stellar spectra taken when the planet is not transiting) and we then divided each spectrum by this master spectrum to remove the stellar lines. The resulting residuals contain the variations of

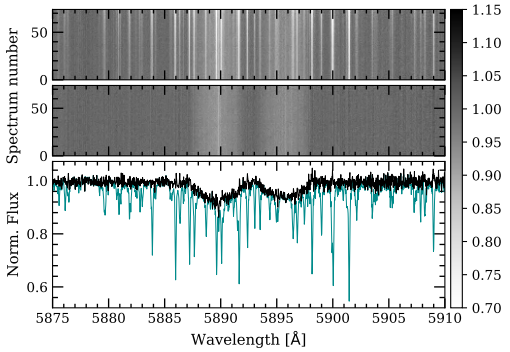

Fig. 4. Telluric correction of CARMENES observations (Night 4) of MASCARA-2b in the NaI doublet region. *Top panel*: observed spectra before the telluric correction; *second panel*: spectra after correcting the telluric contamination with `Molecfit`. For these two panels the *y*-axis corresponds to the spectrum number, the *x*-axis to wavelength in Å, and the normalised flux is shown in the colour bar. *Third panel*: one single spectrum before (blue) and after (black) the telluric correction. The narrow lines observed in the *first and third panels* are telluric lines, while the broad lines centred at 5890 and 5896 Å are the stellar sodium lines. In the *second panel*, where the telluric lines have been subtracted, we observe the interstellar sodium in the centre of the stellar lines and, additionally, the planetary shadow (Rossiter–McLaughlin effect) as a trail moving into the lines. The spectra are presented in the terrestrial rest frame.

the stellar lines profile produced by the presence of the planet and additional systematic effects. These variations include the absorption produced by the exoplanet atmosphere, the CLV and the RME. At this step we find the best-fit model of the absorption, CLV and RME, and the resulting best-fit parameters are used to compute the best-fit CLV and RME model, which is then removed from the residuals (see Sect. 4 for a detailed explanation of the models). Once these effects had been corrected, we shifted the remaining residuals to the planet rest frame and we then combined the in-transit residuals to find the transmission spectrum for each night.

HARPS-N Night 2 and Night 3 are affected by an ADC problem, presenting weird continuum variations similar to a bad blaze function correction. In order to solve this problem, we tried to re-reduce the raw data with the DRS pipeline, without any improvement. This effect introduces differences in the line wings changing in time, and which are more significant in very broad spectral lines, specially in the Hα line. These differences become very important after dividing the spectra by the out-of-transit master spectrum, as the resulting spectra present broad variations that partially hide the narrow residuals we are looking for behind this broad effect. For this reason, after computing the spectra of residuals we applied a very broad median filter using `medfilt` from `scipy` library with a kernel size of 1505 to protect the planetary signals from being diluted and remove only the low frequency variations produced by the variation of the continuum, and the final transmission spectrum was normalised with `UnivariateSplines` from `scipy` in order to remove remaining undulations. This additional correction is only applied to HARPS-N Night 2 and Night 3. Finally, we note that the parameters used during the whole process are those presented in Table 1 except for the epoch (T_0), orbital period (P), and inclination (i), which are from the recalculated parameters of Table 3.

4. Modelling and fitting the CLV and RME

The Rossiter–McLaughlin effect (RME) strongly affects the stellar lines profile of a fast-rotating star such as MASCARA-2b, which has a $v \sin i = 114$ km s^{-1}. As the transit progresses, the light from different regions of the stellar disc is blocked by the planet, producing a lack of flux in different parts of the stellar lines which depends on the geometry of the system. On the other hand, the centre-to-limb variation (CLV) also affects the stellar lines profile (Czesla et al. 2015), which becomes broader and/or deeper than the integrated flux spectrum depending on the stellar properties of the region obscured by the planet.

The stellar spectrum is modelled using `VALD3` (Ryabchikova et al. 2015) line lists and Kurucz `ATLAS9` models, computed with `Spectroscopy Made Easy tool` (SME; Valenti & Piskunov 1996). As presented in Yan et al. (2017), using `SME` we computed the stellar spectrum at 21 different limb-darkening angles (μ) without considering the rotation broadening. For the stellar model computation we used the local thermodynamic equilibrium (LTE) and solar abundance for the hydrogen lines. For the NaI, the solar abundance model strongly differs from the data. For this reason, we fitted the NaI abundance using the `SME` tool. In this process, the spectra used to fit the abundance is the combination of all the out-of-transit data of Night 4 with CARMENES, which have higher S/N. After checking the fitted [Na/H] results for a range of [Fe/H] values from literature ([Fe/H]= -0.02 ± 0.07 in Talens et al. 2018) we noticed that the NaI abundance changes significantly when varying the [Fe/H] value (see below). The most reasonable NaI abundance is obtained in the $1-\sigma$ upper limit value, that is, assuming [Fe/H] = + 0.05 finding [Na/H] = 0.98. As we do not consider non-LTE effects that could be important in this stellar type (Kubát & Korcáková 2004). These [Fe/H], [Na/H] values together with the parameters given in Table 1 are those used to compute the stellar models. We note here that for our computation of these models, we need a good description of the line profile and the actual abundance value is not the focus of our analysis. The maximum relative difference obtained between models when assuming [Fe/H]= −0.29 (Lund et al. 2017) (for which we obtain the [Na/H] = 1.39) or [Fe/H] = +0.05 ([Na/H] = 0.98) is ∼0.08%.

We divide, then, the stellar disc in cells of size 0.01 $R_\star \times 0.01\ R_\star$. Each of these cells contain its own properties, such as the rotation velocity due to $v \sin i$, which depends on its distance to the stellar rotation axis (i.e. the spin-orbit angle, λ), its μ angle value, and could be obscured by the planet at a given time. At the time of each exposure it is possible to compute the position of the planet in the stellar disc using `EXOFAST` (Eastman et al. 2013) and compute the integrated stellar disc flux considering the obscured cells, their proper radial velocity shift caused by the rotation and the correspondent μ spectrum (which are linearly interpolated using the 21 μ angle reference spectra). The only difference between the HARPS-N and CARMENES modelled spectra is the spectral resolution, $\mathcal{R}$ = 115 000 and $\mathcal{R}$ = 94 600, respectively.

The modelled stellar spectra at different orbital phases depend on the geometry of the system but also the planetary radius, R_p. For a particular wavelength, and depending on the amount of material, the atmosphere becomes opaque at a given pressure level or radius of the planet, R_λ. In order to consider this radius change when fitting the data, the modelled stellar spectra is computed for a grid of R_λ, increasing from 0.7 R_p (1 R_p = 1.83 R_J; Talens et al. 2018) to 2.5 R_p in steps of 0.1 R_p. For a given R_λ, we then calculated the stellar spectrum by

linearly interpolating these grid of models. Finally, the modelled residuals were computed dividing all the modelled stellar spectra by the out-of-transit model.

Finally, and similarly to Yan & Henning (2018), in the modelled in-transit residuals we add a Gaussian profile to describe the absorption of the planet. This profile, depends on the centre of the Gaussian (v_0), the full width at half maximum (FWHM) and constrast (h). The centre position is defined as $v_0 = v_p + v_{\rm wind}$ where $v_p = K_p \sin(2\pi\varphi)$ is the planet radial velocity in each in-transit exposure time (φ is the orbital phase) and $v_{\rm wind}$ is the radial velocity of the atmospheric wind.

With this, we performed a Markov chain Monte Carlo (MCMC) analysis to fit the observed residuals using `emcee` (Foreman-Mackey et al. 2013) code. The free parameters are R_λ, h, $v_{\rm wind}$, K_p, and FWHM. We used 14 walkers and 1×10^5 steps. The best-fit R_λ value was used to compute the CLV and RME model, which was then subtracted from the data, leaving only the true planetary absorption remaining. Before combining the data residuals, this absorption was shifted to the planet rest frame using the best-fit K_p value. The MCMC analysis is based on binned spectra (0.05 Å and 0.002 orbital phase bins) and only applied to the fully in-transit data (i.e. excluding the ingress and egress). The planetary absorption spectrum in the ingress and in the egress could present different geometries (Yan & Henning 2018), as shown in Salz et al. (2018).

During the modelling, we observed that in some cases the best-fit value of R_λ is smaller than 1 $R_{\rm p}$. This is possibly due to the intrinsic error of the stellar models, which are computed considering LTE and solar abundance in case of the hydrogen lines (the NaI abundance is fitted). The non-LTE effects in these stellar-types can become strong (Kubát & Korcáková 2004) and, as calculated previously, the abundance of the lines also influences the final model. For two different values of [Fe/H] inside the error bars presented in Lund et al. (2017) and Talens et al. (2018), we can obtain the same intensity of the RME for two different R_λ. Additionally, if we compare two models computed with the same abundance, one calculated for 0.85 $R_{\rm p}$ and one for 1.0 $R_{\rm p}$, in the mid-transit time their relative difference in the RME centre is ~0.2%. Thus, there are different assumptions that can produce variations of the final $R_{\rm p}$ values. However, our main goal here with the model fitting is to remove the strong RME and CLV effects, which are easily observed in the residuals. For this reason, considering the $R_{\rm p}$ change permits us to find the best model that reproduces the effects, even if the best-fit R_λ value is not exactly that expected. This is one of the reasons we have not linked the increase of radius (R_λ) with the absorption that we measured (h) in the models, and we left both free, independently. We do not expect these R_λ values to have any effect on our results and we used the models as a tool to discard the RME and CLV effects from the absorption signatures. When comparing models, we observe that in the mid-transit time the RME is more constraining for the R_λ parameter. In the ingress and egress regions, where the CLV becomes important, both the CLV and RME are constraining R_λ. However, we stress that only the fully in-transit data is used in the fitting procedure, in other words, the location at which the RME most constrains the R_λ parameter.

5. Results

We present here the results obtained in the different wavelength regions. In all cases, we have analysed each individual night separately and, additionally, the three HARPS-N data together, sorting the spectra in time from the mid-transit centre. We note that in this latter case all the spectra were telluric-corrected first.

Here, we show the 2D maps of the final residuals obtained after applying the differential spectroscopy, the final transmission spectrum and the transmission light curves around several spectral lines detectable in MASCARA-2b's transmission spectrum. The 2D maps of individual nights are presented in the Appendix A (Figs. A.1–A.5), their best-fit values in Table B.1 and MCMC correlation diagrams in Appendix D (Figs. D.1–D.7). All light curves are also presented in Appendix C (Figs. C.1–C.6). The absorption depth values measured in the transmission spectra and light curves can be found in Table B.2.

The transmission light curves were obtained by calculating the equivalent width of the residuals after dividing each spectrum by the master out-of-transit spectrum, and then moved to the planet rest frame. The integration to obtain the equivalent width was computed using the `scipy` library (Jones et al. 2001) from `Python2.7`.

In tables and figures hereafter, we refer to the different nights as HARPS-N 1 (Night 1), HARPS-N 2 (Night 2), HARPS-N 3 (Night 3) and CARMENES 1 (Night 4) to avoid confusion between instruments. The combined results of all three HARPS-N nights are presented as HARPS-Nx3.

5.1. Hα

The residuals after computing the ratios of each spectra respectively to the master out-of-transit spectrum, the best-fit models and the transmission spectra around Hα (6562.81 Å) of each individual night can be observed in Fig. 5. The best-fit values and the 1-σ error bars obtained with the MCMC analysis are presented in Table 4.

In Fig. 5 we can see that the three nights observed with the HARPS-N are, in general, more noisy than the night observed with CARMENES, with residuals showing larger standard deviation. No obvious reason for this fact can be derived from checking the weather or seeing logs, only the ADC problem in HARPS-N Nights 2 and 3 are noticeable. During the transit, the RME is observed as a red trail (positive relative flux) moving in the ± 114 km s^{-1} ($v \sin i$) range of velocities and the absorption as a blue trail (negative relative flux) around ± 24 km s^{-1}, approximately.

Due to the noise, specially for Nights 2 and 3 for which it increases during the transit, we are not able to totally fit the planetary absorption for the HARPS-N nights, which becomes underestimated by the model, and cannot be recovered in the region were it intersects with the RME around mid-transit. However, for Night 4 where the S/N is higher, the absorption during the whole transit is recovered. In particular, this underestimation of the absorption can be observed in the residuals of the Gaussian profiles derived from the best-fit model, which seem to present smaller contrast (h) than the absorption observed in the transmission spectrum of HARPS-N (see fourth and fifth row of Fig. 5). When we fit all HARPS-N data together (see Fig. 6), the central absorption still remains within the noise level and the absorption is slightly underestimated. This is possibly caused by the decrease in S/N during the transit. We also analysed the HARPS-N data considering only Nights 1 and 3, with results closer to those obtained for CARMENES in Night 4 but the mid-transit region still remains within the noise level. The final transmission spectra of CARMENES 1 and the analysis combining all three HARPS-N nights, together with the Gaussian profiles derived from the best-fit parameters, can be observed in Fig. 7.

The observed transmission light curves before and after correcting the CLV and RME effects can be observed in Fig. 8. The models are also obtained with the best-fit parameters from

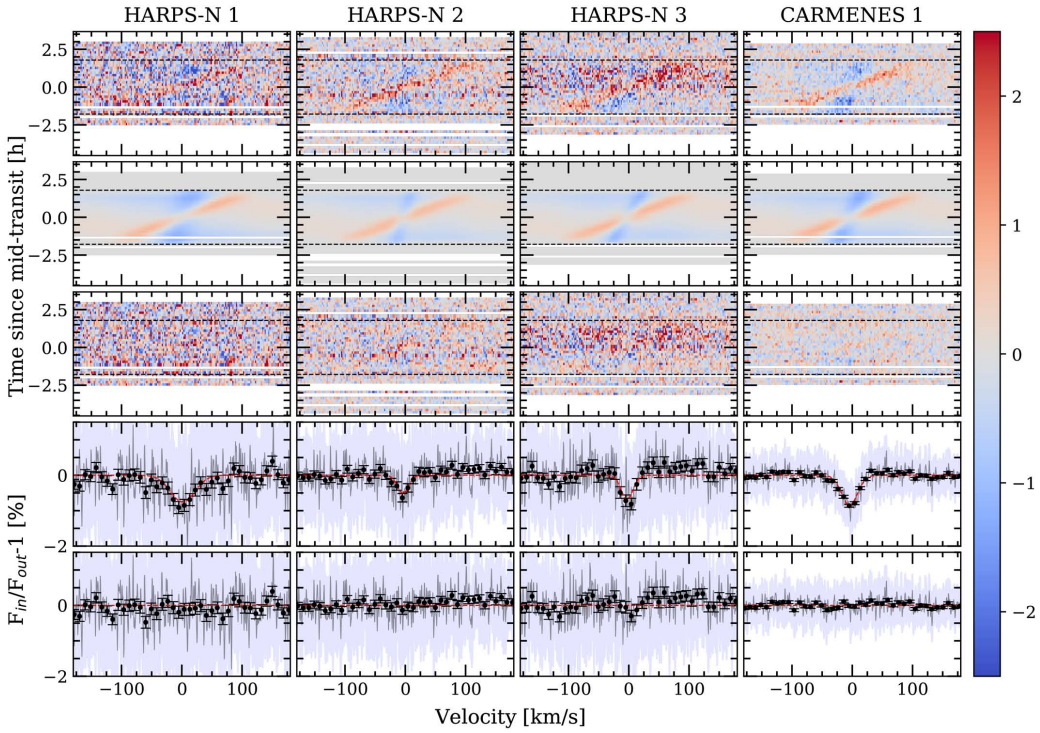

Fig. 5. Results of the Hα line analysis of MASCARA-2b. Each column corresponds to one night. *First row* ,*top*: residuals after dividing each spectrum by the master-out spectrum. *Second row*: best-fit model describing the first panel residuals, including absorption, CLV and RME. *Third row*: residuals after subtracting the best-fit model (*second row*) to the data (*first row*). *Fourth row*: transmission spectrum obtained when combining the in-transit residuals from fourth row in the planetary rest frame. The black dots show the transmission spectrum binned in 0.2 Å intervals and the propagated errors from the photon noise. Light blue shows the standard deviation of the residuals from fourth row. The red lines show the Gaussian profile derived from the best-fit parameters of second row. *Fifth row*: residuals after subtracting the Gaussian profile to the transmission spectrum. In all cases the residuals (rows from 1st to 3rd) are binned in intervals of 0.002 in orbital phase and 0.05 Å in wavelength. The relative flux (F_{in}/F_{out} −1) in % is shown in the colour bar. In white we show the time regions for which we have no information. The horizontal lines show the first and last contact times of the transit.

the general fitting shown in Fig. 5. In these light curves the RME effect and the time regions where the noise is higher can be clearly observed. The error bars are obtained by the error propagation from the photon noise. In order to include the ingress and egress shape of the transmission model we used the `PyLDTk` (Parviainen & Aigrain 2015) and the `PyTransit` (Parviainen 2015) Python packages. The `PyLDTk` estimates the limb-darkening coefficients for a given filter and stellar properties using the library of `PHOENIX` stellar atmospheres (Husser et al. 2013). Then, `PyTransit` allows us to obtain the transit shape with the same absorption (h) measured during the fitting procedure and the limb-darkening coefficients assumed from `PyLDTk`.

The absorption that we measure from the best-fit model in the line core is $0.85 \pm 0.03\%$ for CARMENES data and $0.68 \pm 0.06\%$ for HARPS-N data combined, meaning an effective radius ($R_\lambda(h)$) of $\sim 1.20\, R_p$ as presented in Casasayas-Barris et al. (2018) where only HARPS-N Night 1 was available. We measure a mean standard deviation of 1.3 and 2.3% in the residuals and a S/N of ∼350 and ∼300 around the Hα position (± 180 km s^{-1}) for CARMENES and HARPS-Nx3 analysis, respectively. We note that the results from both instruments are not totally consistent, as explained above. HARPS-N Night 1 and CARMENES observations are the most stable nights, with consistent values, while HARPS-N Nights 2 and 3 present S/N variations during the transit that are then propagated to the final result when combining all three HARPS-N nights. These two nights, especially Night 3, present strong S/N variations during the observation due to the ADC problem. Although this effect is mainly removed during the analysis, in this process we apply additional steps that could introduce small over-corrections and cause variation of the final absorption level in these two nights. On the other hand, for these nights, the RME is not totally removed (see transmission light curves in Fig. 8), and when combining the mid-transit signals we were averaging regions with RME residuals that decrease the absorption depth.

The differences observed in the effective radius values obtained when fitting the CLV and RME models (R_λ) to the 2D residual maps and those derived from the absorption in the core of the lines (R_λ (h)) are possibly caused by intrinsic errors of the models. In particular, in the case of hydrogen atoms, we considered solar abundance and LTE, but for

Table 4. Best-fit parameters and 1-σ error bars from the MCMC analysis of the Hα line for each individual night and combined HARPS-N observations.

	h (%)	$FWHM$ (km s^{-1})	K_p (km s^{-1})	$v_{\rm wind}$ (km s^{-1})	$R_\lambda^{(a)}$ ($R_{\rm p}$)	$R_\lambda\,(h)^{(b)}$ ($R_{\rm p}$)
HARPS-N 1	$-0.75^{+0.10}_{-0.11}$	$34.9^{+7.7}_{-6.4}$	$140.3^{+39.0}_{-42.1}$	$1.3^{+3.0}_{-2.9}$	$1.21^{+0.04}_{-0.05}$	$1.24^{+0.06}_{-0.06}$
HARPS-N 2	$-0.52^{+0.10}_{-0.11}$	$15.6^{+3.7}_{-3.9}$	$101.5^{+33.7}_{-33.5}$	$-3.9^{+2.1}_{-2.4}$	$1.08^{+0.03}_{-0.03}$	$1.17^{+0.06}_{-0.07}$
HARPS-N 3	$-0.69^{+0.10}_{-0.11}$	$16.4^{+2.6}_{-2.4}$	$196.0^{+30.1}_{-32.0}$	$-2.8^{+2.2}_{-2.2}$	$1.15^{+0.04}_{-0.04}$	$1.22^{+0.06}_{-0.06}$
CARMENES 1	$-0.85^{+0.03}_{-0.03}$	$22.6^{+0.9}_{-0.9}$	$166.2^{+7.3}_{-7.4}$	$-4.5^{+0.5}_{-0.5}$	$1.21^{+0.01}_{-0.01}$	$1.27^{+0.02}_{-0.02}$
HARPS-Nx3	$-0.68^{+0.06}_{-0.06}$	$19.0^{+1.7}_{-1.6}$	$165.6^{+16.7}_{-16.6}$	$-3.0^{+1.2}_{-1.2}$	$1.13^{+0.02}_{-0.02}$	$1.22^{+0.04}_{-0.04}$

Notes. $^{(a)}$Effective radius value obtained from the best-fit model of the CLV and RME effects. $^{(b)}$Effective radius calculated considering the absorption value, h, and assuming a continuum level of $(R_{\rm p}/R_\star)^2 = 1.382\%$.

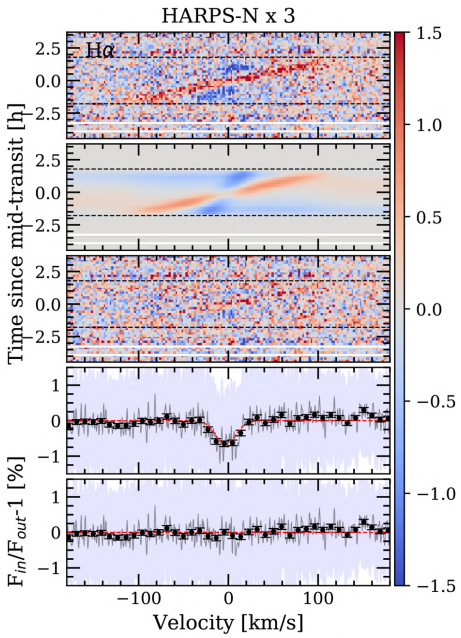

Fig. 6. As Fig. 5 but combining the three nights observed with HARPS-N.

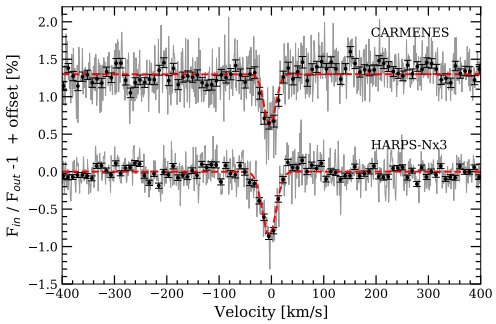

Fig. 7. Transmission spectra around Hα line obtained with all nights of HARPS-N combined and CARMENES data (Night 4), with an offset for a better visualisation. The best-fit Gaussian profiles are shown in red. In grey we show the original transmission spectrum and the black dots show the data binned in 0.2 Å intervals.

MASCARA2 stellar-type we expected the non-LTE effects to become significant (Kubát & Korcáková 2004). There is also the low and variable S/N difficulty added when fitting the data. We can observe that for CARMENES data, which have higher S/N, the RME measurement is better.

We measure, in all cases, a shift of the absorption line with respect to the theoretical position of Hα, which could be indicative of planetary winds. However, as discussed in Sect. 3.2, we did not use the radial-velocity information from the instrument pipeline, and consequently we do not consider possible instrumental offsets in radial-velocity. For this reason, the winds measured here can be influenced by this effect. In all cases, before combining the residuals to obtain the transmission spectrum, we shift these residuals to the planet rest frame using the best-fit K_p parameter of each night. This value has large error bars for the noisiest nights, thus, we checked the differences when combining the spectra with different K_p values within these 1-σ error bars, but only differences inside the noise level are noticeable. From Lund et al. (2017) we estimate that K_p should be about 170 $\pm$ 7 km s^{-1}. We expect all nights and lines present consistent values (within the error bars) close to this estimation, however, caused by irregularities in the maps due to small residuals and the low S/N that makes difficult for the model to distinguish between CLV, RME and absorption regions, the measured K_p values can be far from the expectation for a single night but become consistent after the combination of more nights. Small deviations of these measurements are introduced by the non-corrected reflex motion from the host star.

The absorption depths measured for 1.5 Å passband in the final transmission spectra and light curves are presented in Table 5. We can observe that the results of CARMENES data and the combined HARPS-N nights are consistent, while individual HARPS-N nights give more dispersed values. We also note the slightly different results obtained in the analysis presented here and in Casasayas-Barris et al. (2018) for HARPS-N Night 1. The difference comes because here we are only considering the spectra fully in-transit (the ingress and egress files are not considered when computing the in-transit sample). Additionally, we used different methods of telluric correction, K_p values used

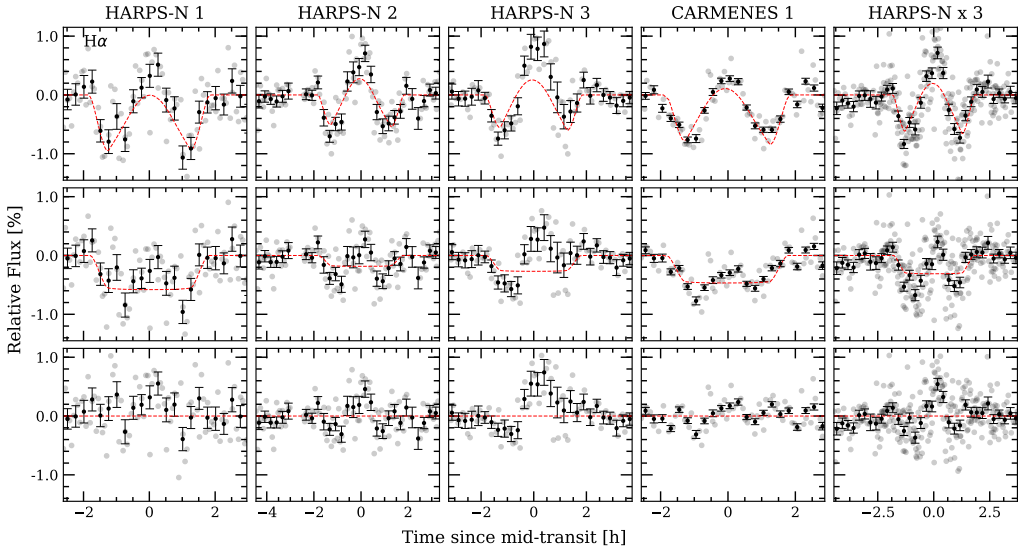

Fig. 8. Hα transmission light curves for 1.5 Å bandwidth. Each column correspond to one night, and the last column (right) to the analysis of all HARPS-N nights together. *First row, top*: observed transmission light curves. These light curves contain the contribution of the CLV, RME and absorption of the planet. The red dashed line shows the best-fit model derived from the fitting procedure of the residuals from Fig. 5. *Second row*: Hα transmission light curve after removing the CLV and RME. In red we show the best-fit absorption model. *Third row*: residuals between the model and the data. In all cases the grey dots are the original data points, in black we show the data binned by 0.003 orbital phase. We note the different x-scale of the different columns, as different nights present different time extension.

when shifting the spectra to the planet rest-frame, and slightly improved corrections of the CLV and RME effects.

5.2. Hβ and Hγ

The method applied to study the Hβ (4861.28 Å) and Hγ (4340.46 Å) lines is exactly the same as for Hα. In Fig. 9 we present the results for the joint analysis of all nights observed with HARPS-N. The best-fit values are shown in Table 5. We note that CARMENES data do not cover this wavelength range, and thus only HARPS-N data are presented. Same as the Hα line, the models were computed for a grid of [0.7 − 2.5] R_p with 0.1 R_p step.

In Casasayas-Barris et al. (2018) we observe noisy features in the transmission spectrum around the Hβ line analysing only Night 1. Here, with three transits and after correcting the strong CLV and RME, we observe absorption centred at the Hβ laboratory value. We note that some CLV and RME residuals remain after removing the best-fit model (see the residuals in Fig. 9). The absorption is observable in the analysis of the individual nights, except for Night 1 where the MCMC fitting is not able to distinguish between the noise and the absorption, in other words the parameters related to the absorption profile (h, K_p and FWHM) are not well determined. However, when combining all three transits the absorption is well recovered. The absorption measured in this case corresponds to -0.45 ± 0.05% in the line core, which is consistent with the value measured in the transmission light curves during the transit (see Table 5). It is noticeable that the R_λ values that we obtain in the fitting procedure are lower than 1 R_p in some cases.

On the other hand, we find a Hγ absorption of -0.4 ± 0.1% in the line core when combining all nights. However, the

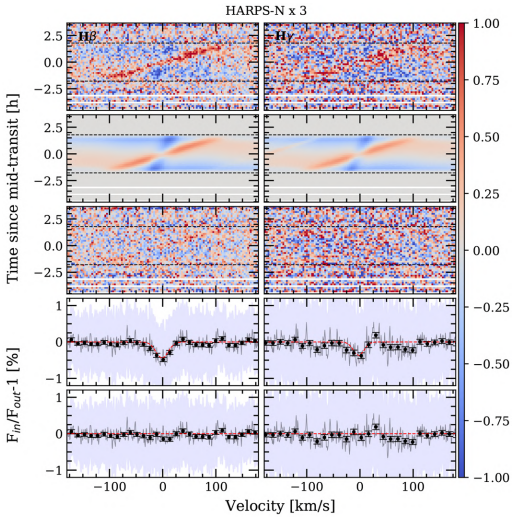

Fig. 9. As Fig. 5, but for Hβ and Hγ lines. The colour bar indicates the flux relative to the continuum (F_{in}/F_{out} −1) in %.

in-transit trail in the 2D maps is not clear, possibly because the signal is less intense and remains partially hidden in the noise. This absorption is only observed when combining all data and in Night 2 when analysing each individual night. Additionally,

Table 5. Summary of the results obtained in the analysis presented here, for the different species and instruments.

		h (%)	$R_\lambda(h)$ (R_p)	v_{wind} (km s^{-1})	$FWHM$ (km s^{-1})	K_p (km s^{-1})	$AD^{1.5Å}_{TS}$ (%)[a]	$AD^{1.5Å}_{TLC}$ (%)[b]	$AD^{1.5Å}_{EMC}$ (%)[c]
Hα	Hx3	-0.68 ± 0.06	1.22 ± 0.04	-3.0 ± 1.2	19.0 ± 1.6	165.6 ± 16.7	0.33 ± 0.05	0.30 ± 0.05	0.36 ± 0.14
	Cx1	-0.85 ± 0.03	1.27 ± 0.02	-4.5 ± 0.5	22.6 ± 0.9	166.2 ± 7.4	0.44 ± 0.04	0.43 ± 0.05	0.40 ± 0.14
Hβ	Hx3	-0.45 ± 0.05	1.15 ± 0.03	-1.2 ± 1.4	19.4 ± 2.5	136.2 ± 18.6	0.13 ± 0.04	0.17 ± 0.04	0.14 ± 0.08
Hγ	Hx3	-0.38 ± 0.08	1.13 ± 0.05	-2.3 ± 2.7	16.6 ± 4.2	135.0 ± 34.8	0.09 ± 0.05	0.07 ± 0.09	0.04 ± 0.09
CaII	Cx1	-0.56 ± 0.05	1.18 ± 0.03	-1.9 ± 0.6	9.2 ± 1.0	157.7 ± 8.2	0.16 ± 0.04	0.14 ± 0.04	0.11 ± 0.09
NaI	Hx3	-0.34 ± 0.05	1.11 ± 0.03	-3.1 ± 0.9	9.2 ± 2.0	176.6 ± 11.7	0.05 ± 0.03	0.08 ± 0.03	0.07 ± 0.05
	Cx1	-0.29 ± 0.04	1.10 ± 0.03	-3.2 ± 0.7	8.0 ± 1.2	182.5 ± 14.3	0.04 ± 0.03	0.03 ± 0.04	0.08 ± 0.08
FeII	Hx3	-0.33 ± 0.05	1.11 ± 0.03	-2.8 ± 0.8	7.2 ± 1.2	174.4 ± 14.0	0.04 ± 0.03	0.01 ± 0.03	0.04 ± 0.04

Notes. Hx3 corresponds to the analysis of three HARPS-N nights combined, and Cx1 to the analysis of the unique transit observed with CARMENES. [a]Absorption depth measured in the transmission spectrum for a 1.5 Å passband. [b]Absorption depth measured in the transmission light curve for a 1.5 Å passband. [c]Centre of the EMC distribution computed for a 1.5 Å passband.

the final transmission spectrum presents some residuals near the line.

In Table 5 we give the absorption depth values measured in the spectra and the transmission light curves of Hβ and Hγ for 1.5 Å passband. The results of each individual night and light curves are presented in Appendices A and C.

5.3. The CaII triplet

The CaII triplet lines are located at 8498.02 , 8542.09 and 8662.14 Å. Only the transit observed with CARMENES (Night 4) was used to analyse these lines, as HARPS-N data do not cover this wavelength range. The telluric contamination observed in this region is low. The second and third lines (ordered in wavelength) are in the limit of two orders meaning that both lines are covered by two different CARMENES orders. The analysis shown here is performed using the orders where these lines are located in a most central region of the order. Although the detection of the lines, at lower S/N, is also possible in the other orders.

In Fig. 10 we show the 2D maps of these lines, where the planetary absorption trail is clear, specially for the second line (λ8542 Å) which is the strongest of the triplet. We measured absorption of 0.52 ± 0.05, 0.60 ± 0.04 and 0.55 ± 0.06% in the lines core, respectively, which correspond to an effective radius of $\sim$1.2 R_P. The transmission spectrum around λ8662 Å show a smaller second absorption peak in the right side of the main absorption feature. Even the telluric contamination is low in this region, it can be caused by a small telluric residual. The transmission light curves of each individual CaII line and the transmission light curve after combining of all three lines (see Appendix C) present consistent absorption depth values in comparison with those measured in the transmission spectra (see Table 5). The transmission light curves and MCMC correlation diagrams can be observed in Appendices C and D.

As absorption residuals are observed at the CaII triplet lines, we also checked the CaII H & K lines, which are only covered with HARPS-N observations. Unfortunately, these lines are located at the beginning of the first echelle order of the CCD and the spectra are too noisy in that region to be of any value. These lines are chromospherically sensitive lines, which could present variations caused by the contrast between different regions of the stellar disc (Cauley et al. 2018). However, as expected for this stellar type, we notice no variations or emissions in the line cores that could be produced by stellar activity.

5.4. Na I doublet

Due to the rotational broadening, the NaI stellar lines expand over a large wavelength range, and a large number of telluric lines fall into the NaI lines, as we showed in Fig. 4. Additionally, interstellar medium (ISM) NaI absorption at the stellar lines core is observed for all nights, affecting the region where we would expect the planetary signal. We used the LISM Kinematic Calculator (Redfield & Linsky 2008) in order to determine the origin of the interstellar NaI lines, which gives us information about the interstellar medium clouds that our line-of-sight traverses while observing a target. Although we expect this ISM NaI absorption at the same spectral position and to be stable during the night, any small variation of this absorption during the transit could mimic a planetary atmospheric absorption. As a first approximation, assuming that the ISM remains totally stable, and not correcting by the stellar reflex motion around the Barycentre of the system, the ISM effects would be removed when dividing each spectrum by the master-out spectrum.

Because of the large telluric contamination of the NaI stellar lines, we included an additional correction. After computing the ratio between each spectrum and the out-of-transit master spectrum, similarly to Snellen et al. (2010), we removed the remaining telluric residuals by fitting the time variation in each pixel by, in this case, linear splines using the `UnivariateSpline` class from `scipy` to refuse outliers. The resulting fit is compared to the data, and those points differing more than 5% from the fit values are set to 1.0 (we note that the residuals spectra are normalised to the unit). This would not affect the possible planetary signals, as they are expected to be smaller than 5%, as observed in Casasayas-Barris et al. (2018).

As explained in Sect. 4, the stellar models computed with `SME` in the NaI lines region assuming solar abundance were observed to be very different compared with the observational data in the same region. For this reason, we fitted the abundance, and the final models were computed using the resulting NaI abundance value ([Na/H]= 0.98). We then fit the residuals after dividing each spectrum by the master out spectrum as we did for the Hα in Sect. 5.1. The MCMC fitting procedure is applied to each NaI D2 and D1 lines separately (for which we take reference positions at 5889.95 and 5895.92 Å, respectively) and the grid of models is computed for [0.7–2.5] R_p with steps of 0.1 R_p. The results for CARMENES and combined HARPS-N data analysis are shown in Fig. 10, and the best-fit parameters are given in Table 5.

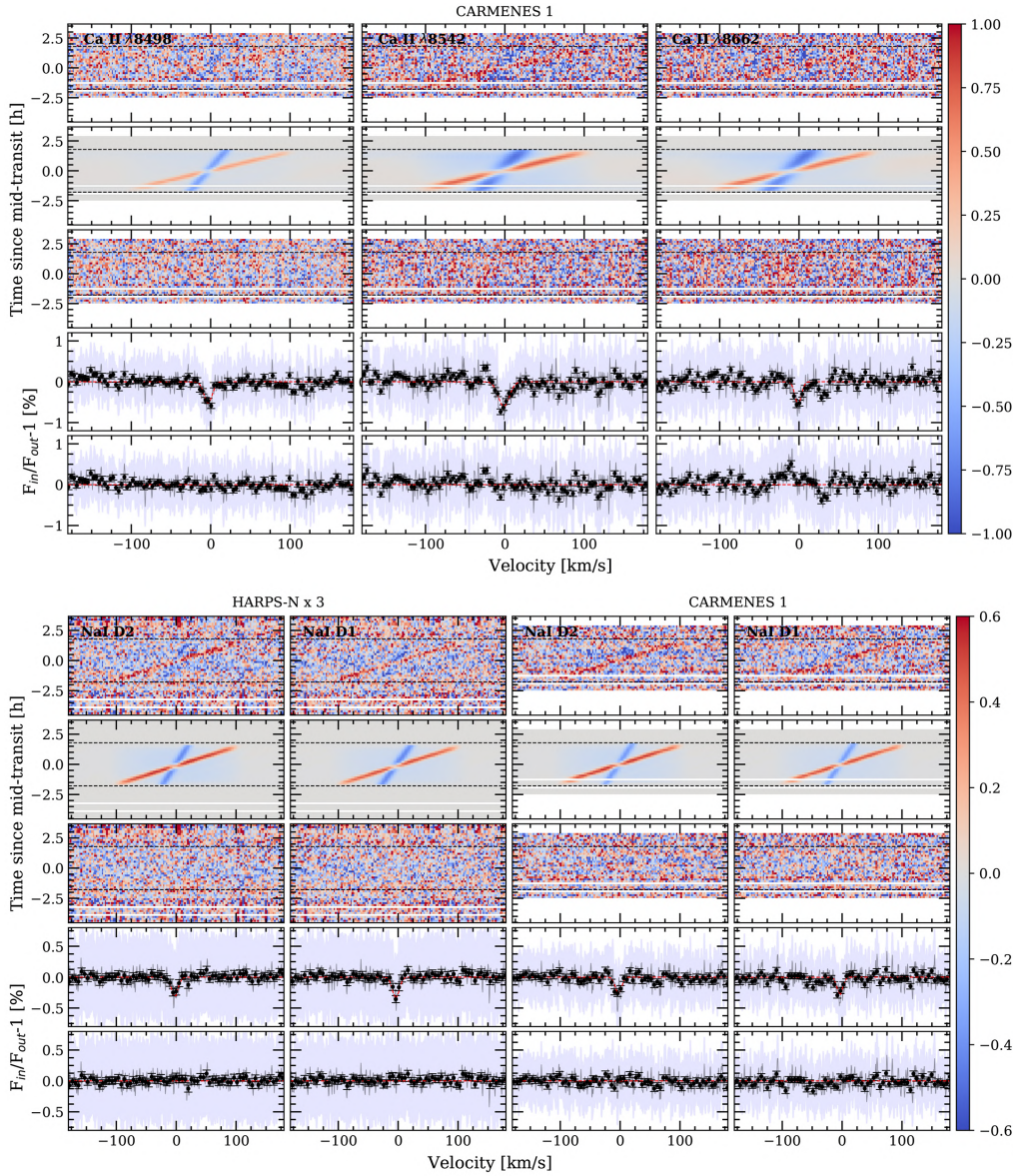

Fig. 10. As Fig. 5, but for CaII (*top*) and NaI lines (*bottom*). The name of the line is indicated in each *top-left panel* and the titles indicate the instrument used to retrieve the data. The transmission spectra are binned by 0.1 Å (black dots). The colour bar indicates the flux relative to the continuum ($F_{in}/F_{out}-1$) in %.

In the 2D maps, the in-transit trail seems to be observable for both D_2 and D_1 lines and both CARMENES and HARPS-N analysis (see Fig. 10), being clearer in HARPS-N. The MCMC analysis is able to distinguish and characterise the absorption, finding a consistent value of K_p with the one theoretically predicted. When we analysed the nights separately, the D_2 line absorption can be reproduced every night except for HARPS-N Night 2, and the D_1 line can be reproduced in Night 1, CARMENES data, and when all HARPS-N data are combined. The measured absorption in the line core (h) is consistent for both analysis, with approximately −0.30%, which corresponds to an effective radius of ∼1.1 R_p of absorption in both lines of

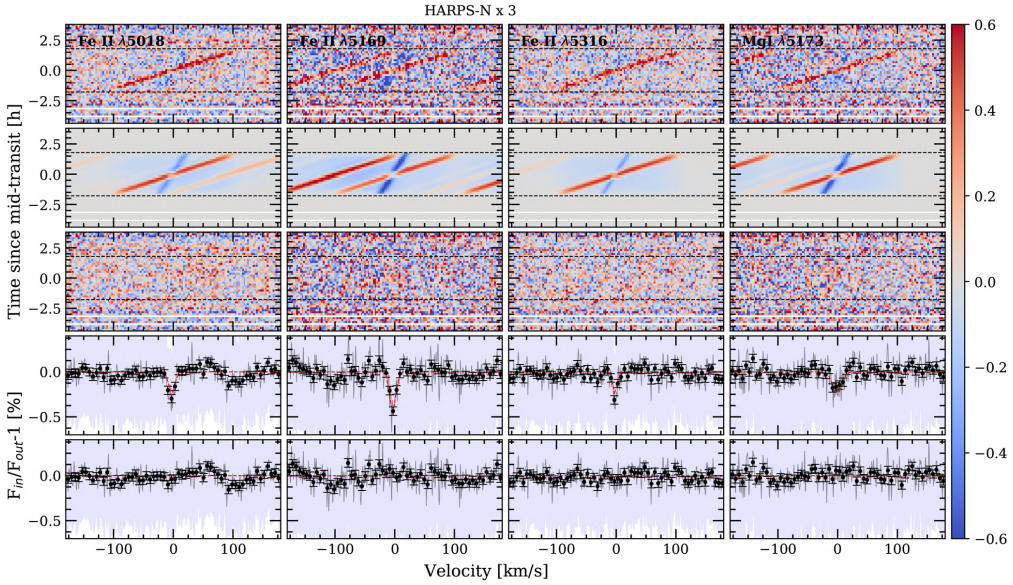

Fig. 11. As Fig. 5, but for FeII and MgI lines. The name of the line is indicated in each *top-left panel*. The transmission spectra are binned by 0.1 Å (black dots). The colour bar indicates the flux relative to the continuum ($F_{in}/F_{out}-1$) in %.

the NaI doublet. These results are also consistent with the results obtained for Night 1 in Casasayas-Barris et al. (2018), who apply a different analysis.

The light curves and transmission spectra present consistent absorption depth (see values in Table 5). See 2D maps of each night and light curves in Appendices A and C. The transmission light curves are computed for each line of the doublet separately and are then combined using the weighted mean.

5.5. FeII

Three other transmission signals are observed when scanning the residuals in the wavelength range covered by both spectrographs. The position of these lines are 5018.38 ± 0.01 , 5168.96 ± 0.01, and 5316.57 ± 0.01 Å, which we attribute to FeII λ5018.43, λ5169.03 and λ5316.61, respectively. However, we note that due to the large rotation velocity of the star, it is difficult to distinguish a single line within the blended stellar lines. The FeII λ5316 Å line is also covered by CARMENES at very low S/N (the mean S/N of this order is around 10). The transmission spectrum obtained shows absorption in the same place as HARPS-N (5316.61 ± 0.02 Å), but we also observe additional features that are not observed in HARPS-N results, and whose origin is not clear, possibly caused by the low S/N (see this results in Appendix A).

In the same way as for the other lines, we removed the RM and CLV, and find the best-fit parameters (see Fig. 11 and Table 5). A faint trail during the transit is observed for each line 2D map, but stronger for FeII λ5169 line, which presents an absorption of 0.47 ± 0.05 in the core. We note that near this line, we observe a second and fainter residual at 5172.66 ± 0.02. The unique specie that overlaps this position is MgI at 5172.68, but the significance of this absorption signal is very low (1.7σ) with an absorption depth of 0.07 ± 0.04% in the transmission spectrum for a 0.75 Å passband, and approximately −0.2% of absorption in the line core (see the results for this MgI residual in Fig. 11).

We computed the transmission light curves of each FeII and MgI lines, and the FeII combined transmission light curve (see Appendix C). We then measured the absorption depth in the transmission spectra and light curves, with values presented in Table 5. The results from the transmission spectra and light curves are consistent.

6. Systematic effects

As presented in Redfield et al. (2008), we were able to measure the stability of the individual observations by quantifying the systematic effects with the empirical Monte Carlo (EMC) or bootstrapping diagnostic. The EMC analysis helps us to quantify the systematic errors, since the absorption depth measurements error bars come from the propagation of the random photon noise from Poisson statistics through the process. This analysis involves the random selection of a number of individual exposures to build the "in-transit" sample and another random selection for the "out-of-transit" sample. With these two samples we then extracted the transmission spectrum and we measure the absorption depth of this result. This process is applied 10 000 times with different random samples in order to have statistical significance. With this, we were able to check how likely it is that the signal we are observing has planetary origin, or is caused by a random combination of the data.

We assumed three different scenarios, as presented in Redfield et al. (2008) and other recent studies such as Wyttenbach et al. (2015, 2017). The first scenario is called "out–out" where we randomly split the out-of-transit

observations in two samples with the same number of individual observations; one of these two samples will be used as the in-transit sample and the other as the out-of-transit sample. The second scenario is called "in–in" and constructed in the same way, but now splitting the in-transit observations. The final scenario is the "in–out" and represent the atmospheric absorption case. Here, the in-transit and out-of-transit samples were built with the in- and out-of-transit observations, respectively. For the in–in and out–out scenarios, we selected the same number of exposures included in the in-transit and in the out-of-transit samples. This means that in the in–in scenario this value is half the total number of real in-transit observations and in the out-out is half the real out-of-transit observations. For the in–out scenario the number of exposures included in each sample changes randomly, never being less than half the total number of real in- or out-of-transit exposures and always accomplishing the number ratio of real in-transit to the out-of-transit observations. We note that each sample including in-transit data is corrected by the CLV and RME effects, computed considering the best-fit parameters of each line presented in Sect. 7.

This analysis is applied to each line analysed here. The distributions for a 1.5 Å passband can be observed in Fig. E.1. In all cases the out–out and in–in scenarios show distributions centred to 0% absorption while the in–out scenario is centred to a different position. The clearest case is the Hα line, where the absorption scenario is centred to 0.36 ± 0.14 and 0.40 ± 0.14% (the error corresponds to the standard deviation of the distribution) for HARPS-N and CARMENES analysis, respectively, consistent with the absorption depth measured from the final transmission spectrum (see Table 5). In case of the CaII we observed the in–out samples centred on 0.10 ± 0.08, 0.12 ± 0.11 and 0.11 ± 0.09 absorption, for the λ8498 , λ8542 and λ8662 Å lines, respectively.

For the NaI doublet case, the in–out scenario distributions clearly present different characteristics in comparison with the other scenarios for HARPS-N analysis. Both D_2 and D_1 distributions are centred to 0.07 ± 0.05%. In the case of CARMENES, the three different scenarios give closer results; in this case, the distributions are centred on 0.05 ± 0.09% for the D_2 line and 0.12 ± 0.08% for the D_1 line. The absorption scenario of Hβ presents a distribution centred to 0.14 ± 0.08%. Finally, for Hγ the scenarios for all three distribution overlapped, being the in–out distribution centred on 0.04 ± 0.09% absorption.

The FeII lines obtained with HARPS-N data show in–out distributions centred to 0.03 ± 0.03, 0.04 ± 0.04 and 0.04 ± 0.03, for the λ5018, λ5169 and λ5316, respectively, close to the in–in and out–out scenarios. Similarly to Hγ, the in–out scenario distributions obtained for FeII λ5316 using CARMENES data and MgI λ5173 using HARPS-N data, show mainly indistinguishable distributions with respect in–in and out–out scenarios, centred to 0.09 ± 0.15 and 0.03 ± 0.05, respectively.

7. Discussion and conclusions

Casasayas-Barris et al. (2018) present the analysis of one HARPS-N transit observation of MASCARA-2b, Night 1 in this paper, and reported the detection of Hα and NaI in its atmosphere, and a hint of Hβ detection. Here we have repeated the analysis after combining two more transit observations of MASCARA-2b with HARPS-N and one more with the CARMENES spectrograph. After analysing the 2D residual transit maps, the transmission spectra, the transmission light curves and EMC results, we conclude that we have detected a hint to the presence of a possible ionosphere around MASCARA2-b, including the detection of CaII, FeII, NaI, Hα, Hβ, and Hγ transitions. We note that, with respect to the previous study, we are using here different telluric correction and only the spectra taken in the fully in-transit time are combined when computing the transmission spectra (the ingress and egress data are excluded from this sample). We summarise the results obtained in Table 5 and Fig. 12.

Focusing on the Balmer lines, the Hα absorption by the planetary atmosphere can be observed by eye in the residuals of each single night, appearing during the transit and ranging different radial-velocities than the RME, which is also clearly observed. The planet orbital radial-velocity semi-amplitude (K_p) values measured are consistent (considering the error bars) with those from the literature. For Hβ, on the other hand, the absorption by the planetary atmosphere is not clear if we do not combine the three transits observed with HARPS-N. But when doing so, the absorption in the transmission spectrum and the light curves is statistically significant (5σ and 6σ, respectively, for a 0.75 Å passband). Finally, the Hγ analysis of each individual night show mainly flat transmission spectra and light curves, but a faint Hγ signal moving at the planetary speed for MASCARA-2b results when combining all the HARPS-N data (3σ for a 0.75 Å passband).

Yan & Henning (2018) detect Hα in the atmosphere of KELT-9b, the ultra-hot Jupiter with highest day-side temperature (4600 K). They measure 1.15 ± 0.05% of absorption which corresponds to a hydrogen atmosphere around 1.64 times the radius of the planet, close to the Roche Lobe ($1.91^{+0.22}_{-0.26}\,R_p$), and an estimated mass loss rate of $\sim 10^{12}$ g s^{-1}. In extreme cases, photo-evaporation causes a transonic planetary wind and the mass loss rate could affect the planetary evolution (Salz et al. 2015). Cauley et al. (2019) reproduced the Hα detection in KELT-9b and also reported significant absorption in Hβ. Here, for MASCARA-2b, the measurement of the Hα absorption is ~0.7%, which corresponds to an atmospheric extension of 1.2 R_p. Considering that the lower-limit of the scale height (H) is 281 km (calculated with μ = 2.3 and the gravity upper-limit from Lund et al. 2017), the atmosphere is extended by 545 H. The atmosphere is expanded due to the gas heating caused by the irradiation received from the host star. For Hβ, on the other hand, the 0.45% of absorption corresponds to 1.15 R_p (525 H). Considering the mass upper-limit from Lund et al. (2017), we estimate that the Roche Lobe radius (Eggleton 1983) of MASCARA-2b is <3.6 R_p. If we now assume a mass of 2 M_J this radius decreases to 3 R_p. The effective radius measured for the different atoms/ions do not reach the Roche Lobe in any of those cases. The measured FWHM of Hα line is ~20 km s^{-1} which is significantly lower than that of KELT-9b (~51 km s^{-1}). The large FWHM of Hα in KELT-9b is a result of high density of excited hydrogen atoms that causes the absorption to be optically thick at the line centre ($\tau \approx 57$). According to our estimation using the analytic Eq. (3) in Huang et al. (2017), the optical depth at the Hα line centre of MASCARA-2b is small ($\tau \approx 2$), indicating that the density of excited hydrogen is much lower than in KELT-9b. Such a lower density also explains why the effective radius of Hα line does not reach a high altitude like in KELT-9b. Thus, we conclude the Balmer lines absorption in MASCARA-2b are from relatively low altitude atmosphere which is far away from the Roche Lobe and therefore cannot be used to estimate the mass loss rate.

For CaII, the individual lines of the triplet are clearly detected in the CARMENES night that covers this wavelength range. The trail of the strongest line (8σ of absorption

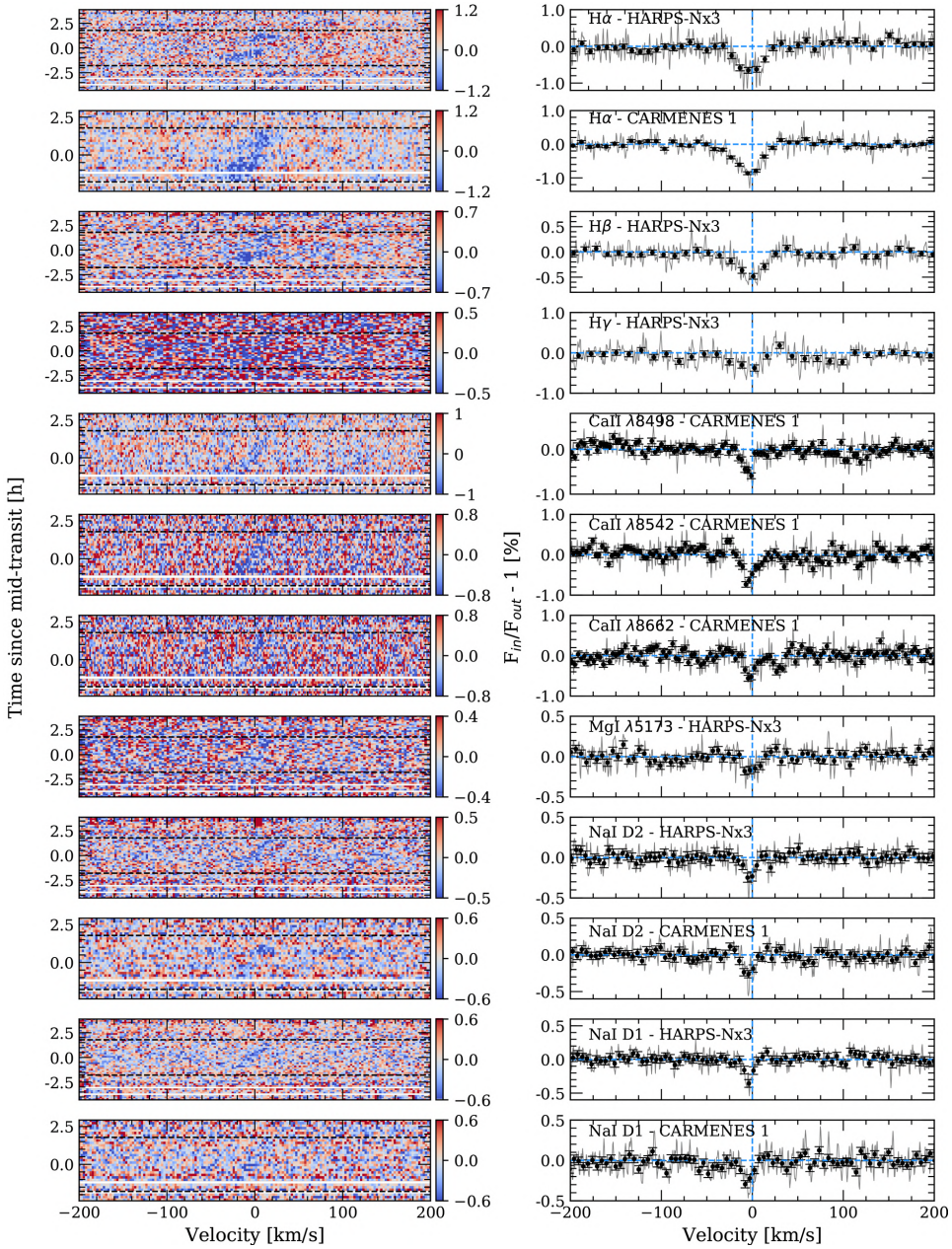

Fig. 12. Summary of the 2D maps with the remaining absorption after the CLV and RM correction (*left column*) and final transmission spectra (*right column*) of all species analysed. Each row corresponds to one line, whose name is indicated inside each transmission spectrum figure. The residual maps data is presented binned by 0.05 Å and 0.002 in orbital phase in order to have better contrast. The transmission spectrum of Balmer lines are shown binned by 0.2 Å and the remaining lines by 0.1 Å (black dots). The colour bar indicates the flux relative to the continuum ($F_{in}/F_{out}-1$) in %.

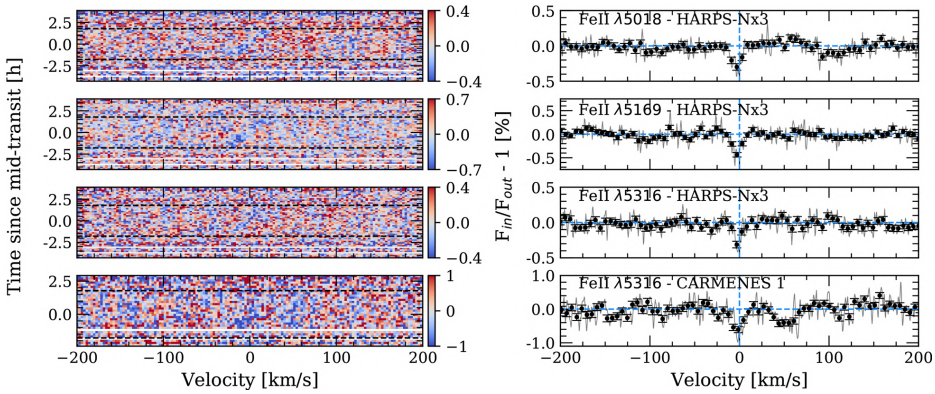

Fig. 12. continued.

significance for 0.75 Å) at λ8542 Å can be observed in the 2D maps tracing the radial-velocity change of the planet during the transit, while the other two lines of the triplet are also significant but fainter (around 5σ). We note that this results from the analysis of only one transit. Using the combination of three HARPS-N nights, we also observe the presence of FeII ions in MASCARA-2b atmosphere at the 2σ level measured in the absorption depth for 0.75 Å passband, and an averaged significance around 7σ in the lines core. Finally, the traces of NaI planetary absorption are observable in each individual night, although the true absorption values retrieved here could be affected by the strong telluric and interstellar contamination in this region of the spectrum. The significance of these lines is around 7σ in the lines core and 2–3σ when averaging the absorption in a 0.75 Å passband, for both instruments.

Absorption excess in neutral Ca lines was firstly reported by Astudillo-Defru & Rojo (2013) in HD 209458b atmosphere, and the Ca^+ triplet lines variation during a transit was studied for the first time by Khalafinejad et al. (2018) as indicator of stellar activity. Hoeijmakers et al. (2018) detected Fe, Fe^+, and Ti^+ atoms in the KELT-9b atmosphere, using the cross-correlation technique. For MASCARA-2b, we are able to resolve individual lines of Ca^+ and Fe^+ in transmission. The individual Fe^+ lines and neutral Mg at λ5173 observed here were also observed in the atmosphere of KELT-9b by Cauley et al. (2019). Fe^+, together with Ti^+, Ca^+, is expected to be more abundant than its neutral form (Helling et al. 2019) due to thermal ionisation. In the high altitude atmosphere of MASCARA-2b, the temperature could be very high causing the Fe^+ more abundant than neutral Fe. Our detection of these species, in a planet with equilibrium temperature almost 2000 K colder that KELT-9b, could indicate that either a large difference between actual and equilibrium temperatures or that there are strong mechanisms of transport to move atmospheric species from day-side to the planet's terminator. Our detection of neutral Na falls in line also with the recent detection of this species in the atmosphere of WASP-76b, a hot planet with equilibrium temperature similar to MASCARA-2b (Seidel et al. 2019).

For all species, the resulting absorption signatures are blueshifted with respect their reference values, with velocities larger than 1 km s^{-1}, while the instrumental drifts for the spectrographs used here are expected to be around 10 m s^{-1}. These blueshifts can be associated to atmospheric winds. For Hα and NaI, the blueshift measured in CARMENES and HARPS-N data are consistent. For the Hβ and Hγ lines, the significance is low (<0.9σ) to determine if the measured blueshift is real. On the other hand, the FWHMs measured for the different lines are consistent for those measured with HARPS-N and CARMENES. The Balmer lines are measured to be broader than CaII, NaI and FeII lines. The line spread function of HARPS-N is 2.7 km s^{-1} while for CARMENES is 3.5 km s^{-1}. In all cases, the FWHM measurements are larger than the resolution element of those instruments, and are probably associated to kinematic and/or thermal broadening. In Fig. 13 we relate the velocity shifts ($v_{\rm wind}$) and FWHM measurements with respect the absorption ($R_\lambda(h)$). In the $v_{\rm wind}$ versus absorption relation no obvious correlation is observed, with a mean $v_{\rm wind}$ value around -2.4 ± 1.0 km s^{-1}. For FWHM versus $R_\lambda(h)$, however, each element relation could be explained by a linear regression. Koll & Komacek (2018) studied the magnitude of the wind speeds expected in hot Jupiters, as a result of the incident flux that they receive and tidally locked spin states. Considering this study, the average wind measurement of -2.4 ± 1.0 km s^{-1} is in agreement with the estimated values, for a planet with the equilibrium temperature of MASCARA-2b, assuming that the dissipation is caused by shear instabilities (Eq. (15)).

Ultra-hot Jupiters lie in the temperature transition region between gas-giants and stars, some of them having very similar temperatures as the coldest stars. As such they are useful tests cases to study the atmospheric chemistry, understand planetary mass loss and provide constrains for planetary theories of formation and evolution. As presented in several studies (Parmentier et al. 2018; Arcangeli et al. 2018 and Bell & Cowan 2018), we expect these extremely hot planets to present close to stellar-like atmospheric temperatures. The stellar radiation heats the atmospheric gas to temperatures considerably higher than 3000 K causing the day-side atmosphere to be composed of atoms rather than molecules in addition to an increased fraction of ions (see discussion in Helling & Rimmer 2019. Such a high irradiation leads to large day-night temperature differences and therefore we expect these planets to present hot days and cold nights, in particular for those planets with short orbital periods. For WASP-18b, for example, a planet with an effective temperature very close to MASCARA-2b, detailed theoretical studies show that we expect two very different sides, a cloudy night-side depleted of elements (which are then left to form atoms, ions, molecules and will make up the atmosphere of the planet) and a cloud-free day-side that forms a thermal ionosphere (Helling et al. 2019). As the

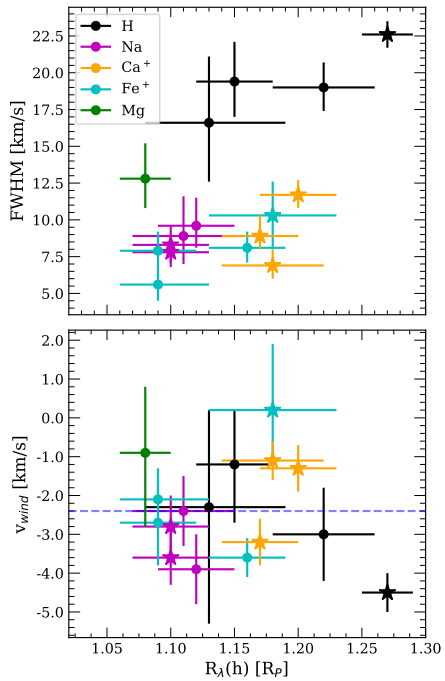

Fig. 13. *Top*: FWHM values versus $R_A(h)$. *Bottom*: v_{wind} values versus $R_A(h)$. The measurements obtained with HARPS-N data are shown in dots while those obtained with CARMENES data are marked with stars. The horizontal blue dashed line shows the mean v_{wind} value at -2.4 ± 1.0 km s^{-1}. All values are extracted from Table 5.

day-side is ≈2500 K hotter than the night-side on WASP-18b, hydrogen is present in its atomic form (HI) such that n(HI) > $n(H_2) \gg n(H_2O)$ in the low-pressure, upper atmospheric regions. The same pattern holds for most atoms, including Na, K, Ca, Ti, Al, Fe, Mg, and Si. Only at higher pressures, molecule like H_2, SiO, AlH are the dominating species of their element. Na, K, Ca, Ti, Al, Fe, Mg, and Si are singly ionised, with Na^+, Ca^+, K^+, Al^+, and Ti^+ being more abundant than their neutral atomic or ionic form. On the night-side, the thermal ionisation is smaller and the elements remain in their neutral state of ionization or are bound in molecules. The detection of HI, NaI, Ca^+ (CaII), and Fe^+ (FeII) in MASCARA-2b using transmission spectroscopy data from the planet's terminator is consistent with this theoretical works. We note, however, that transmission spectroscopy does not probe the day-side directly but rather indirectly through the observation of the terminator regions. The terminator regions are transition regions between the day- and the night-side where the temperature differences will not be as large as between the day- and night-side. The effect on the chemistry will therefore also be less pronounced. The observation of HI, NaI, Ca^+, and Fe^+ is therefore indicative for rather warm terminator regions. The blueshifted HI, NaI, Ca^+, and Fe^+ absorption suggests that strong winds emerge from the day-side transporting hot and considerably ionised material into the respective terminator region, hence, providing us with information about the chemistry on the day-side, too. We would therefore expect the evening terminator to be geometrically more extended than the cooler morning terminator of MASCARA-2b. We note, however, that with the observations presented here we cannot conclude if the heat is coming from the day-side or we are observing at very high altitudes where the atmosphere is hotter.

Thus, the theoretical picture of UHJs possessing extended ionospheres and two differentiated day-side and night-side chemistries is consistent with our MASCARA-2b results. However, more observational evidence is desirable to underpin this hypothesis such as CCF studies. For this planet the detection of several species at the same time has become possible with 3–4 m class telescopes. UHJs present an exciting opportunity to study their detailed composition, with state-of-the-art spectrographs such as ESPRESSO, which will be able to characterise the Hγ features observed in MASCARA-2b and possibly other fainter elements predicted by the theoretical models. In the near future high-resolution spectrographs, such as HIRES for the ELT, will be able to disentangle the complex picture of UHJ atmospheres through the simultaneous detection of multiple species in their atmospheres.

Acknowledgements. The authors would like to thank Dr Sven Buder for his useful comments and discussion about Na abundances. Based on observations made with the Italian Telescopio Nazionale *Galileo* (TNG) operated on the island of La Palma by the Fundación *Galileo* Galilei of the INAF (Istituto Nazionale di Astrofisica) at the Spanish Observatorio del Roque de los Muchachos of the Instituto de Astrofisica de Canarias. CARMENES is an instrument for the Centro Astronómico Hispano-Alemán de Calar Alto (CAHA, Almería, Spain) funded by the German Max-Planck-Gesellschaft (MPG), the Spanish Consejo Superior de Investigaciones Científicas (CSIC), the European Union through FEDER/ERF FICTS-2011-02 funds, and the members of the CARMENES Consortium. This work is partly financed by the Spanish Ministry of Economics and Competitiveness through project ESP2016-80 435-C2-2-R. G.C. acknowledges the support by the National Natural Science Foundation of China (Grant No. 11503088, 11573073, 11573075) and by the project "Technology of Space Telescope Detecting Exoplanet and Life" from National Defense Science and Engineering Bureau civil spaceflight advanced research project (D030201). F.Y. acknowledges the support of the DFG priority programme SPP 1992 "Exploring the Diversity of Extrasolar Planets (RE 1664/16-1)". A.F. acknowledges the support from JSPS KAKENHI Grant Number JP17H04574. This work is partly supported by JSPS KAKENHI Grant Numbers JP18H01265 and 18H05439, and JST PRESTO Grant Number JPMJPR1775. This article is based on observations made with the MuSCAT2 instrument, developed by ABC, at Telescopio Carlos Sánchez operated on the island of Tenerife by the IAC in the Spanish Observatorio del Teide. This work made use of PyAstronomy and of the VALD database, operated at Uppsala University, the Institute of Astronomy RAS in Moscow, and the University of Vienna.

References

Allart, R., Lovis, C., Pino, L., et al. 2017, A&A, 606, A144
Ambikasaran, S., Foreman-Mackey, D., Greengard, L., Hogg, D. W., & O'Neil, M. 2015, IEEE Trans. Pattern Anal. Mach. Intell., 38, 252
Arcangeli, J., Désert, J.-M., Line, M. R., et al. 2018, ApJ, 855, L30
Armstrong, D. J., de Mooij, E., Barstow, J., et al. 2016, Nat. Astron., 1, 0004
Astudillo-Defru, N., & Rojo, P. 2013, A&A, 557, A56
Bauer, F. F., Zechmeister, M., & Reiners, A. 2015, A&A, 581, A117
Bell, T. J., & Cowan, N. B. 2018, ApJ, 857, L20
Caballero, J. A., Guàrdia, J., López del Fresno, M., et al. 2016, Proc. SPIE, 9910, 99100E
Casasayas-Barris, N., Pallé, E., Yan, F., et al. 2018, A&A, 616, A151
Cauley, P. W., Shkolnik, E. L., Llama, J., Bourrier, V., & Moutou, C. 2018, AJ, 156, 262
Cauley, P. W., Shkolnik, E. L., Ilyin, I., et al. 2019, AJ, 157, 69
Chen, G., van Boekel, R., Wang, H., et al. 2014, A&A, 563, A40
Crossfield, I. J. M. 2015, PASP, 127, 941
Czesla, S., Klocová, T., Khalafinejad, S., Wolter, U., & Schmitt, J. H. M. M. 2015, A&A, 582, A51
Deming, L. D., & Seager, S. 2017, J. Geophys. Res. Planets, 122, 53
Drake, J. J., & Kashyap, V. L. 2010, Astrophysics Source Code Library [record ascl:1007.001]
Eastman, J., Gaudi, B. S., & Agol, E. 2013, PASP, 125, 83

Eggleton, P. P. 1983, ApJ, 268, 368
Espinoza, N., & Jordán, A. 2015, MNRAS, 450, 1879
Evans, T. M., Sing, D. K., Kataria, T., et al. 2017, Nature, 548, 58
Foreman-Mackey, D., Hogg, D. W., Lang, D., & Goodman, J. 2013, PASP, 125, 306
Foreman-Mackey, D., Agol, E., Ambikasaran, S., & Angus, R. 2017, AJ, 154, 220
Haynes, K., Mandell, A. M., Madhusudhan, N., Deming, D., & Knutson, H. 2015, ApJ, 806, 146
Helling, C., & Rimmer, P. B. 2019, Philos. Trans. A R. Soc., in press [arXiv:1903.04565]
Helling, C., Gourbin, P., Woitke, P., & Parmentier, V. 2019, A&A, 626, A133
Hoeijmakers, H. J., Ehrenreich, D., Heng, K., et al. 2018, Nature, 560, 453
Huang, C., Arras, P., Christie, D., & Li, Z.-Y. 2017, ApJ, 851, 150
Husser, T.-O., Wende-von Berg, S., Dreizler, S., et al. 2013, A&A, 553, A6
Jensen, A. G., Redfield, S., Endl, M., et al. 2012, ApJ, 751, 86
Jones, E., Oliphant, T., Peterson, P., et al. 2001, SciPy: Open source scientific tools for Python
Kausch, W., Noll, S., Smette, A., et al. 2015, A&A, 576, A78
Khalafinejad, S., Salz, M., Cubillos, P. E., et al. 2018, A&A, 618, A98
Koll, D. D. B., & Komacek, T. D. 2018, ApJ, 853, 133
Kreidberg, L. 2015, PASP, 127, 1161
Kreidberg, L., Line, M. R., Parmentier, V., et al. 2018, AJ, 156, 17
Kubát, J., & Korcáková, D. 2004, in The A-Star Puzzle, eds. J. Zverko, J. Ziznovsky, S. J. Adelman, & W. W. Weiss, IAU Symp., 224, 13
Lothringer, J. D., Barman, T., & Koskinen, T. 2018, ApJ, 866, 27
Lund, M. B., Rodriguez, J. E., Zhou, G., et al. 2017, AJ, 154, 194
Madhusudhan, N., Agúndez, M., Moses, J. I., & Hu, Y. 2016, Space Sci. Rev., 205, 285
Narita, N., Fukui, A., Kusakabe, N., et al. 2019, J. Astron. Telesc. Instrum., Syst., 5, 015001
Nortmann, L., Pallé, E., Salz, M., et al. 2018, Science, 362, 1388
Parmentier, V., Line, M. R., Bean, J. L., et al. 2018, A&A, 617, A110
Parviainen, H. 2015, MNRAS, 450, 3233
Parviainen, H., & Aigrain, S. 2015, MNRAS, 453, 3821
Redfield, S., & Linsky, J. L. 2008, ApJ, 673, 283
Redfield, S., Endl, M., Cochran, W. D., & Koesterke, L. 2008, ApJ, 673, L87
Ryabchikova, T., Piskunov, N., Kurucz, R. L., et al. 2015, Phys. Scr., 90, 054005
Salz, M., Schneider, P. C., Czesla, S., & Schmitt, J. H. M. M. 2015, A&A, 576, A42
Salz, M., Czesla, S., Schneider, P. C., et al. 2018, A&A, 620, A97
Seidel, J. V., Ehrenreich, D., Wyttenbach, A., et al. 2019, A&A, 623, A166
Sheppard, K. B., Mandell, A. M., Tamburo, P., et al. 2017, ApJ, 850, L32
Sing, D. K., Huitson, C. M., Lopez-Morales, M., et al. 2012, MNRAS, 426, 1663
Smette, A., Sana, H., Noll, S., et al. 2015, A&A, 576, A77
Snellen, I. A. G., de Kok, R. J., de Mooij, E. J. W., & Albrecht, S. 2010, Nature, 465, 1049
Talens, G. J. J., Justesen, A. B., Albrecht, S., et al. 2018, A&A, 612, A57
Tody, D. 1986, Proc. SPIE, 627, 733
Valenti, J. A., & Piskunov, N. 1996, A&AS, 118, 595
Wyttenbach, A., Ehrenreich, D., Lovis, C., Udry, S., & Pepe, F. 2015, A&A, 577, A62
Wyttenbach, A., Lovis, C., Ehrenreich, D., et al. 2017, A&A, 602, A36
Yan, F., & Henning, T. 2018, Nat. Astron., 2, 714
Yan, F., Pallé, E., Fosbury, R. A. E., Petr-Gotzens, M. G., & Henning, T. 2017, A&A, 603, A73
Zechmeister, M., Anglada-Escudé, G., & Reiners, A. 2014, A&A, 561, A59

Appendix A: Individual transmission spectra

We present here the transmission spectra obtained for each individual night.

A.1. Hβ

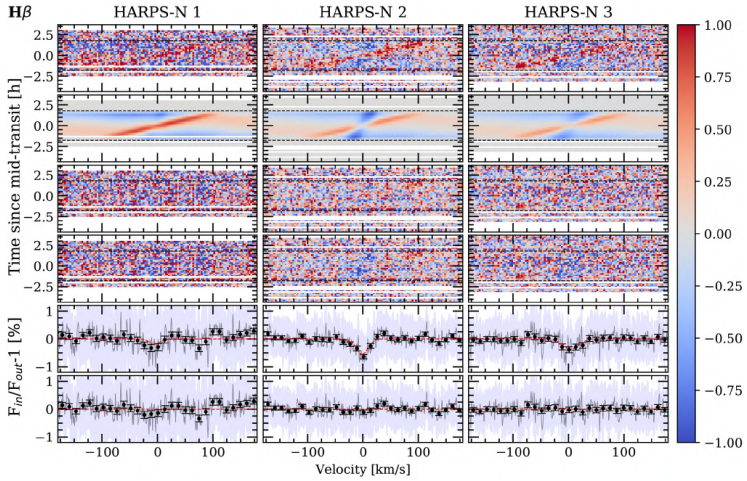

Fig. A.1. Results around the Hβ of Night 1 (*left column*), Night 2 (*middle column*), and Night 3 (*right column*). *First row (top)*: results after dividing each spectrum by the out-of-transit master spectrum. *Second row*: best-fit model of the residuals. The RME is observed in red colour (see colour bar) and the absorption and CLV in blue (negative relative flux). *Third row*: residuals when subtracting the best-fit model (*second row*) to the data (*first row*). *Fourth row*: absorption signature remaining after correcting the CLV and RME effects from first row residuals. *Fifth row*: transmission spectrum. *Sixth row*: residuals of removing the Gaussian profile model to the data in fourth row. Black dots show the result binned by 0.2 Å, the light blue region is the standard deviation of the residuals and the red line is the Gaussian computed with the best-fit parameters. In all panels, except for the last two rows, the data is shown with 0.05 Å bins in wavelength and 0.002 in orbital phase.

A.2. Hγ

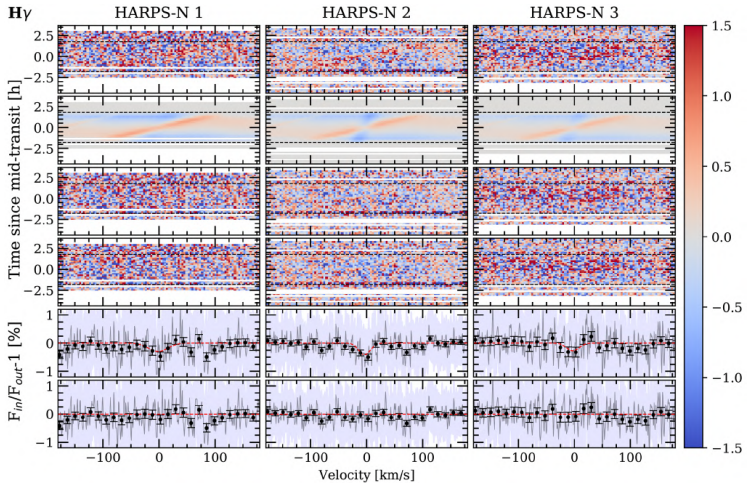

Fig. A.2. As Fig. A.1 but for the Hγ line.

A.3. NaI D_2

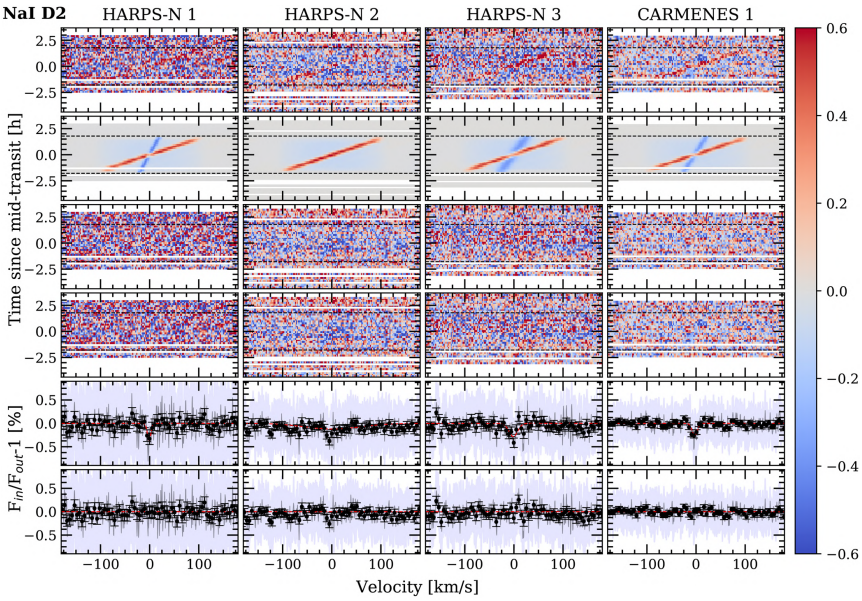

Fig. A.3. Results around the NaI D_2 of HARPS-N Night 1 (*first column starting from left*), Night 2 (*second column*), Night 3 (*third column*) and CARMENES data (*fourth column*). The different panels are explained in Fig. A.1. In the last two rows (starting from top) in black dots we show the result binned by 0.1 Å.

A.4. NaI D_1

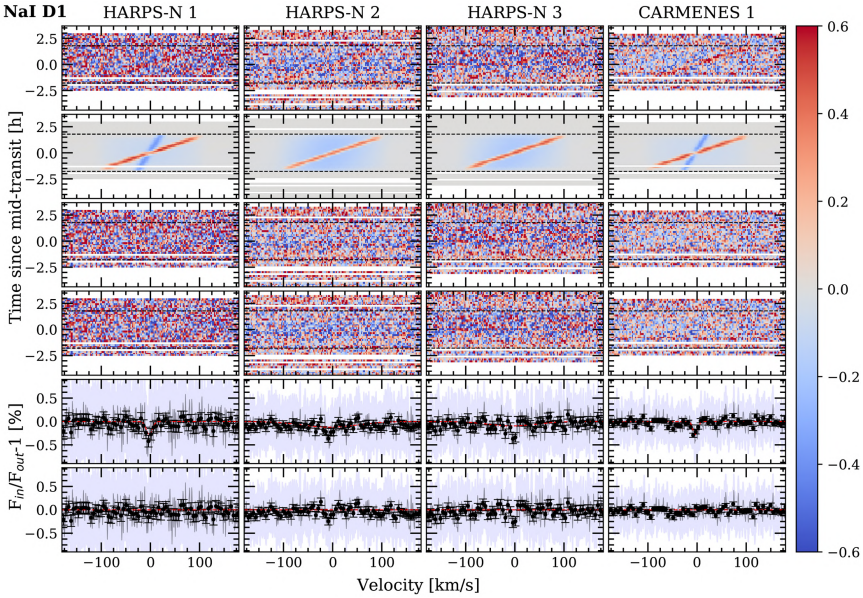

Fig. A.4. As Fig. A.3 but for the Na D_1 line.

A.5. FeII

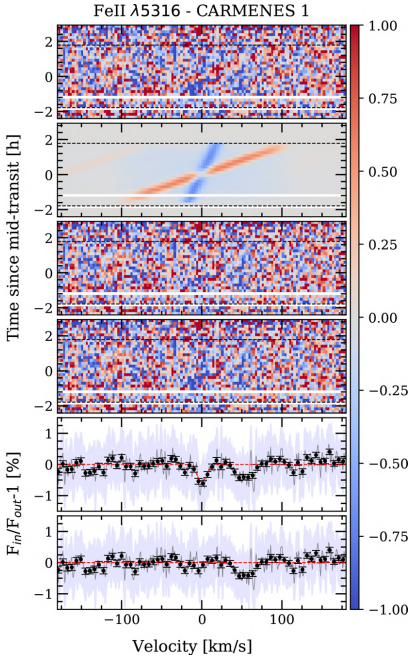

Fig. A.5. As Fig. A.3 but for the FeII λ5316 Å analysis obtained with the night observed with CARMENES. We note the strong residual observed close to the FeII line position.

Appendix B: Best-fit parameters and absorption depth values

We present here the best-fit parameters obtained with the MCMC fitting procedure and the absorption depth values measured in the transmission spectra and light curves.

B.1. MCMC best-fit parameters

Table B.1. Best-fit parameters and 1-σ error bars from the MCMC analysis.

		h (%)	$FWHM$ (km s^{-1})	K_p (km s^{-1})	v_{wind} (km s^{-1})	$R_\lambda^{(a)}$ (R_p)	$R_\lambda\,(h)^{(b)}$ (R_p)
Hβ	HARPS-N 1	$-0.20^{+0.16}_{-0.19}$	$14.7^{+16.0}_{-9.4}$	$110.6^{+85.5}_{-71.7}$	$-5.1^{+8.0}_{-6.6}$	$1.12^{+0.04}_{-0.03}$	$1.07^{+0.11}_{-0.13}$
	HARPS-N 2	$-0.57^{+0.07}_{-0.08}$	$17.9^{+2.8}_{-2.6}$	$131.8^{+19.3}_{-18.4}$	$-1.5^{+1.6}_{-1.7}$	$0.89^{+0.03}_{-0.03}$	$1.19^{+0.04}_{-0.05}$
	HARPS-N 3	$-0.38^{+0.08}_{-0.09}$	$24.2^{+7.0}_{-6.0}$	$166.3^{+55.6}_{-43.7}$	$+4.2^{+3.6}_{-3.5}$	$0.86^{+0.03}_{-0.03}$	$1.13^{+0.05}_{-0.06}$
	HARPS-Nx3	$-0.45^{+0.05}_{-0.05}$	$19.4^{+2.7}_{-2.4}$	$136.2^{+18.7}_{-18.5}$	$-1.2^{+1.4}_{-1.5}$	$0.91^{+0.02}_{-0.02}$	$1.15^{+0.03}_{-0.03}$
Hγ	HARPS-N 1	$-0.29^{+0.13}_{-0.26}$	$29.5^{+56.3}_{-15.8}$	$189.7^{+43.7}_{-105.8}$	$-1.4^{+7.2}_{-6.3}$	$1.01^{+0.05}_{-0.05}$	$1.10^{+0.08}_{-0.17}$
	HARPS-N 2	$-0.43^{+0.10}_{-0.12}$	$16.9^{+5.6}_{-4.6}$	$101.5^{+43.7}_{-105.8}$	$-4.0^{+2.8}_{-3.0}$	$0.86^{+0.03}_{-0.03}$	$1.15^{+0.07}_{-0.08}$
	HARPS-N 3	$-0.28^{+0.17}_{-0.23}$	$18.5^{+18.6}_{-11.2}$	$104.6^{+81.0}_{-65.8}$	$-2.8^{+8.5}_{-7.5}$	$0.78^{+0.05}_{-0.05}$	$1.13^{+0.05}_{-0.06}$
	HARPS-Nx3	$-0.38^{+0.08}_{-0.09}$	$16.6^{+4.5}_{-4.0}$	$135.0^{+34.1}_{-35.6}$	$-2.3^{+2.5}_{-3.0}$	$0.85^{+0.02}_{-0.03}$	$1.13^{+0.05}_{-0.06}$
NaI D_2	HARPS-N 1	$-0.37^{+0.14}_{-0.16}$	$5.93^{+4.0}_{-2.2}$	$151.4^{+35.4}_{-36.4}$	$-0.9^{+2.5}_{-2.6}$	$0.92^{+0.05}_{-0.05}$	$1.13^{+0.09}_{-0.10}$
	HARPS-N 2	$-0.12^{+0.02}_{-0.02}$	$96.4^{+2.7}_{-6.0}$	$137.1^{+78.3}_{-91.1}$	$1.4^{+9.0}_{-9.6}$	$0.97^{+0.04}_{-0.04}$	$1.04^{+0.01}_{-0.01}$
	HARPS-N 3	$-0.28^{+0.08}_{-0.10}$	$14.9^{+8.5}_{-6.2}$	$103.3^{+26.8}_{-26.4}$	$-1.3^{+2.2}_{-2.4}$	$0.94^{+0.04}_{-0.04}$	$1.10^{+0.05}_{-0.07}$
	HARPS-Nx3	$-0.33^{+0.06}_{-0.06}$	$8.9^{+2.7}_{-1.9}$	$171.1^{+15.2}_{-12.8}$	$-2.4^{+0.9}_{-0.9}$	$0.94^{+0.03}_{-0.03}$	$1.11^{+0.04}_{-0.04}$
	CARMENES 1	$-0.29^{+0.04}_{-0.04}$	$8.3^{+1.3}_{-1.2}$	$176.5^{+12.8}_{-12.3}$	$-2.8^{+0.8}_{-0.8}$	$0.91^{+0.02}_{-0.02}$	$1.10^{+0.03}_{-0.03}$
NaI D_1	HARPS-N 1	$-0.29^{+0.11}_{-0.11}$	$10.2^{+5.1}_{-3.2}$	$177.8^{+39.9}_{-41.4}$	$-2.2^{+2.4}_{-2.4}$	$0.97^{+0.06}_{-0.05}$	$1.10^{+0.07}_{-0.07}$
	HARPS-N 2	$-0.12^{+0.01}_{-0.02}$	$95.8^{+3.2}_{-7.5}$	$143.3^{+75.2}_{-93.1}$	$-7.4^{+8.6}_{-5.7}$	$0.90^{+0.04}_{-0.03}$	$1.04^{+0.01}_{-0.01}$
	HARPS-N 3	$-0.09^{+0.02}_{-0.02}$	$81.7^{+12.9}_{-21.8}$	$196.5^{+40.9}_{-79.3}$	$-6.4^{+9.6}_{-6.1}$	$0.97^{+0.04}_{-0.04}$	$1.03^{+0.01}_{-0.02}$
	HARPS-Nx3	$-0.35^{+0.05}_{-0.05}$	$9.6^{+1.9}_{-1.5}$	$194.0^{+15.1}_{-14.4}$	$-3.9^{+0.9}_{-0.9}$	$0.91^{+0.03}_{-0.03}$	$1.12^{+0.03}_{-0.03}$
	CARMENES 1	$-0.29^{+0.04}_{-0.04}$	$7.8^{+1.2}_{-1.0}$	$176.8^{+10.8}_{-10.6}$	$-3.6^{+0.7}_{-0.7}$	$0.90^{+0.02}_{-0.02}$	$1.10^{+0.03}_{-0.03}$
CaII λ8498 Å	CARMENES 1	$-0.52^{+0.05}_{-0.05}$	$8.9^{+1.4}_{-0.9}$	$173.2^{+7.8}_{-7.5}$	$-3.2^{+0.6}_{-0.6}$	$0.87^{+0.03}_{-0.03}$	$1.17^{+0.03}_{-0.03}$
CaII λ8542 Å	CARMENES 1	$-0.60^{+0.04}_{-0.04}$	$11.7^{+1.0}_{-0.9}$	$139.2^{+8.9}_{-9.2}$	$-1.3^{+0.6}_{-0.6}$	$1.09^{+0.02}_{-0.02}$	$1.20^{+0.03}_{-0.03}$
CaII λ8662 Å	CARMENES 1	$-0.55^{+0.06}_{-0.06}$	$6.9^{+1.1}_{-0.9}$	$160.7^{+8.0}_{-7.8}$	$-1.1^{+0.5}_{-0.5}$	$0.95^{+0.02}_{-0.03}$	$1.18^{+0.04}_{-0.04}$
FeII λ5018 Å	HARPS-Nx3	$-0.26^{+0.04}_{-0.05}$	$7.9^{+1.3}_{-1.3}$	$181.9^{+18.3}_{-18.7}$	$-2.7^{+1.1}_{-1.1}$	$1.19^{+0.03}_{-0.03}$	$1.09^{+0.03}_{-0.03}$
FeII λ5169 Å	HARPS-Nx3	$-0.47^{+0.05}_{-0.05}$	$8.1^{+1.1}_{-1.0}$	$170.6^{+8.3}_{-7.8}$	$-3.6^{+0.5}_{-0.5}$	$1.18^{+0.02}_{-0.02}$	$1.16^{+0.03}_{-0.03}$
FeII λ5316 Å	HARPS-Nx3	$-0.26^{+0.05}_{-0.06}$	$5.6^{+1.4}_{-1.1}$	$170.8^{+14.4}_{-16.6}$	$-2.1^{+0.8}_{-0.8}$	$1.18^{+0.03}_{-0.03}$	$1.09^{+0.03}_{-0.04}$
	CARMENES 1	$-0.55^{+0.08}_{-0.09}$	$10.3^{+2.3}_{-2.0}$	$139.6^{+32.3}_{-22.6}$	$+0.2^{+1.7}_{-1.3}$	$1.24^{+0.05}_{-0.06}$	$1.18^{+0.05}_{-0.05}$
MgI λ5173	HARPS-Nx3	$-0.23^{+0.03}_{-0.04}$	$12.8^{+2.4}_{-2.0}$	$159.6^{+30.9}_{-23.8}$	$-0.9^{+1.7}_{-1.9}$	$1.23^{+0.02}_{-0.02}$	$1.08^{+0.02}_{-0.02}$

Notes. [(a)]Effective radius value obtained from the best-fit model of the CLV and RME effects. [(b)]Effective radius calculated considering the absorption value, h, from the best-fit model and assuming a continuum level of $(R_p/R_\star)^2 = 1.382\%$.

B.2. Absorption depth values

Table B.2. Absorption depth (in %) measured for 0.75 and 1.5 Å bandwidths calculated in the final transmission spectra (TS) and transmission light curves (TLC).

		TS		TLC	
		0.75 Å	1.5 Å	0.75 Å	1.5 Å
Hα	HARPS-N 1	0.69 ± 0.10	0.44 ± 0.07	0.69 ± 0.11	0.45 ± 0.10
	HARPS-N 2	0.41 ± 0.08	0.20 ± 0.06	0.37 ± 0.10	0.16 ± 0.08
	HARPS-N 3	0.61 ± 0.10	0.24 ± 0.07	0.45 ± 0.12	0.10 ± 0.10
	HARPS-Nx3	0.59 ± 0.07	0.33 ± 0.05	0.58 ± 0.06	0.30 ± 0.05
	CARMENES 1	0.68 ± 0.05	0.44 ± 0.04	0.68 ± 0.06	0.43 ± 0.05
Hβ	HARPS-N 1	0.30 ± 0.09	0.17 ± 0.06	0.35 ± 0.10	0.22 ± 0.08
	HARPS-N 2	0.35 ± 0.07	0.14 ± 0.05	0.37 ± 0.08	0.17 ± 0.07
	HARPS-N 3	0.23 ± 0.08	0.10 ± 0.06	0.28 ± 0.10	0.15 ± 0.08
	HARPS-Nx3	0.28 ± 0.06	0.13 ± 0.04	0.31 ± 0.05	0.17 ± 0.04
Hγ	HARPS-N 1	0.19 ± 0.10	0.09 ± 0.07	0.18 ± 0.11	0.09 ± 0.10
	HARPS-N 2	0.28 ± 0.08	0.14 ± 0.06	0.29 ± 0.09	0.15 ± 0.08
	HARPS-N 3	0.13 ± 0.10	0.04 ± 0.07	0.08 ± 0.13	0.00 ± 0.11
	HARPS-Nx3	0.21 ± 0.07	0.09 ± 0.05	0.17 ± 0.06	0.07 ± 0.05
NaI D_2	HARPS-N 1	0.07 ± 0.07	0.02 ± 0.05	0.06 ± 0.08	0.01 ± 0.07
	HARPS-N 2	0.12 ± 0.06	0.05 ± 0.04	0.15 ± 0.07	0.09 ± 0.06
	HARPS-N 3	0.10 ± 0.06	0.06 ± 0.05	0.10 ± 0.08	0.06 ± 0.07
	HARPS-Nx3	0.09 ± 0.05	0.05 ± 0.03	0.15 ± 0.04	0.07 ± 0.04
	CARMENES 1	0.10 ± 0.05	0.03 ± 0.03	0.08 ± 0.05	0.01 ± 0.05
NaI D_1	HARPS-N 1	0.16 ± 0.07	0.10 ± 0.05	0.14 ± 0.04	0.08 ± 0.07
	HARPS-N 2	0.09 ± 0.06	0.04 ± 0.04	0.05 ± 0.07	0.01 ± 0.06
	HARPS-N 3	0.11 ± 0.06	0.05 ± 0.05	0.10 ± 0.08	0.04 ± 0.07
	HARPS-Nx3	0.10 ± 0.05	0.06 ± 0.03	0.16 ± 0.04	0.09 ± 0.04
	CARMENES 1	0.11 ± 0.04	0.06 ± 0.03	0.09 ± 0.05	0.04 ± 0.04
Na $D_{21}^{(a)}$	HARPS-N 1	0.11 ± 0.07	0.06 ± 0.05	0.10 ± 0.07	0.05 ± 0.06
	HARPS-N 2	0.10 ± 0.06	0.04 ± 0.04	0.10 ± 0.06	0.05 ± 0.05
	HARPS-N 3	0.10 ± 0.06	0.05 ± 0.05	0.10 ± 0.07	0.05 ± 0.06
	HARPS-Nx3	0.09 ± 0.05	0.05 ± 0.03	0.15 ± 0.04	0.08 ± 0.03
	CARMENES 1	0.11 ± 0.04	0.04 ± 0.03	0.09 ± 0.04	0.03 ± 0.04
CaII λ8498 Å	CARMENES 1	0.28 ± 0.05	0.15 ± 0.04	0.28 ± 0.06	0.14 ± 0.05
CaII λ8542 Å	CARMENES 1	0.41 ± 0.05	0.18 ± 0.04	0.40 ± 0.06	0.17 ± 0.05
CaII λ8662 Å	CARMENES 1	0.27 ± 0.06	0.14 ± 0.04	0.26 ± 0.07	0.15 ± 0.04
CaII Combined$^{(b)}$	CARMENES 1	0.32 ± 0.05	0.16 ± 0.04	0.31 ± 0.05	0.14 ± 0.04
FeII λ5018 Å	HARPS-Nx3	0.09 ± 0.04	0.04 ± 0.03	0.03 ± 0.04	0.02 ± 0.03
FeII λ5169 Å	HARPS-Nx3	0.09 ± 0.04	0.04 ± 0.03	0.12 ± 0.04	0.05 ± 0.03
FeII λ5316 Å	HARPS-Nx3	0.07 ± 0.04	0.04 ± 0.03	0.04 ± 0.03	0.00 ± 0.03
FeII Combined$^{(c)}$	HARPS-Nx3	0.08 ± 0.04	0.04 ± 0.03	0.06 ± 0.03	0.01 ± 0.03
MgI λ5173 Å HARPS-Nx3	HARPS-Nx3	0.07 ± 0.04	0.02 ± 0.03	0.09 ± 0.04	0.04 ± 0.03

Notes. $^{(a)}$Combined absorption depth of both NaI D_2 and D_1 lines. $^{(b)}$Combined absorption depth of the three CaII lines. $^{(c)}$Combined absorption depth of the three FeII lines.

Appendix C: Individual transmission light curves

We present here the transmission light curves obtained for each species analysed in this work.

C.1. Hβ

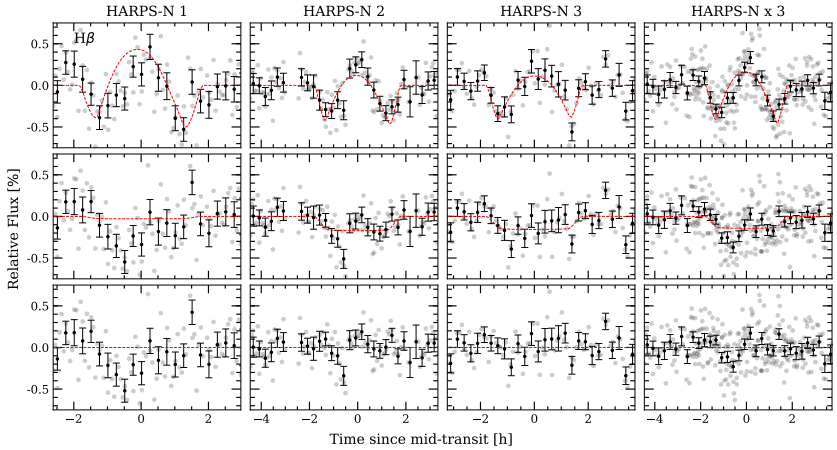

Fig. C.1. Hβ transmission light curves of HARPS-N Night 1 (*first column, left*), Night 2 (*second column*), Night 3 (*third column*) and join analysis of all HARPS-N observations (*fourth column, right*) computed for 1.5 Å passband. *First row, top*: observed transmission light curve. *Second row*: after correcting for the CLV and RME. *Third row, bottom*: residuals when subtracting the model to the data. The grey dots are the original data, the black dots is the data binned 0.003 in orbital phase. The red dashed line of the first row is the best-fit model containing the CLV, RME and absorption. The red dashed line of the second row corresponds to the model containing only absorption. In the third row, the red line is a reference showing the null flux level.

C.2. Hγ

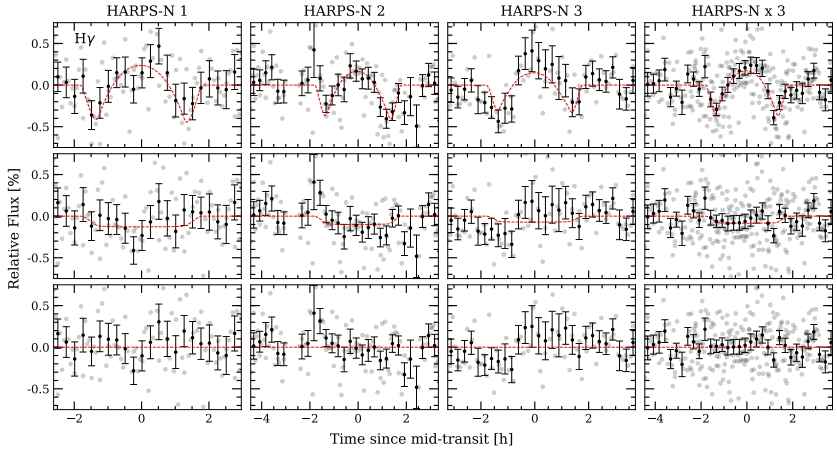

Fig. C.2. As Fig. C.1 but for the Hγ line.

C.3. CaII triplet

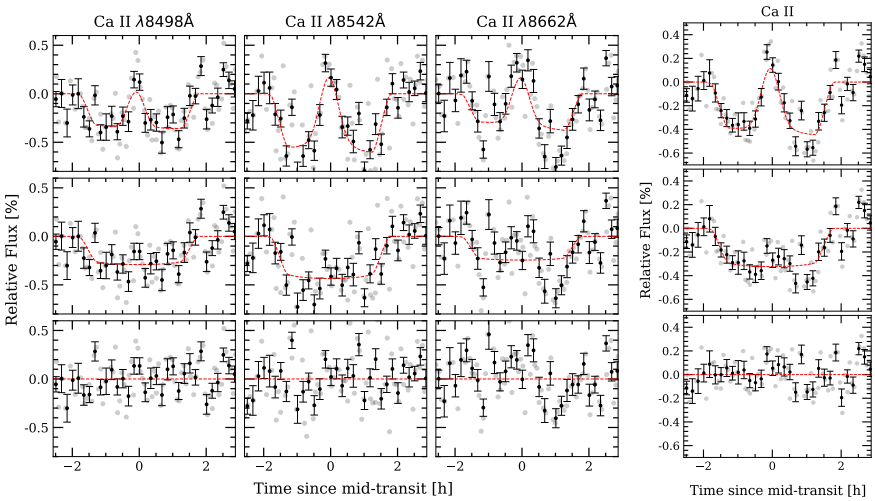

Fig. C.3. CaII transmission light curves obtained with CARMENES data. *Left*: as Fig. C.1 but for the CaII triplet lines. The analysis of each line is shown in one column. *Right*: combined light curve (using the weighted mean) of the three individual light curves of CaII triplet lines observed in the left panel. These are the results for a 0.75 Å passband analysis. Data binned 0.002 in orbital phase.

C.4. NaI doublet

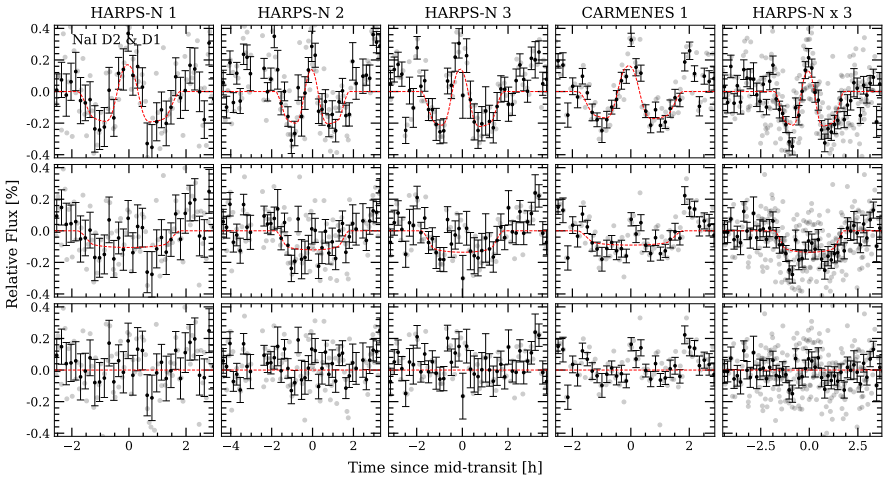

Fig. C.4. As Fig. C.1 but for both NaI D_2 and D_1 lines. This is the result of computing the weighted mean of both individual NaI D lines transmission light curves for a 0.75 Å passband. Data binned 0.002 in orbital phase.

C.5. FeII

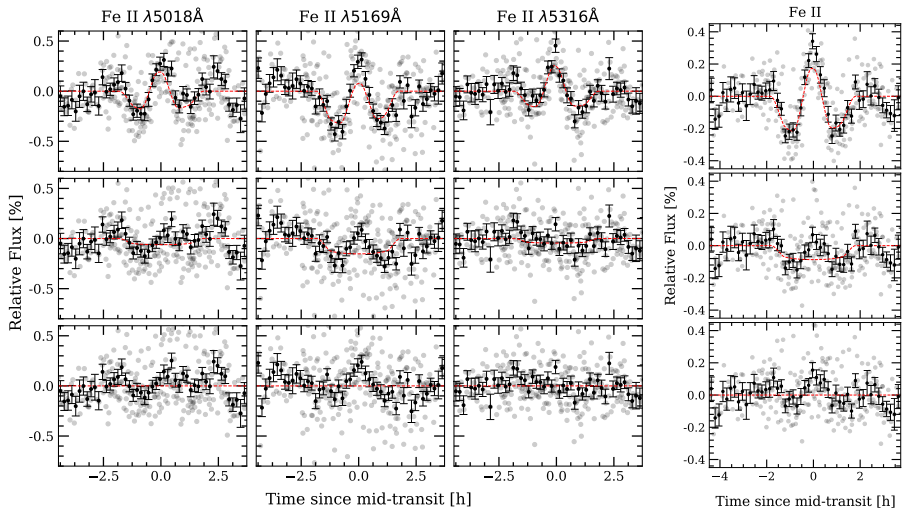

Fig. C.5. FeII transmission light curves obtained combining the three nights of HARPS-N data. *Left*: as Fig. C.3 but for three individual FeII lines and using a 0.75 Å passband. We note the asymmetry of the observed transmission light curve (*first row*) of the FeIIλ5169 line, caused by the RM effect from the closest line crossing the position of the FeII for times close to the egress. *Right*: transmission light curve after combining the three individual FeII lines. The data is binned by 0.002 in orbital phase.

C.6. MgI

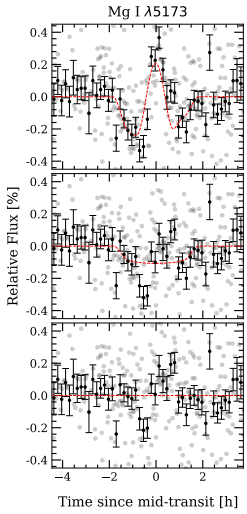

Fig. C.6. As Fig. C.5 right but for the MgI λ5173 Å. We note the asymmetry of the observed transmission light curve (*first row*) caused by a second RM effect from the closest line crossing the position (see Fig. 11).

Appendix D: Correlation diagrams of the best-fit models

We present here the correlation diagrams of the best-fit CLV, RME and absorption model for the different nights and wavelength regions.

D.1. Hα

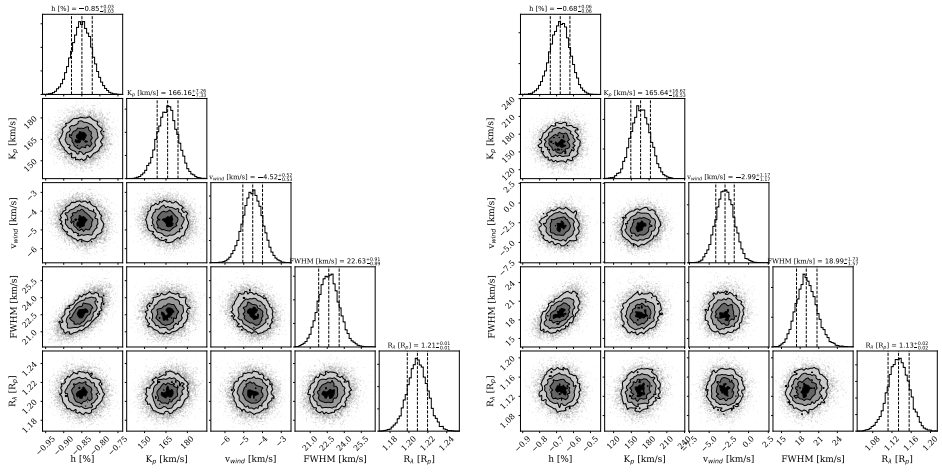

Fig. D.1. Correlation diagrams of MCMC analysis of the Hα line of CARMENES (*left*) and HARPS-N data analysis (*right*).

D.2. Hβ and Hγ

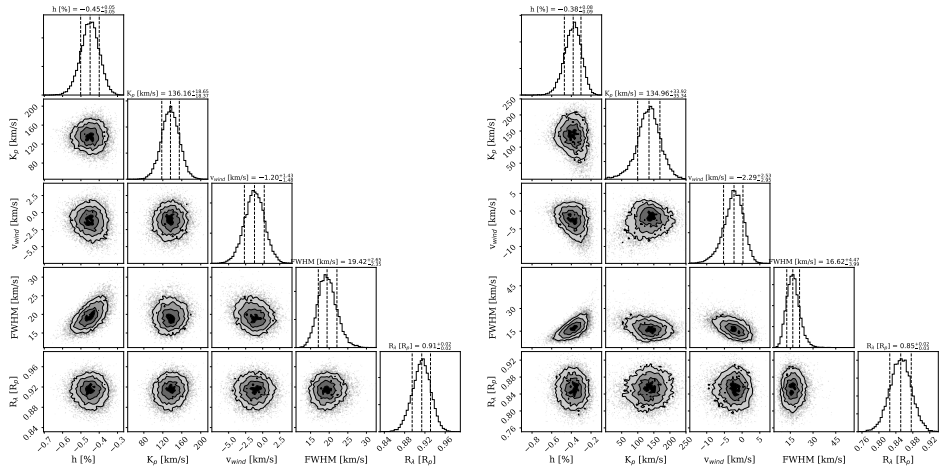

Fig. D.2. Correlation diagrams of MCMC analysis of the Hβ (*left*) and Hγ (*right*) lines obtained with the HARPS-N data analysis.

D.3. CaII

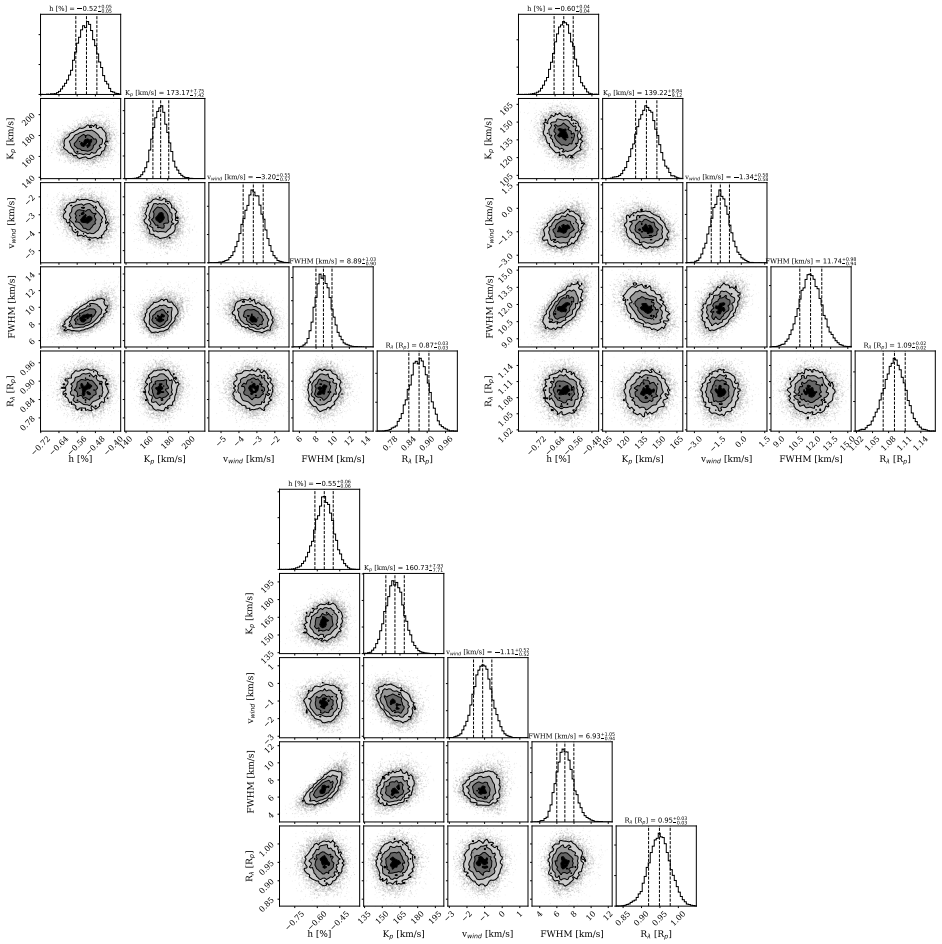

Fig. D.3. Correlation diagrams of MCMC analysis of the CaII triplet lines of CARMENES. *Top left panel*: CaII λ8498 Å, *top right*: CaII λ8542 Å, *bottom panel*: λ8662 Å.

D.4. NaI

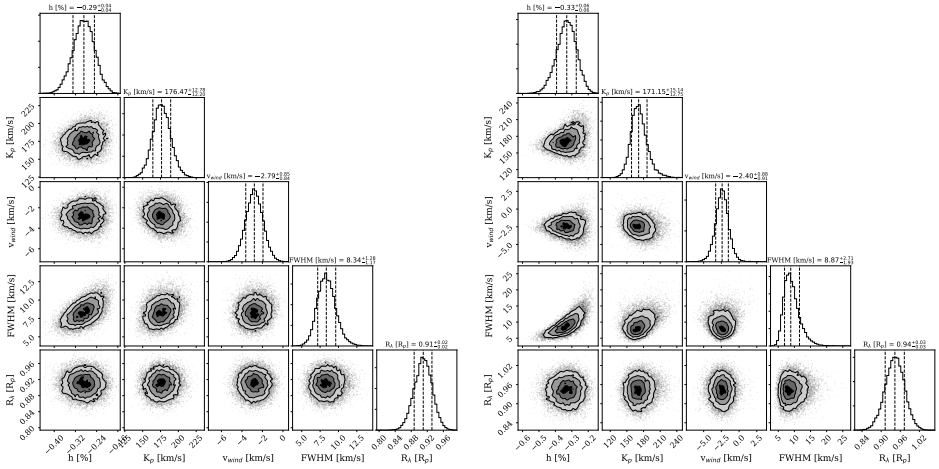

Fig. D.4. Correlation diagrams of MCMC analysis of the NaI D_2 line of CARMENES (*left*) and HARPS-N data analysis (*right*).

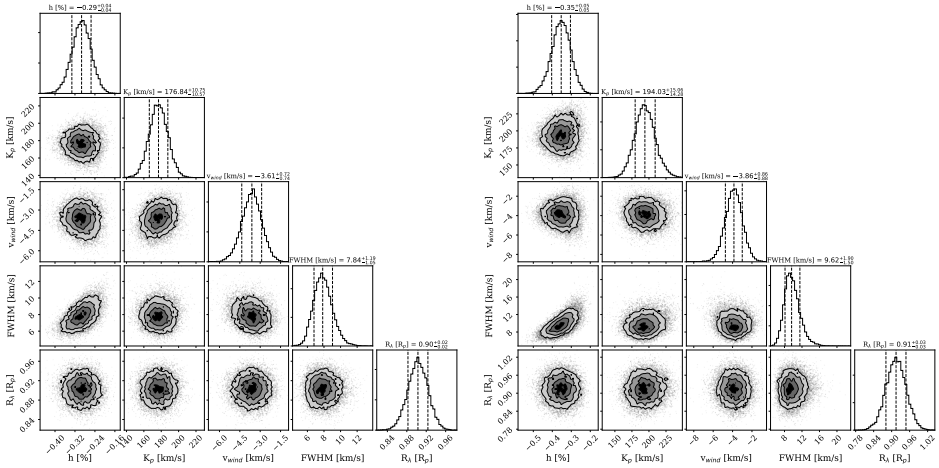

Fig. D.5. Correlation diagrams of MCMC analysis of the NaI D_1 line of CARMENES (*left*) and HARPS-N data analysis (*right*).

D.5. FeII

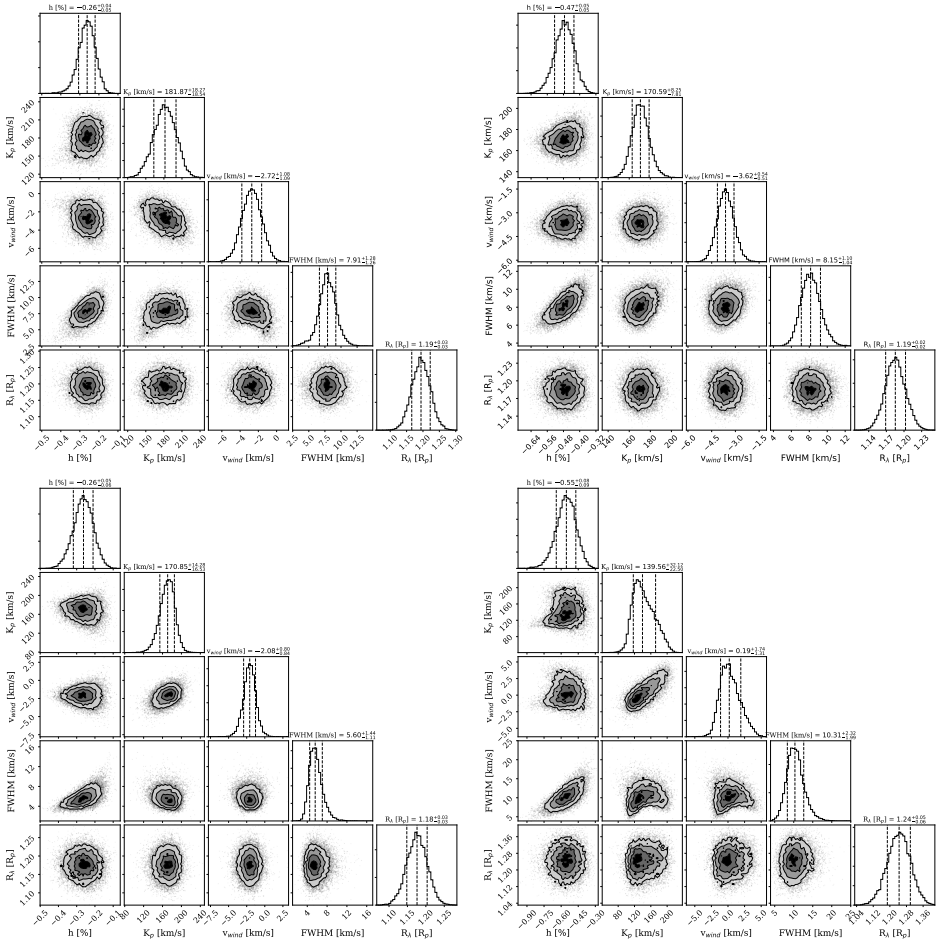

Fig. D.6. Correlation diagrams of MCMC analysis of the FeII triplet lines. The FeII λ5018 Å diagram is shown on *top left* and the FeII λ5169 Å in *top right*, both result from the HARPS-N combined data analysis. The FeII λ5316 Å diagrams are shown in the *bottom panels*: the HARPS-N analysis on the *left* and CARMENES on the *right*.

D.6. MgI

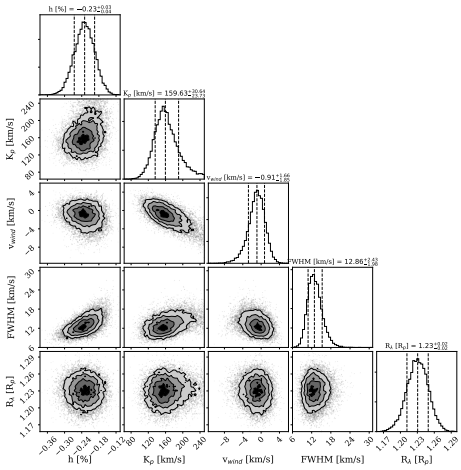

Fig. D.7. Correlation diagrams of MCMC analysis of the MgI line at 5173 Å.

Appendix E: Empirical Monte-Carlo distributions

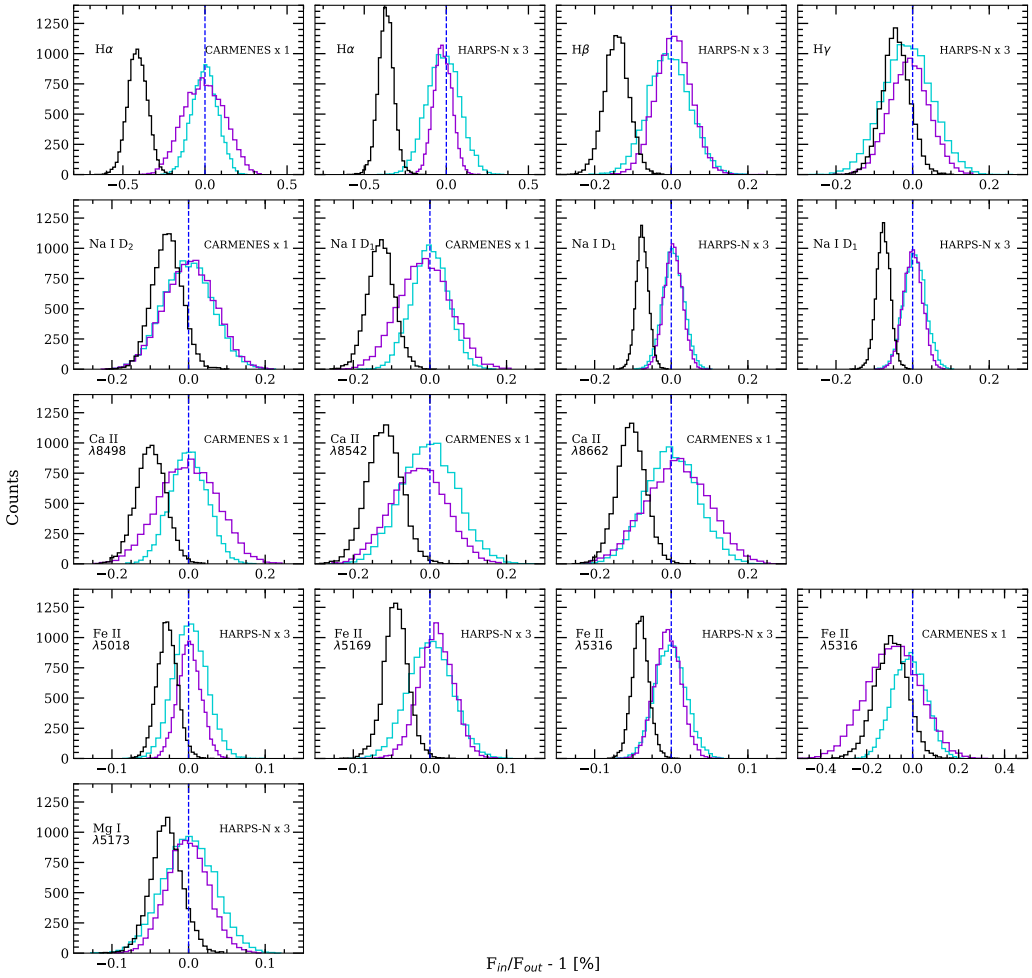

Fig. E.1. Distributions of the empirical Monte-Carlo analysis of the different lines, for a 1.5 Å passband. Each individual panel corresponds to the analysis of one line and one instrument, which are detailed in text. In violet we present the "out–out" scenario, in cyan the "in–in" scenario and in black the "in–out" scenario. The blue dashed vertical line shows the null absorption level. The CARMENES and HARPS-N analysis have different number of spectra, which means that the distributions will have different number of counts. This is also the case for the three scenarios in which the number of spectra considered is also different.

5

Is there sodium in HD 209458b's atmosphere?

-Ellie, still waiting for E.T. to call?

–Contact, 1997

HD 209458b was the first transiting exoplanet discovered (Charbonneau et al., 2000), and it was also the first exoplanet for which the detection of the atmosphere was claimed (Charbonneau et al., 2002), finding evidence of the NaI doublet lines at 590 nm. Over the years, there have been several studies of its atmosphere using low and high resolution spectroscopy facilities, resulting in the detection of different atomic and molecular species (e.g. Sing et al. 2008; Snellen et al. 2008; Albrecht et al. 2009; Désert et al. 2008). In this chapter we revisit the transmission spectrum of this benchmark exoplanet using archival observations obtained with CARMENES and HARPS-N spectrographs, and estimate the obliquity of the system. The analysis presented in this chapter is published in A&A, under the bibcode: 2020A&A...635A.206C (Casasayas-Barris et al., 2020b).

Taking advantage of the nine transit observations of HD 209458b available in the archive of HARPS-N and CARMENES, we measure the spin-orbit angle of the system with traditional velocimetric analysis of the RM effect. To this aim, we extract the stellar radial-velocity measurements with the SERVAL code (Zechmeister et al., 2018), and use an MCMC fitting procedure using Ohta

et al. (2005) models. We estimate an almost aligned system with obliquity $\lambda = -1.6 \pm 0.3$ deg, consistent with previous measurements by Winn et al. (2005) and Albrecht et al. (2012).

Using the five transit observations with higher S/N, we extract the transmission spectrum and light curves of HD 209458b following the methodology presented in the previous chapters. We focus on the analysis of the NaI lines and other regions of interest of the transmission spectrum (MgI, Hα, KI, and CaII). Despite the low S/N, the results of individual and combined nights reveal no detectable species with planetary origin, but emission-like signals produced by strong stellar lines profile deformation due to the RM effect and the CLV during the transit. In this study we present the modelling of these two effects following Yan et al. (2015) and Yan & Henning (2018). The deformation is able to describe the features observed in the transmission spectrum of HD 209458b, where the RM is the main contribution.

We discuss how previous studies of HD 209458b may have missed these effects. In particular, we compare the transmission spectrum obtained around the NaI doublet lines using HARPS-N and CARMENES with those obtained with the Space Telescope Imaging Spectrograph (STIS) aboard the *Hubble Space Telescope* (HST) by Sing et al. (2008), and the NaI transmission light curves obtained with the High Dispersion Spectrograph (HDS) at Subaru telescope (Snellen et al., 2008) and the Ultraviolet and Visual Echelle Spectrograph (UVES) at VLT (Albrecht et al., 2009).

A&A 635, A206 (2020)
https://doi.org/10.1051/0004-6361/201937221

Astronomy & Astrophysics

Is there Na I in the atmosphere of HD 209458b?

Effect of the centre-to-limb variation and Rossiter-McLaughlin effect in transmission spectroscopy studies

N. Casasayas-Barris[1,2], E. Pallé[1,2], F. Yan[3], G. Chen[4], R. Luque[1,2], M. Stangret[1,2], E. Nagel[5], M. Zechmeister[3], M. Oshagh[3], J. Sanz-Forcada[6], L. Nortmann[1,2], F. J. Alonso-Floriano[7], P. J. Amado[8], J. A. Caballero[6], S. Czesla[5], S. Khalafinejad[14], M. López-Puertas[8], J. López-Santiago[9,10], K. Molaverdikhani[11], D. Montes[15], A. Quirrenbach[14], A. Reiners[3], I. Ribas[12,13], A. Sánchez-López[8], and M. R. Zapatero Osorio[6]

[1] Instituto de Astrofísica de Canarias, Vía Láctea s/n, 38205 La Laguna, Tenerife, Spain
e-mail: nuriacb@iac.es
[2] Departamento de Astrofísica, Universidad de La Laguna, Spain
[3] Institut für Astrophysik, Georg-August-Universität, Friedrich- Hund-Platz 1, 37077 Göttingen, Germany
[4] Key Laboratory of Planetary Sciences, Purple Mountain Observatory, Chinese Academy of Sciences, Nanjing 210033, PR China
[5] Hamburger Sternwarte, Universität Hamburg, Gojenbergsweg 112, 21029 Hamburg, Germany
[6] Centro de Astrobiología (CSIC-INTA), ESAC, Camino bajo del castillo s/n, 28692 Villanueva de la Cañada, Madrid, Spain
[7] Leiden Observatory, Leiden University, Postbus 9513, 2300 RA, Leiden, The Netherlands
[8] Instituto de Astrofísica de Andalucía (IAA-CSIC), Glorieta de la Astronomía s/n, 18008 Granada, Spain
[9] Department of Signal Theory and Communications, Universidad Carlos III de Madrid, Av. de la Universidad 30, Leganés, 28911 Madrid, Spain
[10] Gregorio Marañon Health Research Institute, Doctor Esquerdo 46, 28007 Madrid, Spain
[11] Max-Planck-Institut für Astronomie, Königstuhl 17, 69117 Heidelberg, Germany
[12] Institut de Ciències de l'Espai (ICE,CSIC), Campus UAB, c/ de Can Magrans s/n, 08193 Bellaterra, Barcelona, Spain
[13] Institut d'Estudis Espacials de Catalunya (IEEC), 08034 Barcelona, Spain
[14] Landessternwarte, Zentrum für Astronomie der Universität Heidelberg, Königstuhl 12, 69117 Heidelberg, Germany
[15] Departamento de Física de la Tierra y Astrofísica and IPARCOS-UCM (Intituto de Física de Partículas y del Cosmos de la UCM), Facultad de Ciencias Físicas, Universidad Complutense de Madrid, 28040 Madrid, Spain

Received 29 November 2019 / Accepted 17 February 2020

ABSTRACT

HD 209458b was the first transiting planet discovered, and the first for which an atmosphere, in particular Na I, was detected. With time, it has become one of the most frequently studied planets, with a large diversity of atmospheric studies using low- and high-resolution spectroscopy. Here, we present transit spectroscopy observations of HD 209458b using the HARPS-N and CARMENES spectrographs. We fit the Rossiter-McLaughlin effect by combining radial velocity data from both instruments (nine transits in total), measuring a projected spin-orbit angle of -1.6 ± 0.3 deg. We also present the analysis of high-resolution transmission spectroscopy around the Na I region at 590 nm, using a total of five transit observations. In contrast to previous studies where atmospheric Na I absorption is detected, we find that for all of the nights, whether individually or combined, the transmission spectra can be explained by the combination of the centre-to-limb variation and the Rossiter-McLaughlin effect. This is also observed in the time-evolution maps and transmission light curves, but at lower signal-to-noise ratio. Other strong lines such as Hα, Ca II IRT, the Mg I triplet region, and K I D1 are analysed, and are also consistent with the modelled effects, without considering any contribution from the exoplanet atmosphere. Thus, the transmission spectrum reveals no detectable Na I absorption in HD 209458b. We discuss how previous pioneering studies of this benchmark object may have overlooked these effects. While for some star–planet systems these effects are small, for other planetary atmospheres the results reported in the literature may require revision.

Key words. planetary systems – planets and satellites: individual: HD 209458b – planets and satellites: atmospheres – methods: observational – techniques: spectroscopic

1. Introduction

HD 209458b was the first exoplanet discovered that transits in front of its host star (Charbonneau et al. 2000; Henry et al. 2000), and it was also the first exoplanet for which an atmosphere was detected (Charbonneau et al. 2002). Charbonneau and collaborators detected neutral sodium (Na I) in HD 209458b using data from the Space Telescope Imaging Spectrograph (STIS) onboard the *Hubble* Space Telescope (HST). The same data were used by Sing et al. (2008), who resolved both the Na I D2 and D1 lines. With high-dispersion spectroscopy, Na I absorption was also detected by Snellen et al. (2008) using the High Dispersion Spectrograph (HDS) at the Subaru telescope, and it was tentatively confirmed by Jensen et al. (2011) using the Hobby–Eberly Telescope. Additionally, Albrecht et al. (2009) detected Na I in two Ultraviolet and Visual Echelle Spectrograph (UVES) data sets taken with the Very Large Telescope (VLT).

Table 1. Observing log of the HD 209458b transit observations.

Night	Tel.	Instrument	Date of observation	t_{exp} [s]	N_{obs}	$S/N^{(a)}$ Na I order	$S/N^{(b)}$ Na I core	Analysis atmosphere/RM fit	Fibre B
1	TNG	HARPS-N	2015-09-26	600	32	162	51	Yes/Yes	Na I sky emission
2	TNG	HARPS-N	2016-07-25	600	42	63	20	No/Yes	Na I sky emission
3	TNG	HARPS-N	2016-09-16	600	45	136	43	Yes/Yes	Fabry-Pérot observations
4	TNG	HARPS-N	2017-07-16	300/600	38	64	20	No/Yes	Na I sky emission
5	TNG	HARPS-N	2017-09-07	300	61	108	33	Yes/Yes	Fabry-Pérot observations
6	CA 3.5 m	CARMENES	2016-09-09	180	38	82	37	No/Yes	No observable Na I sky emission
7	CA 3.5 m	CARMENES	2016-09-16	180	70	87	40	Yes/Yes	Na I sky emission
8	CA 3.5 m	CARMENES	2016-11-08	180	80	54	22	No/Yes	Na I sky emission
9	CA 3.5 m	CARMENES	2018-09-05	192	82	84	38	Yes/Yes	No observable Na I sky emission

Notes. $^{(a)}$Averaged S/N per extracted pixel calculated in the Na I order (53 for HARPS-N and 104 for CARMENES) for each night. $^{(b)}$Averaged S/N in the Na I D2 and D1 line cores (calculated in ±5 km s^{-1} centred on the cores). This calculation is performed by dividing the flux of each pixel by its photon noise.

The Rossiter–McLaughlin (RM) effect (Rossiter 1924; McLaughlin 1924) is produced when a planet transits in front of its host star, occulting a part of the stellar disc. When the stellar rotation is assumed to be in the same direction as the orbital motion of the planet, the most strongly blue-shifted wings of the stellar disc are partly occulted when the transit starts, yielding red-shifted lines; similarly, the end of transit yields blue-shifted lines. The opposite situation (stellar spin opposite to the revolution of the planet) yields red-shifted lines at the beginning of the transit, and blue-shifted lines at the end. Thus the RM effect allows us to know the geometry of the stellar rotation as compared to the planetary motion, and even to calculate the projected spin-orbit angle. This effect is identified in the radial velocity curve. If this effect is not correctly taken into account, it may lead to a misidentification of the planetary atmospheric spectral lines during transits, which are only a manifestation of the RM effect.

Centre-to-limb variations (CLVs) may also potentially affect the line profiles during transits. The stellar continuum in the photosphere has a lower intensity near the stellar limb than at the centre of the disc. This effect is related to the optical depth of the photosphere. A more subtle effect arises from Fraunhofer lines that form at different heights in the stellar atmosphere; the balance between the lines that form at different heights depends on the limb angle and stellar latitude (Abetti & Castelli 1935; Appenzeller & Schröter 1967). The strength of the CLV-induced effect can be of the same order as signals found from hot-Jupiter atmospheres (Yan et al. 2017; Czesla et al. 2015; Khalafinejad et al. 2017).

Here, we report our observations of the benchmark planet HD 209458b using the high-dispersion spectrographs HARPS-N and CARMENES. With the combination of several transits with each instrument and the use of models for the CLV and RM effects, we revisited the observational evidence for the detection of Na I in the atmosphere of HD 209458b.

This paper is organised as follows. In Sect. 2 we detail the observations. In Sect. 3 we estimate the obliquity of the HD 209458b system. The methods for extracting the high-resolution transmission spectra and light curves are explained in Sect. 4. In Sect. 5 we present the results obtained in the analysis of high-resolution transmission spectra around the Na I and other lines, and the analysis of systematic effects. In Sect. 6 our results are compared with previous studies of the same planet around Na I. The discussion and conclusions are presented in Sect. 7.

2. Observations

We used archival transit observations of HD 209458b obtained with the HARPS-N and CARMENES spectrographs. A total of nine transits are available in the archives. However, only five of them are considered in this atmospheric analysis. The other four nights are discarded because the signal-to-noise ratio (S/N) of the observations was low. The information related to the observations is summarised in Table 1. Nights 3 and 7 are the same night, observed simultaneously with the HARPS-N and CARMENES spectrographs.

2.1. HARPS-N observations

A total of five transit observations of HD 209458b are publicly available in the Telescopio Nazionale *Galileo* (TNG) archive. The HARPS-N (High Accuracy Radial velocity Planet Searcher for the Northern hemisphere) spectrograph (Mayor et al. 2003, Cosentino et al. 2012) is mounted on the 3.58 m TNG telescope, located at the Observatorio del Roque de los Muchachos (ORM, La Palma), and covers the optical range from 383 to 690 nm. The observations were carried out under programs A32TAC_41 and A35TAC_14. These observations were performed with continuous exposures during the transit, and some additional exposures were taken before and after.

The two observations with lower S/N (~60) in the Na I order (nights 2 and 4 in Table 1) were discarded for the atmospheric analysis. For night 1 no data were taken during the ingress, and only three stellar spectra are observed before the transit. The sky emission is observed in fibre B in nights 1, 2, and 4. In nights 3 and 5, fibre B was used for Fabry–Pérot observations, which means that we lack information on possible sky emission during the night. The position of the telluric Na I emission lines for these nights (if existing) is expected to be around 8 and 12 km s^{-1} from the stellar Na I line cores, respectively. At these separations, the presence of sky contamination would affect the results. The sky emission of night 1 was corrected for by subtracting the sky spectrum in fibre B from the science spectrum in fibre A. Unfortunately, the sensitivity of fibre A and B might not be the same. In this case, it would result in an imperfect removal of the telluric sky emission, which would be propagated throughout the process. As this emission is observed inside the Na I line wings and not in the continuum, we are not able to see it in the stellar spectrum (fibre A), and consequently, the sensitivity of the two fibres cannot be compared. However, the residuals related to

an imperfect sky emission correction would not reproduce the results presented here. If existing, however, they could affect the amplitude of the results. No interstellar Na I is observable in the spectra.

2.2. CARMENES observations

Four more transits were observed with the CARMENES spectrograph (Calar Alto high-Resolution search for M dwarfs with Exo-earths with Near-infrared and optical Echelle Spectrographs; Quirrenbach et al. 2014, 2018) located on the Calar Alto Observatory. CARMENES is a two-channel spectrograph that simultaneously covers the optical range from 520 to 960 nm and the near-infrared range from 960 to 1710 nm. In this study we only use the optical observations. The observations were carried out under programs H16-3.5-24, H16-3.5-22, and H18-3.5-22, and the infrared data were studied by Sánchez-López et al. (2019) and Alonso-Floriano et al. (2019). The observing strategy was the same as for the HARPS-N observations.

We discarded night 8 observations from our atmospheric study because of their lower S/N (around 50). The observations of night 6 could not be used because a technical problem of the telescope led to the loss of the first half of the transit. For this reason, only nights 7 and 9 were used in the atmospheric analysis. In all CARMENES observations, fibre B was used to monitor the sky contribution. When the sky spectra were checked, telluric Na I sky emission was observed in nights 7 and 8.

3. Estimating the obliquity of HD 209458b

The radial velocity anomaly due to the RM effect can be observed in the stellar radial velocity measurements of HD 209458 in all transit observations. In order to obtain the system parameters related to this effect, we performed a joint analysis of the radial velocity values from HARPS-N and CARMENES. To this end, we used all five nights observed with HARPS-N and all four nights observed with CARMENES. Radial velocities for both instruments were obtained using the SERVAL programme (Zechmeister et al. 2018), which uses least-squares fitting with a high S/N template created by co-adding all available spectra of the star to compute the radial velocities.

The fitting procedure of the RM effect model to the radial velocity data was performed using the Markov chain Monte Carlo (MCMC) algorithm implemented in `emcee` (Foreman-Mackey et al. 2013). We used the RM effect model presented in Ohta et al. (2005) together with a circular orbital radial velocity (both contributions implemented in `PyAstronomy` (Czesla et al. 2019) as `modelSuite.RmcL` and `modelSuite.radVel`, respectively). The RM model depends on the orbital period (P), the transit epoch (T_c), ratio of the planet-to-star radius ($R_p/R_\star$), the angular rotation velocity of the host star (Ω), the linear limb-darkening coefficient (ϵ), the inclination of the orbit (i), the inclination of the stellar rotation axis ($i_\star$), the sky-projected angle between the stellar rotation axis and the normal to the plane of planetary orbit (λ), and the scaled semi-major axis ($a/R_\star$). The circular orbit radial velocity contribution depends on P, T_c, the stellar velocity semi-amplitude ($K_\star$), and the offset with respect to the null radial velocity (Δv).

As in Casasayas-Barris et al. (2017), we fixed $i_\star$ to 90 deg, and P, $a/R_\star$, $R_p/R_\star$, $R_\star$, and i were taken from the values presented in Table 2, while the other parameters remained free. Because we fitted different HARPS-N and CARMENES nights, we needed to take into account that some free parameters should be fitted jointly for all nights and instruments, and others that could change. Ω, λ, and T_c were jointly fitted in all cases, while for each night we considered different Δv and $K_\star$ values. We note that the offset between the model and the data can vary from night to night because in addition to the systematic velocity, the radial velocity information contains possible instrumental and stellar activity effects that are reflected as additional offsets to the data. $K_\star$ could also be affected by activity and become different for different nights (Oshagh et al. 2018). Finally, because CARMENES and HARPS-N cover different wavelength regions, we defined two different linear limb-darkening coefficient parameters, ϵ^C and ϵ^H for the CARMENES and HARPS-N data, respectively.

The system was analysed using 100 walkers with 10^5 steps. The first 7000 steps were discarded as burn-in. Each step was started at a random point near the expected values from the literature, and λ was constrained to ±180 deg. On the other hand, Ω was constrained to (0.25, 0.50) rad d^{-1}. The median values of the posteriors were adopted as the best-fit values, and their error bars correspond to the 1σ statistical errors at the corresponding percentiles. The MCMC results are presented in Table 3 (Case 1) and the detrended data and best-fit model in Fig. 1. The radial velocity curves were detrended using the best-fit $K_\star$ and Δv values of each night. The data and best-fit model for each night and correlation diagrams for the probability distribution are shown in Figs. A.1 and A.2, respectively. All Δv and $K_\star$ best-fit values are presented in Table A.1.

The best-fit T_c value can be compared to the value measured by Evans et al. (2015) by propagating over different orbits using the orbital period from Table 2. We obtain a transit centre of 2 454 560.8061 ± 0.0002 BJD, which corresponds to a difference of ∼19 s with the measurement reported by Evans et al. (2015). Both measurements are consistent considering the reported uncertainties. The error bar of the propagated transit centre was calculated by considering the T_c uncertainty from Table 3 and the orbital period uncertainty from Table 2.

In Table A.1 we observe that $K_\star$ has different values for different nights. When these values are compared with the value reported by Bonomo et al. (2017) (see Table 2), nights 5, 7, and 9 do not present consistent results (at 3σ). In addition to the possible $K_\star$ variations induced by stellar activity (Oshagh et al. 2018), telluric contamination is particularly high when radial velocities are extracted. During the extraction with the SERVAL pipeline, we realised that telluric lines are not entirely masked during the process and introduce radial velocity gradients, which leads to $K_\star$ variations. Thus, the differences observed in different nights might be produced by the combination of these two factors.

With one transit of HD 209458b, Winn et al. (2005) measured an almost aligned system with $\lambda = -4.4 \pm 1.4$ and $v \sin i_\star = 4.70 \pm 0.16$ km s^{-1}. On the other hand, Albrecht et al. (2012) found $\lambda = -5 \pm 7$ deg and $v \sin i_\star = 4.4 \pm 0.2$ km s^{-1}. Here, with nine transits, we measure a spin-orbit angle of -1.6 ± 0.3 deg and an angular rotation velocity of 0.540 ± 0.002 rad d^{-1}. We note that the slight difference (smaller than 2σ) between the previous results and our λ estimate might arise because λ and Ω are degenerate (Brown et al. 2017; Albrecht et al. 2012). In addition, as reported by Bourrier et al. (2017), a traditional velocimetric analysis of the RM effect could lead to biases in the measured spin-orbit angle as a result of changes in the local CCF shape.

In order to determine the dependence of the reported results on the $i_\star$ value, we fitted the data by leaving this parameter free, constrained to (0–180) deg, hereafter Case 2. As expected, we observe a strong correlation between Ω and $i_\star$, while the remaining parameters maintain consistency with the results obtained

Table 2. Physical and orbital parameters of the HD 209458 system from previous studies.

Description	Symbol [units]	Value
	Stellar parameters	
Effective temperature [(a)]	$T_{\rm eff}$ [K]	6065 ± 50
Projected rotation speed [(b)]	$v \sin i_\star$ [km s^{-1}]	4.70 ± 0.16
Surface gravity [(a)]	$\log g$ [cgs]	$4.361^{+0.007}_{-0.008}$
Metallicity [(a)]	[Fe/H]	0.00 ± 0.05
Stellar mass [(a)]	$M_\star$ [$M_\odot$]	1.119 ± 0.033
Stellar radius [(a)]	$R_\star$ [$R_\odot$]	$1.155^{+0.014}_{-0.016}$
	Planet parameters	
Planet mass [(a)]	$M_{\rm p}$ [$M_{\rm Jup}$]	$0.682^{+0.015}_{-0.014}$
Planet radius [(a)]	$R_{\rm p}$ [$R_{\rm Jup}$]	$1.359^{+0.016}_{-0.019}$
Equilibrium temperature [(a)]	$T_{\rm eq}$ [K]	1449 ± 12
	Transit parameters	
Epoch [(c)]	$T_{\rm c}$ [BJD$_{\rm TDB}$]	$2454560.80588 \pm 0.00008$
Period [(d)]	P [day]	$3.52474859 \pm 0.00000038$
Transit duration [(e)]	T_{14} [h]	2.978 ± 0.051
Full in-transit duration [(e)]	T_{23} [h]	2.254 ± 0.058
	System parameters	
Semi-major axis [(a)]	a [au]	$0.04707^{+0.00046}_{-0.00047}$
Scaled semi-major axis [(a)]	$a/R_\star$	8.76 ± 0.04
Inclination [(a)]	i [deg]	86.71 ± 0.05
Systemic velocity [(f)]	γ [km s^{-1}]	-14.741 ± 0.002
Stellar velocity semi-amplitude [(d)]	$K_\star$ [m s^{-1}]	$84.27^{+0.69}_{-0.70}$
Projected obliquity [(b)]	λ [deg]	-4.4 ± 1.4

References. [(a)]Torres et al. (2008). [(b)]Winn et al. (2005). [(c)]Evans et al. (2015). [(d)]Bonomo et al. (2017). [(e)]Richardson et al. (2006). [(f)]Naef et al. (2004).

assuming $i_\star = 90$ deg (i.e. Case 1). This same exercise was performed with the eccentricity (now fixing $i_\star$ to 90 deg), hereafter Case 3. We left the eccentricity (e) and the argument of periapsis passage (ω) as free parameters, constrained to (0, 1) and (0–180) deg, respectively. We observe that the radial velocity offset Δv and $K_\star$ parameters are strongly correlated with ω and e, respectively. On the other hand, even the best-fit parameters are consistent with the values obtained under the assumption of a circular orbit (i.e. Cases 1 and 2), the projected obliquity λ presents a small correlation with ω value. The best-fit values obtained in these two cases are shown in Tables 3 and A.1 as Cases 2 and 3, respectively. In both cases, the MCMC analysis was performed using 80 walkers and 10^4 steps.

4. Methods

4.1. Transmission spectrum and light-curve extraction

The HARPS-N observations were reduced with the HARPS-N Data reduction Software (DRS), version 3.7 (Cosentino et al. 2014, Smareglia et al. 2014). The DRS extracts the spectra order by order, and they are then flat-fielded. A blaze correction and the wavelength calibration are applied to each spectral order, and finally, all the spectral orders from each two-dimensional échelle spectrum are combined and resampled with a wavelength step of 0.01 Å into a one-dimensional spectrum. The spectra are referenced to the barycentric rest frame and the wavelengths are given in air.

CARMENES observations were processed with the CARMENES pipeline CARACAL (CARMENES Reduction And Calibration; Caballero et al. 2016), which considers bias, flat-relative optimal extraction (Zechmeister et al. 2014), cosmic-ray correction, and the wavelength calibration described in Bauer et al. (2015). The reduced spectra are referenced to the terrestrial rest frame and the wavelengths are given in vacuum.

The transmission spectrum of each night was extracted as presented in Casasayas-Barris et al. (2018, 2019). In summary, we first corrected the telluric absorption contamination using Molecfit (Smette et al. 2015 and Kausch et al. 2015). Then, the spectra were shifted to the stellar rest frame using the stellar radial velocity semi-amplitude $K_\star = 84.27$ m s^{-1} measured by Bonomo et al. (2017), the barycentric radial velocity information, and the system velocity (see the physical and orbital parameters used in Table 2). The RM radial-velocity anomaly during the transit was not considered when we moved the spectra to the stellar rest frame. After the stellar spectra were aligned, we combined all the data taken when the planet was not transiting to a high S/N master spectrum (master out-of-transit spectrum). After this, the ratio of all spectra by the master spectrum was computed, and these residual spectra were moved to the planet rest frame. For this, we computed the planet radial velocity semi-amplitude, $K_{\rm p} = 144.89$ km s^{-1}, using the parameters in Table 2. Finally, the in-transit residuals between second and third contacts of the transit were combined to determine the individual transmission spectrum of each night. It should be noted that these operations were all carried out on

Table 3. RM effect MCMC best-fit values with 1σ and 3σ uncertainties using different assumptions.

Symbol	Units	Value	1σ	3σ
T_c	BJD	2 452 826.62980	±0.00009	$^{+0.00026}_{-0.00025}$
ϵ^H	...	0.94	±0.01	±0.03
ϵ^C	...	0.84	±0.03	±0.08
		Case 1		
λ	deg	-1.6	±0.3	±0.8
Ω	rad d^{-1}	0.540	±0.002	±0.006
$i_\star$	deg	90 (fixed)	...	...
e	...	0 (fixed)	...	...
ω	deg	90 (fixed)	...	...
		Case 2		
λ	deg	-1.6	±0.3	±0.8
Ω	rad d^{-1}	0.63	±0.04	$^{+0.06}_{-0.08}$
$i_\star$	deg	58.7	$^{+7.9}_{-5.2}$	$^{+19.3}_{-7.5}$
e	...	0 (fixed)	...	...
ω	deg	90 (fixed)	...	...
		Case 3		
λ	deg	-1.5	$^{+0.4}_{-0.3}$	±1.0
Ω	rad d^{-1}	0.540	±0.002	$^{+0.007}_{-0.005}$
$i_\star$	deg	90 (fixed)	...	...
e	...	0.05	$^{+0.05}_{-0.04}$	$^{+0.09}_{-0.05}$
ω	deg	89.3	$^{+4.7}_{-5.7}$	$^{+13.9}_{-14.4}$

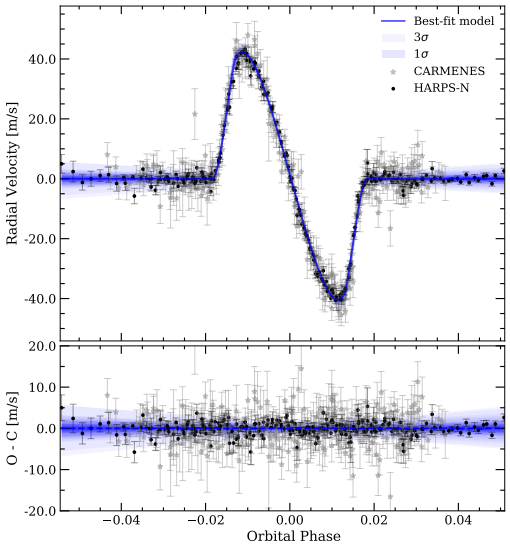

Fig. 1. Radial velocity anomaly due to the RM effect (*top panel*) and residuals between the data and model (*bottom panel*). The detrended stellar radial velocity values observed with CARMENES (four transits) are presented as grey stars. HARPS-N data sets (five transits) are presented as black dots. The blue line shows the model resulting from the combination of the HARPS-N and CARMENES best-fit models. In light blue we present the 1σ and 3σ uncertainties of the model.

continuum-normalised spectra. Therefore the transit is not visible outside the spectral lines.

A small difference with respect to the previous studies is that here, this master out-of-transit spectrum is computed using the S/N of the Na I order as weights. The reason of using the weighted mean to compute this spectrum is that the S/N inside the Na I line cores is low. In order to determine one transmission spectrum per instrument, we averaged the results of the individual nights using the mean S/N of each night as weights.

As presented in Yan & Henning (2018) and Casasayas-Barris et al. (2019), we measured the transmission light curves after computing the ratio of the spectra by the master-out spectrum, moved to the planet rest frame. These light curves were measured by integrating the flux (using trapezoidal integration) inside two different bandwidths: 0.4 and 0.75 Å. We strongly note that computing the light curves as detailed here (after computing the ratio of spectra) produces different results than if we had followed the method presented in Snellen et al. (2008) and Albrecht et al. (2009), for example. In these studies, the flux inside a passband centred on the stellar lines is averaged (using the stellar spectra) and is then compared with adjacent passbands of the same size. For this reason, the results cannot be directly compared. The light curves of different nights and instruments were combined by sorting the values measured at different time stamps in chronological order with respect to the centre of the transit. In this way, we avoided an interpolation to a common time axis.

In both transmission spectra and light curve analysis we used the transit centre obtained in the RM fitting presented in Sect. 3 (see Table 3). For the remaining parameters we assumed the literature values presented in Table 2.

4.2. Modelling the RM and CLV effects

To evaluate the stellar variation during the transit, we modelled the CLV and RM effects in the Na I lines as presented in recent studies such as Yan & Henning (2018), Yan et al. (2019), Casasayas-Barris et al. (2019), and Czesla et al. (2015). The stellar spectra were modelled using MARCS (Gustafsson et al. 2008), assuming solar abundance, local thermodynamic equilibrium (LTE), and the stellar parameters presented in Table 2. With the spectroscopy made easy (SME) tool (Piskunov & Valenti 2017) we were then able to compute the stellar spectra for different limb-darkening angles and instrumental resolutions. We used the line lists from the VALD database (Ryabchikova et al. 2015). After this, the CLV for different orbital phases of the planet was modelled following Yan et al. (2017), together with the RM effect as presented by Yan et al. (2019), assuming the system parameters obtained in Sect. 3. The differences observed in the modelled spectra when the obliquity (λ) was assumed to be zero, the value measured in this work or the measurements from Winn et al. (2005) and Albrecht et al. (2012) are not significant when compared with the data.

To observe the variation of the modelled stellar line profiles during the transit of HD 209458b, we divided each continuum-normalised stellar spectrum by the modelled out-of-transit spectrum, as we did for the data (see Sect. 4.1). The evolution of these effects with the orbital phase of the planet can be observed in Fig. 2 in the form of what, hereafter, we call 2D maps. In these maps, we show the wavelength on the horizontal axis, the orbital phase of the planet on the vertical axis, and the relative flux is shown in colour. In this figure, we show the contribution of each individual effect and their combination, which clearly shows that the main contribution comes from the RM effect.

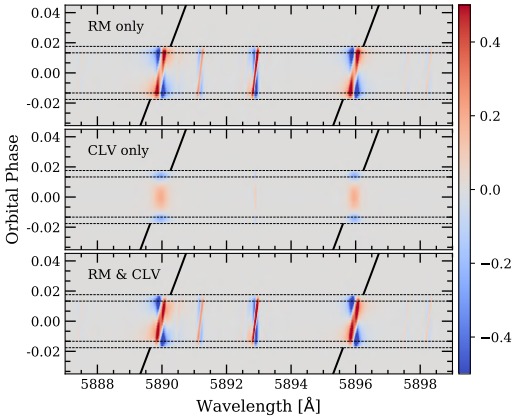

Fig. 2. Two-dimensional map of the modelled CLV and RM effects of HD 209458 system around the Na I lines after dividing all stellar models by the out-of-transit spectrum, shown in the stellar rest frame. *Top panel*: model containing only the RM effect. *Middle panel*: model containing only the CLV effect. *Bottom panel*: model containing both the RM and CLV effects. The black solid lines show the calculated position of the planetary trail extrapolated to the out-of-transit time for better visualisation of the in-transit residuals. The horizontal dashed lines show the four contacts of the transit. The colour bar describes the relative flux ($F_{in}/F_{out} - 1$) in %.

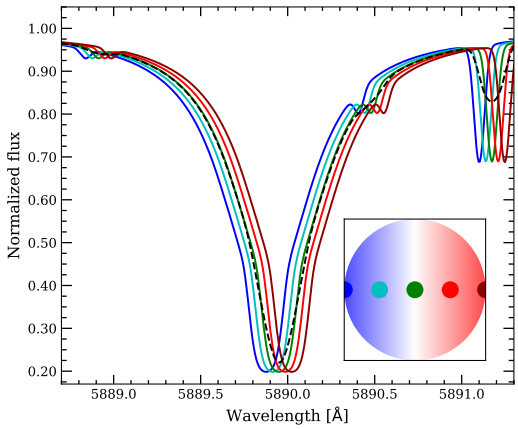

Fig. 3. Modelled stellar spectra around the Na I D2 line of HD 209458 system, containing only the RM effect. The black dashed line shows the out-of-transit spectrum (integrated stellar disc). The coloured lines show the spectra of the regions that are blocked by the planet at five different orbital phases, which are then subtracted from the integrated stellar disc spectrum to compute the final stellar models. We note that these spectra are all normalised by their own continuum level for a better comparison of the line profile. However, in the real subtraction the blocked spectra represent only a small part of the light received from the stellar disc. The approximate position of the planet in each calculation (colours) is indicated in the subplot located in the bottom right corner of the main figure.

The double feature caused by the RM effect (blue and red regions in the 2D maps) is easily recognised. This behaviour can be understood by studying Fig. 3. When the planet crosses the stellar disc, it blocks the stellar light from different regions of the disc, which have different radial velocities. In our calculation, we first computed the integrated stellar disc spectrum when the planet was not transiting (out-of-transit). Then, we computed the spectrum of the regions of the disc that were blocked by the planet at different orbital phases. At a given position of the planet, the spectrum of the blocked region does not contribute to the final integrated disc spectrum, for this reason, it was then subtracted from the integrated stellar spectrum. In Fig. 3 we show the modelled out-of-transit spectrum profile (black) and the spectra of the regions that are blocked by the planet (colours) at different orbital phases (in this case, we only include the RM effect). As expected, the out-of-transit profile is centred at the laboratory position because it includes all velocities from the stellar disc. On the other hand, the coloured spectra are shifted with respect to the out-of-transit spectrum because they come from regions of the stellar disc that are described by different radial velocities. These different shifts and line shapes of the blocked spectra with respect to the integrated disc spectrum produce the double feature observed in the modelled RM effect. We note that in this figure, the spectra have been normalised by their continuum level for better visualisation of the line profile. The real contribution of the blocked regions to the out-of-transit spectrum is, of course, very small compared to the integrated disc spectrum, which produces the effects depicted in Fig. 2.

When the transmission spectrum and light curve models are computed, it is very important to follow the same method as is applied to the data. The CLV and RM effects in the transmission spectrum and light curves strongly depend on how we perform this calculation. For example, the transmission spectrum that was computed including only the spectra between the second and third transit contacts is different from the spectrum in which the ingress and egress spectra are included, especially when the modelled spectrum only contains the CLV effect (see its dependence on orbital phase in Fig. 2). The CLV and RM effects are also partially compensated for when the in-transit exposures were moved to the stellar rest frame considering the RM radial velocity anomaly because of the misalignment that it introduces with respect to the out-of-transit spectra. On the other hand, for the transmission light curves, when we follow the method presented in Snellen et al. (2008) and Albrecht et al. (2009), where the flux is measured in the Na I stellar lines core (in the stellar rest frame), the curves are different than when we use the method presented here (in the planet rest frame and after computing the ratio between the individual spectra and the master-out spectrum; see also Sect. 7). This is particularly important for small bandwidths because the positive part (in relative flux) of the RM effect follows the radial velocities of the planet (see Fig. 2). In Fig. 4 we show some transmission spectra and light-curve models that were computed using different methods. As an example, we also show the CLV effect model presented by Yan et al. (2017), which is computed using non-LTE and in the stellar rest frame. We note how significant the effects become (especially the RM effect) in both transmission spectra and light curves when the spectra are moved to the planetary rest frame. In this particular case, for example, the CLV contribution in the transmission spectrum is more than four times smaller than the RM contribution. The importance of considering the RM effect for atmospheric studies was noted for the first time by Louden & Wheatley (2015). In this same paper, the RM effect in the transmission spectrum of HD 189733b was shown in the planet and in the stellar rest frames, noting how these effects are compensated for in the stellar rest frame.

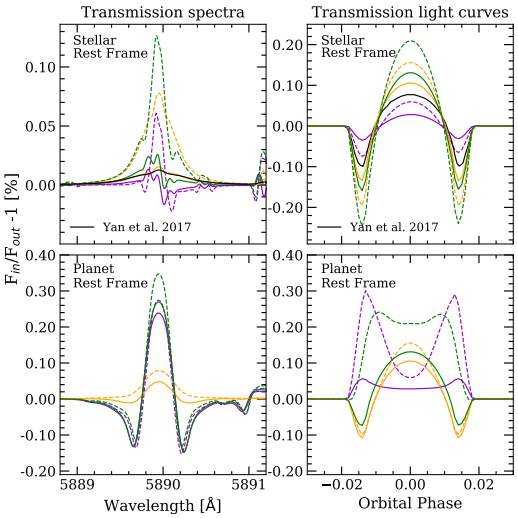

Fig. 4. Modelled transmission spectra (*left*) and light curves (*right*) around the Na I D2 line of the system, containing only the CLV (yellow), only the RM effect (violet) and both effects together (green). In the *top row* we show the results computed in the stellar rest frame, while in the *bottom row* they are computed in the planet rest frame. For the modelled transmission spectra, we show with solid lines the results obtained by combining the data between the first and fourth transit contacts, while the dashed lines show only the data between the second and third contacts. For the transmission light curves, the solid lines correspond to a bandwidth of 0.75 Å, and the dashed lines correspond to 0.4 Å passband. The (black) line shown in the stellar rest frame results corresponds to the models presented in Yan et al. (2017), which considered non-LTE effects in the stellar models calculation and measured the light curves using a different method.

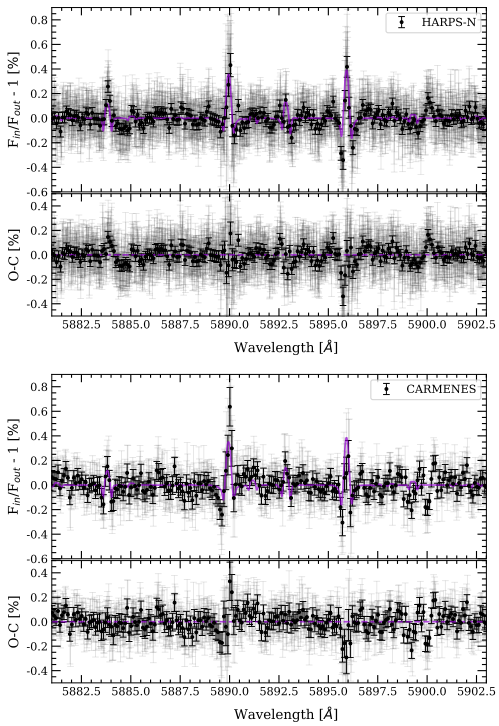

Fig. 5. HD 209458b transmission spectrum around the Na I doublet after combining three nights observed with HARPS-N (*top panel*) and two with CARMENES (*bottom panel*). The light grey dots show the original data and the black dots the binned data using a bin width of 0.1 Å. The purple line is the RM+CLV model. In each panel, the lower plot shows the residuals after the model is subtracted from the data.

5. Analysis and results

5.1. Na I transmission spectrum

The transmission spectra around the Na I lines of HD 209458b are presented in Fig. 5 and a zoom-in on the lines in Fig. 6. The results are the combination of three transits observed with HARPS-N and two with CARMENES. The individual transmission spectra obtained for each night are shown in Figs. B.1 and B.2. The laboratory wavelength of the Na I D2 and D1 lines used here are 5889.951 and 5895.924 Å (in air), from the NIST database (Kramida et al. 2019).

For all individual nights and instruments (including the noisiest nights, which are not shown here and were excluded from the analysis), instead of atmospheric absorption from the planet, we observe a pseudo-emission signal centred on the Na I D2 and D1 line positions. When the data are compared with the model containing CLV and RM contributions (see Fig. 6), we find that the data and the models are consistent. We point out that we directly compared the modelled effects with the data, without any fitting or re-scaling procedure.

Other stellar lines in this wavelength range (at 5884 and 5893 Å for example, consistent with Fe I and Ni I) also follow the expected modelled effects. We measure an averaged relative flux of 0.20 ± 0.05 and 0.12 ± 0.04% in the Na I D2 and D1 lines, respectively, using a passband of 0.4 Å in the transmission spectrum obtained using HARPS-N data. For CARMENES, we get 0.31 ± 0.08 and 0.07 ± 0.06%, respectively. If this same measurement is performed in our modelled transmission spectrum, which contains no planetary atmosphere, we obtain 0.22% in both lines. When subtracting the model from the transmission spectrum, some absorption-like residuals remain. This probably results from the combination of the limited model accuracy and the smaller S/N in the line cores.

The 2D maps around the Na I doublet combining the different nights are presented in Fig. 6. The S/N achieved around the Na I line cores is relatively low (see values in Table 1). Even with this low S/N, we are able to visually distinguish the behaviour observed in the modelled CLV+RM effects from Fig. 2 in the in-transit time region when the different nights are combined, however. We note that we did not consider any correction related to the different exposure times of the different nights when the individual results were combined. For CARMENES, a similar exposure time was used in both nights, while for HARPS-N one of the nights has a very different exposure time (300 s less than the others). This produces different smoothing of the signals because in 300 s the projected planetary radial velocity changes by around 0.9 km s^{-1} during the transit, although 0.9 km s^{-1} in

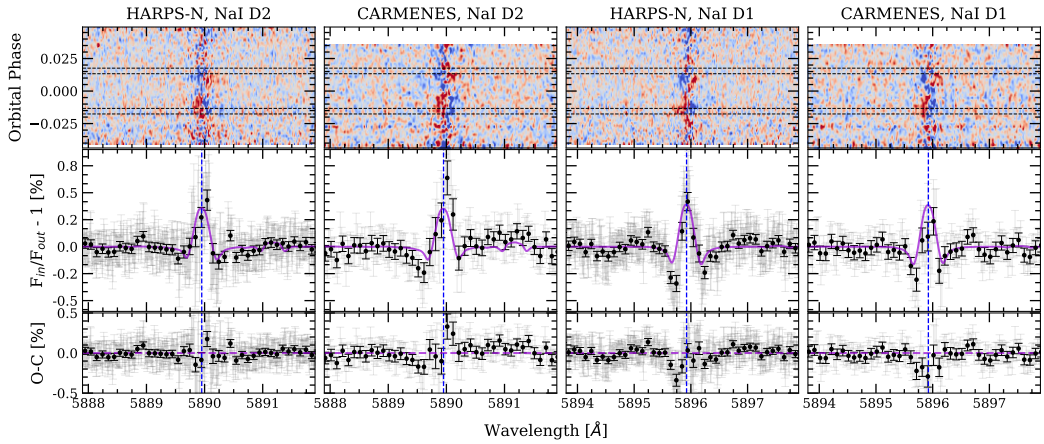

Fig. 6. Same transmission spectra as shown in Fig. 5, but zooming into each line of the Na I doublet. The blue vertical dashed lines show the laboratory value of the Na I D2 or D1 line. In addition to the transmission spectrum of each line, we show the observed 2D maps around each particular line in the stellar rest frame. In these maps the spectra have been binned in orbital phase with a bin size of 0.002. In colour we show the relative flux (blue and red correspond to negative and positive flux, respectively). The horizontal black dashed lines mark the four transit contacts.

HARPS-N correspond to around one pixel, that is, the effect is expected to be small.

5.2. Na I transmission light curves

The combined transmission light curves of the Na I D2 and D1 lines from both instruments are presented in Fig. 7. In Appendix C we present the individual transmission light curves of each instrument and line.

Because we measured the transmission light curves in the planet rest frame, the modelled light curves were computed in the same way. For small passbands (smaller than 0.4 Å) we mainly included the positive (in relative flux) contribution of the RM effect in the light curves, while for larger passbands the negative contribution was also included, which decreased the overall effect (see Fig. 2) because they cancel each other out. This is the case when a passband of 0.75 Å is used, for example.

Both instruments and individual lines show similar results. For the small 0.4 Å passband, the light curves do not show a transit-like shape, but follow the model describing the RM effect. For broader passbands, the CLV+RM model curve shows very small change in amplitude, which is difficult to observe at the S/N of our data, and indeed, the light curves observed in a 0.75 Å passband are mainly flat, with large scatter. In terms of the absorption depth, we measure 0.25 and 0.07% in the modelled light RM and CLV curves during the transit (T2-T3) for the 0.4 and 0.75 Å passbands, respectively. In the observed transmission light curves we measure absorption depths of ∼0.15 and approximately − 0.02%, respectively.

Near the central time of transit, the observed transmission light curves show a drop in the relative flux. This might be caused by the fact that the S/N of the stellar Na I lines is very low in the central cores. At zero orbital phase we measure the flux blocked by the planet in the line core, while for shorter and longer orbital phases, this measurement is performed in the wings of the stellar lines, with a higher S/N (because of the orbital motion of the planet). However, this is not reflected in the error bars because

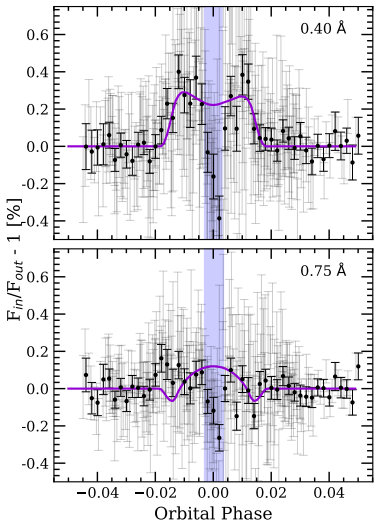

Fig. 7. Na I observed transmission light curves calculated using the passbands of 0.40 Å (*top panel*) and 0.75 Å (*bottom panel*). In light grey we show the original data containing the combined HARPS-N and CARMENES results. The black dots are the data binned by 0.002 in orbital phase. In purple we present the transmission light curve modelled considering the CLV and RM effects. In light blue we mark the region around zero orbital phase where the data present an unexpected behaviour.

they are calculated using the error propagation from the photon noise level of the observed spectra. In the 2D maps from Fig. 6 the noise in the central regions of the lines (around 0 km s^{-1}) is clearly observed. These maps are shown in the stellar rest frame,

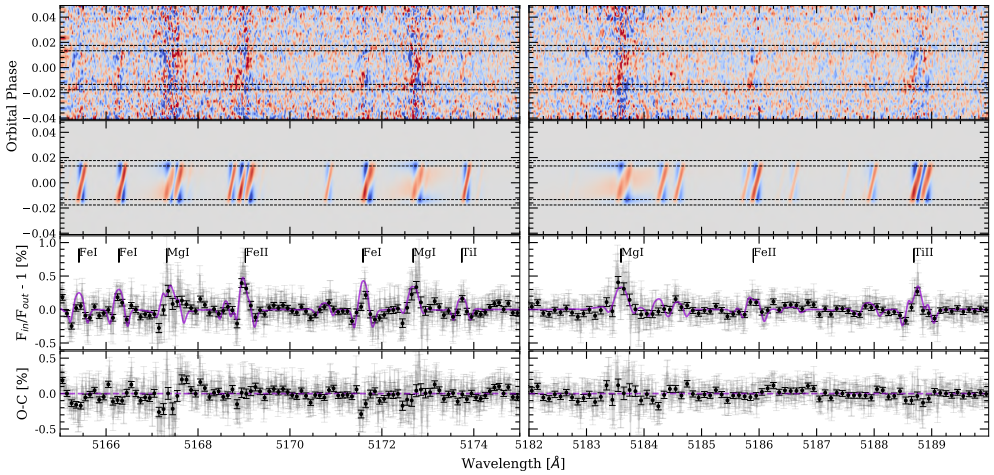

Fig. 8. Same as Fig. 6, but in the Mg I triplet (520 nm) region, obtained with HARPS-N data. The wavelength range is divided into *two panels* (*left and right*) for better visualisation. The strongest species are indicated inside the panels. We note that in most of the cases, the effects are not only due to the species specified inside the panel, as the lines are blended. In the second row (starting from top) we additionally include the modelled effects in the stellar rest frame, so that the observed and modelled 2D maps can be easily compared.

but if they are shifted to the planet rest frame (i.e. in the frame we work in), the noisier region moves to different velocities depending on the orbital phases. At zero orbital phase, however, this noise remains at 0 km s^{-1} (i.e. where the measurement is performed).

5.3. Other lines

Following the same method, we explored other strong lines in the spectrum of HD 209458. Specifically, we analysed the Hα line (6562.81 Å) using CARMENES and HARPS-N data sets, the Mg I triplet region (5167.32, 5172.68 and 5183.60 Å) using HARPS-N, and K I D1 (7698.96 Å) and Ca II IRT (8498.02, 8542.09 and 8662.14 Å) using CARMENES data sets.

The effects studied here are especially noticeable around the Mg I region, from around 5165–5190 Å. In addition to Mg I, other strong lines are present in this region, such as Fe I, Fe II, Ti I, and Ti II. The stellar line cores in this region have higher S/N than in the Na I cores and are not affected by contamination from the Earth atmosphere. Consequently, the combined effects (dominated by the RM effect), which are strong for these lines, are clearly observed (see Fig. 8). In this same figure, we show the observed and modelled 2D maps in the Mg I region. The effects can be observed in the position shown in the models, and are recovered in the transmission spectrum. For the strongest lines (Fe II at 5172, Mg I at 5173, and Mg I at 5183 Å), we computed the transmission light curves, which are presented in Fig. D.1.

For Hα, the transmission spectrum does not show any significant feature. The predicted CLV and RM effects of Hα are weak. The measured contrast is around 0.1% at the line centre. Using CARMENES, we also measured the transmission spectra around the Ca II IRT and K I D1 lines. These transmission spectra are presented in Figs. E.1–E.3. In all cases the transmission spectrum shows emission-like features that can be explained by the RM effect. For the Ca II IRT lines, the estimated effects do not describe the observations as well as for other lines. One of the reasons, and which would similarly affect Hα, is that these lines are created in the upper chromosphere and might therefore be affected differently.

5.4. Systematic effects

The error estimates of our measurements come from the propagation of the photon noise through the full analysis, and systematic effects are therefore not taken into account. One way of quantifying the systematic effects is the empirical Monte Carlo (EMC) analysis, presented by Redfield et al. (2008). The EMC is based on the random selection of individual exposures to build the in-transit and the out-of-transit samples. These samples are then used to compute the transmission spectrum, for which the absorption depth is then measured. In order to have statistical significance, this process was applied 20 000 times with different random samples. With this, we determined the probability that the measured signal is of planetary origin or is caused by a random combination of the data. This method has been applied in several atmospheric studies such as Wyttenbach et al. (2017, 2015) and Jensen et al. (2012, 2011).

We investigated four different scenarios, three of them described in Redfield et al. (2008). In summary, the first scenario, called "in–in", takes half of the spectra taken during the transit as the in-transit sample, and the other half as the out-of-transit sample. The second scenario is called "out–out" and takes half of the spectra taken when the planet is not transiting as the in-transit sample and the other half as the out-of-transit sample. At each iteration we randomly selected the spectra that form each sample. The "in–out" scenario is the real case, where the in- and out-of-transit samples correspond to the data taken when the planet is transiting and when it is not, respectively. In this case, the number of spectra in each sample changes in each iteration, but it is always ensured that the number ratio is the same as in the observations and that the smallest number is half the observed in-transit sample. The fourth scenario is called

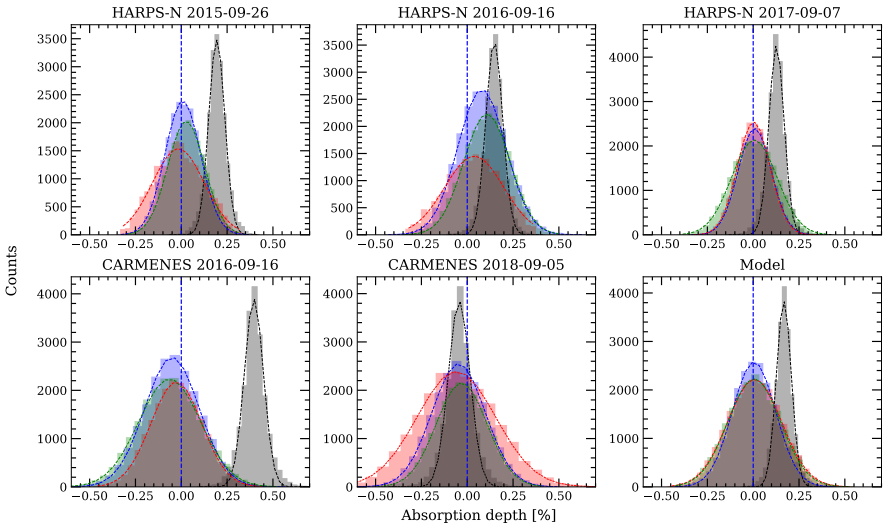

Fig. 9. Distributions of the EMC analysis of the Na I lines for the 0.4 Å passband. Each individual panel corresponds to the analysis of one night. In green we present the out-out scenario, in red the in-in, in blue the mix-mix, and in grey the in-out. The blue dashed vertical lines show the zero absorption level. We show the Gaussian fit to the histograms as coloured dashed lines.

"mix–mix". In this case, the in- and out-of-transit samples contain randomly mixed exposures taken when the planet is and is not transiting. For each scenario, we measured the absorption depth in each of the 20 000 results. This absorption was measured as the averaged flux inside a passband of 0.4 Å centred on the Na I D2 and D1 lines, respectively. For comparison, the EMC was also applied to the modelled spectra containing both the CLV and RM effects. We added random noise to the model considering a standard deviation of 0.010, measured in the continuum of HARPS-N normalised data of night 5, and we used the same number of in- and out-of-transit exposures as in this particular night. The histograms with the absorption depth measured for the 20 000 cases are shown in Fig. 9.

In all cases, the three control scenarios (in–in, out–out, and mix–mix) present distributions that are centred around 0% of absorption. The in-out scenario presents distributions centred at 0.19 ± 0.04, 0.15 ± 0.05, and 0.13 ± 0.04% for the three HARPS-N nights. For the two nights observed with CARMENES, these distributions are centred at 0.39 ± 0.05 and -0.04 ± 0.06%. On the other hand, the model shows an in-out distribution centred at 0.17 ± 0.04%. The error bars of the values correspond to the standard deviation of the distributions (see the absorption depth values summarised in Table 4).

Although we observe that the S/N in the line cores is very low as a result of the deep stellar lines, in contrast with the control distributions (which are centred at 0%), the in-out distributions are centred at a positive absorption depth, as measured in the transmission spectra. This does not occur in the case of the CARMENES night 9 observation, for which the in-out distribution is centred near ∼0%. In the individual transmission spectrum (see right panel of Fig. B.2) a drop in flux can be observed at the left side of the laboratory position for both Na I D2 and D1 lines because the spectra are noisier. In the 0.4 Å passband, this region is partially included and decreases the absorption depth.

Table 4. Absorption depth (in %) measured on the EMC distributions computed using the 0.4 Å passband.

	In–out	In–in	Out–out	Mix–mix
Night 1	0.19 ± 0.04	-0.01 ± 0.14	0.03 ± 0.10	0.01 ± 0.10
Night 3	0.15 ± 0.05	0.04 ± 0.16	0.11 ± 0.13	0.08 ± 0.13
Night 5	0.13 ± 0.04	0.00 ± 0.09	0.01 ± 0.12	0.01 ± 0.09
Night 7	0.39 ± 0.05	-0.03 ± 0.14	-0.06 ± 0.17	-0.05 ± 0.15
Night 9	-0.04 ± 0.06	-0.06 ± 0.21	-0.03 ± 0.14	-0.05 ± 0.14
Model	0.17 ± 0.04	0.01 ± 0.15	0.00 ± 0.14	0.00 ± 0.12

6. Comparison with previous results

HD 209458b is one of the most frequently studied planets, with several detections of the Na I doublet using different facilities. Here, we compare our results around these spectral lines with those presented in Sing et al. (2008), Snellen et al. (2008), and Albrecht et al. (2009).

We compared our results with the transmission spectrum obtained by Sing et al. (2008) using mid-resolution ($\Re$ = 5540) observations with the STIS at HST (see Fig. 10). For this comparison, we binned the transmission spectra from Fig. 5 in 0.55 Å intervals, which is the STIS pixel size. The centre of each bin was located at the positions presented in Sing et al. (2008). The modelled spectrum was computed using only the orbital phases covered by HST, and was then binned at the same intervals as the data. Our high-resolution binned data and our model are consistent with the HST observations. Sing et al. (2008) discarded the two points falling on the Na I line cores from their analysis because of possible telluric contamination: their wavelength positions were consistent with the Earth's radial velocities during the observations. However, our results reveal that an alternative explanation is the combination of the RM+CLV effects, which is also valid for other wavelengths such as the Ni I position at

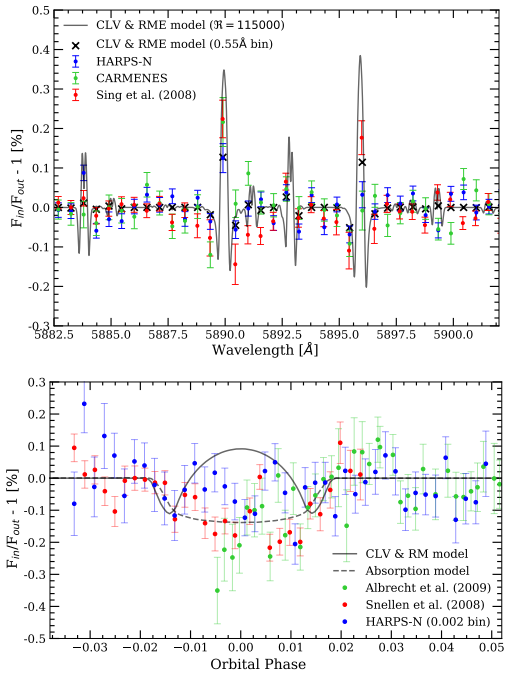

Fig. 10. *Top panel*: comparison of the CARMENES and HARPS-N transmission spectra with the result presented in Sing et al. (2008). The CARMENES and HARPS-N results are presented using a binning width of 0.55 Å. *Bottom panel*: HD 209458b transmission light curves from Snellen et al. (2008), Albrecht et al. (2009), and this work (binned by 0.002 in orbital phase). The dashed line shows the transmission model as presented in those studies, while the solid line is the expected CLV and RM effects obtained with the same method.

5893 Å, which is also visible in the figure. In HST observations, this telluric contamination is absent in other strong lines such as Fe I, while the CLV and RM effects should remain (see Fig. 8), although they are perhaps not detectable by STIS. When we compared the results, we noted an offset of −0.2 Å (half of the STIS pixel size) between HST and the results presented here.

Snellen et al. (2008) and Albrecht et al. (2009) measured the transmission light curves by integrating the flux inside the stellar line cores, in the stellar rest frame, and compared the flux with the one measured inside two reference passbands. They measured a Na I absorption of 0.135 ± 0.017% with a passband of 0.75 Å. Following this same method, we built a transmission light curve with the HARPS-N data. In Fig. 10 we compare our own light curve with those presented in Snellen et al. (2008) and Albrecht et al. (2009). None of the results agrees with the modelled CLV and RM effects light curve. On the other hand, although we are not able to reproduce the full transmission light curve from their results with our data, most of the points are consistent considering the error bars. Light curve observations with higher S/N might help solve these issues. Nevertheless, the agreement between our models and the transmission spectrum results obtained in Sect. 5 (Figs. 5, 6, and 8) gives us confidence that the signals seen in our analysis can be explained without invoking planetary absorption.

Finally, Keles et al. (2019) studied the presence of K I in the atmosphere of HD 209458b. Interestingly, they reported an emission-like behaviour at low bandwidths, which would be consistent with the RM effect and non-detection of K I line at 7699 Å reported in this work.

7. Discussion and conclusions

We combined nine transit observations (five with HARPS-N and four with CARMENES) to measure the RM effect using the radial velocity measurements obtained from SERVAL. The best-fit model shows a projected spin-orbit angle of $\lambda = -1.6 \pm 0.3$, indicating a well-aligned orbit, as presented by Winn et al. (2005) and Albrecht et al. (2012). Because of its brightness and the RM amplitude, HD 209458b is an excellent planet for chromatic RM studies (Snellen 2004, Di Gloria et al. 2015, and Yan et al. 2015), especially using ESPRESSO-like observations with high S/N.

We also computed the transmission spectrum of HD 209458b around the Na I using three archival nights observed with HARPS-N, and two with CARMENES. The importance of considering the CLV and RM effect in atmospheric studies has previously been pointed out. Yan et al. (2017) predicted the significance of the CLV effect in atmospheric studies of HD 209458b around Na I. In particular, we observe that this effect becomes significant in the transmission light curves (∼0.1% of contrast, see Fig. 4). Here, in addition to this effect, we also considered the RM effect contribution, which is found to strongly increase the residual effects in the line cores of the transmission spectrum by a factor of about four when computed in the planet rest frame. For all individual nights, the resulted transmission spectra of the exoplanetary atmosphere show an emission-like signal instead of an expected absorption signal, as has been found in previous studies by Albrecht et al. (2009), Snellen et al. (2008), Sing et al. (2008), and Charbonneau et al. (2002). The transmission spectra presented here are consistent with the modelled CLV and RM effects on the stellar line profiles without considering any contribution from the exoplanet atmosphere.

The same is observed in the transmission light curves that are computed using narrow passbands, where the positive contribution of the RM effect is the dominating factor. For wide passbands, however, the effects are diluted and the transmission light curves do not present enough S/N to observe any clear behaviour. Further observations are needed at higher S/N to build reliable light curves that can be compared to our models.

Finally, we compared our measurements and models to previous studies of the presence of Na I in the atmosphere of HD 209458b. Our results reveal that an alternative explanation for the transmission spectrum derived from HST observations is the combination of the RM and CLV effects. When we compared this to High-Dispersion Spectrograph/Subaru observations, we were unable to reproduce the full transmission light curve from their results with our data, but most of the points are consistent considering the error bars. Moreover, none of the light curves are consistent with the modelled effects. Light curve observations with higher S/N are needed to solve this issue. Nevertheless, the agreement between our models and the transmission spectrum results obtained in Sect. 5 (Figs. 5, 6 and 8) gives us confidence that the signals seen in all data sets can be explained without invoking planetary absorption by Na I in the atmosphere of HD 209458b. Our results also imply that the

detection of atmospheric features needs to account for these effects. Detailed modelling of both RM and CLV effects like this is mandatory when the characterisation of small Earth-like planets around low-mass stars is attempted with the ELTs in the coming decades.

Acknowledgements. Based on observations made with the Italian Telescopio Nazionale *Galileo* (TNG) operated on the island of La Palma by the Fundación Galileo Galilei of the INAF (Istituto Nazionale di Astrofisica) at the Spanish Observatorio del Roque de los Muchachos of the Instituto de Astrofisica de Canarias. CARMENES is an instrument for the Centro Astronómico Hispano-Alemán de Calar Alto (CAHA, Almería, Spain). CARMENES is funded by the German Max-Planck-Gesellschaft (MPG), the Spanish Consejo Superior de Investigaciones Científicas (CSIC), the European Union through FEDER/ERF FICTS-2011-02 funds, and the members of the CARMENES Consortium (Max-Planck-Institut für Astronomie, Instituto de Astrofísica de Andalucía, Landessternwarte Königstuhl, Institut de Ciències de l'Espai, Insitut für Astrophysik Göttingen, Universidad Complutense de Madrid, Thüringer Landessternwarte Tautenburg, Instituto de Astrofísica de Canarias, Hamburger Sternwarte, Centro de Astrobiología and Centro Astronómico Hispano- Alemán), with additional contributions by the Spanish Ministry of Economy, the German Science Foundation through the Major Research Instrumentation Programme and DFG Research Unit FOR2544 "Blue Planets around Red Stars", the Klaus Tschira Stiftung, the states of Baden-Württemberg and Niedersachsen, and by the Junta de Andalucía. This work is partly financed by the Spanish Ministry of Economics and Competitiveness through project ESP2016-80435-C2-2-R and ESP2017-87143-R. G.C. acknowledges the support by the Natural Science Foundation of Jiangsu Province (Grant No. BK20190110), the National Natural Science Foundation of China (Grant No. 11503088, 11573073, 11573075). F.Y. acknowledges the support of the DFG priority program SPP 1992 "Exploring the Diversity of Extrasolar Planets (RE 1664/16-1)". This work made use of PyAstronomy and of the VALD database, operated at Uppsala University, the Institute of Astronomy RAS in Moscow, and the University of Vienna.

References

Abetti, G., & Castelli, I. 1935, Osservazioni e memorie dell'Osservatorio astrofisico di Arcetri, 53, 25
Albrecht, S., Snellen, I., de Mooij, E., & Le Poole, R. 2009, IAU Symp., 253, 520
Albrecht, S., Winn, J. N., Johnson, J. A., et al. 2012, ApJ, 757, 18
Alonso-Floriano, F. J., Snellen, I. A. G., Czesla, S., et al. 2019, A&A, 629, A110
Appenzeller, I., & Schröter, E. H. 1967, ApJ, 147, 1100
Bauer, F. F., Zechmeister, M., & Reiners, A. 2015, A&A, 581, A117
Bonomo, A. S., Desidera, S., Benatti, S., et al. 2017, A&A, 602, A107
Bourrier, V., Cegla, H. M., Lovis, C., & Wyttenbach, A. 2017, A&A, 599, A33
Brown, D. J. A., Triaud, A. H. M. J., Doyle, A. P., et al. 2017, MNRAS, 464, 810
Caballero, J. A., Guàrdia, J., López del Fresno, M., et al. 2016, SPIE Conf. Ser., 9910, 99100E
Casasayas-Barris, N., Palle, E., Nowak, G., et al. 2017, A&A, 608, A135
Casasayas-Barris, N., Pallé, E., Yan, F., et al. 2018, A&A, 616, A151
Casasayas-Barris, N., Pallé, E., Yan, F., et al. 2019, A&A, 628, A9
Charbonneau, D., Brown, T. M., Latham, D. W., & Mayor, M. 2000, ApJ, 529, L45
Charbonneau, D., Brown, T. M., Noyes, R. W., & Gilliland, R. L. 2002, ApJ, 568, 377
Cosentino, R., Lovis, C., Pepe, F., et al. 2012, Proc. SPIE, 8446, 84461V
Cosentino, R., Lovis, C., Pepe, F., et al. 2014, SPIE Conf. Ser., 9147, 91478C
Czesla, S., Klocová, T., Khalafinejad, S., Wolter, U., & Schmitt, J. H. M. M. 2015, A&A, 582, A51
Czesla, S., Schröter, S., Schneider, C. P., et al. 2019, PyA: Python astronomy-related packages
Di Gloria, E., Snellen, I. A. G., & Albrecht, S. 2015, A&A, 580, A84
Evans, T. M., Aigrain, S., Gibson, N., et al. 2015, MNRAS, 451, 680
Foreman-Mackey, D., Hogg, D. W., Lang, D., & Goodman, J. 2013, PASP, 125, 306
Gustafsson, B., Edvardsson, B., Eriksson, K., et al. 2008, A&A, 486, 951
Henry, G. W., Marcy, G. W., Butler, R. P., & Vogt, S. S. 2000, ApJ, 529, L41
Jensen, A. G., Redfield, S., Endl, M., et al. 2011, ApJ, 743, 203
Jensen, A. G., Redfield, S., Endl, M., et al. 2012, ApJ, 751, 86
Kausch, W., Noll, S., Smette, A., et al. 2015, A&A, 576, A78
Keles, E., Mallonn, M., von Essen, C., et al. 2019, MNRAS, 489, L37
Khalafinejad, S., von Essen, C., Hoeijmakers, H. J., et al. 2017, A&A, 598, A131
Kramida, A., Yu. Ralchenko, Reader, J., & NIST ASD Team. 2019, NIST Atomic Spectra Database (ver. 5.5.2), [Online], available: https://physics.nist.gov/asd [2019, September 15]. National Institute of Standards and Technology, Gaithersburg, MD.
Louden, T., & Wheatley, P. J. 2015, ApJ, 814, L24
Mayor, M., Pepe, F., Queloz, D., et al. 2003, The Messenger, 114, 20
McLaughlin, D. B. 1924, ApJ, 60, 22
Naef, D., Mayor, M., Beuzit, J. L., et al. 2004, A&A, 414, 351
Ohta, Y., Taruya, A., & Suto, Y. 2005, ApJ, 622, 1118
Oshagh, M., Triaud, A. H. M. J., Burdanov, A., et al. 2018, A&A, 619, A150
Piskunov, N., & Valenti, J. A. 2017, A&A, 597, A16
Quirrenbach, A., Amado, P. J., Caballero, J. A., et al. 2014, Proc. SPIE, 9147, 91471F
Quirrenbach, A., Amado, P. J., Ribas, I., et al. 2018, SPIE Conf. Ser., 10702, 107020W
Redfield, S., Endl, M., Cochran, W. D., & Koesterke, L. 2008, ApJ, 673, L87
Richardson, L. J., Harrington, J., Seager, S., & Deming, D. 2006, ApJ, 649, 1043
Rossiter, R. A. 1924, ApJ, 60, 15
Ryabchikova, T., Piskunov, N., Kurucz, R. L., et al. 2015, Phys. Scr, 90, 054005
Sánchez-López, A., Alonso-Floriano, F. J., López-Puertas, M., et al. 2019, A&A, 630, A53
Sing, D. K., Vidal-Madjar, A., Désert, J. M., Lecavelier des Etangs, A., & Ballester, G. 2008, ApJ, 686, 658
Smareglia, R., Bignamini, A., Knapic, C., Molinaro, M., & GAPS Collaboration 2014, ASP Conf. Ser., 485, 435
Smette, A., Sana, H., Noll, S., et al. 2015, A&A, 576, A77
Snellen, I. A. G. 2004, MNRAS, 353, L1
Snellen, I. A. G., Albrecht, S., de Mooij, E. J. W., & Le Poole, R. S. 2008, A&A, 487, 357
Torres, G., Winn, J. N., & Holman, M. J. 2008, ApJ, 677, 1324
Winn, J. N., Noyes, R. W., Holman, M. J., et al. 2005, ApJ, 631, 1215
Wyttenbach, A., Ehrenreich, D., Lovis, C., Udry, S., & Pepe, F. 2015, A&A, 577, A62
Wyttenbach, A., Lovis, C., Ehrenreich, D., et al. 2017, A&A, 602, A36
Yan, F., & Henning, T. 2018, Nat. Astron., 2, 714
Yan, F., Fosbury, R. A. E., Petr-Gotzens, M. G., Pallé, E., & Zhao, G. 2015, ApJ, 806, L23
Yan, F., Pallé, E., Fosbury, R. A. E., Petr-Gotzens, M. G., & Henning, T. 2017, A&A, 603, A73
Yan, F., Casasayas-Barris, N., Molaverdikhani, K., et al. 2019, A&A, 632, A69
Zechmeister, M., Anglada-Escudé, G., & Reiners, A. 2014, A&A, 561, A59
Zechmeister, M., Reiners, A., Amado, P. J., et al. 2018, A&A, 609, A12

Appendix A: MCMC results and probability distributions

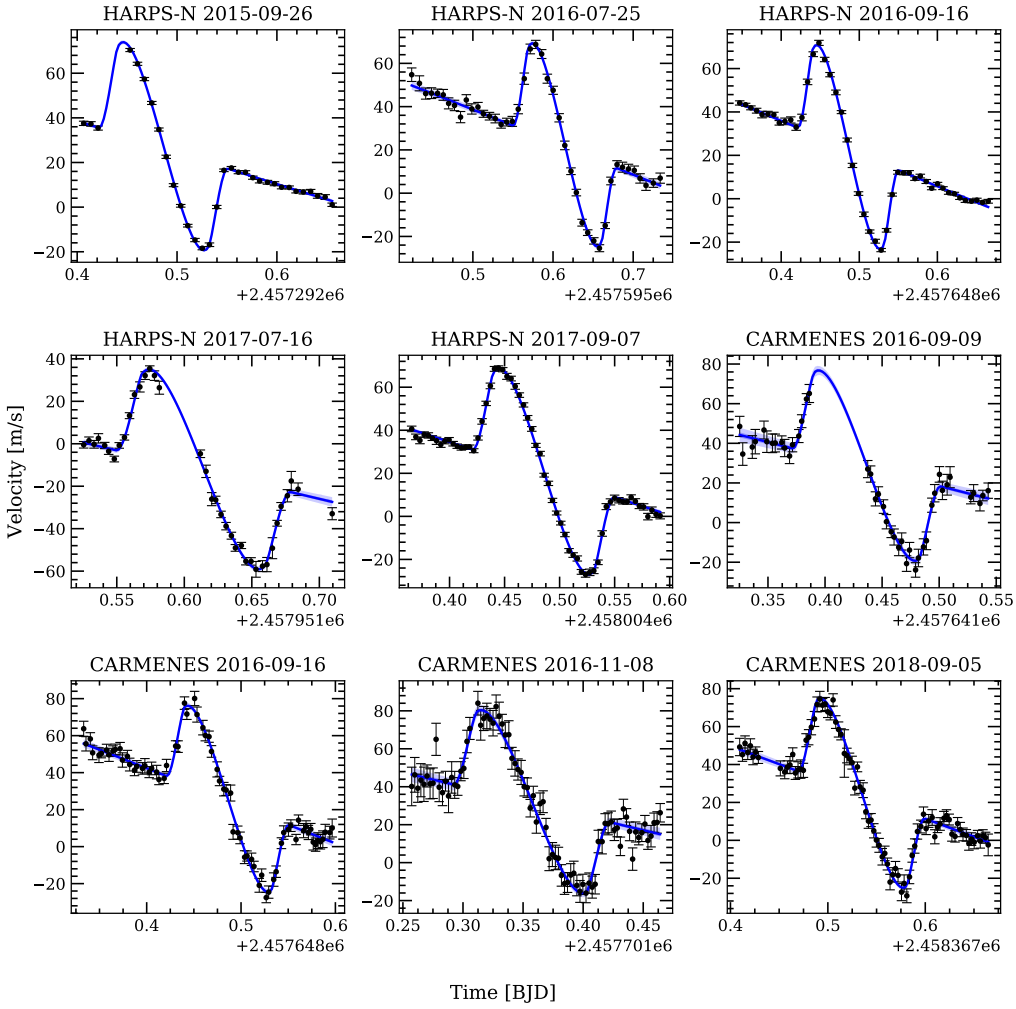

Fig. A.1. Measured stellar radial velocities of HD 209458 during the transit (black) for different nights and instruments. In blue we show the best-fit model obtained with the MCMC procedure.

Table A.1. Extension of Table 3.

		Case 1			Case 2			Case 3		
Parameter	Units	Value	1σ	3σ	Value	1σ	3σ	Value	1σ	3σ
Δv^{H1}	m s^{-1}	26.4	±0.2	±0.6	26.4	±0.2	$^{+0.6}_{-0.7}$	25.4	$^{+6.0}_{-7.5}$	$^{+17.8}_{-18.8}$
Δv^{H2}	m s^{-1}	21.4	±0.3	±0.9	21.4	±0.3	$^{+1.0}_{-0.8}$	20.4	$^{+6.4}_{-8.0}$	$^{+18.3}_{-19.9}$
Δv^{H3}	m s^{-1}	22.9	±0.2	$^{+0.5}_{-0.4}$	22.9	±0.2	±0.4	21.9	$^{+6.4}_{-8.0}$	$^{+19.0}_{-20.1}$
Δv^{H4}	m s^{-1}	−12.9	±0.3	±1.0	−12.9	±0.4	±1.0	−13.8	$^{+6.3}_{-8.1}$	$^{+18.9}_{-20.0}$
Δv^{H5}	m s^{-1}	20.0	±0.2	±0.5	20.0	±0.2	±0.5	18.9	$^{+7.2}_{-9.1}$	$^{+20.7}_{-22.5}$
Δv^{C1}	m s^{-1}	27.9	±0.6	$^{+1.7}_{-1.8}$	27.9	±0.6	$^{+1.8}_{-1.7}$	26.8	$^{+6.5}_{-8.1}$	$^{+18.1}_{-20.2}$
Δv^{C2}	m s^{-1}	24.9	±0.4	±1.2	24.9	±0.4	$^{+1.3}_{-1.1}$	23.5	$^{+8.7}_{-10.9}$	$^{+24.9}_{-27.7}$
Δv^{C3}	m s^{-1}	31.2	±0.7	$^{+2.0}_{-1.9}$	31.1	±0.6	$^{+1.9}_{-1.7}$	30.4	$^{+6.6}_{-8.2}$	$^{+19.2}_{-21.7}$
Δv^{C4}	m s^{-1}	24.0	±0.4	±1.2	24.0	±0.4	±1.1	22.7	$^{+8.1}_{-10.1}$	$^{+24.2}_{-25.9}$
$K_\star^{H1}$	m s^{-1}	79.6	±1.3	$^{+3.8}_{-3.6}$	79.8	$^{+1.2}_{-1.3}$	$^{+3.7}_{-3.8}$	71.9	$^{+5.5}_{-6.5}$	$^{+9.9}_{-11.6}$
$K_\star^{H2}$	m s^{-1}	84.9	±2.1	$^{+6.0}_{-6.1}$	84.0	$^{+2.1}_{-2.2}$	$^{+5.3}_{-6.7}$	77.1	$^{+5.7}_{-7.1}$	$^{+11.1}_{-14.8}$
$K_\star^{H3}$	m s^{-1}	85.2	±0.8	±2.4	85.4	$^{+0.8}_{-0.9}$	$^{+2.4}_{-2.6}$	77.2	$^{+5.8}_{-7.0}$	$^{+10.3}_{-13.0}$
$K_\star^{H4}$	m s^{-1}	85.5	$^{+3.5}_{-3.4}$	$^{+10.2}_{-9.8}$	84.5	$^{+3.7}_{-3.4}$	$^{+10.0}_{-9.5}$	77.2	$^{+6.4}_{-7.6}$	$^{+14.0}_{-15.5}$
$K_\star^{H5}$	m s^{-1}	95.9	±1.4	$^{+3.7}_{-4.1}$	95.5	$^{+1.4}_{-1.3}$	$^{+4.0}_{-3.9}$	86.7	$^{+7.0}_{-7.9}$	$^{+11.8}_{-15.5}$
$K_\star^{C1}$	m s^{-1}	83.1	$^{+5.5}_{-5.2}$	$^{+14.9}_{-15.0}$	85.9	±5.2	$^{+15.0}_{-15.5}$	75.3	$^{+7.8}_{-7.9}$	$^{+20.4}_{-15.1}$
$K_\star^{C2}$	m s^{-1}	114.5	±2.9	$^{+8.5}_{-8.0}$	113.9	±2.9	$^{+6.0}_{-8.6}$	103.4	$^{+8.4}_{-9.5}$	$^{+15.8}_{-20.3}$
$K_\star^{C3}$	m s^{-1}	85.8	$^{+6.0}_{-6.2}$	$^{+13.7}_{-18.2}$	79.5	±4.9	$^{+19.7}_{-13.7}$	78.1	$^{+8.6}_{-8.2}$	$^{+22.7}_{-17.0}$
$K_\star^{C4}$	m s^{-1}	108.0	$^{+3.1}_{-3.0}$	$^{+8.7}_{-8.9}$	109.1	$^{+3.0}_{-3.1}$	$^{+8.4}_{-8.9}$	97.4	$^{+7.3}_{-8.9}$	$^{+15.8}_{-18.6}$

Notes. MCMC best-fit Δv and $K_\star$ values with 1σ, and 3σ error bars for different assumptions: $i_\star = 90$ deg and circular orbit (Case 1), $i_\star$ free and circular orbit (Case 2), and $i_\star = 90$ deg and free eccentricity (Case 3).

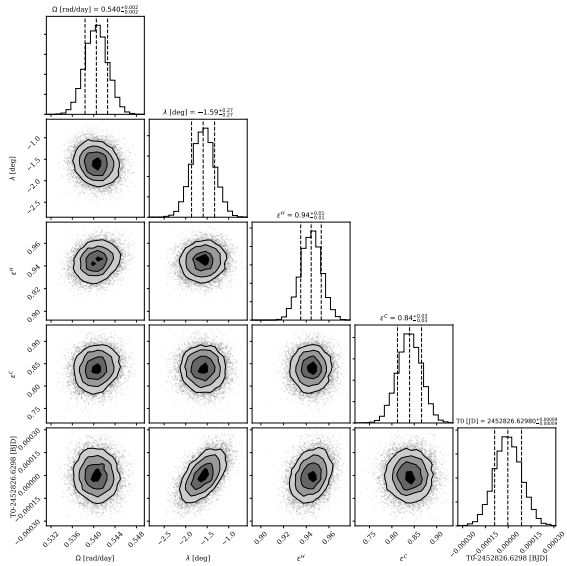

Fig. A.2. Correlation diagrams for the probability distribution of the RM model parameters for HD 209458b, obtained assuming $i_\star = 90$ deg and circular orbit (Case 1). The dashed lines overimposed on the histograms correspond to the 16 and 84 percentiles used to obtain the 1σ statistical errors. One hundred walkers and 10^5 steps are used in this analysis.

Appendix B: Individual transmission spectra

B.1. HARPS-N data

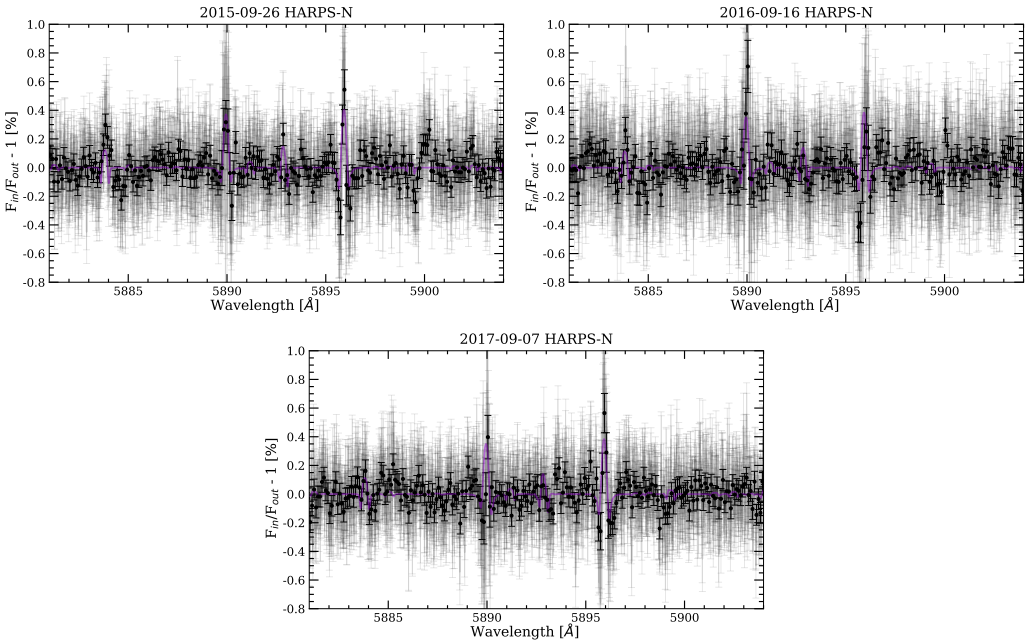

Fig. B.1. HD 209458b transmission spectra around the Na I doublet for three different HARPS-N data sets. In light grey we show the original data, and as black dots the data binned by 0.1 Å. In purple we show the RME+CLV model for each data set.

B.2. CARMENES data

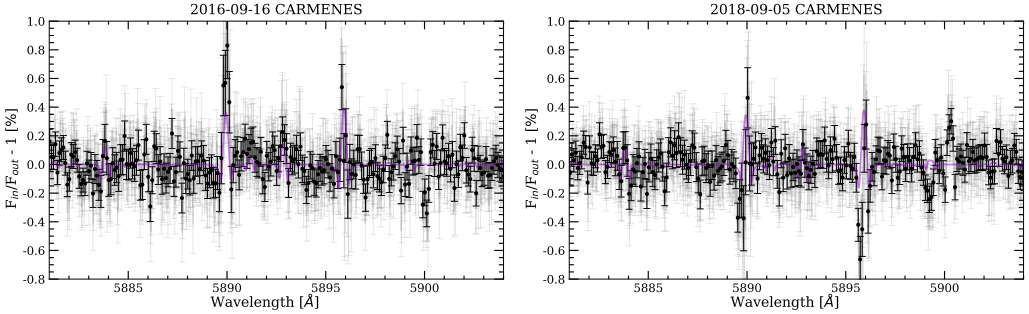

Fig. B.2. Same as Fig. B.1, but for CARMENES data.

Appendix C: Individual instrument and Na I lines transmission light curves

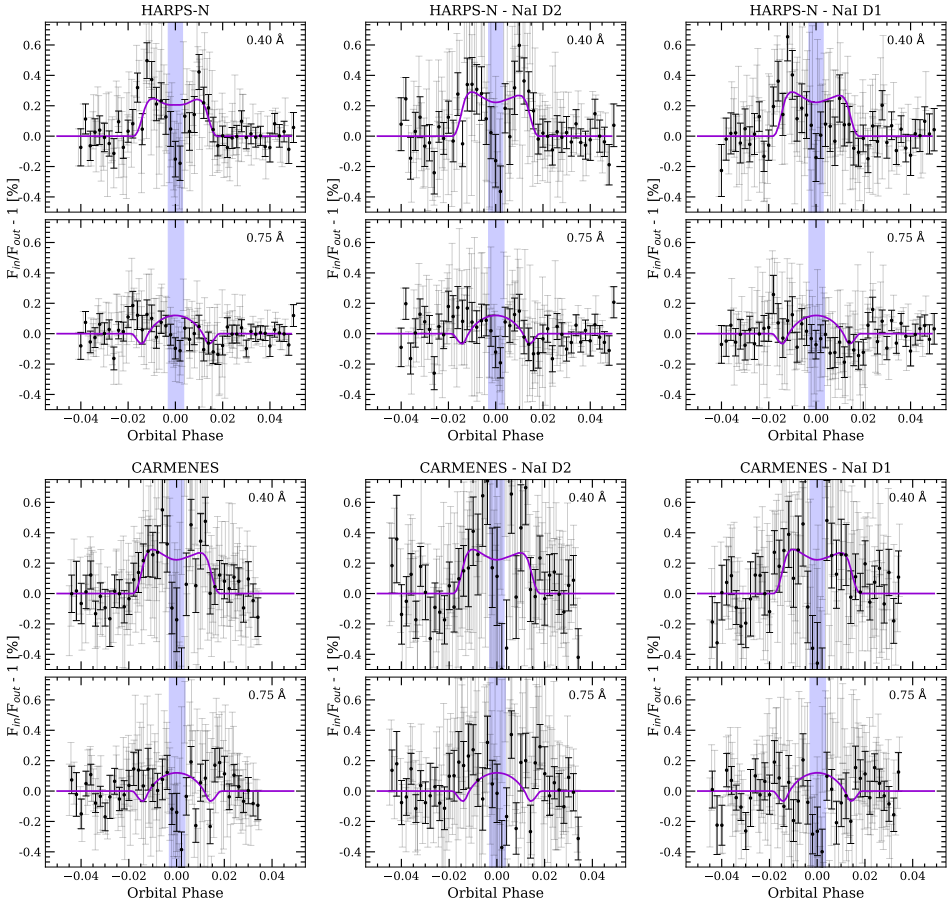

Fig. C.1. Observed transmission light curves for the Na I doublet computed using HARPS-N (*top row panels*) and CARMENES (*bottom row panels*) data sets. In each panel we show the light curves for two different passbands: 0.4 Å (*top row*) and 0.75 Å (*bottom row*). Each column corresponds to a different computation: the Na I D2 and D1 lines combined (*left column*), only Na I D2 (*middle column*), and only Na I D1 (*right column*). In all cases, the light grey data correspond to the original data, while the black dots are the data binned by 0.002 in orbital phase. In purple we show the modelled light curves containing the CLV and RM effects.

Appendix D: Transmission light curves around Fe II λ5169, Mg I λ5173, and Mg I λ5183

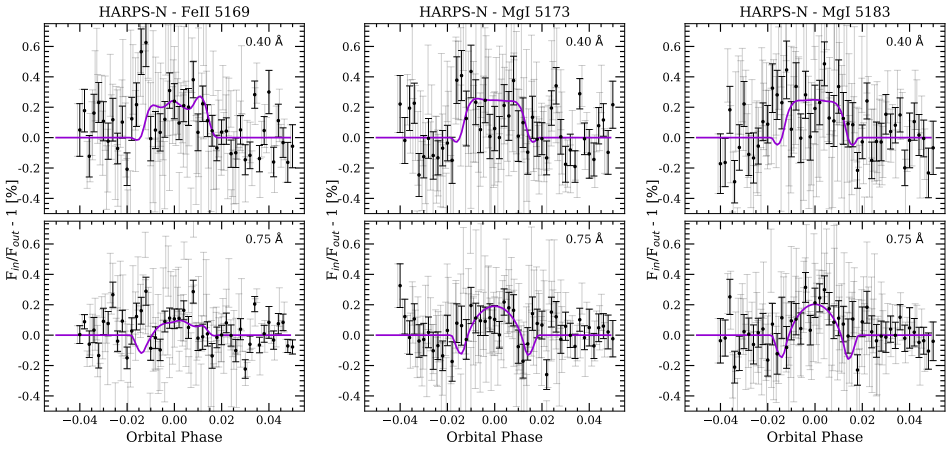

Fig. D.1. Same as Fig. C.1, but for the Fe II line at 5169 Å (*left*), the Mg I line at 5173 Å (*middle*), and for Mg I 5183 Å (*right*).

Appendix E: Transmission spectra around Hα, K I D1, and Ca II IRT

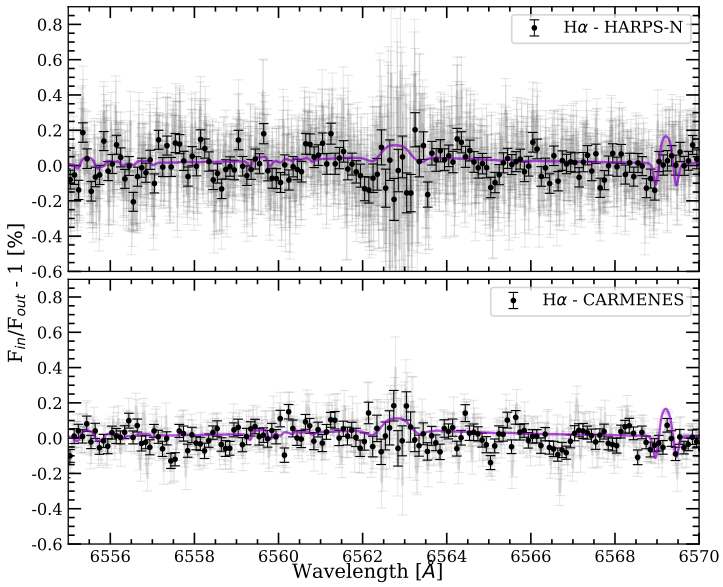

Fig. E.1. Same as Fig. B.1, but around the Hα line. In the *top panel* we show the results combining three HARPS-N transits, and in the *bottom panel* the results after combining two CARMENES observations.

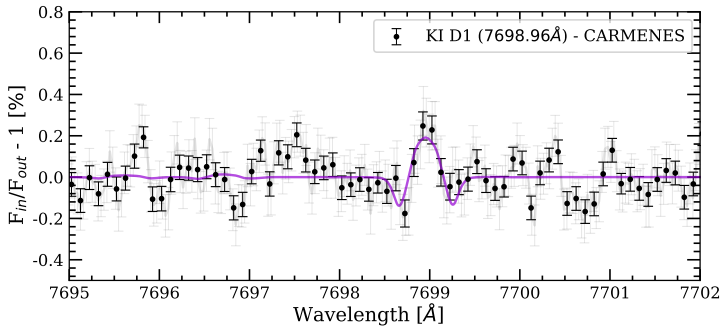

Fig. E.2. Same as Fig. B.1, but around the K I D1 line at 7698.96 Å. This result is the combination of two CARMENES observations (HARPS-N does not cover this wavelength region).

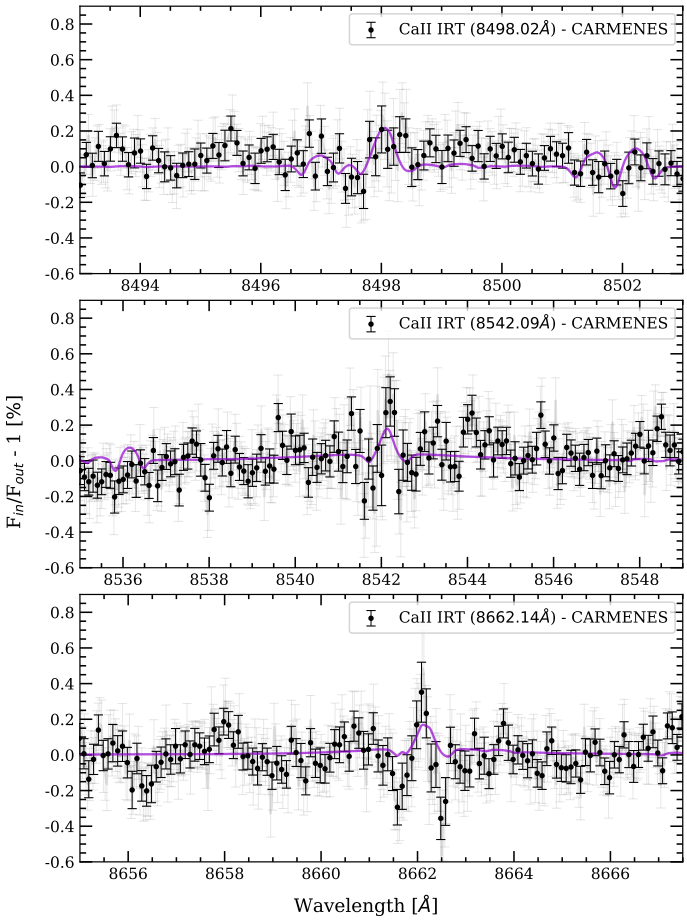

Fig. E.3. Same as Fig. B.1, but around the Ca II IRT triplet. This result is the combination of two CARMENES observations (HARPS-N does not cover this wavelength region). In each panel we show the transmission spectrum around one of the Ca II IRT lines. Each line is specified inside the panel. We note that for these lines the model seems to be less intense than the data.

6

HD 209458b's atmosphere seen by ESPRESSO

If we're both going crazy,
then we'll go crazy together, right?

–Stranger Things, 2016

In this chapter we present the confirmation of the results presented in Chapter 5 using two high quality transit observations of HD 209458b obtained with the ESPRESSO spectrograph ($\Re \sim 140\,000$). These observations are based on Guaranteed Time Observations collected at the European Southern Observatory by the ESPRESSO Consortium. Following the same methodology used in chapter 5 we extract the transmission spectrum and light curves of HD 209458b in different wavelength regions covered by ESPRESSO. In particular, we focus on the NaI doublet, Hα, MgI, FeI, and KI individual lines. Additionally, we apply the cross-correlation technique in order to search for atoms and molecules that may originate tens to thousands of individual absorption lines in the transmission spectrum. Using this technique we search for FeI, FeII, CaI, TiO, VO and VI signatures produced by the exoplanet atmosphere. The results presented in this chapter are accepted for publication in A&A (Casasayas-Barris et al., 2020a).

As observed in the HARPS-N and CARMENES results, ESPRESSO observations clearly show strong emission-like features in the transmission spectra

located at the position of all stellar lines. These features are consistent with the modelled RM and CLV deformation of the stellar lines profile. For the HD 209458b system, the velocity of the planet during the transit and the RM deformation overlap, making the detection of atmospheric features that are also present in the stellar spectrum extremely challenging. TiO and VO molecules are not expected to be present in the stellar atmosphere, and we find no evidence of these species in HD 209458b, potentially caused by the inaccurate line lists available for these molecules at high spectral resolution.

Here, given the high S/N of ESPRESSO data, we are able to compare the modelled CLV and RM effects when assuming different stellar atmospheric models. We observe that using the local thermodynamic equilibrium (LTE) approximation, the effects remain underestimated in comparison with the observations. When the non-LTE is assumed, the modelled effects describe the transmission spectrum better. When exploring the time-variations of these effects and comparing with the data, we observe that the results are better explained when the models include only the RM deformation, probably indicating an overestimation of the CLV. This is also suggested by the extracted local stellar spectra.

Astronomy & Astrophysics manuscript no. output
December 11, 2020

The atmosphere of HD 209458b seen with ESPRESSO*

No detectable planetary absorptions at high resolution

N. Casasayas-Barris[1,2], E. Palle[1,2], M. Stangret[1,2], V Bourrier[3], H. M. Tabernero[4], F. Yan[5], F. Borsa[6], R. Allart[3], M.R. Zapatero Osorio[7], C. Lovis[3], S. G. Sousa[4], G. Chen[8], M. Oshagh[1,2], N. C. Santos[4,9], F. Pepe[3], R. Rebolo[1,2,13], P. Molaro[11,12], S. Cristiani[11], V. Adibekyan[4,9], Y. Alibert[10], C. Allende Prieto[1,2], F. Bouchy[3], O. D. S. Demangeon[4,9,16], P. Di Marcantonio[11], V. D'Odorico[11,12], D. Ehrenreich[3], P. Figueira[4,14], R. Génova Santos[1,2], J. I. González Hernández[1,2], B. Lavie[3], J. Lillo-Box[14], G. Lo Curto[15], C. J. A. P. Martins[4,16], A. Mehner[17], G. Micela[18], N. J. Nunes[19], E. Poretti[6,20], A. Sozzetti[21], A. Suárez Mascareño[1,2], and S. Udry[3]

[1] Instituto de Astrofísica de Canarias, Vía Láctea s/n, 38205 La Laguna, Tenerife, Spain
e-mail: nuriacb@iac.es
[2] Departamento de Astrofısica, Universidad de La Laguna, E-38206, La Laguna, Tenerife, Spain
[3] Observatoire Astronomique de l'Université de Genève, Chemin Pegasi 51b, Sauverny, CH-1290, Switzerland
[4] Instituto de Astrofísica e Ciências do Espaço, Universidade do Porto, CAUP, Rua das Estrelas, 4150-762 Porto, Portugal
[5] Institut für Astrophysik, Georg-August-Universität, Friedrich-Hund-Platz 1, D-37077 Göttingen, Germany
[6] INAF - Osservatorio Astronomico di Brera, Via Bianchi 46, 23807 Merate, Italy
[7] Centro de Astrobiología (CSIC-INTA), Carretera de Ajalvir, km 4. E-28850 Torrejón de Ardoz, Madrid, Spain
[8] Key Laboratory of Planetary Sciences, Purple Mountain Observatory, Chinese Academy of Sciences, Nanjing 210023, China
[9] Departamento de Física e Astronomia, Faculdade de Ciências, Universidade do Porto, Rua Campo Alegre, 4169-007, Porto, Portugal
[10] Physics Institute, University of Bern, Sidlerstrasse 5, 3012 Bern, Switzerland
[11] INAF - Osservatorio Astronomico di Trieste, via G. B. Tiepolo 11, I-34143 Trieste, Italy
[12] Institute for Fundamental Physics of the Universe, Via Beirut 2, I-34151 Grignano, Trieste, Italy
[13] Consejo Superior de Investigaciones Científicas, Spain
[14] Centro de Astrobiología (CSIC-INTA), ESAC campus, E-28692 Villanueva de la Cañada, Madrid, Spain
[15] European Southern Observatory, Karl-Schwarzschild-Strasse 2, 85748, Garching b. München, Germany
[16] Centro de Astrofísica da Universidade do Porto, Rua das Estrelas, 4150-762 Porto, Portugal
[17] European Southern Observatory, Alonso de Coórdova 3107, Vitacura, Regioón Metropolitana, Chile
[18] INAF - Osservatorio Astronomico di Palermo, Piazza del Parlamento 1, I-90134 Palermo, Italy
[19] Instituto de Astrofísica e Ciências do Espaço, Faculdade de Ciências da Universidade de Lisboa, Campo Grande, PT1749-016 Lisboa, Portugal
[20] INAF - Fundación Galileo Galilei, Rambla José Ana Fernandez Pérez 7, 38712 Breña Baja, Tenerife, Spain
[21] INAF - Osservatorio Astrofisico di Torino, via Osservatorio 20, 10025 Pino Torinese, Italy

Received 28 September 2020 / Accepted 09 December 2020

ABSTRACT

We observed two transits of the iconic gas giant HD 209458b between 380 and 780 nm using the high-resolution ESPRESSO spectrograph. The derived planetary transmission spectrum has features at all wavelengths where the parent star shows strong absorption lines, for example, Na I, Mg I, Fe I, Fe II, Ca I, V I, Hα, and K I. We interpreted these features as the signature of the deformation of the stellar lines profiles due to the Rossiter-McLaughlin effect, combined with the centre-to-limb effects on the stellar surface, which agrees with recent similar reports in the literature. We also searched for species that might be present in the planetary atmosphere, but not in the stellar spectra, for example, TiO and VO, with negative results. Thus, we find no evidence of any planetary absorption, including previously reported Na I, in HD 209458b's atmosphere. The high signal-to-noise ratio in the transmission spectrum ($\sim$ 1700 at 590 nm) allows us to compare the modelled deformation of the stellar lines assuming different one-dimensional stellar atmospheric models. We conclude that the differences between various models and observations remain within the precision of data. However, the transmission light curves are better explained when the centre-to-limb variation is not included in the computation, and only the Rossiter-McLaughlin deformation is considered. This demonstrates that ESPRESSO is currently the best facility to spatially resolve the stellar surface spectrum in the optical range using transit observations, and to empirically validate stellar models.

Key words. planetary systems – planets and satellites: individual: HD 209458b – planets and satellites: atmospheres – methods: observational – techniques: spectroscopic

* Based on Guaranteed Time Observations collected at the European Southern Observatory under ESO programme 1102.C-0744 by the ESPRESSO Consortium.

1. Introduction

High dispersion spectroscopy has become one of the most powerful tools for the atmospheric characterisation of exoplanets.

The technique relies on the wavelength separation of the planetary, stellar, and telluric spectral lines due to their differential velocities (Snellen et al. 2010). So far high dispersion spectroscopy has been applied to both transiting (e.g. Sánchez-López et al. 2019; Brogi et al. 2018) and non-transiting planets (e.g. Brogi et al. 2014; Guilluy et al. 2019) and has led to the detection of several species in exoplanetary atmospheres, including: alkali lines and molecules in hot Jupiter atmospheres (Redfield et al. 2008; Wyttenbach et al. 2015, 2017; Chen et al. 2020; Birkby et al. 2017), tracing evaporation and escape processes (Yan & Henning 2018; Nortmann et al. 2018; Allart et al. 2018), and ionospheric species in ultra hot Jupiter atmospheres (Hoeijmakers et al. 2018; Casasayas-Barris et al. 2019; Seidel et al. 2019; Pino et al. 2020).

With the start of operation of ESPRESSO (Echelle SPectrograph for Rocky Exoplanets and Stable Spectroscopic Observations; Pepe et al. 2010, 2014, 2020), our capabilities for this type of studies are enhanced at optical wavelengths. ESPRESSO is already delivering ground-breaking measurements of time-resolved transmission spectra (Ehrenreich et al. 2020; Borsa et al. 2020), accurate Rossiter-McLaughlin (RM) measurements (Santos et al. 2020) and high-precision characterisation measurements of multiple-planet systems (Damasso et al. 2020; Suárez Mascareño et al. 2020). Moreover, relatively small effects such as the impact of the stellar centre-to-limb variation (CLV) and the RM effect on the transmission spectra, which fell within the signal-to-noise ratio (S/N) of previous studies, can now be measured and taken into account given the very high S/N and extreme quality of the ESPRESSO data. The impact of the RM effect in atmospheric studies was already described by Louden & Wheatley (2015) and similarly, other studies (Czesla et al. 2015; Khalafinejad et al. 2017) pointed out the importance of the CLV. The detailed understanding of these effects is crucial for the success of future observations of small rocky planet atmospheres with the ELTs (Snellen 2013).

Here, we revisit the atmosphere of the benchmark exoplanet HD 209458b using two transit observations with ESPRESSO. It was the first planet to be observed transiting its host star (Charbonneau et al. 2000; Henry et al. 2000) and the first for which the detection of an atmosphere was claimed (Charbonneau et al. 2002) using the *Hubble Space Telescope* (HST) observations. HD 209458b is one of the most studied planets to date. This hot Jupiter orbits an F9-type star, and has a mass of 0.682 M_J, radius of 1.39 R_J, and equilibrium temperature of 1449 K (see more parameters in Table 2). Over the years, there have been several studies of its atmosphere using low and high-resolution spectroscopy facilities. At low resolution, several detections have been performed using the HST observations. For example, Charbonneau et al. (2002) and Sing et al. (2008) reported Na I absorption, Deming et al. (2013) found water in the atmosphere of the planet, and Désert et al. (2008) found tentative features of TiO and VO.

High-resolution spectroscopy studies have shown the detection of different atomic and molecular species. Using the High Dispersion Spectrograph (HDS) on the Subaru telescope, Narita et al. (2005) reported upper limits of several lines, including the Na I doublet. With the same data sets, Snellen et al. 2008 found absorption of Na I in the transmission light curves, and Astudillo-Defru & Rojo (2013) detected calcium, possibly scandium and hydrogen (Hα) in the atmosphere of the planet, and reconfirmed the Na I detection. Similarly, Na I absorption was reported by Albrecht et al. (2009) using the Ultraviolet and Visual Echelle Spectrograph (UVES) at the Very Large Telescope (VLT), and tentative features were shown by Langland-Shula et al. (2009) and Jensen et al. (2011) using the High Resolution Echelle Spectrometer (HIRES) at Keck and the High-Resolution Spectrograph (HRS) at Hobby-Eberly Telescope (HET), respectively. On the other hand, Winn et al. (2004) were unable to detect Hα absorption using observations with HDS at Subaru, while Jensen et al. (2012) found a broad feature correlated with orbital phase centred at the Hα position using observations with the HET.

More recently Yan et al. (2017) studied the impact of the CLV when attempting to study the atmosphere of this planet using high resolution spectroscopy. Casasayas-Barris et al. (2020), on the other hand, analysed transit observations of HD 209458b with the HARPS-N (High Accuracy Radial velocity Planet Searcher in North hemisphere; Cosentino et al. 2012) and CARMENES (Calar Alto high-Resolution search for M dwarfs with Exoearths with Near-infrared and optical Echelle Spectrographs; Quirrenbach et al. 2014, 2018) spectrographs, suggesting that the features observed in the high-resolution transmission spectrum could be explained by the combination of the RM effect and the CLV. With the current ESPRESSO observations, we aim at a better characterisation of the signals in the transmission spectra and at exploring the presence of species in the planetary spectrum that are not present in the stellar spectrum.

This paper is organised as follows. In Sect. 2 we present the observations. The methods for extracting the stellar parameters, the reloaded-RM technique, the atmospheric analysis and stellar contamination modelling are presented in Sect. 3. In Sect. 4 we present the results obtained in the atmospheric analysis of HD 209458b around individual lines and using cross-correlation techniques. In Sect. 5 we discuss the systematic effects and accuracy of the modelled stellar contamination. The conclusions are presented in Sect. 6.

2. Observations and data reduction

Two transits of HD 209458b were observed with ESPRESSO, a fiber-fed spectrograph located at the Very Large Telecope (VLT) that covers the optical wavelength range between 3800 and 7880 Å, the nights of 2019-07-20 and 2019-09-11. Both observations were performed at the UT3 Melipal telescope, as part of the Guaranteed Time Observation under programme 1102.C-0744, using the HR21 observing mode which considers 1-arcsec fiber, a binning of a factor of 2 along the spatial direction, achieving a resolving power $\mathcal{R} \sim 140\,000$ (Pepe et al. 2020).

The observations were performed following the typical observing strategy for transmission spectroscopy studies of exoplanets: monitoring the star with consecutive exposures before, during, and after the transit of the exoplanet. During the first night, one hour was dedicated to observe before and after the transit. For the second night, one hour was used before the transit and one hour and a half after the transit. We used fiber A observing the target and fiber B to monitor and subtract the sky signature. We used the same exposure time on both occasions (175 s) obtaining a total of 89 and 85 exposures with an averaged S/N of 234 and 193 at 588 nm (physical order 104) during the two nights, respectively. The observations are summarised in Table 1. Due to limitations in the atmospheric dispersion compensator, the exposures with airmass larger than 2 are excluded from the analysis. This affects the six first exposures of the first night (2019-07-20). Therefore, a total of 83 spectra are used from that night, achieving an averaged S/N of 239.

Here, we use the one-dimensional spectra (s1d sky subtracted products) extracted by the Data Reduction Software (DRS) pipeline version 2.0. When inspecting the sky spectra we

notice that telluric Na I emission is present in both nights, but corrected in the target spectra by the pipeline when the sky subtraction is applied. We also observe and correct for telluric Na I absorption, which can not be monitored by fiber B (see Sect. 3).

3. Analysis

3.1. Stellar parameters

Based on the ESPRESSO spectra, we derive the stellar atmospheric parameters of HD 209458 using the Equivalent Width method by means of the StePar[1] code (Tabernero et al. 2019), following the same methodology applied in recent ESPRESSO observations (Tabernero et al. 2020; Ehrenreich et al. 2020). In summary, StePar relies on the 2017 version of the MOOG code (Sneden 1973) and a grid of MARCS stellar atmospheric models (Gustafsson et al. 2008). We use the Fe I and Fe II line list from (Tabernero et al. 2019) for metal rich main sequence stars.

For comparison, we also used ARES+MOOG (Sousa 2014; Santos et al. 2013) to derive the stellar atmospheric parameters and respective uncertainties. We used the usual line list from Sousa et al. (2008) where the equivalent widths were measured with the ARES code[2] (Sousa et al. 2007, 2015). In the minimisation process we find the ionisation and excitation equilibrium to converge in the best set of spectroscopic parameters. This process uses a grid of Kurucz model atmospheres (Kurucz 1993) and the radiative transfer code MOOG (Sneden 1973).

Using StePar, we measure an effective temperature ($T_{\rm eff}$) of 6069 ± 54 K, gravity ($\log g$) of 4.41 ± 0.13 cgs, metallicity ([Fe/H]) of 0.02 ± 0.04, and microturbulence velocity (ξ) of 1.03 ± 0.08 km s^{-1}. On the other hand, using ARES+MOOG, $T_{\rm eff}$ = 6139 ± 62 K, $\log g$ = 4.46 ± 0.10 cgs, [Fe/H]= 0.05 ± 0.04, and ξ = 1.221 ± 0.025 km s^{-1}. Using these previous spectroscopic values and PARAM1.3[3] (da Silva et al. 2006), we derive a stellar radius and mass of $R_\star$ = 1.136 ± 0.027 $R_\odot$ and $M_\star$ = 1.153±0.029 $M_\odot$ for StePar parameters, and $R_\star$ = 1.160± 0.027 $R_\odot$ and $M_\star$ = 1.116 ± 0.029 $M_\odot$ using ARES+MOOG results. These values are consistent with most of the previous studies (Torres et al. 2008; Bonomo et al. 2017; Stassun et al. 2017; Sousa et al. 2008; del Burgo & Allende Prieto 2016, among others). The stellar parameters derived here are summarised in Table 2.

3.2. Reloaded Rossiter-McLaughlin technique

The CCFs generated by the ESPRESSO DRS (here after $\rm CCF_{DI}$, for disk-integrated) originate from starlight integrated over the disk of HD 209458. We used the reloaded RM technique (Cegla et al. 2016a, see also Bourrier et al. 2017, 2018, 2020; Ehrenreich et al. 2020) to isolate the local CCFs (heareafter $\rm CCF_{loc}$) from the regions of the photosphere that are occulted by HD 209458 b during its transit. The $\rm CCF_{DI}$ were first aligned by removing the Doppler-reflex motion of the star induced by the planet, calculated with the orbital properties in Table 2. Since the ESPRESSO observations are not calibrated photometrically, each $\rm CCF_{DI}$ has to be continuum-scaled to reflect the planetary disk absorption. This was done using a light curve computed with the batman package (Kreidberg 2015) and the properties from Table 2. $\rm CCF_{DI}$ outside of the transit were co-added to build a master-out $\rm CCF_{DI}$ representative of the unocculted star. We then aligned all $\rm CCF_{DI}$ in the star rest frame using the systemic velocity measured via a Gaussian fit to the master-out in each visit, to account for possible nightly offsets in the instrumental, atmospheric, and astrophysical noise. Residual $\rm CCF_{loc}$ were then obtained by subtracting the scaled $\rm CCF_{DI}$ from the master-out in each visit (Fig. 1). Errors were propagated at each step from the $\rm CCF_{DI}$ to the $\rm CCF_{loc}$.

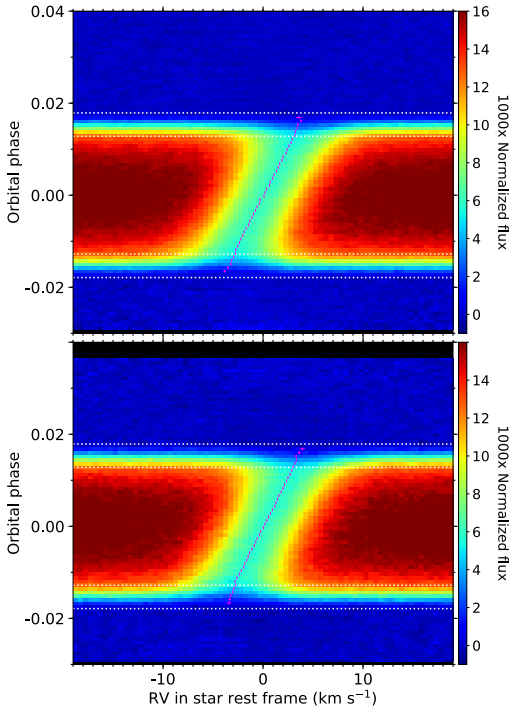

Fig. 1: Map of the $\rm CCF_{loc}$ series in the first (top panel) and second (bottom panel) night, as a function of orbital phase (in ordinate) and radial velocity in the stellar rest frame (in abscissa). Maps were obtained for the adjusted transit parameters (see text). Colors indicate flux values. The four horizontal dashed white lines show the times of transit contacts. In-transit $\rm CCF_{loc}$ show the average stellar line profiles from the regions occulted by HD 209458 b across the stellar disk. The magenta crosses are the measured centroids of the average stellar line profiles, corresponding to the local RVs of the planet-occulted regions.

The $\rm CCF_{loc}$ spectrally and spatially resolve the photosphere of the star along the transit chord. The average stellar lines from the planet-occulted regions were fitted with independent Gaussian profiles and Levenberg-Marquardt least-squares minimization to derive the local RVs of the stellar surface. The average local stellar lines are well fitted with Gaussian profiles, and are detected in all exposures except the first and last ones of ingress and egress in each night (the detection criterion is

[1] https://github.com/hmtabernero/StePar
[2] The last version of ARES code (ARES v2 - http://www.astro.up.pt/~sousasag/ares; https://github.com/sousasag/ARES
[3] http://stev.oapd.inaf.it/cgi-bin/param_1.3

Table 1: Observing log of the HD 209458b transit observations.

Night	Telescope	Date of observation	Start [UT]	End [UT]	Airmass[a] change	T_{exp} [s]	N_{obs}	S/N[b] Na I order
1	VLT-UT3	2019-07-20	03:43	09:30	2.23–1.38–1.89	175	89	122-261
2	VLT-UT3	2019-09-11	00:35	06:06	2.00–1.38–1.93	175	85	132-228

Notes.[a] Airmass change during the observation. [(b)] Minimum and maximum S/N for each night, calculated in the Na I echelle order.

Table 2: Physical and orbital parameters of the HD 209458 system.

Parameter	Value	Reference
Stellar parameters		
T_{eff} [K]	6069 ± 54	This work (SteParr)
	6139 ± 62	This work (ARES+MOOG)
ξ [km s^{-1}]	1.03 ± 0.08	This work (SteParr)
	1.221 ± 0.025	This work (ARES+MOOG)
log g [cgs]	4.41 ± 0.13	This work (SteParr)
	4.45 ± 0.10	This work (ARES+MOOG)
[Fe/H]	0.02 ± 0.04	This work (SteParr)
	0.05 ± 0.04	This work (ARES+MOOG)
$M_\star$ [$M_\odot$]	1.116 ± 0.029	This work (SteParr)
	1.153 ± 0.029	This work (ARES+MOOG)
$R_\star$ [$R_\odot$]	1.160 ± 0.027	This work (SteParr)
	1.136 ± 0.027	This work (ARES+MOOG)
$v \sin i_\star$ [km s^{-1}]	4.228 ± 0.007	This work (reloaded-RM)
Planet parameters		
M_p [M_{Jup}]	$0.682^{+0.015}_{-0.014}$	Torres et al. (2008)
$R_p/R_\star$	0.12086 ± 0.00010	Torres et al. (2008)
K_p [km s^{-1}]	145.0 ± 1.6	This work[a]
Transit parameters		
T_0 [BJD$_{TDB}$]	2454560.80588 ± 0.00008	Evans et al. (2015)
P [day]	3.52474859 ± 0.00000038	Bonomo et al. (2017)
T_{14} [h]	2.978 ± 0.051	Richardson et al. (2006)
T_{23} [h]	2.254 ± 0.058	Richardson et al. (2006)
System parameters		
$a/R_\star$	8.87 ± 0.05	Evans et al. (2015)
i [deg]	86.78 ± 0.07	Evans et al. (2015)
a [au]	$0.04707^{+0.00045}_{-0.00047}$	Bonomo et al. (2017)
e	0	Bonomo et al. (2017)
ω [deg]	90	Bonomo et al. (2017)
$K_\star$ [m s^{-1}]	$84.27^{+0.69}_{-0.70}$	Bonomo et al. (2017)
γ [km s^{-1}]	−14.741 ± 0.002	Naef et al. (2004)
λ [deg]	1.58 ± 0.08	This work (reloaded-RM)
b	0.511	This work (reloaded-RM)

Notes. [(a)] Derived assuming zero eccentricity ($e = 0$): $K_p = 2\pi a \sin(i)/P$

that the amplitude of the model CCF_{loc} is four times larger than the dispersion in the measured CCF_{loc} continuum). ESPRESSO thus allows us to sample with a high temporal resolution the full transit window, which translates into a fine spatial sampling of the full transit chord out to the limbs of the star (Fig. 2). This led us to identify an abnormal deviation of the local RVs during ingress. We found that the local RVs series, in particular at the limbs, is highly sensitive to minute variations in the assumed mid-transit time and impact parameter. The efficiency of the reloaded RM technique relies on the possibility to analyze spectrocopic data using photometry of similar quality, so that the shape of the transit light curve and the orbital phase of the exposures are known to a sufficient precision. Deviations from the true photometric scaling and phasing of the CCF_{DI} can otherwise bias the extracted CCF_{loc} and their measured centroid. Here, the high quality of HD 209458 b observations with ESPRESSO is not matched by our knowledge of its transit properties, derived from photometry obtained several years ago and resulting in a present-day uncertainty on T_0 of about 40 s.

In order to estimate the precision required on the transit properties and their impact on the derived obliquity λ and projected stellar rotational velocity $v \sin i_\star$, we assumed that HD 209458 rotates as a solid body and performed the extraction of the local RVs over a grid of T_0 and b values. Different values for these properties can change which exposures are considered in-transit, and which ingress/egress exposures yield a detection for the average local stellar line. Thus different extractions can yields different series of local RVs, preventing us from using χ^2 minimization. We searched instead for the approximate T_0 and b values that minimize the dispersion of the residuals between a given local RVs series and its best-fit solid-body model (described in Cegla et al. 2016a, Bourrier et al. 2017). We found that the local RVs best agree with solid-body rotation when the mid-transit time is shifted by 76 s (2454560.80676 BJD), and the impact parameter equals 0.511 (Fig. 2). Provided that those properties are correct and HD 209458 rotates as a solid-body, we then derive $\lambda = 1.58 \pm 0.08°$ and $v \sin i_\star = 4.228 \pm 0.007$ km s^{-1}. We caution that these uncertainties are underestimated, as they do not account for the additional uncertainty on the transit depth (Table 2) and limb-darkening coefficients (set using the code provided by Espinoza & Jordán 2015). Nonetheless, varying those properties changes the derived $v \sin i_\star$ by less than 50 m s^{-1} and has a negligible impact on λ. Even fitting the biased local RVs associated with Evans et al. (2015) transit properties only changes λ by ∼1° (0.48°) and $v \sin i_\star$ by 44 m s^{-1} (4.184 km s^{-1}). Therefore, while our adjusted values for T_0 and b should be considered with caution, the derived obliquity is likely precise within a degree and the projected stellar rotational velocity within 100 m s^{-1}. We note that the analysis of the HD 209458b data by Santos et al. (2020), based on the classical RM approach, similarly yields a mid-transit time shifted to later values. We also note the high repeatability of the local RV series, despite them being separated by about two months, which highlights the stability of ESPRESSO.

Despite the strong influence of T_0 and b on the RM analysis of HD 209458 b, our adjusted values differ by less than 2σ from the nominal values of Evans et al. (2015). Reaching a high accuracy on λ and $v \sin i_\star$ in the HD 209458 system, and searching for fine RV variations associated with the stellar surface motion (e.g., differential rotation, convective blueshift), will require an extreme precision of the transit properties that only a space-based facility like CHEOPS or TESS can provide.

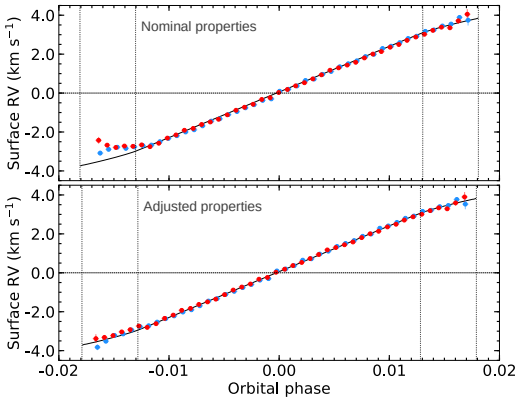

Fig. 2: RVs of the stellar surface regions occulted by HD 209458 b in the first (blue points) and second (red points) night. Their extraction was performed for the nominal transit properties from Evans et al. (2015) in the top panel, and for the adjusted properties in the bottom panel. The solid black line is the best-fit solid-body model to the RVs obtained for the adjusted properties. Vertical dotted lines show the times of transit contacts.

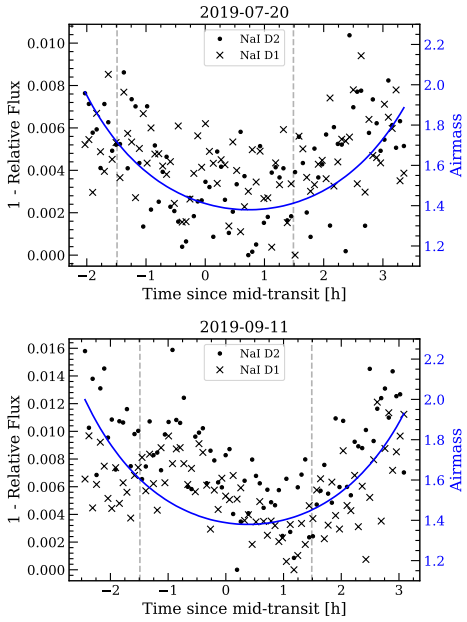

Fig. 3: Integrated flux in a ±5 km s^{-1} passband centred on the telluric Na I absorption lines of the first night (*top panel*) and second night (*bottom panel*). The integrated flux is normalised to its maximum value. In dots we show the results for the Na I D2 line, and in crosses the results of the Na I D1 line. The vertical dashed lines mark the origin and end of the transit.

3.3. Telluric correction

As in other recent studies using ESPRESSO observations (Chen et al. 2020; Tabernero et al. 2020; Allart et al. 2020), we use `molecfit` (Smette et al. 2015 and Kausch et al. 2015) to correct for the telluric absorption contamination (O_2 and H_2O) from the Earth's atmosphere as presented in Allart et al. (2017). In this first correction, other telluric contamination such as emission and/or absorption of Na I, for example, are not considered.

In the ESPRESSO observations used here, we observe both telluric Na I emission and absorption contamination. The telluric emission is monitored with fiber B and is already corrected by the DRS during the sky subtraction, but this is not the case of the telluric absorption. The mean Earth radial-velocity is 17.6 km^{-1} and −3.8 km^{-1} for the first and second night, respectively. Considering the systemic velocity of HD 209458 ($\gamma = -14.7$ km^{-1}), the telluric absorption is located at 32.3 km s^{-1} (0.6 Å) and 10.9 km s^{-1} (0.2 Å) from the Na I lines core. Although its presence does not impact the results of the first night because of the distance with respect the stellar Na I lines core, it is indeed important for the second night and needs to be corrected.

It is known that the telluric Na I absorption can show strong seasonable variability (Snellen et al. 2008). However, in order to correct for this contamination we assume that, within a night, the telluric Na I can be corrected as presented, for example, in Borsa et al. (2020), Wyttenbach et al. (2015), Zhou & Bayliss (2012), and Vidal-Madjar et al. (2010). This is, assuming that the contrast variation of these lines during the observations is correlated with the airmass. This correction is only applied in a small region of ±5 km s^{-1} centred at the position of the telluric Na I absorption lines in order to not influence other regions. In Figure 3 we show the flux variation of this region with time. For the first night, the absorption lines follow the airmass change for the full observation while for the second night this only happens in the out-of-transit exposures. This is because the telluric Na I of the second night is very close to the lines core and thus influenced by the line profile changes produced by the planet during the transit. For the first night, telluric Na I is far from the lines core.

3.4. Transmission spectrum and light curves extraction

After correcting for the telluric contamination we extract the transmission spectrum as presented in previous studies (such as Wyttenbach et al. 2015; Casasayas-Barris et al. 2017; Yan & Henning 2018; Borsa et al. 2020; Allart et al. 2017). First the spectra are normalised and then moved to the stellar rest frame. To do this, we use the Keplerian model computed with the parameters presented in Table 2 using the `SinRadVel` model from `PyAstronomy` (Czesla et al. 2019). Then, we compute the master stellar spectrum resulting from the combination of all out-of-transit spectra, and divide each individual spectrum by this master spectrum.

After computing the ratio of each stellar spectrum by the master stellar spectrum, we could notice a clear wiggle (sinusoidal) pattern already observed in recent ESPRESSO observations (Tabernero et al. 2020; Borsa et al. 2020), with amplitudes around 1 % and periods ∼ 30 − 40 Å. In order to correct for this pattern, we follow the methodology presented by Borsa et al. (2020): we fit a sinusoidal curve with varying period, amplitude, and phase at each individual spectrum after being divided by the master spectrum. The data is normalised using the result-

ing best fit model. We then move all the residuals to the planet rest frame by using the planet radial-velocity semi-amplitude $K_p = 145.0 \pm 1.6\,\mathrm{km\ s^{-1}}$, calculated assuming zero eccentricity ($K_p = 2\pi a \sin(i)/P$). Finally, the in-transit residuals are combined to compute the transmission spectrum. The combination of the in-transit residuals is performed using the simple average, as the residuals change at different orbital phases. The weighted average gives more importance to the orbital phases with higher S/N and, consequently, modifies the shape of the transmission spectrum features.

In the final transmission spectra we can observe a second sinusoidal pattern, which is particularly clear in the pseudo-continuum (see Figure 4) due to the high S/N of the data. The origin of these patterns lies in non-flatfielded interference patterns that occur in some optical elements of the Coudé Train (CT), i.e. in the system that routes the light from the telescope to the instrument. This system is not spectrally flat-fielded by the calibration sources, which are injected downstream. Due to the (small) changes of the light path through the optical elements during the observations, the fringe pattern will evolve spectrally, and will eventually pop up in transmission spectroscopy when dividing by each other spectra taken at different moments of the night [4]. In order to remove the pattern from the final transmission spectrum, we fit a sinusoidal curve to the data, masking the strong features observed in the Na I position, and we then use the solution to normalise the full wavelength range of the transmission spectrum. As it can be observed in the top spectrum of Figure 4, although the period of the oscillations is almost constant, their amplitude changes in wavelength ($\sim \pm 0.1$ % at bluer wavelengths for the first night). For this reason, we let the amplitude of the sinusoidal change linearly in wavelength, while the remaining free parameters (period and phase of the origin) only have one value in a particular wavelength range.

On the other hand, the period of the oscillations is first estimated by applying a Fourier transform on the combination of all in- and out-of-transit residuals and it is then fitted. The period we derive in both Fourier transform and the sinusoidal fit is 0.75 Å around the Na I and it slightly varies in wavelength. This correction is applied to all transmission spectra presented here, fitting the pattern in each case in a wavelength region centred around the line of interest.

In order to calculate the transmission light curves, once the residuals are moved to the planet rest frame, we fix a passband of a given width centred on the specific line we want to analyse. Then, we integrate the flux inside this passband using trapezoidal integration. The method is the same as presented in Casasayas-Barris et al. (2020). The transmission light curves are presented in Section 4, in particular, in Figures 6 and 9.

3.5. Cross-correlation

In addition to the analysis of individual lines we apply the cross-correlation technique in order to search for atoms and molecules that may originate from hundreds to thousands of individual absorption lines in the transmission spectrum, if present in the atmosphere of the planet. Using the cross-correlation method, the contribution of all these lines is combined, reducing the photon noise and reaching the detection of particular atoms and molecules hidden in the noise when analysed individually (Snellen et al. 2010).

[4] A forthcoming paper will explain in details the origin of those wiggles.

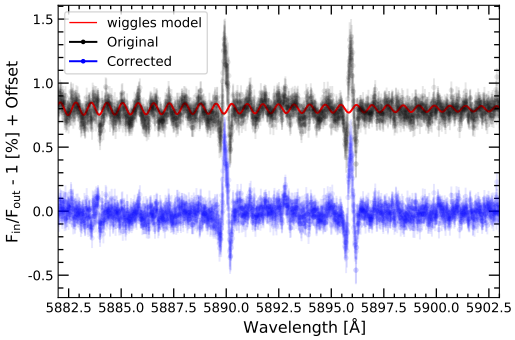

Fig. 4: Correction of the interference pattern in the final mid-transit transmission spectrum of the first night (2019 July 20). The original transmission spectrum in shown in black, and the corrected transmission spectrum is shown in blue. In red and on-top of the uncorrected spectrum we show the best fit sinusoidal curve. An offset between the two spectra is added for a better visualisation.

Here, we use the one-dimensional `molecfit`-corrected spectra, which are then normalised and moved to the stellar rest frame. We divide each spectrum by the master stellar spectrum (computed using only the out-of-transit data), remove the wiggle pattern as presented in Section 3.4, and cross-correlate the result with atmospheric models, as presented in Sánchez-López et al. (2019) and Stangret et al. (2020). We discard the strong telluric contaminated regions around 690 nm and 760 nm where the telluric correction is not accurate, and the first few blue bins from 380 to 450 nm due to their lower S/N. With this, all spectra of the two nights have a S/N larger than 90 in each order.

The atmospheric models used to cross-correlate with the residuals are computed using the `petitRADTRANS` code (Mollière et al. 2019) which allows generating high-resolution models of atoms and molecules for exoplanet atmospheres. Here we generate Fe I, Fe II, and Ca I models assuming the parameters presented in Table 2, isothermal temperature profile of 1459 K, a continuum level of 1 mbar, and the volume mixing ratio (VMR) set to solar abundance. For these atomic species the Kurucz line lists are used (Kurucz 1993). The resulting models are convolved to match the ESPRESSO spectral resolution. On the other hand, we generate the atmospheric models of TiO and VO molecules using two different methodologies. First, we use `petitRADTRANS` as described above and considering $\mathrm{VMR_{TiO}} = 10^{-7}$ and $\mathrm{VMR_{VO}} = 10^{-8}$ (solar abundance), and the line lists presented in Plez (1998). Second, as presented in Tabernero et al. (2020), we use `HELIOS` code[5] (Malik et al. 2017, 2019) to calculate the atmospheric structure of HD 209458b. Then, the radiative transfer problem is solved using `turbospectrum`[6] (Plez 2012). We use the TiO line list from Plez (1998) and the VO list from `exomol` (McKemmish et al. 2016). The cross-correlation results are presented in Section 4.

[5] https://github.com/exoclime/HELIOS
[6] https://github.com/bertrandplez/Turbospectrum2019

3.6. Transit effects on the stellar lines

Following Yan et al. (2017) and Yan & Henning (2018), we model the CLV and RM effects in the stellar lines profile. This method involves the `Spectroscopy Made Easy Tool` (SME; Valenti & Piskunov 1996) and the line list from `VALD`[7] database (Piskunov et al. 1995; Kupka et al. 1999). Using SME we are able to compute synthetic stellar spectra at different limb-darkening angles. With this information it is possible to compute the disc integrated stellar spectrum considering the stellar rotation ($v \sin i_\star$), but also to exclude the spectrum of those regions blocked by the planet at each exposure when the integrated disc spectrum is built, producing the RM and CLV deformation.

This has already been applied to different high resolution atmospheric studies such as Casasayas-Barris et al. (2019), Yan et al. (2019), Chen et al. (2020), and Borsa et al. (2020). For this computation we need accurate measurements of the system and stellar parameters. Here, we take advantage of the high precision achieved with the reloaded RM technique in the $v \sin i_\star$ and λ measurements (see Sect. 3.2). These parameters are presented in Table 2. In Sect. 5, we examine the resulting modelled effects depending on the stellar atmospheric models that are used for their computation.

Although for some planets these effects are not important, it has been observed that they can become important for particular planets (Czesla et al. 2015; Khalafinejad et al. 2017; Louden & Wheatley 2015), and specially when using very high S/N observations (see Borsa et al. 2020). In most cases, the RM effect can influence the final absorption from the planet atmosphere if both contributions (RM and atmosphere) overlap at some point during the transit (Yan & Henning 2018; Hoeijmakers et al. 2018). Here, as observed by Casasayas-Barris et al. (2020), we are in an extreme case where the RM (almost) fully overlaps with the expected planetary atmosphere track. This deformation is not constant along the planet transit, hence, it is particularly important to use the same steps when processing the models and the data for useful comparisons.

4. Results

In this section we present the results obtained in the analysis of individual atomic lines (Na I, Fe I, Mg I, Hα, and K I D1), and forests of atomic lines (Fe I, Fe II, Ca I, and V I) using the cross-correlation technique. For comparison, we show the results together with the RM and CLV models computed using MARCS (Gustafsson et al. 2008) stellar atmospheric models and assuming LTE approximation. The models containing both CLV and RM effects combined and only RM are shown. Using the cross-correlation technique we search for relevant molecules such as TiO and VO.

4.1. Na I doublet

The transmission spectrum and tomography maps around the Na I of both nights combined are presented in Figure 5, and the results of the individual nights are shown in Figure A.1 in the Appendix. In all cases, as presented in Casasayas-Barris et al. (2020), at the Na I line positions in the transmission spectrum we observe emission-like features consistent with the deformation of the stellar lines profile during the transit of HD 209458b, which are due to the RM and CLV effects. The particularity of HD 209458 system is that the expected exoplanet atmosphere and the RM effect deformation (which is the main contribution of the final transmission spectrum shape) fall at almost the same radial velocities (see tomography maps of Figure 5). For this reason, when the individual transmission spectra are moved to the planet rest frame before being combined, the positive part of the RM effect is almost aligned with the Na I position and creates an emission-like feature in the transmission spectrum.

Due to the system geometry, the stellar lines deformation is asymmetric along the transit. With the high S/N of ESPRESSO data, these asymmetries can be explored by computing the transmission spectrum during different transit times. In Figure 5, we present the transmission spectrum computed using the spectra obtained during the ingress (T1-T2), the egress (T3-T4), between the first and last contacts of the transit (T1-T4), and between the second and third contacts (T2-T3). For the ingress and egress transmission spectra we use around 6 spectra per night. The asymmetries of the ingress and egress regions can be clearly observed, and are predicted by the CLV and RM modelled effects. In the time-regions of orbital phases $[-0.0175, -0.0100]$ and $[+0.0100, +0.0175]$ the planet radial-velocities do not fully overlap with the RM effect. However, we are not able to distinguish absorption due to the exoplanet atmosphere.

The asymmetries of the stellar line shapes during the transit are particularly important, specially if some orbital phases of the planet are not covered during the observations, as they could result in false absorption-like signals depending on the geometry of the system (see Chen et al. 2020). In Figure 5, we also see how the transmission spectra of the ingress and egress show absorption-like features shifted from the laboratory Na I lines position, which result from the deformation of the lines and are not from atmospheric origin. Although the impact of the effects is smaller in the mid-transit times when the RM radial-velocities are used to move the spectra to the stellar rest frame, these asymmetries increase, specially during the ingress and egress.

In addition, we compute the transmission light curves for two different bandwidths (0.4 Å and 0.75 Å). The small passband size is selected to only include the positive RM effect ($\sim 10\,\mathrm{km\,s^{-1}}$), while the larger passband includes the overall RM effect and has also been used in previous studies (Snellen et al. 2008; Albrecht et al. 2009). In Figure 6 we present the results after combining both nights, and in Figure A.2 of the Appendix we show the results of each individual night. In all cases both Na I lines of the doublet are combined. We note that the second night (2019 September 11) could be partially affected by telluric Na I absorption residuals. As they are calculated in the planet rest frame, for the narrower passband we are mainly combining the positive part of the RM deformation, while with the wider passband both contributions are included, resulting in a compensation of the final effects. The transmission light curves follow the general shape predicted by the model containing only RM deformation, especially clear for the 0.4 Å passband where the differences with the out-of-transit are more intense. In this case, in the centre of the transit, the transmission light curve clearly deviates from the model containing the CLV (see discussion in Sect. 5).

4.2. Other atomic lines

The deformation of the lines profile caused by the RM presented in Sect. 4.1 is expected to have an impact in all the stellar spectral lines, although at different amplitudes depending on the transition. In order to check this, we analyse the cross-correlation function (CCF) from the DRS as presented in Borsa et al. (2020).

[7] http://vald.astro.uu.se

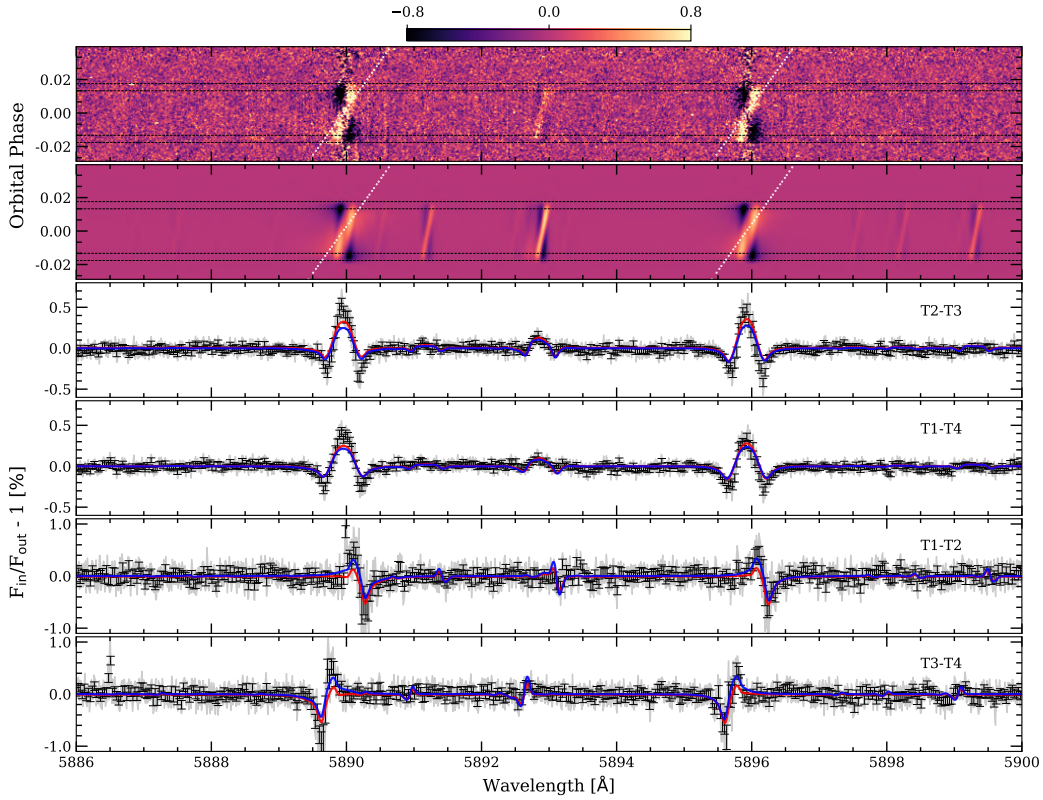

Fig. 5: *First panel (top)*: two-dimensional map of the individual transmission spectra around the Na I doublet lines of HD 209458b. *Second panel*: two-dimensional map of the modelled CLV and RM effects around the Na I doublet. In both panels the results are presented in the stellar rest frame and the color bar shows the relative flux (F_{in}/F_{out}-1) in %. The black horizontal dashed lines indicate the four contacts of the transit and the dotted white line marks the expected position of the planet trail during the observations. *Third panel*: transmission spectrum computed combining the data between the second and third contacts of the transit, in the . *Fourth panel*: combination of the in-transit exposures from the first to fourth contacts. *Fifth panel*: combination of ingress exposures. *Sixth panel (bottom)*: combination of egress exposures. The transmission spectra are computed combining the data in the planet rest frame. The original data error bars are shown in light grey, and the data binned by 0.03 Å is shown in black.
We note the different y-scale in the different panels. In red we show the CLV and RM effects in the final transmission spectrum, and in blue the deformation due to the RM alone.

In this case, the CCF values are generated with a F9 stellar mask using the DRS ESO version 2.0, with a step of 0.5 km s^{-1}. In order to extract the deformation of the lines profile propagated in the CCFs we use the same process as for the transmission spectrum (see Sect. 3.4): we move each CCF in the stellar rest frame, and divide each of them by the averaged out-of-transit CCF. The result is presented in Figure 7, where the RM effect is clearly observed in the CCF values. As Fe I lines are the major contributor to the stellar mask used to compute the CCFs (Ehrenreich et al. 2020), the RM deformation observed in the CCF tomography is dominated by the Fe I lines. In contrast with Borsa et al. (2020) where the atmospheric trail of the planet is clearly intercepted by the mask, we are not able to observe any feature with possible atmospheric origin in the HD 209458b CCFs.

In addition, we search for Fe I, Fe II, Ca I, and V I absorption cross-correlating the residuals spectra with the atmospheric templates described in Sect. 3.5. The results can be observed in Figure 8. For Fe I, Fe II, and Ca I the deformation of the stellar line profiles is visible at high S/N, without any clear feature of atmospheric origin in the ingress and egress regions where the planet atmosphere could be disentangled from the stellar contamination. For V I the strength of the deformation is fainter, probably indicating that this specie is poorly (or not) present in the stellar spectrum, given the spectral type of the star. The S/N of the bottom row panels from Figure 8 is calculated dividing the cross-correlation values by the standard deviation calculated far from the position of the signal, as presented in Birkby et al. (2017), Brogi et al. (2018), and Sánchez-López et al. (2019). Here, we use the ranges from −150 to −50 km s^{-1}, and from

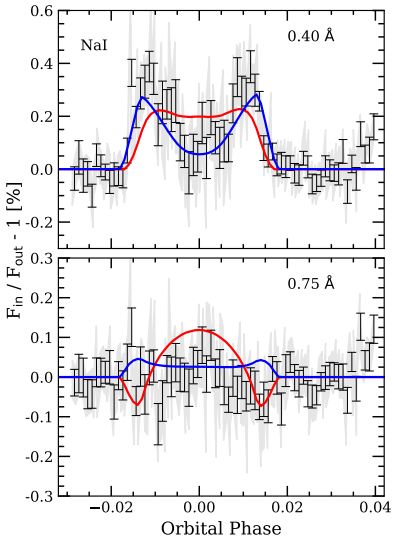

Fig. 6: Transmission light curves calculated in Na I doublet after combining both nights, using a 0.4 Å (*top*) and 0.75 Å (*bottom*) passbands. In light grey we show the original data. In black, we show the data binned by 0.001 in orbital phase. In red we show the impact of the CLV and RM effects in the transmission light curve. In blue only the RM effect is considered.

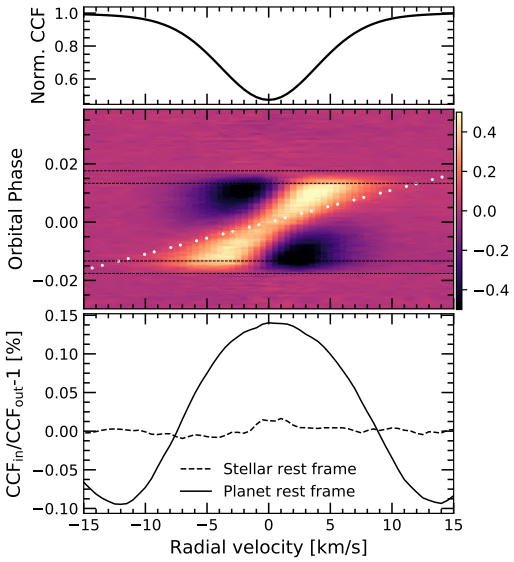

Fig. 7: *Top panel:* Average out-of-transit stellar CCF. *Middle panel:* Tomography of the CCFs deformation for the two transits combined in the stellar rest frame. The dotted white line indicates the planet radial velocities and the black horizontal dashed lines show the four contacts of the transit. The colour bar shows the relative variation of the CCFs with respect the combined out-of-transit CCF in %. *Bottom panel*: Combination of the CCF residuals from *middle panel* in the stellar rest frame (dashed line) and in the planet rest frame (solid line) between the first and fourth contact.

+50 to +150 km s^{-1}. In these units, a positive S/N means correlation with the atmospheric absorption template, and negative S/N means anti-correlation. We note that increasing the temperature of the isothermal models to 2000 K for Fe I, Fe II and Ca I, and to 3000 K for V I, the results do not change significantly.

The scenario observed in Na I, Fe I, Fe II and Ca I is repeated for the spectral lines observed in the full stellar spectrum when we attempt to detect the exoplanet atmosphere. As example, we compute the transmission spectrum for particular individual lines such as Mg I at 5183.60 Å, Fe I at 5270.36 Å, Hα at 6562.81 Å, and K I D1 line at 7698.96 Å. The results are presented in Figure 9. As in the case of Na I, in all cases, the transmission spectra are consistent with the modelled RM effect, with and without considering the CLV effect due to the small (within the measurements error bars) difference this last one introduces. However, the light curves seem to be better explained when considering only the RM effect, even at lower S/N. The estimated effects on the Hα transmission spectrum do not describe the observations as well as for the other lines. In Figure A.4 the modelled stellar lines profile, computed using the MARCS stellar models and LTE, are shown together with the observations. It is clear that the Mg I and Fe I lines, for example, are better reproduced by the stellar models than Hα. This is probably due to its chromospheric origin, as also observed for the Ca II IRT in Casasayas-Barris et al. (2020). These lines require more accurate stellar modelling.

4.3. Systematic effects analysis

The error bars of the measurements come from the propagation of the random photon noise. Following Redfield et al. (2008), we can statistically quantify the systematic effects of our data using the Empirical Monte Carlo (EMC) analysis. This method has already been applied in several atmospheric studies such as Wyttenbach et al. (2015, 2017), Jensen et al. (2011, 2012), Chen et al. (2020). It consists in measuring the absorption depth of a transmission spectrum calculated using different in- and out-of-transit samples (scenarios), which do not need to match the real in- and out-of-transit data. With this, if a feature appears only during the transit, we would expect it to be only measured when the real in- and out-of-transit data are considered in the samples.

Here, we assume the four different scenarios described in Casasayas-Barris et al. (2020), called "out-out", "in-in", "mix-mix" and "in-out" depending on the data considered as in- and out-of-transit samples, respectively. For each scenario we run the EMC 20 000 times, measuring the absorption depth in the expected position of the line using a 0.4 Å passband. In Figure B.1 of the Appendix we show the absorption depth distributions. For the Na I, it is clear that the "in-out" samples of both nights are centred at a different position in comparison with the control distributions. Their position are 0.19% in average for the two nights. The control distributions are all centred at 0%, and the standard deviation of the Gaussian profiles from the "out-out"

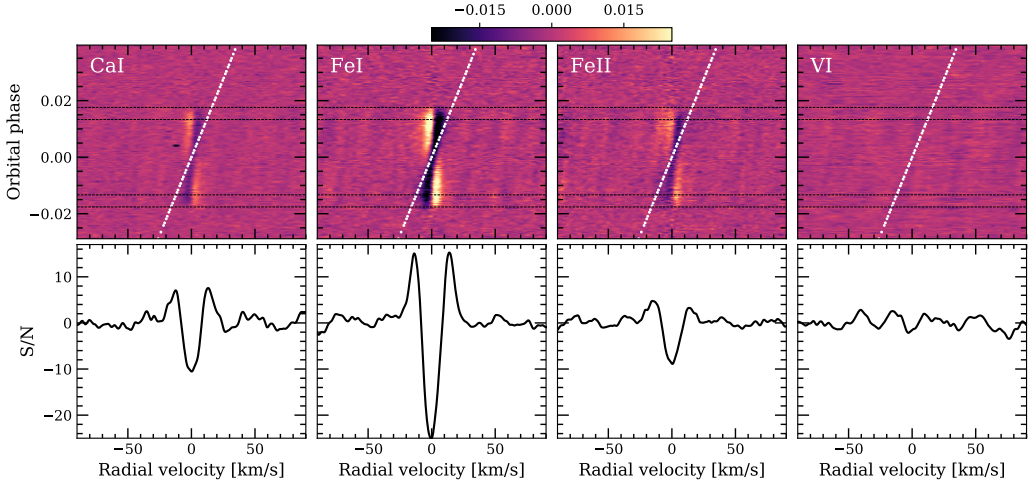

Fig. 8: Cross-correlation results of both nights combined for Ca I, Fe I, Fe II, and V I (from left to right, respectively). *Top panel*: cross-correlation maps of the three different species. *Bottom panel*: average of the in-transit cross-correlation values in the planet rest frame between the first and fourth contacts. The y-axis is shown in S/N units, where negative values mean anti-correlation (see the cross-correlation coefficients in the colour bar).

distribution are 0.04% and 0.05% (for the first and second night, in the same order), which give us an idea of the noise level of the data.

This exercise is also applied to the other lines analysed here (Mg I λ5184, Fe I λ5270, Hα, and K I D1). As for the Na I case, in all these lines, the absorption scenario shows distributions centred at positive absorption depth values (0.12%, 0.15% 0.03%, and 0.12%, respectively) while the control distributions remain centred at 0%. We note that for Hα, as the line is broader, we use a larger passband of 0.5 Å, and the expected effects in this line are fainter (see Figure 9). The EMC histograms of these lines are presented in Figure B.1 in the Appendix.

4.4. Searching for molecules

In contrast with the atomic lines analysed in the previous sections, CLV and RM effects are not expected to impact the search for those atoms and molecules in the exoplanet atmosphere which are not present in the stellar spectrum, in case there is no overlap with other stellar lines. For this reason, we attempt to search for the presence of molecules such as TiO and VO. Spectral features possibly associated to these same molecules were tentatively observed in HD 209458b atmosphere around 6 000 − 8000 Å by Désert et al. (2008) using HST-STIS observations. However, other studies at high resolution spectroscopy such as Hoeijmakers et al. (2015) found no evidence of TiO in this same planet.

Here, in the wavelength region covered by ESPRESSO and using the different TiO and VO models generated as described in Sect. 3.5, we find no evidence of these species in the atmosphere of HD 209458b. In the final cross-correlation residuals (see Figure C.1) we observe several faint structures produced by the RM effect of closer stellar lines that are introduced in the radial-velocity space explored in the cross-correlation, but not at the expected planet position ($\sim$ 0 km s^{-1}). It is known that the TiO and VO line lists are not very accurate at high spectral resolution (Merritt et al. 2020; McKemmish et al. 2019). As already studied by Hoeijmakers et al. (2015), the lack of an accurate line list can become a critical aspect when attempting to detect atmospheric features using the cross-correlation technique.

5. Accuracy of the modelled transit effects

In Sect. 4.1, 4.2 we observe that the transmission spectra can be explained by the combination of both CLV and RM effects, but also when only the dominant effect (the RM) is included in the calculations, considering the error bars of the data. The differences between both assumptions are small when the in-transit residuals are combined in the planet rest frame, as the CLV effect at the Na I D2 line position is more than four times smaller than the RM when calculated using the MARCS LTE stellar models. However, in the transmission light curves (Figures 6 and 9) we are sensitive to time variations of a particular spectral region. In this case, we observe that the results are better described when only the RM effect in the stellar lines is considered, probably indicating an overestimation of the CLV effect.

Casasayas-Barris et al. (2020) and previous sections of this work use the MARCS stellar atmospheric models (Gustafsson et al. 2008) assuming local thermodynamic equilibrium (LTE). We use solar abundances, as from Adibekyan et al. (2012) we know that HD 209458 has [Na/H]= 0.010 ± 0.057. Here, thanks to the unprecedented S/N achieved by the ESPRESSO observations, we analyse the differences in the modelled effects when considering different stellar atmospheric models. In particular, we compare the results around the Na I when assuming MARCS stellar models calculated with LTE and non-LTE approximations (Mashonkina et al. 2008). We also use ATLAS9 (Castelli & Kurucz 2003) and ATLAS12 (Kurucz 2013) models assuming LTE. We note that non-LTE grids are only offered for MARCS mod-

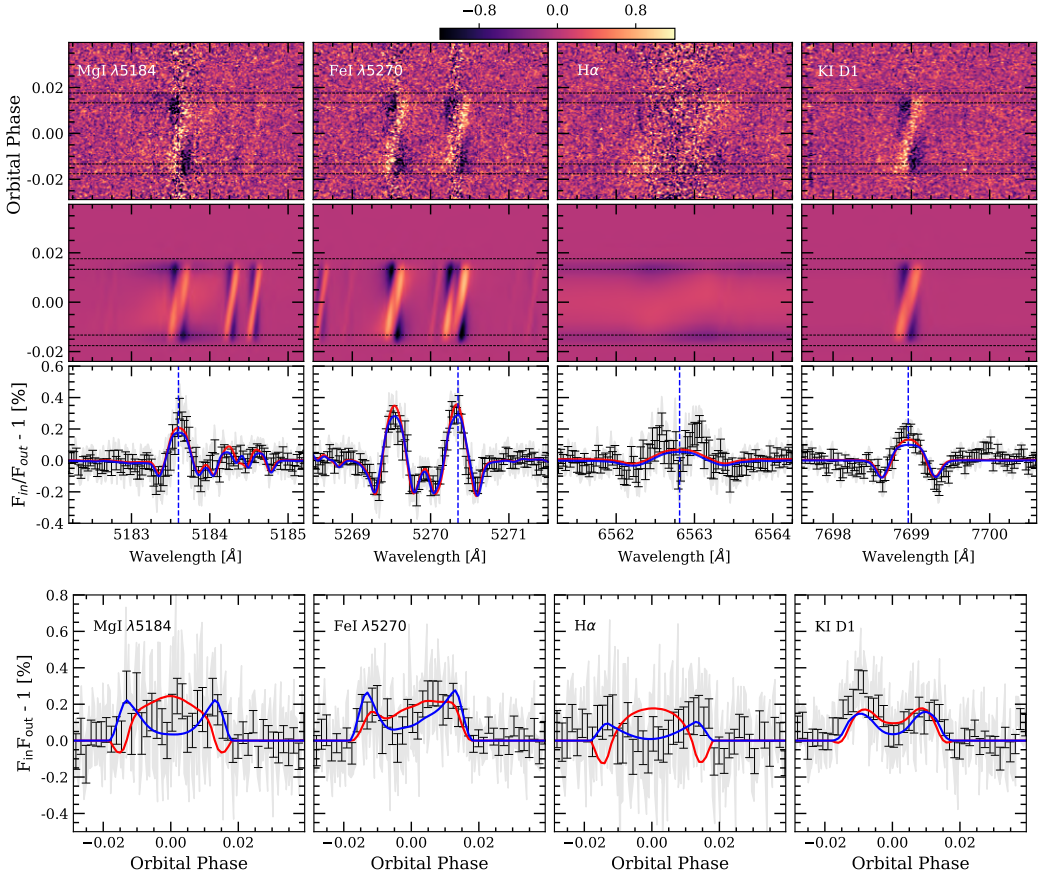

Fig. 9: Results around the Mg I λ5184 (first column), Fe I λ5270 (second column), Hα (third column) and K I D1 (fourth column) spectral lines. *Top panel*, *first row*: two-dimensional map of the transmission residuals of HD 209458b around different spectral lines. *Second row*: two-dimensional map of the modelled CLV and RM effects. In both panels the residuals are presented in the stellar rest frame. The black horizontal dashed lines indicate the four contacts of the transit. *Third row*: transmission spectrum computed in the planet rest frame considering the data between the first and fourth contacts of the transit. The original data is shown in light gray and the data binned by 0.03 Å is shown in black. The blue-dashed vertical lines show the laboratory position of the lines. The colour bar shows the relative flux (F_{in}/F_{out}-1) in %. *Bottom panel:* transmission light curves calculated for each line using 0.4 Å bandwidth and 0.5 Å for Hα. In light grey we show the original data and in black the data binned by 0.0015 in orbital phase. In both panels the red and blue lines correspond to the RM model with and without considering the CLV effect, respectively.

els (Piskunov & Valenti 2017). The results are presented in Figure 10. In Figure A.3 the modelled stellar spectra in the Na I region can be compared with the observed stellar spectrum.

In the transmission spectrum we observe that the different models and assumptions produce different intensities of the line deformations (left panel of Figure 10). The different models assuming LTE approximation produce very similar results, while the models assuming non-LTE differ by ~ 0.2% in relative flux at the Na I lines centre. Around the Na I, LTE models remain underestimated in comparison with the data and the non-LTE models seem to reproduce the results much better. We observe that the CLV impact at the Na I lines core of the transmission spectrum changes of a factor of two depending on the stellar model selection. When we model the transmission light curves in the planetary rest frame (third panel of Figure 10), we clearly see that the observations are better reproduced when only the RM deformation is considered, specially at the centre of the transit. As presented in Louden & Wheatley (2015) and Borsa & Zannoni (2018), in the planet rest frame the RM symmetry is broken, resulting in spurious residuals in the stellar line position. For the transmission light curve calculated in the stellar rest frame (right panel of Figure 10), where we are actually tracking the stellar line deformations in their own frame, the RM symmetry is maintained and thus averaged out when integrating the full ef-

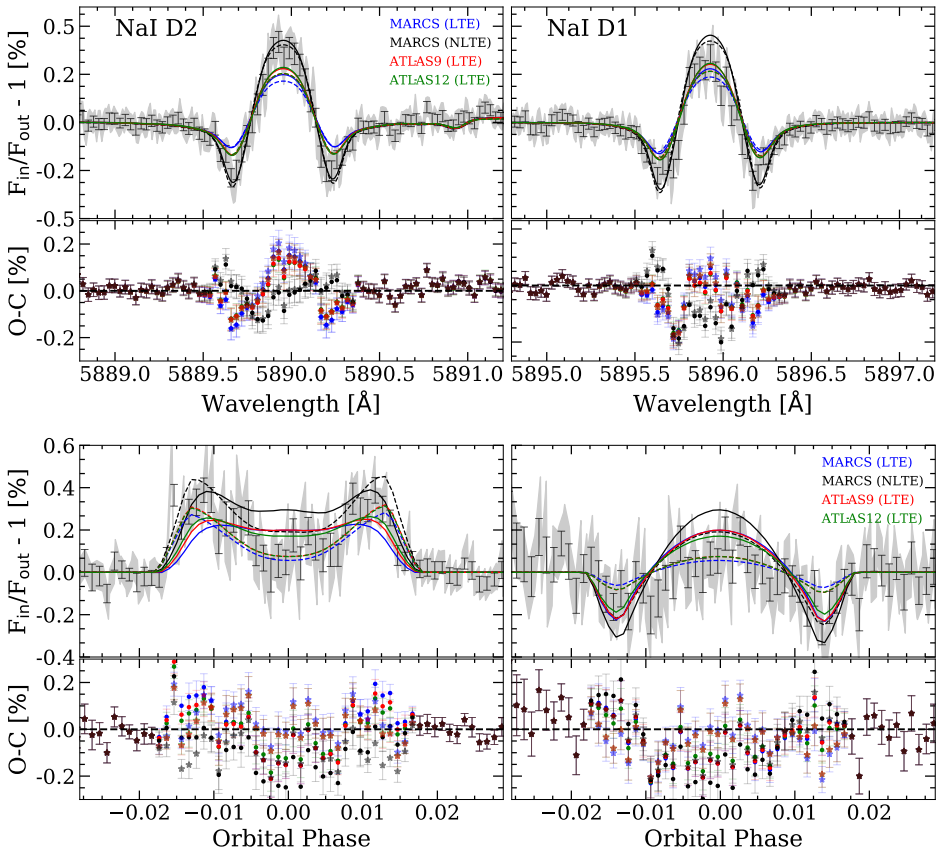

Fig. 10: Top panel, from left to right: modelled CLV and RM effects of the Na I doublet lines assuming different stellar atmospheric models compared with the transmission spectrum around Na I D2 (*left panel*) and D1 (*right panel*). Bottom panel: transmission light curve of both lines combined calculated in the planet rest frame (*left panel*), and the transmission light curve in the stellar rest frame (*right panel*). In solid lines we show the models containing the CLV and RM deformation. In dashed lines only the RM is considered. In light grey we show the original data and in black error bars the data binned by 0.03 Å (top panels), and 0.001 in orbital phase (bottom panels). The different stellar models are shown in different colours and indicated in the legends. Bottom row: residuals between the data and the models. The colours indicate the residuals between the data and the model shown with the same colour. In stars we indicate the residuals with the models computed considering only the RM deformation, and in dots the residuals with the models containing the CLV and RM deformation.

fect inside the 0.4 Å passband. In this frame, the CLV is the main contribution of the transmission light curve. As can be observed in the figure, the ingress and egress regions are better described considering the CLV contribution, as expected, but the overall effect in the mid-transit time region remains slightly overestimated.

When the residuals between the models and the data are computed (see bottom row of Figure 10), we observe a large scatter expanding approximately ±0.2 % depending on the model used. Therefore, attempting to measure features at these atmospheric absorption levels can become very challenging for HD 209458b. Using a 0.75 Å passband centred at the Na I lines position in the residuals, we measure a mean excess ranging from −0.05 % to −0.02 %, depending on the stellar model considered in the subtraction. In the transmission light curves, the in-transit residuals show an excess change between −0.09 % and +0.04 %.

With the S/N achieved with ESPRESSO observations, we are able to obtain the local stellar spectrum following the methodology presented in Section 3.2. The local stellar spectrum is the spectrum of those regions in the stellar surface that are blocked by the planet at each exposure during the transit, and which are therefore missing in the integrated disc spectrum observations. In Figure 11 we show the local spectrum around the Na I doublet lines at different orbital phases of the planet. A similar analysis is shown in Dravins et al. (2017) for this same planet using several

Fe I lines. Here, we observe that, during the transit, the exoplanet obscures blue-shifted regions of the stellar disc and continues to the red-shifted stellar surface, producing the RM effect that is propagated to the transmission spectrum. We also observe that the predicted models are able to reproduce the observations, although the lines core remain slightly underestimated. If the local stellar spectra are normalised to their continuum level and the two lines of the doublet are combined to get higher S/N profiles, we observe the expected wavelength shift of the lines produced by RM effect, but the CLV is not clearly seen in the data, although predicted by the stellar models (see Figure A.5). This is one more indication of the CLV overestimation for this particular star.

The importance of the CLV for atmospheric characterisation of exoplanets has been pointed out in several studies (e.g. Czesla et al. 2015; Yan et al. 2017; Khalafinejad et al. 2017; Casasayas-Barris et al. 2017). The CLV in the stellar atmosphere strongly depends on wavelength, and it is expected to be more intense for cooler stars. In the optical, it is strong in the deep stellar absorption lines profile such as Na I D and Ca II H&K lines (Czesla et al. 2015). In the study of exoplanet transit light-curves, the CLV is one of the critical parameters (Müller et al. 2013). Using HD 209458b transit light curves, Hayek et al. (2012) compared the CLV predictions resulting from MARCS one-dimensional (1D) atmospheric models and three-dimensional (3D) models, concluding that the 3D model provides a considerably better description of the atmospheric temperature structure of HD 209458. Chiavassa & Brogi (2019) also show that, in general, 1D stellar models can differ significantly from 3D models.

On the other hand, the differences could be also produced by the combination of different stellar phenomena that are not contemplated in the stellar spectra and/or due to a misinterpretation of the stellar atmospheric structure. For example, the RM could be affected by convective shifts (Cegla et al. 2016a; Dravins et al. 2017). The convective shifts are a consequence of the stellar granulation and occurs because the emerging granules are brighter than the surroundings and cover a greater fraction of the stellar surface (Dravins 1982). It typically results in an additional blue shift between the position of the stellar lines and their laboratory position, with expected amplitudes of $0 - 500\,\mathrm{m\,s^{-1}}$ for G-type stars (Meunier et al. 2017), and it is less intense in those deep lines formed higher in the stellar atmosphere (Allende Prieto & Garcia Lopez 1998; Reiners et al. 2016), such as Na I. Moreover, it is known that granulation and star-spots can produce asymmetric line profiles on the stellar disc, which could be considered using 3D magneto-hydrodynamic solar simulations as presented in Cegla et al. (2016b). On the other hand, solar-like differential rotation can become important in main sequence stars (Karoff et al. 2018), and it is expected to be stronger in F-G stars (Balona & Abedigamba 2016). In our calculations we assume solid-body rotation, meaning that we are not considering the amplitude variation of the RM signal that could be introduced by this effect (Serrano et al. 2020).

Currently, ESPRESSO is the best facility to spatially resolve the stellar surface by means of transit spectroscopy observations. This will help to empirically validate the stellar models, and constrain the 3D hydrodynamic models of stellar photosphere (Dravins et al. 2015, 2017).

6. Summary and conclusions

Using two transit observations with ESPRESSO we revisit the transmission spectrum of HD 209458b and the system architecture using the reloaded-RM technique. We analyse individual atomic lines (Na I doublet, Mg I λ5184, Fe I λ5270, Hα, and K I D1), and we also use the cross-correlation technique to search for atomic lines (Fe I, Ca I, Fe II, and V I) and molecules (TiO and VO).

The ESPRESSO observations confirm the results obtained in Casasayas-Barris et al. (2020), where the Na I features observed in the transmission spectrum can be explained by the deformation of the stellar lines profile due to the transit of HD 209458b, mainly produced by the RM effect, and without the need of absorption from the exoplanet atmosphere. This is also observed in the transmission spectra around other atomic lines and in the results obtained using the cross-correlation techniques. Moreover, we examine the CCF values computed by the DRS as presented in Borsa et al. (2020), where the deformation of the lines profile is clearly visible. This effect is present for all stellar lines, and it is thus propagated through the method when attempting to extract any exoplanet atmospheric signals. Similarly, this change in the stellar lines profile is imprinted in the CCF values when a stellar template is cross-correlated with the stellar spectra (Borsa & Zannoni 2018). The radial-velocity change of the planet during the transit is very similar to the velocity range affected by the RM deformation, and only a small time-region in the ingress and egress regions could be used to disentangle the exoplanet atmospheric signals by the stellar contamination.

Several atomic lines, including the Na I, have been previously detected in the atmosphere of HD 209458b using high-resolution spectroscopy observations. This is the case of the 0.135 ± 0.017 % Na I absorption detected in the transmission light curves by Snellen et al. (2008) and Albrecht et al. (2009), for example. The Na I transmission light curve obtained with ESPRESSO observations and following the methodology presented in these previous studies (see Figure A.6) does not reproduce the absorption and, in contrast, shows a better agreement with the modelled RM light curve. On the other hand, Langland-Shula et al. (2009) found $> 3\sigma$ Na I absorption and also $> 2\sigma$ absorption in Fe I and Ni I lines. Jensen et al. (2011) tentatively detected Na I absorption, and Astudillo-Defru & Rojo (2013) found significant absorption excess due to Ca I, Hα, Na I, and possibly Sc II. All these lines are present in the stellar atmosphere and we can detect the RM deformation at high S/N in our analysis, however, we do not find evidences of absorption due to the exoplanet atmosphere. Focusing on Hα, Jensen et al. (2012) detected a feature with reflectional symmetry correlated in orbital phase and expanding ~ 15 Å. This broad feature can not be reproduced with the methodology presented here.

The S/N of the observations used in these previous studies is similar to the observations used in this work. This is the case of the Subaru observations used by Narita et al. (2005), Snellen et al. (2008) and Astudillo-Defru & Rojo (2013), for example, which achieved a S/N$\sim$ 350 per pixel in the continuum using 500 s exposures. The observations used here show a mean S/N of $\sim$ 220 in the Na I order, but using exposures of 175 s which results in a larger number of spectra. However, most of these studies used a different methodology. Thanks to the different high-resolution studies, the method to extract the transmission spectrum of the exoplanets has rapidly improved, including some steps that were not considered before, such as the planet radial-velocity correction. In the particular case of HD 209458b, using different methodology or partial transit observations leads to significantly different transmission spectra (see Figures 5 and 10) due to the RM deformation, and which could be easily misinterpreted.

At high resolution, the RM contamination could be avoided by searching for molecules not present in the stellar atmosphere

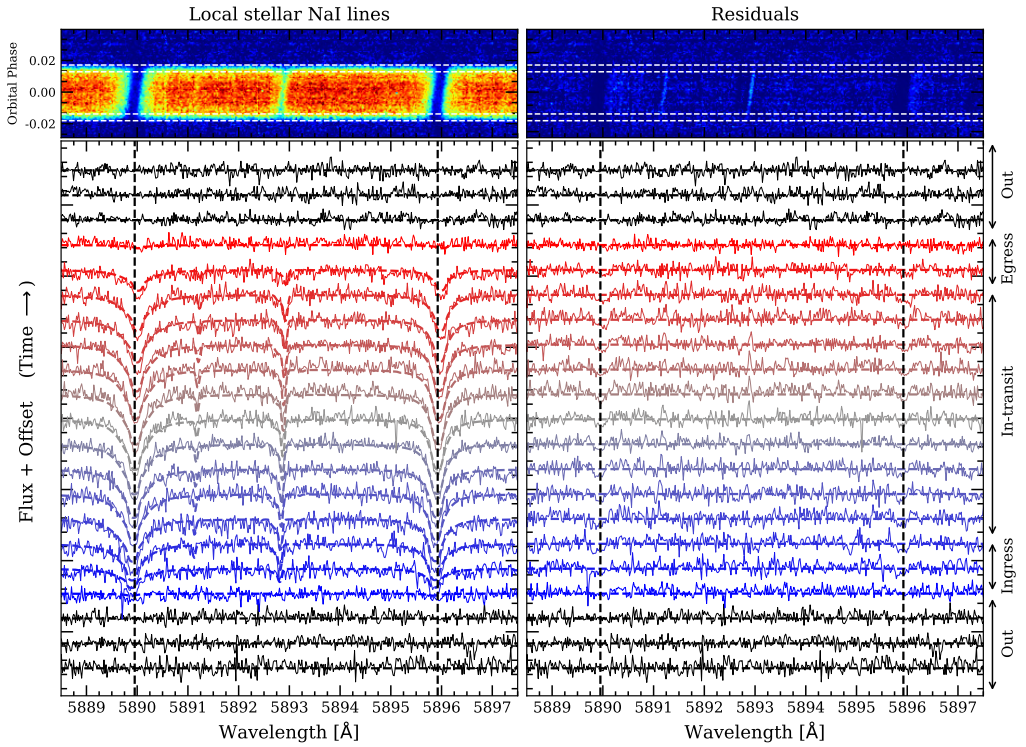

Fig. 11: *Left panel*: local stellar spectrum of HD 209458 around the Na I doublet lines. In the *top-left panel* we show the local stellar spectrum following the same format presented in Figure 1, but around the Na I doublet. The *bottom-left panel* shows the time-evolution of the local stellar spectrum presented in the top panel but, in this case, the flux information is shown in the vertical axis. The spectra are not normalised to their own continuum level, so they still contain the flux information (the normalised profiles are shown in Figure A.5). For a clear visualisation, we have modified the continuum flux including an offset so the spectra are shown ordered in orbital phase. The colours are indicative of the orbital phase of the planet and, therefore, the radial-velocity of the stellar disc surface. The observations are shown with solid lines and the stellar models with dashed lines of the same colour. The stellar models are computed using MARCS in LTE. The out-of-transit results are shown in black. The spectra are shown binned by 0.02 Å and 0.0025 in orbital phase. The black-dashed vertical lines indicate the position of the Na I doublet lines. *Right panel:* residuals between the observed and modelled local spectra presented in the left panel.

(if they fall far from other deep stellar lines). Here, we explore the presence of TiO and VO, as it was tentatively observed in Désert et al. (2008). These molecules are expected at temperatures above 1800 K, in strongly irradiated hot Jupiters (Seager & Sasselov 1998; Fortney et al. 2008). Indeed, TiO has already been tentatively detected in ultra hot planets (T_{eq} > 2000 K) such as WASP-19b (Sedaghati et al. 2017) and WASP-121b (Evans et al. 2016). However, one of the main difficulties when attempting to detect these molecules using the cross-correlation techniques is the lack of accurate line lists (Hoeijmakers et al. 2015). HD 209458b has an equilibrium temperature (T_{eq}) around 1400 K (Torres et al. 2008), and it is probably too cold for these species to be present in its atmosphere. Despite the high S/N of our data, we are not able to identify in the residuals any clear feature that could be generated by these molecules.

In atmospheric analysis performed at high resolution, a relatively small region around the lines core is probed and the continuum information is lost, while at low resolution the wings of the atmospheric lines are probed, which may present widths as large as 100 nm (see Sing et al. 2016, for example). The RM contamination seen in the Na I lines occupies ∼ 1 Å in the high-resolution transmission spectrum. At low resolution, this contamination would be completely included in the wavelength bin centred on the Na I doublet lines. For this reason, with our ESPRESSO data we can not exclude the atmospheric detections reported using broad-band transmission spectroscopy methods (e.g. Charbonneau et al. 2002). However, this particular scenario, where the broad wings of Na I are detected but not the cores of the lines is difficult to explain in terms of atmospheric physics.

Here, thanks to the S/N achieved with ESPRESSO observations, we are able to observe that the resulting transmission light curves can be better explained when only the RM contribution is considered, specially at the centre of the transit. However, during the ingress and egress, the contribution of the CLV is needed

to fit the observations. We additionally explore the differences of the modelled RM and CLV effects when assuming different 1D stellar atmospheric models. It is clear, however, that the modelled CLV and RM effects do not fully reproduce the results around the Na I, probably due to the approximations that their computation assumes and stellar phenomena that are not considered (1D, solid-body rotation, no convective blue shift, among others), although the non-LTE models describe the transmission spectrum better. Resolving the stellar surface using transit observations of the exoplanets (Dravins et al. 2015) would help to empirically validate and constrain the stellar atmospheric models and, consequently, improve the characterisation of the exoplanet atmospheres. Currently, ESPRESSO is the best opportunity to perform these observations.

Acknowledgements. This work is partly financed by the Spanish Ministry of Science, Innovation and Universities through project ESP2016-80435-C2-2-R, ESP2017-87143-R, AYA2017-86389-P, AYA2016-79425-C3-2-P, and PID2019-109522GB-C51. G.C. acknowledges the support by the National Natural Science Foundation of China (Grant No. 42075122) and the Natural Science Foundation of Jiangsu Province (Grant No. BK20190110). F.Y. acknowledges the support of the DFG priority program SPP 1992 "Exploring the Diversity of Extrasolar Planets (RE 1664/16-1)". This project has received funding from the European Research Council (ERC) under the European Union's Horizon 2020 research and innovation programme (project Four Aces grant agreement No 724427). N.J.N acknowledges support from FCT through Investigador FCT contract and exploratory project IF/00852/2015, and project PTDC/FIS-OUT/29048/2017. This work was supported by FCT - Fundação para a Ciência e a Tecnologia through national funds and by FEDER through COMPETE2020 - Programa Operacional Competitividade e Internacionalização by these grants: UID/FIS/04434/2019; UIDB/04434/2020; UIDP/04434/2020; PTDC/FIS-AST/32113/2017 & POCI-01-0145-FEDER-032113; PTDC/FIS-AST/28953/2017 & POCI-01-0145-FEDER-028953; PTDC/FIS-AST/28987/2017 & POCI-01-0145-FEDER-028987. V.A. acknowledges the support from FCT through Investigador FCT contracts nr. IF/00650/2015/CP1273/CT0001. S.G.S acknowledges the support from FCT through Investigador FCT contract nr. CEECIND/00826/2018 and POPH/FSE (EC). O.D.S.D. is supported in the form of work contract (DL 57/2016/CP1364/CT0004) funded by FCT. This research has been funded by the Spanish State Research Agency (AEI) Projects No.ESP2017-87676-C5-1-R and No. MDM-2017-0737 Unidad de Excelencia "María de Maeztu"-Centro de Astrobiología (INTA-CSIC). The INAF authors acknowledge financial support of the Italian Ministry of Education, University, and Research with PRIN 201278X4FL and the "Progetti Premiali" funding scheme. FPE and CLO would like to acknowledge the Swiss National Science Foundation (SNSF) for supporting research with ESPRESSO through the SNSF grants nr. 140649, 152721, 166227 and 184618. J.I.G.H. acknowledges financial support from Spanish Ministry of Science and Innovation (MICINN) under the 2013 Ramón y Cajal program RYC-2013-14875. A.S.M. acknowledges financial support from the Spanish MICINN under the 2019 Juan de la Cierva Programme. C.A.P., J.I.G.H., R.R., and A.S.M. acknowledge financial support from the Spanish MICINN AYA2017-86389-P. This work has been carried out within the framework of the National Centre of Competence in Research Planets supported by the Swiss National Science Foundation. The authors acknowledge the financial support of the SNSF. The ESPRESSO Instrument Project was partially funded through SNSF's FLARE Programme for large infrastructures. This work made use of PyAstronomy and of the VALD database, operated at Uppsala University, the Institute of Astronomy RAS in Moscow, and the University of Vienna.

References

Adibekyan, V. Z., Sousa, S. G., Santos, N. C., et al. 2012, A&A, 545, A32
Albrecht, S., Snellen, I., de Mooij, E., & Le Poole, R. 2009, in IAU Symposium, Vol. 253, Transiting Planets, ed. F. Pont, D. Sasselov, & M. J. Holman, 520–523
Allart, R., Bourrier, V., Lovis, C., et al. 2018, Science, 362, 1384
Allart, R., Lovis, C., Pino, L., et al. 2017, A&A, 606, A144
Allart, R., Pino, L., Lovis, C., et al. 2020, arXiv e-prints, arXiv:2010.15143
Allende Prieto, C. & Garcia Lopez, R. J. 1998, A&AS, 129, 41
Astudillo-Defru, N. & Rojo, P. 2013, A&A, 557, A56
Balona, L. A. & Abedigamba, O. P. 2016, MNRAS, 461, 497
Birkby, J. L., de Kok, R. J., Brogi, M., Schwarz, H., & Snellen, I. A. G. 2017, AJ, 153, 138
Bonomo, A. S., Desidera, S., Benatti, S., et al. 2017, A&A, 602, A107
Borsa, F., Allart, R., Casasayas-Barris, N., et al. 2020, arXiv e-prints, arXiv:2011.01245
Borsa, F. & Zannoni, A. 2018, A&A, 617, A134
Bourrier, V., Cegla, H. M., Lovis, C., & Wyttenbach, A. 2017, A&A, 599, A33
Bourrier, V., Ehrenreich, D., Lendl, M., et al. 2020, A&A, 635, A205
Bourrier, V., Lovis, C., Beust, H., et al. 2018, Nature, 553, 477
Brogi, M., de Kok, R. J., Birkby, J. L., Schwarz, H., & Snellen, I. A. G. 2014, A&A, 565, A124
Brogi, M., Giacobbe, P., Guilluy, G., et al. 2018, A&A, 615, A16
Casasayas-Barris, N., Palle, E., Nowak, G., et al. 2017, A&A, 608, A135
Casasayas-Barris, N., Pallé, E., Yan, F., et al. 2019, A&A, 628, A9
Casasayas-Barris, N., Pallé, E., Yan, F., et al. 2020, A&A, 635, A206
Castelli, F. & Kurucz, R. L. 2003, in IAU Symposium, Vol. 210, Modelling of Stellar Atmospheres, ed. N. Piskunov, W. W. Weiss, & D. F. Gray, A20
Cegla, H. M., Lovis, C., Bourrier, V., et al. 2016a, A&A, 588, A127
Cegla, H. M., Oshagh, M., Watson, C. A., et al. 2016b, ApJ, 819, 67
Charbonneau, D., Brown, T. M., Latham, D. W., & Mayor, M. 2000, ApJ, 529, L45
Charbonneau, D., Brown, T. M., Noyes, R. W., & Gilliland, R. L. 2002, ApJ, 568, 377
Chen, G., Casasayas-Barris, N., Pallé, E., et al. 2020, A&A, 635, A171
Chiavassa, A. & Brogi, M. 2019, A&A, 631, A100
Cosentino, R., Lovis, C., Pepe, F., et al. 2012, in Proc. SPIE, Vol. 8446, Ground-based and Airborne Instrumentation for Astronomy IV, 84461V
Czesla, S., Klocová, T., Khalafinejad, S., Wolter, U., & Schmitt, J. H. M. M. 2015, A&A, 582, A51
Czesla, S., Schröter, S., Schneider, C. P., et al. 2019, PyA: Python astronomy-related packages
da Silva, L., Girardi, L., Pasquini, L., et al. 2006, A&A, 458, 609
Damasso, M., Sozzetti, A., Lovis, C., et al. 2020, arXiv e-prints, arXiv:2007.06410
del Burgo, C. & Allende Prieto, C. 2016, MNRAS, 463, 1400
Deming, D., Wilkins, A., McCullough, P., et al. 2013, ApJ, 774, 95
Désert, J. M., Vidal-Madjar, A., Lecavelier Des Etangs, A., et al. 2008, A&A, 492, 585
Dravins, D. 1982, ARA&A, 20, 61
Dravins, D., Ludwig, H.-G., Dahlen, E., & Pazira, H. 2015, in Cambridge Workshop on Cool Stars, Stellar Systems, and the Sun, Vol. 18, 18th Cambridge Workshop on Cool Stars, Stellar Systems, and the Sun, 853–868
Dravins, D., Ludwig, H.-G., Dahlén, E., & Pazira, H. 2017, A&A, 605, A90
Ehrenreich, D., Lovis, C., Allart, R., et al. 2020, Nature, 580, 597
Espinoza, N. & Jordán, A. 2015, MNRAS, 450, 1879
Evans, T. M., Aigrain, S., Gibson, N., et al. 2015, MNRAS, 451, 680
Evans, T. M., Sing, D. K., Wakeford, H. R., et al. 2016, ApJ, 822, L4
Fortney, J. J., Lodders, K., Marley, M. S., & Freedman, R. S. 2008, ApJ, 678, 1419
Guilluy, G., Sozzetti, A., Brogi, M., et al. 2019, A&A, 625, A107
Gustafsson, B., Edvardsson, B., Eriksson, K., et al. 2008, A&A, 486, 951
Hayek, W., Sing, D., Pont, F., & Asplund, M. 2012, A&A, 539, A102
Henry, G. W., Marcy, G. W., Butler, R. P., & Vogt, S. S. 2000, ApJ, 529, L41
Hoeijmakers, H. J., de Kok, R. J., Snellen, I. A. G., et al. 2015, A&A, 575, A20
Hoeijmakers, H. J., Ehrenreich, D., Heng, K., et al. 2018, Nature, 560, 453
Jensen, A. G., Redfield, S., Endl, M., et al. 2012, ApJ, 751, 86
Jensen, A. G., Redfield, S., Endl, M., et al. 2011, ApJ, 743, 203
Karoff, C., Metcalfe, T. S., Santos, Â. R. G., et al. 2018, ApJ, 852, 46
Kausch, W., Noll, S., Smette, A., et al. 2015, A&A, 576, A78
Khalafinejad, S., von Essen, C., Hoeijmakers, H. J., et al. 2017, A&A, 598, A131
Kreidberg, L. 2015, PASP, 127, 1161
Kupka, F., Piskunov, N., Ryabchikova, T. A., Stempels, H. C., & Weiss, W. W. 1999, A&AS, 138, 119
Kurucz, R. L. 1993, SYNTHE spectrum synthesis programs and line data
Kurucz, R. L. 2013, ATLAS12: Opacity sampling model atmosphere program
Langland-Shula, L. E., Vogt, S. S., Charbonneau, D., Butler, P., & Marcy, G. 2009, ApJ, 696, 1355
Louden, T. & Wheatley, P. J. 2015, ApJ, 814, L24
Malik, M., Grosheintz, L., Mendonça, J. M., et al. 2017, AJ, 153, 56
Malik, M., Kitzmann, D., Mendonça, J. M., et al. 2019, AJ, 157, 170
Mashonkina, L., Zhao, G., Gehren, T., et al. 2008, A&A, 478, 529
McKemmish, L. K., Masseron, T., Hoeijmakers, H. J., et al. 2019, MNRAS, 488, 2836
McKemmish, L. K., Yurchenko, S. N., & Tennyson, J. 2016, MNRAS, 463, 771
Merritt, S. R., Gibson, N. P., Nugroho, S. K., et al. 2020, A&A, 636, A117
Meunier, N., Mignon, L., & Lagrange, A. M. 2017, A&A, 607, A124
Mollière, P., Wardenier, J. P., van Boekel, R., et al. 2019, A&A, 627, A67
Müller, H. M., Huber, K. F., Czesla, S., Wolter, U., & Schmitt, J. H. M. M. 2013, A&A, 560, A112
Naef, D., Mayor, M., Beuzit, J. L., et al. 2004, A&A, 414, 351
Narita, N., Suto, Y., Winn, J. N., et al. 2005, PASJ, 57, 471
Nortmann, L., Pallé, E., Salz, M., et al. 2018, Science, 362, 1388

Pepe, F., Damasso, M., Cristiani, S., Rebolo, R., & Santos, N. C. a. 2020, Å
Pepe, F., Molaro, P., Cristiani, S., et al. 2014, Astronomische Nachrichten, 335, 8
Pepe, F. A., Cristiani, S., Rebolo Lopez, R., et al. 2010, Society of Photo-Optical Instrumentation Engineers (SPIE) Conference Series, Vol. 7735, ESPRESSO: the Echelle spectrograph for rocky exoplanets and stable spectroscopic observations, 77350F
Pino, L., Désert, J.-M., Brogi, M., et al. 2020, ApJ, 894, L27
Piskunov, N. & Valenti, J. A. 2017, A&A, 597, A16
Piskunov, N. E., Kupka, F., Ryabchikova, T. A., Weiss, W. W., & Jeffery, C. S. 1995, A&AS, 112, 525
Plez, B. 1998, A&A, 337, 495
Plez, B. 2012, Turbospectrum: Code for spectral synthesis
Quirrenbach, A., Amado, P. J., Caballero, J. A., et al. 2014, in Proc. SPIE, Vol. 9147, Ground-based and Airborne Instrumentation for Astronomy V, 91471F
Quirrenbach, A., Amado, P. J., Ribas, I., et al. 2018, in Society of Photo-Optical Instrumentation Engineers (SPIE) Conference Series, Vol. 10702, Ground-based and Airborne Instrumentation for Astronomy VII, 107020W
Redfield, S., Endl, M., Cochran, W. D., & Koesterke, L. 2008, ApJ, 673, L87
Reiners, A., Mrotzek, N., Lemke, U., Hinrichs, J., & Reinsch, K. 2016, A&A, 587, A65
Richardson, L. J., Harrington, J., Seager, S., & Deming, D. 2006, The Astrophysical Journal, 649, 1043
Sánchez-López, A., Alonso-Floriano, F. J., López-Puertas, M., et al. 2019, A&A, 630, A53
Santos, N. C., Cristo, E., Demangeon, O., et al. 2020, A&A, 644, A51
Santos, N. C., Sousa, S. G., Mortier, A., et al. 2013, A&A, 556, A150
Seager, S. & Sasselov, D. D. 1998, ApJ, 502, L157
Sedaghati, E., Boffin, H. M. J., MacDonald, R. J., et al. 2017, Nature, 549, 238
Seidel, J. V., Ehrenreich, D., Wyttenbach, A., et al. 2019, A&A, 623, A166
Serrano, L. M., Oshagh, M., Cegla, H. M., et al. 2020, MNRAS, 493, 5928
Sing, D. K., Fortney, J. J., Nikolov, N., et al. 2016, Nature, 529, 59
Sing, D. K., Vidal-Madjar, A., Désert, J. M., Lecavelier des Etangs, A., & Ballester, G. 2008, ApJ, 686, 658
Smette, A., Sana, H., Noll, S., et al. 2015, A&A, 576, A77
Sneden, C. 1973, ApJ, 184, 839
Snellen, I. 2013, in European Physical Journal Web of Conferences, Vol. 47, European Physical Journal Web of Conferences, 11001
Snellen, I. A. G., Albrecht, S., de Mooij, E. J. W., & Le Poole, R. S. 2008, A&A, 487, 357
Snellen, I. A. G., de Kok, R. J., de Mooij, E. J. W., & Albrecht, S. 2010, Nature, 465, 1049
Sousa, S. G. 2014, ARES + MOOG: A Practical Overview of an Equivalent Width (EW) Method to Derive Stellar Parameters, 297–310
Sousa, S. G., Santos, N. C., Adibekyan, V., Delgado-Mena, E., & Israelian, G. 2015, A&A, 577, A67
Sousa, S. G., Santos, N. C., Israelian, G., Mayor, M., & Monteiro, M. J. P. F. G. 2007, A&A, 469, 783
Sousa, S. G., Santos, N. C., Mayor, M., et al. 2008, A&A, 487, 373
Stangret, M., Casasayas-Barris, N., Pallé, E., et al. 2020, A&A, 638, A26
Stassun, K. G., Collins, K. A., & Gaudi, B. S. 2017, AJ, 153, 136
Suárez Mascareño, A., Faria, J. P., Figueira, P., et al. 2020, A&A, 639, A77
Tabernero, H. M., Marfil, E., Montes, D., & González Hernández, J. I. 2019, A&A, 628, A131
Tabernero, H. M., Zapatero Osorio, M. R., Allart, R., et al. 2020, arXiv e-prints, arXiv:2011.12197
Torres, G., Winn, J. N., & Holman, M. J. 2008, ApJ, 677, 1324
Valenti, J. A. & Piskunov, N. 1996, A&AS, 118, 595
Vidal-Madjar, A., Arnold, L., Ehrenreich, D., et al. 2010, A&A, 523, A57
Winn, J. N., Suto, Y., Turner, E. L., et al. 2004, PASJ, 56, 655
Wyttenbach, A., Ehrenreich, D., Lovis, C., Udry, S., & Pepe, F. 2015, A&A, 577, A62
Wyttenbach, A., Lovis, C., Ehrenreich, D., et al. 2017, A&A, 602, A36
Yan, F., Casasayas-Barris, N., Molaverdikhani, K., et al. 2019, A&A, 632, A69
Yan, F. & Henning, T. 2018, Nature Astronomy, 2, 714
Yan, F., Pallé, E., Fosbury, R. A. E., Petr-Gotzens, M. G., & Henning, T. 2017, A&A, 603, A73
Zhou, G. & Bayliss, D. D. R. 2012, MNRAS, 426, 2483

Appendix A: Additional results around the Na I

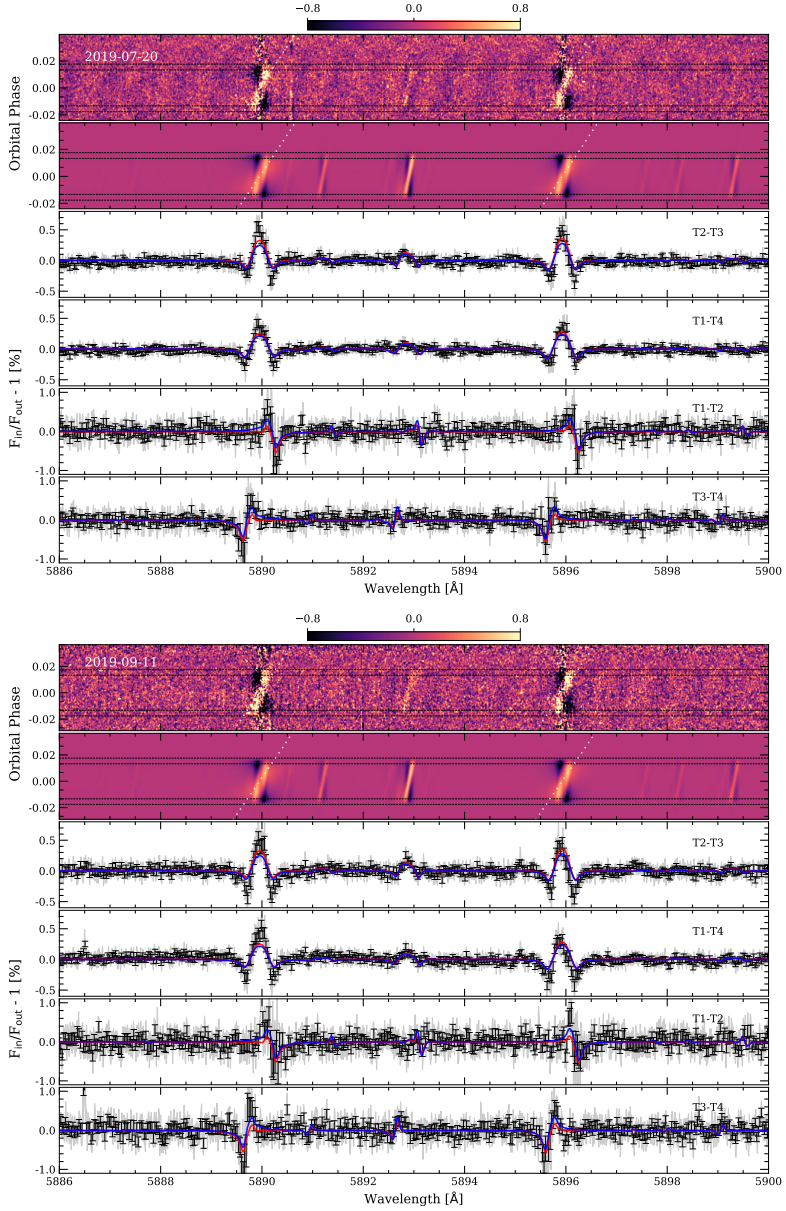

Fig. A.1: Same as Figure 5 but for the individual nights. The first night (2019-07-20) is presented in the *top panel*, and the second night (2019-09-11) is show in the *bottom panel*.

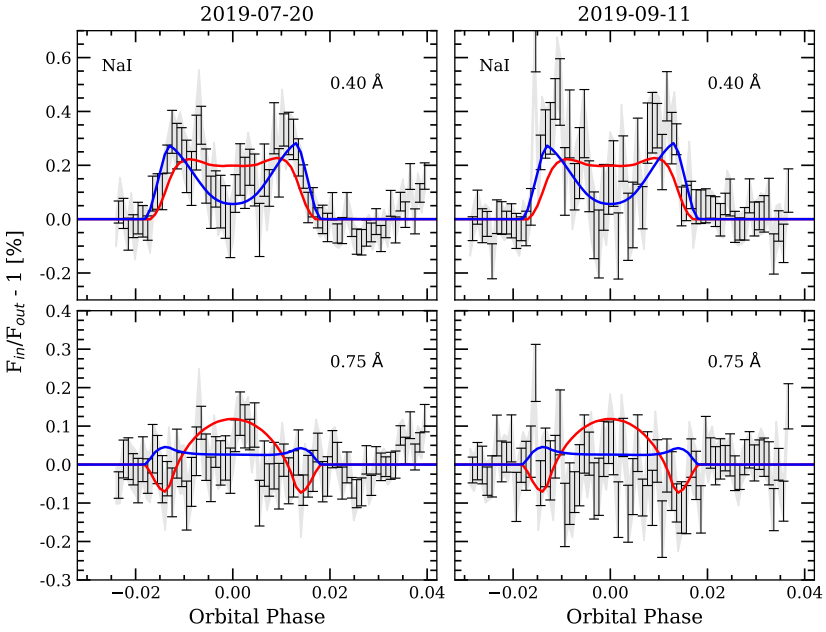

Fig. A.2: Same as Figure 6 but for the individual nights: first night (2019-07-20) in the *left column*, and second night (2019-09-11) in the *right column*. We note that the second night results could be partially affected by telluric Na I absorption residuals.

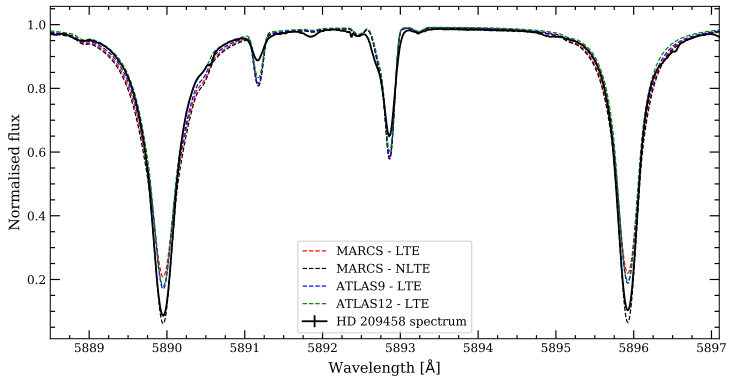

Fig. A.3: Master stellar spectrum in the Na I region of HD 209458 (black) computed as the combination of all out-of-transit spectra of the first night (2019-07-20). For comparison, in different colours we show the synthetic stellar spectrum computed with the different stellar models used in this work.

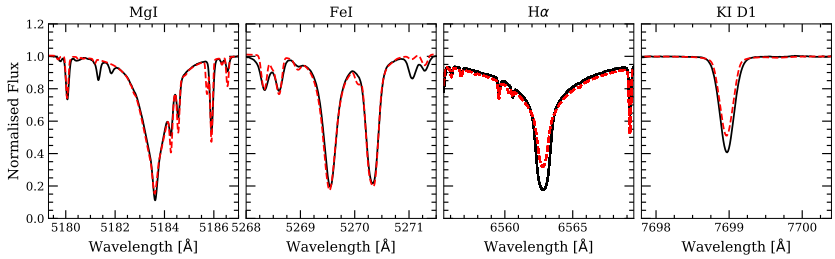

Fig. A.4: Master stellar spectrum of HD 209458 (black) computed as the combination of all out-of-transit spectra of the first night (2019-07-20) in different wavelength regions. For comparison, we show in red colour the synthetic stellar spectrum computed with the MARCS stellar models assuming the stellar parameters from Table 2, solar abundance, and LTE.

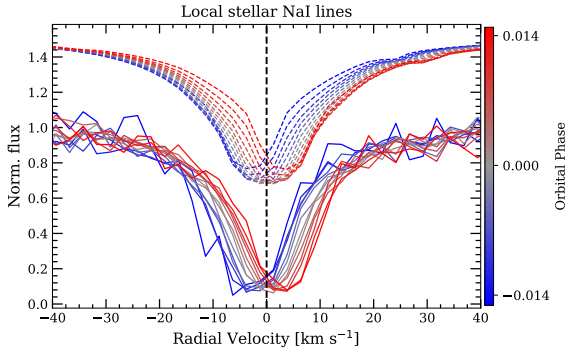

Fig. A.5: Observed (solid lines) and modelled (dashed lines) local stellar sodium Na I profiles at different orbital phases during the transit. The profiles are shown normalised to their continuum level, and result from the combination of both Na I D lines of the two nights of observation. The data is shown binned by 2.5 km s^{-1} and each profile is the result of combining the individual local stellar lines every 0.0025 in orbital phase. The models are shown with an offset to the vertical axis for better visualisation, and are computed using the MARCS stellar models in LTE. The colours indicate the orbital phase of the planet (see colour bar). The vertical black-dashed line is a reference at 0 km s^{-1}.

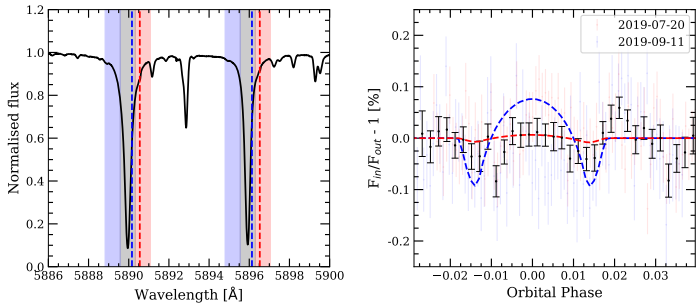

Fig. A.6: Transmission light curves around the Na I computed as presented in Snellen et al. (2008) and Albrecht et al. (2009). *Left panel:* stellar spectrum around the Na I showing the central (grey) and reference (blue and red) passbands of each line of the doublet, all of them with a bandwidth of 0.75 Å. The vertical dashed lines show the position of the telluric Na I absorption residuals for the night of 2019-07-20 (red) and 2019-09-11 (blue). *Right panel:* Na I transmission light curve of each night (in colours) and the combination of the two nights (black dots). The combined result is binned by 0.002 in orbital phase, similar to the results presented in the previous literature. The blue-dashed line corresponds to the modelled transmission light curve considering the RM and CLV effects in the stellar spectrum. The red-dashed line considers only the RM effect.

Appendix B: Empirical Monte Carlo distributions

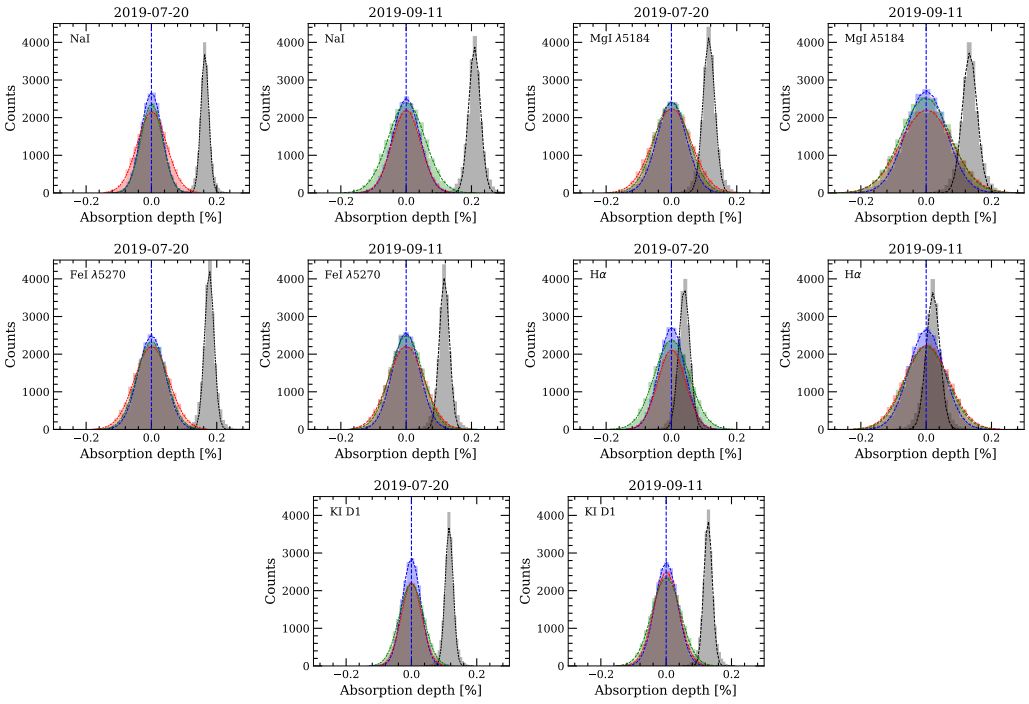

Fig. B.1: Distributions of the EMC analysis of each individual night for different spectral lines: Na I D1 and D2, Mg I λ5184, Fe I λ5270, Hα, and K I D1. The absorption depth calculations are performed using 0.4 Å bandwidth except for the Hα for which we use 0.5 Å. In green we present the "out-out" scenario, in red the "in-in", in blue the "mix-mix", and in grey the "in-out". The blue dashed vertical lines show the zero absorption level. In coloured dashed lines we show the Gaussian fit to the histograms.

Appendix C: TiO and VO cross-correlation maps

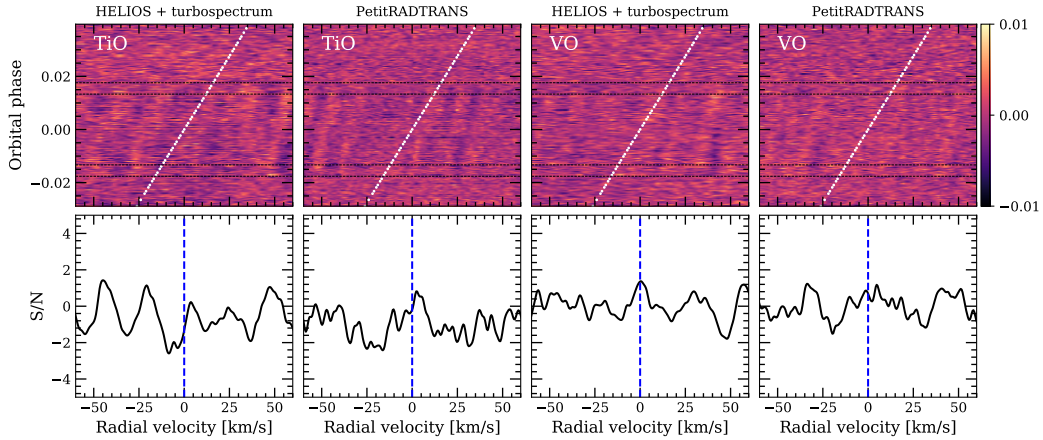

Fig. C.1: Cross-correlation results of both nights combined for TiO and VO, obtained assuming different atmospheric models (HELIOS+`turbospectrum` and `PetitRADTRANS`). *Top panel*: cross-correlation maps of the TiO (first and second columns) and VO (third and fourth columns). *Bottom panel:* average of the in-transit cross-correlation values in the planet rest frame between the first and fourth contacts. The vertical axis is shown in S/N units for a better visualisation of the features strength, computed as described in Section 4.2. Positive S/N means correlation (see CCF values in the colour bar).

7

Summary, conclusions and future work

Alright the way I see it, there's only two possible outcomes. Either I make it down there in one piece and I have one hell of a story to tell, or I burn up in the next ten minutes. Either way whichever way, no harm no foul. Cause either way, it'll be one hell of a ride. I'm ready.

– *Gravity,* 2013

In this thesis, we have analysed transit observations of four exoplanets obtained with several high-resolution spectrographs, paying special attention to the methodology and other phenomena that could influence the atmospheric detections. This chapter summarises the main results and conclusions of this work, and describes complementary studies that could be carried out in the near future in line with the ones presented here.

7.1 Summary of the main results

High resolution spectroscopy observations are currently one of the most powerful tools to study the atmosphere of exoplanets. After the first atmospheric study using a high-dispersion spectrograph by Redfield et al. (2008), the number of studies rapidly increased, leading to the characterisation of tens of exoplanets at the moment of writing this thesis. During the last few years, the community has gained strong experience in high-resolution spectroscopy observations, leading to a considerable improvement of the methodologies and of the observa-

tional discovery and understanding of theoretically predicted phenomena that can make the atmospheric characterisation more challenging, but also more interesting at the same time.

TABLE 7.1— Summary of my publications related to the characterisation of exoplanet atmospheres by means of high resolution spectroscopy. The publications included in this thesis are in bold.

Exoplanet	Spectrograph	Detected[a]	Reference
HD 189733 b	HARPS	NaI	**Casasayas-Barris et al. (2017)**
	CARMENES	HeI	Salz et al. (2018)
WASP-69 b	HARPS-N	NaI	**Casasayas-Barris et al. (2017)**
	CARMENES	HeI	Nortmann et al. (2018)
MASCARA-2 b	HARPS-N	NaI, HI	**Casasayas-Barris et al. (2018)**
	HARPS-N/CARMENES	NaI, HI, FeII, CaII	**Casasayas-Barris et al. (2019)**
	HARPS-N	FeI, FeII	Stangret et al. (2020)
WASP-33 b	HARPS-N/CARMENES	CaII	Yan et al. (2019)
WASP-33 b	HARPS-N/CARMENES	HI	Yan et al. (2020b; submitted)
KELT-9 b	HARPS-N/CARMENES	CaII	Yan et al. (2019)
WASP-52 b	ESPRESSO	NaI, KI, HI	Chen et al. (2020b)
HD 209458 b	CARMENES	H_2O	Sánchez-López et al. (2019)
	HARPS-N/CARMENES	–	**Casasayas-Barris et al. (2020b)**
	ESPRESSO	–	**Casasayas-Barris et al. (2020a)**
WASP-76 b	ESPRESSO	FeI	Ehrenreich et al. (2020)
	ESPRESSO	LiI, NaI, MgI, CaII, MnI, FeI, KI, ~~TiO~~, ~~VO~~, ~~ZrO~~	Tabernero et al. (2020; submitted)
GJ 3470 b	CARMENES	HeI	Palle et al. (2020a)
Au Mic b	ESPRESSO	–	Palle et al. (2020b)
WASP-74 b	HARPS-N	~~HI~~	Luque et al. (2020)
WASP-21 b	HARPS/-N	NaI	Chen et al. (2020a)
WASP-189 b	HARPS-N	FeI	Yan et al. (2020)
WASP-121 b	ESPRESSO	NaI, HI, KI, Li, CaII MgI, FeI, FeII, CrI, VI	Borsa et al. (2020)
WASP-127 b	ESPRESSO	NaI, ~~Li~~, ~~KI~~, ~~HI~~	Allart et al. (2020)
GJ 9827 b	CARMENES	~~HeI~~	Carleo et al. (2020; submitted)
TOI-1431 b	HARPS-N	~~FeI~~, ~~FeH~~, ~~CaI~~, ~~TiO~~, ~~VO~~, ~~HK~~	Stangret et al. (2020b; in prep.)

[a] '–' means that the transmission spectrum could not be characterised for some reason. A crossed specie means a negative result on the search for that particular specie (non-detection), which was a priori expected.

This thesis is based on the atmospheric characterisation of four different exoplanets using observations performed with several high resolution spectroscopy facilities, which resulted in five publications (Casasayas-Barris et al. 2017, 2018,

2019, 2020a, 2020b) presented in Chapters 2 to 6. In parallel with the main results of this thesis, I have established several collaborations, resulting in several publications in this same field. Table 7.1 summarises the results of these publications where I am coauthor, and the studies included in this thesis.

The first exoplanet studied here is HD 189733b. Following the methodology and using the same observations as did Wyttenbach et al. (2015), the NaI detection in HD 189733b atmosphere is reproduced. At the same time, following the same exact methodology, new WASP-69b HARPS-N observations are analysed, showing the presence of NaI in the atmosphere of this planet, but only resolving one line of the doublet (see Chapter 2). In contrast with Wyttenbach et al. (2015), the methodology used to correct the imprints from the Earth atmosphere is based on atmospheric models and considers the Earth movement during the observations. Moreover, the analysis presented here takes into account, for the first time, the presence of two effects that occur during the transit of an exoplanet and have an impact on the transmission spectrum: the Rossiter-McLaughlin (RM) and the centre-to-limb variation (CLV).

In Chapters 3 and 4, HARPS-N and CARMENES transit observations of the ultra hot Jupiter MASCARA-2b are analysed. The methodology used to extract the transmission spectrum corrects the RM and CLV deformation of the stellar lines, which can be easily distinguished from the atmospheric absorption produced by the exoplanet atmosphere. The two-dimensional analysis of the spectral time series clearly show the stellar CLV and RM effects, but also the exoplanet atmosphere, which changes its position in time at the expected radial-velocity of the exoplanet during the transit. The resulting transmission spectrum shows absorption lines centred at the Hα, Hβ, NaI, CaII triplet and the FeII position. These results are consistent with the theoretical predictions for ultra-hot Jupiters presented in Helling et al. (2019), among others. Due to the large amount of irradiation received from the host star and their tidally locked orbit, the molecules are dissociated and the permanent extremely hot day-side atmosphere is mainly composed by ions.

Chapters 5 and 6 show the analysis of HD 209458b, one of the most famous and well-studied exoplanets. Using several archival observations with HARPS-N and CARMENES, the results show that the high resolution transmission spectrum of the exoplanet is consistent with the modelled CLV and RM effects on the stellar line profiles, but at low S/N. When comparing with previous measurements, our results reveal that previous HST NaI detections by Sing et al. (2008) can alternatively be explained as the combination of both effects. On the other hand, the NaI transmission light curves by Snellen et al. (2008) and Albrecht et al. (2009) seem to be consistent with the results obtained with HARPS-N and CARMENES, which show relatively low S/N and can not be

easily interpreted. With new ESPRESSO observations, the results obtained with HARPS-N and CARMENES are confirmed at high S/N. The RM effect is clearly visible in the observations, which overlaps with the position where the planet atmospheric features are expected in the transmission spectrum. At the precision of ESPRESSO observations, the results are better explained when only the most intense effect, the RM, is considered in the modelling, suggesting an overestimation of the CLV. On the other hand, the strengths of the modelled CLV and RM effects are compared when assuming different stellar atmospheric models, showing a better agreement with those NaI models that consider non-local thermodynamic equilibrium. However, due to the intrinsic uncertainties of the modelled effects, we are not able to prove whether a 0.1% of absorption derived from Snellen et al. (2008) is hidden under the RM deformation of our observations. We conclude that the detection of Na in HD 209458b by the current set of high-resolution spectroscopic observational data is not supported. However, at low resolution where the broad wings of the spectral lines are probed, the situation could be different.

7.2 Conclusions

This thesis has grown up with the fast improvement of high resolution spectroscopy methodologies and the increasing knowledge of particular phenomena that should be considered in these kind of atmospheric studies. It starts with Chapter 2, mainly based on finding the methodology to extract the transmission spectrum when only a couple of results existed in the literature and ends with high precision ESPRESSO observations dealing with stellar surface variations (Chapter 6), made when atmospheric studies using high resolution spectroscopy have become relatively common. This thesis improves some aspects of the methodology to extract the transmission spectrum of exoplanets, but also contributes with several discoveries.

Conclusions related to the methodology

The excess of absorption produced by the exoplanet atmosphere in the stellar spectrum is usually of the order of 1 %. This means that small variations in the observations can easily lead to a wrong interpretation of the results. Below, we summarise the points related to the methodology addressed in this thesis.

- Removing the contamination from the Earth atmosphere (telluric lines) is one of the first challenges of the search for faint atmospheric features from the exoplanet atmosphere using high resolution spectroscopy observations. One of the main techniques to correct this contamination was

based on the telluric lines dependence with airmass, in order to scale the telluric absorption lines of all time series to the same airmass, that is, to the same absorption level (e.g. Wyttenbach et al. 2015). However, during the observations, the telluric lines change their position due to the Earth's movement with respect the Solar System's barycentre. Although this change is usually sub-pixel sized, after dividing each exposure by the averaged stellar spectrum, small spurious signals appear in the telluric lines' positions. In Chapter 2 we stress this issue and suggest an alternative method based on scaling a telluric model, which takes into account the Earth radial-velocity at each exposure. Lately, an ESO tool called `Molecfit` (Smette et al., 2015; Kausch et al., 2015) has become one of the most used ones to remove the O_2 and H_2O telluric absorption contamination, due to its ability to achieve photon noise precision. The accuracy of the telluric lines removal is a key factor to determine the signals from the exoplanet atmosphere. The exoplanet atmosphere imprints extremely faint features in the stellar spectrum, which can be easily mimicked or erased by telluric residuals. This becomes extremely important in the search for water vapour, for example, where the contamination introduced by the Earth atmosphere becomes critical.

- The Earth atmosphere imprints absorption and emission lines in the observed spectra. The emission lines are not corrected with the common model-based methodologies described in the previous point, which only consider O_2 and H_2O telluric absorption lines. This is the case, for example, of the NaI sky emission detected in some of the observations presented in Chapter 2 and Chapter 5. When the observations are performed with fibre-fed spectrographs, the sky emission can be monitored simultaneously to the science object using a second fibre. Although the efficiency of both fibres is not exactly the same, one can use the sky spectrum to check the existence and find the position of these emission lines. Similarly to the telluric absorption lines, the emission lines change with the airmass during the observations. Small uncorrected variations could introduce features in the transmission spectrum which can be easily interpreted as signals from the exoplanet atmosphere. The importance of simultaneous sky observations is firstly pointed out in Chapter 2, where the telluric NaI emission is directly corrected with the sky observations. In consequence, current observing strategies for atmospheric studies of exoplanets using high dispersion spectrographs include simultaneous sky observations.

- Using high resolution spectroscopy, the observations are sensitive to the

exoplanet's movement. This means that, if the planet imprints a detectable transmission spectrum in the observations, the atmospheric features will change their position in the spectrum with time. The evolution of these features can be observed using two-dimensional (2D) maps, showing the results of each exposure. Although these analysis are relatively common when using cross-correlation techniques due to the higher S/N achieved in the results, this is not the case in the analysis of single lines. In Chapter 3, the first 2D analysis of the time series around several single lines is performed, where the RM effect and absorption from the exoplanet atmosphere can be tentatively observed during the transit. In Chapter 4, after combining more observations, the RM, CLV, and absorption of different spectral lines are clearly observed in the data, showing the expected evolution in time during the transit. These 2D analysis can also help to distinguish stellar activity (e.g. Palle et al. 2020b) and pulsations (e.g. Yan et al. 2019). The features that the planet imprints in the stellar spectrum are usually masked by the noise, and different phenomena can easily reproduce an absorption-like feature. However, if this absorption signal only appears during the transit, and if it changes its position in time following the radial-velocity of the exoplanet, it has a large probability to have an atmospheric origin. 2D maps, together with other tests, are now used in almost all atmospheric studies as a verification of the nature of the features observed in the transmission spectrum, adding robustness to the detections.

Conclusions related to the science

This work shows the discovery of several species in the atmosphere of particular exoplanets and important stellar phenomena that may affect their transmission spectra. The following points describe the conclusions of these discoveries.

- Ultra hot Jupiter planets are located very close to their host stars receiving a large amount of irradiation on the day-side atmosphere, expecting them to present close to stellar-like atmospheric temperatures (Parmentier et al., 2018; Arcangeli et al., 2018). KELT-9b was the first ultra hot Jupiter studied at high-resolution spectroscopy, which ended up with the detection of several atomic and ionised metals by Hoeijmakers et al. (2018, 2019) in its atmosphere. In Chapter 3 and 4, we present the transmission spectrum of MASCARA-2b, the second ultra hot Jupiter whose atmosphere has been analysed at high resolution. We show the detection

of metals: NaI, the first ever detections of CaII triplet and individual FeII single lines, and the tentative detection of MgI. These results are consistent with theoretical simulations by Helling & Rimmer (2019), which predict an upper day-side atmosphere with a temperature higher than 3000 K due to the stellar radiation, causing these atmospheres to be composed of atoms and ions rather than molecules, which become dissociated at those temperatures. Moreover, Helling et al. (2019) show that two very different hemispheres are expected in the atmospheres of ultra hot Jupiters, due to their proximity to the host star and their tidally locked orbits: a cloudy night-side and a cloud-free day-side that forms a thermal ionosphere. Transmission spectroscopy observations explore the terminator of the exoplanet atmosphere where both day- and night-sides are mixed up. The relatively large diversity of ions and atoms detected in MASCARA-2b (HI, NaI, MgI, CaII and FeII) suggests the presence of an ionosphere in the day-side atmosphere of ultra hot Jupiters as theoretically predicted, and shows that these exoplanets are excellent laboratories to study the atmospheric chemistry. Recently, the presence of these species has been confirmed in MASCARA-2b by Stangret et al. (2020), Nugroho et al. (2020) and Hoeijmakers et al. (2020a) using the cross-correlation technique, together with the new detection of FeI. Other atmospheric studies have also shown the presence of metals in the atmosphere of ultra hot Jupiters (e.g Yan et al. 2019; Seidel et al. 2019; Borsa et al. 2020). In the near future, high-resolution spectrographs such as HIRES for the ELT, will be able to disentangle the complex picture of ultra hot Jupiters atmospheres through the detailed sampling of the composition at different altitudes and hemispheres (e.g. Ehrenreich et al. 2020).

- In Chapter 3, we present the first (tentative) detection of Hα in an ultra hot Jupiter, which is confirmed in Chapter 4, after combining several nights of observations. These planets typically receive a large amount of extreme ultraviolet radiation from the host star, which produces the expansion of their atmosphere and excites the atomic hydrogen to produce Hα absorption (Bourrier et al., 2016). In extreme cases, photo-evaporation causes a transonic planetary wind, and the mass loss rate could affect the planetary evolution (Salz et al., 2015). The Hα detection in MASCARA-2b corresponds to a hydrogen exosphere (Gebek & Oza, 2020) extending to 1.2 times the radius of the planet, far from its Roche Lobe radius. However, Yan & Henning (2018) present the detection of Hα around KELT-9b, the ultra hot Jupiter with highest day-side temperature (4600 K), measuring a hydrogen exosphere around 1.64 times the radius

of the planet, close to its Roche Lobe. Cauley et al. (2019) reproduced the Hα detection in KELT-9b and reported significant absorption in Hβ. On the other hand, Wyttenbach et al. (2020) recently reported the Hγ and Hδ measurements in this same planet. The transmission spectrum of MASCARA-2b presented in Chapter 4 shows the Hβ detection and a tentative feature of Hγ. These results show that ultra hot Jupiters present an exciting opportunity to study photoevaporation and mass loss processes with state-of-the-art spectrographs such as ESPRESSO, which will be able to characterise the Hγ features observed in MASCARA-2b, and provide constrains for planetary theories of formation and evolution.

- Although Louden & Wheatley (2015) and Yan et al. (2017) were the first studies pointing out the importance of the RM and CLV effects in atmospheric studies, their initial importance remained limited. With the discovery of new exoplanets around bright stars with potential interest for atmospheric studies, the CLV and RM effects have gained importance when their impact became clear in higher S/N observations. Their impact on the transmission spectra depends, basically, on the system geometry. For some systems, they do not prevent the detection of the atmosphere but modify the measured absorption (see Chapters 3 and 4). However, for other systems, as observed for HD 209458b in Chapters 5 and 6, their impact on the transmission spectrum makes the detection of the atmosphere particularly challenging. The studies presented in this thesis point out the necessity of accounting for the CLV and RM effects for a correct interpretation of the features observed in the transmission spectra of exoplanets, and stress the importance of detailed modelling of both effects when the characterisation of small Earth-like planets around low-mass stars is attempted with the ELTs in the coming decades. Moreover, we show that previous atmospheric studies have overlooked these effects and may need to be revised.

7.3 Future work

In this thesis, we have studied the transmission spectrum of several exoplanets, including hot and ultra hot Jupiters. These analysis have contributed to a better characterisation and understanding of their atmospheres. However, complementary research in this line could be done in the near future in order to understand other aspects of these atmospheres and refine the high resolution methodologies.

Understanding the chemistry and dynamics of ultra hot Jupiter atmospheres

Brown dwarfs are defined as the intermediate objects between low-mass stars and gas giant planets, ranging from 11-16 M_J, the approximate mass for the deuterium fusion, to 75-80 M_J, the approximate mass for the hydrogen fusion, depending on the chemical composition of the objects (Baraffe et al., 2002; Spiegel et al., 2011). Although brown dwarfs have been studied as analogues of giant planets because their spectral observations are more feasible than for extrasolar planets, the differences and/or similarities between brown dwarfs and giant planets are still under debate. A class of massive exoplanets with equilibrium temperatures comparable to stellar objects has recently been uncovered: the ultra hot Jupiters (UHJ, Parmentier et al. 2018).

One of the most massive UHJ known to date is WASP-18b, which has a mass of 10 M_J, a period shorter than 1 day and an equilibrium temperature of 2400 K (Hellier et al., 2009). The theoretical simulations made by Helling et al. (2019) show that the high temperatures of the day-side do not allow condensation and, in consequence, clouds are not formed. These high temperatures in the upper atmosphere imply that the day-side is mainly composed of atoms and ions (Helling & Rimmer, 2019) and, in extreme conditions, emission from Hα, O, C, Si, AlII, TiII, FeII could also be present in their spectrum. Using eclipse observations of brown dwarfs and UHJ, it is possible to probe the day-side atmosphere of these objects, and compare their composition and dynamics. Using HST observations of planet secondary eclipses, the temperature inversion in the day-side of WASP-18b was already proven by Sheppard et al. (2017), which seems to be a recurrent scenario for other less massive UHJ, such as WASP-33b (Haynes et al., 2015; Nugroho et al., 2017), WASP-121b (Evans et al., 2017), and WASP-103b (Kreidberg et al., 2018), for example. Similarly, brown dwarfs irradiated by white dwarfs show emission lines at high altitudes, which originate at the hot upper atmospheric regions (Longstaff et al., 2017). Also, it has been shown that the ionisation of the atmospheric gas in the upper high-altitude regions of brown dwarfs is increased by the external radiation, as observed in the day-side of UHJ. Recently, FeI emission from the day-side has been detected in two different UHJ by Pino et al. (2020) and Yan et al. (2020) using eclipse observations with HARPS-N, which proves the thermal inversion of the day-side. These studies, if also applied to brown dwarfs, will lead to a better understanding of the transition between gas giants and brown dwarfs, which remains unclear, and also to an improved characterisation of the day-side atmosphere of these extreme objects.

On the other hand, the large temperature differences between day- and night-side hemispheres of UHJs lead to different composition and circulation

from day-side to night-side. Using high resolution transit spectroscopy observations, there have been several atmospheric studies of these planets showing the presence of a large diversity of species in their terminator (see Chapter 4). Ehrenreich et al. (2020) detected, for the first time, FeI variations between the morning and evening terminators of WASP-76b, suggesting that FeI atoms may be condensing on the night-side of the planet. A similar study was performed by Salz et al. (2018) but in the near infrared region (HeI) using CARMENES observations. These chemical and dynamical differences can be studied by focusing on the variations of the transmission spectrum extracted during in the ingress, mid-transit and egress of the planet during the transit. As some of these UHJ orbit around very bright stars and have already been observed with different facilities, a first preliminary study would be possible using archival data from 3.5m telescopes such as HARPS, HARPS-N, and CARMENES. With the precision of high resolution spectrographs located at larger telescopes such as ESPRESSO at VLT, we would be able to check the transmission spectrum of the potential candidates, and study the wind speed, equivalent width values and temperature profile differences in the exoplanet hemispheres.

Obliquity measurements of ultra hot Jupiters

During this thesis, a relative large number of transits have been observed using high resolution spectroscopy. Although only the analysis of MASCARA-2b is included here, a total of eight UHJ have been observed with the time awarded to this thesis. Because of weather conditions, not all data sets have been useful for atmospheric studies due to the signal-to-noise ratio achieved, but they are still useful for other scientific purposes. This is the case, for example, of measuring the obliquity (or spin-orbit alignment) of the systems.

Most UHJ orbit around fast rotating early type stars, whose spectra present only a few broad lines, resulting in low precision radial-velocity measurements. Fortunately, the expected RM amplitude for these planets is relatively large (see equation 1.1). Although some of these exoplanets already have obliquity measurements in the literature, most of them have been performed using observations with lower precision. The observations performed with HARPS-N and CARMENES show more accurate radial-velocity measurements that could be used to better constrain their spin-orbit alignments.

Going one step further, this study could be homogeneously applied to existing high-resolution transit spectroscopy observations of other UHJ, which have not been analysed for this kind of studies. These measurements would help to populate the λ-T_{eff} diagram from Winn et al. (2010) (see Figure 1.3), which suggests a transition around an effective temperature of 6250 K between those

systems showing aligned and misaligned orbits, and to better understand their evolution histories. Moreover, it would help constrain the system parameters to better characterise the exoplanet atmospheres.

Rossiter-McLaughlin and centre-to-limb variation modelling improvement

As shown in the different analysis presented in this thesis, the RM and CLV effects on the stellar line profiles are one of the challenges when attempting to characterise the signals from an exoplanet's atmosphere using high resolution spectroscopy observations. The impact of the RM effect in the transmission spectrum of an exoplanet depends on the geometry of the system and the rotation velocity of the star. For MASCARA-2b (see Chapters 3 and 4), for example, although the impact of the RM is not critical in order to claim or not a detection, the absorption depth measurements differ if this effect is not corrected. In other cases, the RM effect falls exactly where we expect the planetary atmospheric signature (at the same radial-velocities) making it very difficult to disentangle the different contributions. This is the case of the hot Jupiter HD 209458b (see Chapters 5 and 6). The CLV, on the other hand, strongly depends on the stellar spectral type. For the exoplanets studied in this thesis, the CLV is not the main contribution, but it could become important for cooler stars. The impact of these effects in the transmission spectrum of exoplanets is now starting to be considered in most of the atmospheric analysis presented by the community. However, several previous atmospheric studies missed them, and the interpretation of the transmission spectrum may need to be revised.

In this thesis, both RM and CLV effects are modelled as presented in Yan & Henning (2018) and Yan et al. (2017). Currently, this computation depends on one-dimensional (1D) stellar atmospheric models usually computed under the local thermodynamic equilibrium assumption, and assume solid body rotation in the RM effect computation, which is not necessarily correct for all systems. For those systems where the effects and the atmospheric absorption can be easily (and visually) disentangled, such as MASCARA-2b, the models can be scaled to the intensity of the observations and be removed (see for example Yan & Henning 2018). This is not the case for planets like HD 209458b where the different contributions overlap. In these cases, accurate models are needed to be sure that the resulting transmission spectrum does or does not contain contributions from the exoplanet atmosphere.

There are different phenomena that could be incorporated to the computation in order to improve the accuracy of the modelled CLV and RM effects. The RM could be affected by convective blue shift (Dravins et al., 2017), a consequence of the stellar granulation that occurs because the emerging gran-

ules are brighter than the surroundings (Dravins, 1982). This produces a blue shift of the stellar lines that becomes less intense in deep lines formed higher in the stellar atmosphere (Reiners et al., 2016). Granulation and star-spots can produce asymmetric line profiles, and could be considered using 3D magneto-hydrodynamic simulations (Cegla et al., 2016b). Similarly, it has been observed that the CLV predictions are better described using 3D stellar atmospheric models than using the 1D approximation (Hayek et al., 2012), due to the description of the atmospheric temperature structure. In addition, differential rotation can become important in main sequence stars (Karoff et al., 2018), producing an amplitude variation of the RM signal during the transit, and could be considered as presented in Serrano et al. (2020).

Exploration of the near-infrared wavelengths

At high resolution spectroscopy, the near-infrared wavelength region has mainly been explored using the cross-correlation technique, looking for molecules such as H_2O (Birkby et al., 2013), CO (Snellen et al., 2010), and CH_4 (Guilluy et al., 2019). The analysis of single lines, however, has been focused on the search for metastable helium (HeI) at 10830 Å, after its discovery by Nortmann et al. (2018) and Allart et al. (2018) in the atmosphere of two exoplanets using observations performed with the CARMENES spectrograph. Thanks to the wide wavelength coverage of the CARMENES visible channel, the first detection of the CaII IRT at 8500 Å has also been possible (see Chapter 4).

Contrarily to the visible range, the near-infrared exploration is still limited, mainly due to the limited number of high-resolution spectrographs covering those regions, and the strong telluric contamination. Currently, CARMENES at a 3.5m telescope is one of the best instruments for high resolution spectroscopy near-infrared studies. On the other hand, the high-resolution near-infrared spectrograph GIANO-B on the 3.6 m TNG has recently shown its feasibility for atmospheric studies in Brogi et al. (2018) and Guilluy et al. (2019, 2020). Both instruments have several data sets publicly available that could be examined. For example, Kesseli et al. (2020) recently applied a massive search of FeH in the CARMENES near-infrared observations of twelve exoplanets, showing some tentative detections.

A search for high opacity molecules and atoms in the near infrared wavelengths for very different exoplanets in terms of the irradiation received from their host star, for example, could be theoretically performed using atmospheric simulations with tools such as `petitRADTRANS` (Mollière et al., 2019). With this information, an homogeneous observational search for the most promising species could be carried out using archival near-infrared data from 3.5m

telescopes of different exoplanets. With the upcoming CRIRES+ near-infrared spectrograph at VLT (planned to be offered to the community on February-March 2021) it would be possible to confirm some potential prior results, that were limited by signal-to-noise. This study would help to statistically understand the composition of the exoplanets depending on their system properties and how the atmospheric constituents correlate with particular parameters. Last but not least, for a better understanding of the results, such a study would require an accurate study of the RM and CLV effects on the near-infrared spectral lines, not contemplated in most of the previous atmospheric studies, but shown to be important in the near-infrared wavelengths (Brogi et al., 2016).

Characterising exoplanet atmospheres with the ELTs

The ultimate objective of the exoplanet research is the detection of extraterrestrial life evidence using biomarkers. The next generation of extremely large ground-based telescopes, the so-called ELTs, will push the exoplanet community one step further towards this goal. The ELTs are a group of three telescopes that are planed to be offered to the community in a decade. This is the case of the 25 m diameter Giant Magellan Telescope (GMT; Johns 2008), the 30 m Thirty Meter Telescope (TMT; Nelson & Sanders 2008), and the 39 m European-Extremely Large Telescope (E-ELT; Gilmozzi & Spyromilio 2007). All three telescopes will be equipped with high resolution spectrographs, being able to discover and characterise smaller planets. With an aperture of around 40 meters, for example, the E-ELT will collect 24 times more photons than one VLT (whose aperture is 8 m), corresponding to objects with 3.5 magnitudes fainter. This particular telescope will be equipped with two high resolution spectrographs ($\Re \sim 100\ 000$): the Mid-infrared E-ELT Imager and Spectrograph (METIS; Brandl et al. 2008), covering from 2.9 to 5.0 μm, and the High Resolution Spectrograph (HIRES; Marconi et al. 2016), with a wavelength coverage from 0.37 to 2.5 μm.

Using high dispersion spectroscopy observations with ELTs it will be possible to detect individual spectral lines from the atmosphere of gas giants at high precision, constructing the real spectrum of the planet at high resolution instead of needing the combined lines' signal, obtained by using the cross-correlation technique. This will permit an accurate study of the strength of individual molecular and atomic lines. As different spectral lines are formed at different altitudes, this will prove the temperature-pressure profiles of the atmospheres. Also, the study of the lines' broadening and the velocity shifts that the spectral lines experience during the ingress and egress of a transit will reveal information about circulation and planet rotation, as tentatively observed by Showman

et al. (2010). This would help understanding the global circulation on an exoplanet and, consequently, describe the physics of their atmospheres. Besides transmission spectroscopy, due to the larger apertures, with the ELTs it will be possible to sample the exoplanet spectrum at different orbital phases, observing variations of the molecular signals as function of the planet longitude and, therefore, we may observe the changes in the temperature structure of their atmosphere (Cho et al., 2003).

Despite that several transit observations will be required, the ELTs will enable the atmospheric characterisation of smaller planets, such as super-Earths. In addition to the detailed study of their atmospheric composition, the measurement of ratios of isotopes will provide important insights in the atmospheric evolution of these exoplanets (Mollière & Snellen, 2019). The ELTs will also be able to characterise Earth-like planets and to detect oxygen after combining the observations of a few dozens of transits (Snellen et al., 2013). Although the detection of oxygen will not be sufficient to claim the existence of extraterrestrial life, its discovery in a rocky planet located in the habitable zone will be a huge progress and a motivation to continue the search for an inhabited Earth-like twin.

Bibliography

Abetti, G. & Castelli, I. 1935, Osservazioni e memorie dell'Osservatorio astrofisico di Arcetri, 53, 25

Addison, B. C., Horner, J., Wittenmyer, R. A., et al. 2020, arXiv e-prints, arXiv:2006.13675

Albrecht, S. 2012, in From Interacting Binaries to Exoplanets: Essential Modeling Tools, ed. M. T. Richards & I. Hubeny, Vol. 282, 379–384

Albrecht, S., Snellen, I., de Mooij, E., & Le Poole, R. 2009, in IAU Symposium, Vol. 253, Transiting Planets, ed. F. Pont, D. Sasselov, & M. J. Holman, 520–523

Albrecht, S., Winn, J. N., Johnson, J. A., et al. 2012, ApJ, 757, 18

Allart, R., Bourrier, V., Lovis, C., et al. 2018, Science, 362, 1384

Allart, R., Pino, L., Lovis, C., et al. 2020, arXiv e-prints, arXiv:2010.15143

Alonso-Floriano, F. J., Sánchez-López, A., Snellen, I. A. G., et al. 2019a, A&A, 621, A74

Alonso-Floriano, F. J., Snellen, I. A. G., Czesla, S., et al. 2019b, A&A, 629, A110

Appenzeller, I. & Schröter, E. H. 1967, ApJ, 147, 1100

Arcangeli, J., Désert, J.-M., Line, M. R., et al. 2018, ApJL, 855, L30

Astudillo-Defru, N. & Rojo, P. 2013, A&A, 557, A56

Bailey, E. & Batygin, K. 2018, ApJL, 866, L2

Baraffe, I., Chabrier, G., Allard, F., & Hauschildt, P. H. 2002, A&A, 382, 563

Batalha, N. M., Rowe, J. F., Bryson, S. T., et al. 2013, ApJS, 204, 24

Batygin, K., Bodenheimer, P. H., & Laughlin, G. P. 2016, ApJ, 829, 114

Birkby, J. L. 2018, Spectroscopic Direct Detection of Exoplanets, 16

Birkby, J. L., de Kok, R. J., Brogi, M., et al. 2013, MNRAS, 436, L35

Birkby, J. L., de Kok, R. J., Brogi, M., Schwarz, H., & Snellen, I. A. G. 2017, AJ, 153, 138

Borsa, F., Allart, R., Casasayas-Barris, N., et al. 2020, arXiv e-prints, arXiv:2011.01245

Borucki, W. J., Koch, D., Basri, G., et al. 2010, Science, 327, 977

Bourrier, V., Cegla, H. M., Lovis, C., & Wyttenbach, A. 2017, A&A, 599, A33

Bourrier, V., Ehrenreich, D., Lendl, M., et al. 2020, A&A, 635, A205

Bourrier, V., Lecavelier des Etangs, A., Ehrenreich, D., Tanaka, Y. A., & Vidotto, A. A. 2016, A&A, 591, A121

Bozza, V., Mancini, L., & Sozzetti, A. 2018, Astrophysics of Exoplanetary Atmospheres, Vol. 450

Brandl, B. R., Lenzen, R., Pantin, E., et al. 2008, in Society of Photo-Optical Instrumentation Engineers (SPIE) Conference Series, Vol. 7014, Ground-based and Airborne Instrumentation for Astronomy II, 70141N

Brogi, M., de Kok, R. J., Albrecht, S., et al. 2016, ApJ, 817, 106

Brogi, M., Giacobbe, P., Guilluy, G., et al. 2018, A&A, 615, A16

Brogi, M., Line, M., Bean, J., Désert, J. M., & Schwarz, H. 2017, ApJL, 839, L2

Brogi, M., Snellen, I. A. G., de Kok, R. J., et al. 2012, Nature, 486, 502

Brown, T. M. 2001, ApJ, 553, 1006

Bryson, S., Kunimoto, M., Kopparapu, R. K., et al. 2020, arXiv e-prints, arXiv:2010.14812

Burrows, A., Hubbard, W. B., Lunine, J. I., Marley, M., & Saumon, D. 1998, arXiv e-prints, astro

Casasayas-Barris, N., Palle, E., Nowak, G., et al. 2017, A&A, 608, A135

Casasayas-Barris, N., Palle, E., Stangret, M., et al. 2020a, A&A

Casasayas-Barris, N., Pallé, E., Yan, F., et al. 2018, A&A, 616, A151

Casasayas-Barris, N., Pallé, E., Yan, F., et al. 2019, A&A, 628, A9

Casasayas-Barris, N., Pallé, E., Yan, F., et al. 2020b, A&A, 635, A206

Cauley, P. W., Kuckein, C., Redfield, S., et al. 2018a, AJ, 156, 189

Cauley, P. W., Shkolnik, E. L., Ilyin, I., et al. 2019, AJ, 157, 69

Cauley, P. W., Shkolnik, E. L., Ilyin, I., et al. 2020, Research Notes of the American Astronomical Society, 4, 53

Cauley, P. W., Shkolnik, E. L., Llama, J., Bourrier, V., & Moutou, C. 2018b, AJ, 156, 262

Cegla, H. M., Lovis, C., Bourrier, V., et al. 2016a, A&A, 588, A127

Cegla, H. M., Oshagh, M., Watson, C. A., et al. 2016b, ApJ, 819, 67

Charbonneau, D., Allen, L. E., Megeath, S. T., et al. 2005, ApJ, 626, 523

Charbonneau, D., Brown, T. M., Latham, D. W., & Mayor, M. 2000, ApJL, 529, L45

Charbonneau, D., Brown, T. M., Noyes, R. W., & Gilliland, R. L. 2002, ApJ, 568, 377

Chen, G., Casasayas-Barris, N., Palle, E., et al. 2020a, arXiv e-prints, arXiv:2007.13429

Chen, G., Casasayas-Barris, N., Pallé, E., et al. 2020b, A&A, 635, A171

Chen, G., Guenther, E. W., Pallé, E., et al. 2017a, A&A, 600, A138

Chen, G., Pallé, E., Nortmann, L., et al. 2017b, A&A, 600, L11

Chen, G., Pallé, E., Welbanks, L., et al. 2018, A&A, 616, A145

Cho, J. Y. K., Menou, K., Hansen, B. M. S., & Seager, S. 2003, ApJL, 587, L117

Collier Cameron, A., Bruce, V. A., Miller, G. R. M., Triaud, A. H. M. J., & Queloz, D. 2010, MNRAS, 403, 151

Cowan, N. B. & Fujii, Y. 2018, Mapping Exoplanets, ed. H. J. Deeg & J. A. Belmonte, 147

Crossfield, I. J. M. 2015, PASP, 127, 941

Cumming, A., Marcy, G. W., & Butler, R. P. 1999, ApJ, 526, 890

Czesla, S., Klocová, T., Khalafinejad, S., Wolter, U., & Schmitt, J. H. M. M. 2015, A&A, 582, A51

de Kok, R. J., Birkby, J., Brogi, M., et al. 2014, A&A, 561, A150

de Kok, R. J., Brogi, M., Snellen, I. A. G., et al. 2013, A&A, 554, A82

de Mooij, E. J. W. & Snellen, I. A. G. 2009, A&A, 493, L35

Deming, D., Seager, S., Richardson, L. J., & Harrington, J. 2005, Nature, 434, 740

Deming, D., Seager, S., Winn, J., et al. 2009, PASP, 121, 952

Deming, D., Wilkins, A., McCullough, P., et al. 2013, ApJ, 774, 95

Deming, L. D. & Seager, S. 2017, Journal of Geophysical Research (Planets), 122, 53

Désert, J. M., Vidal-Madjar, A., Lecavelier Des Etangs, A., et al. 2008, A&A, 492, 585

Dravins, D. 1982, ARA&A, 20, 61

Dravins, D., Ludwig, H.-G., Dahlén, E., & Pazira, H. 2017, A&A, 605, A90

Ehrenreich, D., Bourrier, V., Wheatley, P. J., et al. 2015, Nature, 522, 459

Ehrenreich, D., Lovis, C., Allart, R., et al. 2020, Nature, 580, 597

Evans, T. M., Sing, D. K., Goyal, J. M., et al. 2018, AJ, 156, 283

Evans, T. M., Sing, D. K., Kataria, T., et al. 2017, Nature, 548, 58

Fabrycky, D. & Tremaine, S. 2007, ApJ, 669, 1298

Fortney, J. J. 2005, MNRAS, 364, 649

Fossati, L., Haswell, C. A., Linsky, J. L., & Kislyakova, K. G. 2015, Astrophysics and Space Science Library, Vol. 411, Observations of Exoplanet Atmospheres and Surrounding Environments, ed. H. Lammer & M. Khodachenko, 59

Frasca, A., Freire Ferrero, R., Marilli, E., & Catalano, S. 2000, A&A, 364, 179

Fulton, B. J., Petigura, E. A., Howard, A. W., et al. 2017, AJ, 154, 109

Gebek, A. & Oza, A. V. 2020, MNRAS, 497, 5271

Gilmozzi, R. & Spyromilio, J. 2007, The Messenger, 127, 11

Guilluy, G., Andretta, V., Borsa, F., et al. 2020, A&A, 639, A49

Guilluy, G., Sozzetti, A., Brogi, M., et al. 2019, A&A, 625, A107

Gustafsson, B., Edvardsson, B., Eriksson, K., et al. 2008, A&A, 486, 951

Hansen, B. M. S. & Murray, N. 2012, ApJ, 751, 158

Hayek, W., Sing, D., Pont, F., & Asplund, M. 2012, A&A, 539, A102

Haynes, K., Mandell, A. M., Madhusudhan, N., Deming, D., & Knutson, H. 2015, ApJ, 806, 146

Hellier, C., Anderson, D. R., Collier Cameron, A., et al. 2009, Nature, 460, 1098

Helling, C., Gourbin, P., Woitke, P., & Parmentier, V. 2019, A&A, 626, A133

Helling, C. & Rimmer, P. B. 2019, arXiv e-prints, arXiv:1903.04565

Henry, G. W., Marcy, G. W., Butler, R. P., & Vogt, S. S. 2000, ApJL, 529, L41

Hirano, T., Suto, Y., Winn, J. N., et al. 2011, ApJ, 742, 69

Hoeijmakers, H. J., Cabot, S. H. C., Zhao, L., et al. 2020a, A&A, 641, A120

Hoeijmakers, H. J., de Kok, R. J., Snellen, I. A. G., et al. 2015, A&A, 575, A20

Hoeijmakers, H. J., Ehrenreich, D., Heng, K., et al. 2018, Nature, 560, 453

Hoeijmakers, H. J., Ehrenreich, D., Kitzmann, D., et al. 2019, A&A, 627, A165

Hoeijmakers, H. J., Seidel, J. V., Pino, L., et al. 2020b, A&A, 641, A123

Huitson, C. M., Sing, D. K., Vidal-Madjar, A., et al. 2012, MNRAS, 422, 2477

Jensen, A. G., Cauley, P. W., Redfield, S., Cochran, W. D., & Endl, M. 2018, AJ, 156, 154

Johns, M. 2008, in Society of Photo-Optical Instrumentation Engineers (SPIE) Conference Series, Vol. 6986, Extremely Large Telescopes: Which Wavelengths? Retirement Symposium for Arne Ardeberg, 698603

Karoff, C., Metcalfe, T. S., Santos, Â. R. G., et al. 2018, ApJ, 852, 46

Kausch, W., Noll, S., Smette, A., et al. 2015, A&A, 576, A78

Kempton, E. M. R., Bean, J. L., Louie, D. R., et al. 2018, PASP, 130, 114401

Kesseli, A., Snellen, I. A. G., Alonso-Floriano, F. J., Molliere, P., & Serindag, D. B. 2020, arXiv e-prints, arXiv:2009.04474

Khalafinejad, S., von Essen, C., Hoeijmakers, H. J., et al. 2017, A&A, 598, A131

Kley, W. & Nelson, R. P. 2012, ARA&A, 50, 211

Knutson, H. A., Charbonneau, D., Allen, L. E., Burrows, A., & Megeath, S. T. 2008, ApJ, 673, 526

Knutson, H. A., Charbonneau, D., Allen, L. E., et al. 2007, Nature, 447, 183

Komacek, T. D. & Showman, A. P. 2016, ApJ, 821, 16

Kreidberg, L., Line, M. R., Parmentier, V., et al. 2018, AJ, 156, 17

Lecavelier Des Etangs, A., Pont, F., Vidal-Madjar, A., & Sing, D. 2008, A&A, 481, L83

Lin, D. N. C., Bodenheimer, P., & Richardson, D. C. 1996, Nature, 380, 606

Longstaff, E. S., Casewell, S. L., Wynn, G. A., Maxted, P. F. L., & Helling, C. 2017, MNRAS, 471, 1728

Lothringer, J. D. & Barman, T. 2019, ApJ, 876, 69

Louden, T. & Wheatley, P. J. 2015, ApJL, 814, L24

Lovis, C., Snellen, I., Mouillet, D., et al. 2017, A&A, 599, A16

Lund, M. B., Rodriguez, J. E., Zhou, G., et al. 2017, AJ, 154, 194

Lundkvist, M. S., Kjeldsen, H., Albrecht, S., et al. 2016, Nature Communications, 7, 11201

Luque, R., Casasayas-Barris, N., Parviainen, H., et al. 2020, arXiv e-prints, arXiv:2007.11851

Majeau, C., Agol, E., & Cowan, N. B. 2012, ApJL, 747, L20

Malik, M., Grosheintz, L., Mendonça, J. M., et al. 2017, AJ, 153, 56

Malik, M., Kitzmann, D., Mendonça, J. M., et al. 2019, AJ, 157, 170

Marconi, A., Di Marcantonio, P., D'Odorico, V., et al. 2016, in Society of Photo-Optical Instrumentation Engineers (SPIE) Conference Series, Vol. 9908, Ground-based and Airborne Instrumentation for Astronomy VI, 990823

Mayor, M. & Queloz, D. 1995, Nature, 378, 355

McKemmish, L. K., Masseron, T., Hoeijmakers, H. J., et al. 2019, MNRAS, 488, 2836

McLaughlin, D. B. 1924, ApJ, 60, 22

Merritt, S. R., Gibson, N. P., Nugroho, S. K., et al. 2020, A&A, 636, A117

Mollière, P. & Snellen, I. A. G. 2019, A&A, 622, A139

Mollière, P., Wardenier, J. P., van Boekel, R., et al. 2019, A&A, 627, A67

Mordasini, C., Alibert, Y., & Benz, W. 2009, A&A, 501, 1139

Mordasini, C., Alibert, Y., Georgy, C., et al. 2012, A&A, 547, A112

Murgas, F., Chen, G., Nortmann, L., Palle, E., & Nowak, G. 2020, A&A, 641, A158

Murgas, F., Pallé, E., Parviainen, H., et al. 2017, A&A, 605, A114

Murtagh, F. & Heck, A. 1987, A&AS, 68, 113

Naoz, S., Farr, W. M., Lithwick, Y., Rasio, F. A., & Teyssandier, J. 2011, Nature, 473, 187

Nelson, J. & Sanders, G. H. 2008, in Society of Photo-Optical Instrumentation Engineers (SPIE) Conference Series, Vol. 7012, Ground-based and Airborne Telescopes II, ed. L. M. Stepp & R. Gilmozzi, 70121A

Nortmann, L., Pallé, E., Salz, M., et al. 2018, Science, 362, 1388

Nugroho, S. K., Gibson, N. P., de Mooij, E. J. W., et al. 2020, MNRAS, 496, 504

Nugroho, S. K., Kawahara, H., Masuda, K., et al. 2017, AJ, 154, 221

Ohta, Y., Taruya, A., & Suto, Y. 2005, ApJ, 622, 1118

Oklopčić, A. & Hirata, C. M. 2018, ApJL, 855, L11

Oshagh, M., Santos, N. C., Ehrenreich, D., et al. 2014, A&A, 568, A99

Owen, J. E. 2019, Annual Review of Earth and Planetary Sciences, 47, 67

Owen, J. E. & Wu, Y. 2013, ApJ, 775, 105

Owen, J. E. & Wu, Y. 2017, ApJ, 847, 29

Palle, E., Nortmann, L., Casasayas-Barris, N., et al. 2020a, A&A, 638, A61

Palle, E., Oshagh, M., Casasayas-Barris, N., et al. 2020b, arXiv e-prints, arXiv:2006.13609

Parmentier, V., Line, M. R., Bean, J. L., et al. 2018, A&A, 617, A110

Parviainen, H. 2015, MNRAS, 450, 3233

Pepe, F., Molaro, P., Cristiani, S., et al. 2014, Astronomische Nachrichten, 335, 8

Pepe, F. A., Cristiani, S., Rebolo Lopez, R., et al. 2010, Society of Photo-Optical Instrumentation Engineers (SPIE) Conference Series, Vol. 7735, ESPRESSO: the Echelle spectrograph for rocky exoplanets and stable spectroscopic observations, 77350F

Pino, L., Désert, J.-M., Brogi, M., et al. 2020, ApJL, 894, L27

Pino, L., Ehrenreich, D., Wyttenbach, A., et al. 2018, A&A, 612, A53

Piskunov, N. & Valenti, J. A. 2017, A&A, 597, A16

Plez, B. 2012, Turbospectrum: Code for spectral synthesis

Pollack, J. B., Hubickyj, O., Bodenheimer, P., et al. 1996, Icarus, 124, 62

Pont, F., Sing, D. K., Gibson, N. P., et al. 2013, MNRAS, 432, 2917

Press, W. H., Teukolsky, S. A., Vetterling, W. T., & Flannery, B. P. 1992, Numerical recipes in FORTRAN. The art of scientific computing

Quirrenbach, A., Amado, P. J., Caballero, J. A., et al. 2014, in , Vol. 9147, Ground-based and Airborne Instrumentation for Astronomy V, 91471F

Quirrenbach, A., Amado, P. J., Ribas, I., et al. 2018, in Society of Photo-Optical Instrumentation Engineers (SPIE) Conference Series, Vol. 10702, Ground-based and Airborne Instrumentation for Astronomy VII, 107020W

Redfield, S., Endl, M., Cochran, W. D., & Koesterke, L. 2008, ApJL, 673, L87

Reiners, A., Mrotzek, N., Lemke, U., Hinrichs, J., & Reinsch, K. 2016, A&A, 587, A65

Ricker, G. R., Winn, J. N., Vanderspek, R., et al. 2015, Journal of Astronomical Telescopes, Instruments, and Systems, 1, 014003

Rogers, L. A. 2015, ApJ, 801, 41

Rossiter, R. A. 1924, ApJ, 60, 15

Ryabchikova, T., Piskunov, N., Kurucz, R. L., et al. 2015, Physica Scripta, 90, 054005

Salz, M., Czesla, S., Schneider, P. C., et al. 2018, A&A, 620, A97

Salz, M., Schneider, P. C., Czesla, S., & Schmitt, J. H. M. M. 2015, A&A, 576, A42

Sánchez-López, A., Alonso-Floriano, F. J., López-Puertas, M., et al. 2019, A&A, 630, A53

Schlaufman, K. C. 2010, ApJ, 719, 602

Seager, S. 2010, Exoplanet Atmospheres: Physical Processes

Seager, S. & Sasselov, D. D. 1998, ApJL, 502, L157

Seager, S. & Sasselov, D. D. 2000, ApJ, 537, 916

Seidel, J. V., Ehrenreich, D., Wyttenbach, A., et al. 2019, A&A, 623, A166

Serrano, L. M., Oshagh, M., Cegla, H. M., et al. 2020, MNRAS, 493, 5928

Sheppard, K. B., Mandell, A. M., Tamburo, P., et al. 2017, ApJL, 850, L32

Showman, A. P., Cho, J. Y. K., & Menou, K. 2010, Atmospheric Circulation of Exoplanets, ed. S. Seager, 471–516

Sing, D. K., Fortney, J. J., Nikolov, N., et al. 2016, Nature, 529, 59

Sing, D. K., Vidal-Madjar, A., Désert, J. M., Lecavelier des Etangs, A., & Ballester, G. 2008, ApJ, 686, 658

Smette, A., Sana, H., Noll, S., et al. 2015, A&A, 576, A77

Snellen, I. A. G., Albrecht, S., de Mooij, E. J. W., & Le Poole, R. S. 2008, A&A, 487, 357

Snellen, I. A. G., de Kok, R. J., de Mooij, E. J. W., & Albrecht, S. 2010, Nature, 465, 1049

Snellen, I. A. G., de Kok, R. J., le Poole, R., Brogi, M., & Birkby, J. 2013, ApJ, 764, 182

Southworth, J. 2011, Monthly Notices of the Royal Astronomical Society, 417, 2166

Spiegel, D. S., Burrows, A., & Milsom, J. A. 2011, ApJ, 727, 57

Stangret, M., Casasayas-Barris, N., Pallé, E., et al. 2020, A&A, 638, A26

Stevenson, K. B., Désert, J.-M., Line, M. R., et al. 2014, Science, 346, 838

Tabernero, H. M., Zapatero Osorio, M. R., Allart, R., & Borsa, F. a. 2020, A&A

Talens, G. J. J., Justesen, A. B., Albrecht, S., et al. 2018, A&A, 612, A57

Tamuz, O., Mazeh, T., & Zucker, S. 2005, MNRAS, 356, 1466

Todorov, K. O., Deming, D., Burrows, A., & Grillmair, C. J. 2014, ApJ, 796, 100

Triaud, A. H. M. J. 2017, The Rossiter–McLaughlin Effect in Exoplanet Research, ed. H. J. Deeg & J. A. Belmonte (Cham: Springer International Publishing), 1–27

Triaud, A. H. M. J., Queloz, D., Bouchy, F., et al. 2009, A&A, 506, 377

Valenti, J. A. & Piskunov, N. 1996, A&AS, 118, 595

Vidal-Madjar, A., Arnold, L., Ehrenreich, D., et al. 2010, A&A, 523, A57

Vidal-Madjar, A., Désert, J. M., Lecavelier des Etangs, A., et al. 2004, ApJL, 604, L69

Vidal-Madjar, A., Lecavelier des Etangs, A., Désert, J. M., et al. 2003, Nature, 422, 143

von Essen, C., Czesla, S., Wolter, U., et al. 2014, A&A, 561, A48

Wakeford, H. R., Sing, D. K., Kataria, T., et al. 2017, Science, 356, 628

Weiss, L. M. & Marcy, G. W. 2014, ApJL, 783, L6

Winn, J. N., Fabrycky, D., Albrecht, S., & Johnson, J. A. 2010, The Astrophysical Journal, 718, L145

Winn, J. N., Johnson, J. A., Marcy, G. W., et al. 2006, ApJL, 653, L69

Winn, J. N., Noyes, R. W., Holman, M. J., et al. 2005, ApJ, 631, 1215

Wolszczan, A. & Frail, D. A. 1992, Nature, 355, 145

Wright, J. T. & Eastman, J. D. 2014, PASP, 126, 838

Wu, Y. & Lithwick, Y. 2013, ApJ, 772, 74

Wyttenbach, A., Ehrenreich, D., Lovis, C., Udry, S., & Pepe, F. 2015, A&A, 577, A62

Wyttenbach, A., Lovis, C., Ehrenreich, D., et al. 2017, A&A, 602, A36

Wyttenbach, A., Mollière, P., Ehrenreich, D., et al. 2020, A&A, 638, A87

Yan, F., Casasayas-Barris, N., Molaverdikhani, K., et al. 2019, A&A, 632, A69

Yan, F., Fosbury, R. A. E., Petr-Gotzens, M. G., et al. 2015, International Journal of Astrobiology, 14, 255

Yan, F. & Henning, T. 2018, Nature Astronomy, 2, 714

Yan, F., Pallé, E., Fosbury, R. A. E., Petr-Gotzens, M. G., & Henning, T. 2017, A&A, 603, A73

Yan, F., Pallé, E., Reiners, A., et al. 2020, arXiv e-prints, arXiv:2007.02716

Zechmeister, M., Reiners, A., Amado, P. J., et al. 2018, A&A, 609, A12